PENNSTATE

Center for Advanced Materials

SUPERCRITICAL WATER OXIDATION STUDIES:
Understanding the Chemistry and Electrochemistry of SCWO Systems

FINAL PROGRESS REPORT

Digby D. Macdonald, Heidi Arthur, Ritwik Biswas, Keith Eklund, Nobuyoshi Hara, Girish Kelkar, Leo Kriksunov, Chun Liu, Serguei Lvov, and Jan Mankowski
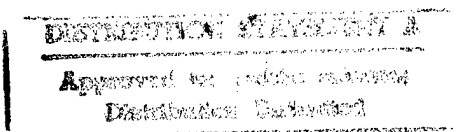
February, 1997

19970528089

DTIC QUALITY INSPECTED 3

Center for Advanced Materials
The Pennsylvania State University
517 Deike Building
University Park, PA 16802

College of Earth and Mineral Sciences

REPORT DOCUMENTATION PAGE

Public reporting burden for this collection of information is estimated to average 1 hour per response, including the time for reviewing instructions, searching existing data sources, gathering and maintaining the data needed, and completing and reviewing the collection of information. Send comment regarding this burden estimates or any other aspect of this collection of information, including suggestions for reducing this burden, to Washington Headquarters Services, Directorate for information Operations and Reports, 1215 Jefferson Davis Highway, Suite 1204, Arlington, VA 22202-4302, and to the Office of Management and Budget, Paperwork Reduction Project (0704-0188), Washington, DC 20503.

1. AGENCY USE ONLY (Leave blank)	2. REPORT DATE February 1997	3. REPORT TYPE AND DATES COVERED Final Progress Report

4. TITLE AND SUBTITLE

SUPERCRITICAL WATER OXIDATION STUDIES: Understanding the Chemistry and Electrochemistry of SCWO Systems

5. FUNDING NUMBERS

DAAL03-92-G-0397

6. AUTHOR(S)

Digby D. Macdonald, Heidi Arthur, Ritwik Biswas, Keith Eklund, Nobuyoshi Hara, Girish Kelkar, Leo Kriksunov, Chun Liu, Serguei Lvov, and Jan Mankowski

7. PERFORMING ORGANIZATION NAMES(S) AND ADDRESS(ES)

Center for Advanced Materials
The Pennsylvania State University
517 Deike Building
University Park, PA 16802

8. PERFORMING ORGANIZATION REPORT NUMBER

9. SPONSORING / MONITORING AGENCY NAME(S) AND ADDRESS(ES)

U.S. Army Research Office
P.O. Box 12211
Research Triangle Park, NC 27709-2211

10. SPONSORING / MONITORING AGENCY REPORT NUMBER

ARO 30513.18-CH

11. SUPPLEMENTARY NOTES

The views, opinions and/or findings contained in this report are those of the author(s) and should not be construed as an official Department of the Army position, policy or decision, unless so designated by other documentation.

12a. DISTRIBUTION / AVAILABILITY STATEMENT

Approved for public release; distribution unlimited.

12 b. DISTRIBUTION CODE

13. ABSTRACT (Maximum 200 words)

SuperCritical Water Oxidation (SCWO) is being actively developed as a means of destroying highly toxic organic waste and as a way of reducing the volume of low-level nuclear waste. The technology employs water at temperatures above the critical temperature (374.15K) as the reaction medium as well as high partial pressures of oxygen or high concentrations of hydrogen peroxide. These conditions lead to extraordinarily high corrosion rates within $\pm 50°C$ of T_c, which can be characterized in terms of the pH and redox potential of the medium. In this report, techniques that have been developed under ARO sponsorship for measuring pH, redox potential, $[O_2]$, $[H_2]$, and corrosion activity at high subcritical and at supercritical temperatures are described. We show that measurement of many important chemistry and corrosion parameters is technically developed in this study will allow for in close control of the reaction medium.

14. SUBJECT TERMS

15. NUMBER IF PAGES
325

16. PRICE CODE

17. SECURITY CLASSIFICATION OR REPORT UNCLASSIFIED	18. SECURITY CLASSIFICATION OF THIS PAGE UNCLASSIFIED	19. SECURITY CLASSIFICATION OF ABSTRACT UNCLASSIFIED	20. LIMITATION OF ABSTRACT UL

NSN 7540-01-280-5500

Enclosure 1

Standard Form 298 (Rev. 2-89)
Prescribed by ANSI Std. 239-18
298-102

SUPERCRITICAL WATER OXIDATION STUDIES:
Understanding the Chemistry and Electrochemistry of SCWO Systems

FINAL PROGRESS REPORT

Digby D. Macdonald, Heidi Arthur, Ritwik Biswas, Keith Eklund, Nobuyoshi Hara, Girish Kelkar, Leo Kriksunov, Chun Liu, Serguei Lvov, and Jan Mankowski

February, 1997

U.S. Army Research Office

Center for Advanced Materials
The Pennsylvania State University
517 Deike Building
University Park, PA 16802

EXECUTIVE SUMMARY

Supercritical water exhibits properties that are characteristic of both a liquid and a vapor. For example, the density of SCW (and all of its bulk physical-chemical properties) can be significantly changed by changing system pressure. Supercritical water also has a strong and unusual extraction capacity, which is also a function of density. In addition, supercritical solutions of electrolytes exhibit good conductivity, provided that the density is sufficiently high. One application of SCW is Supercritical Water Oxidation (SCWO), which is now being developed for treating highly toxic organic waste (including physiological agents) and to reduce the volume of low-level nuclear waste. Another application of SCW is its use as a heat transport fluid in supercritical thermal power plants.

Since the mid-1980s, many studies have been conducted on the properties, chemistry, and applications of SCW. This interest was mainly stimulated by the prospect of using SCWO to eliminate various wastes. This process offers virtually no emissions with very impressive destruction rates. However, the initial attempts to implement the SCWO process faced difficulties due to a lack of knowledge of the fundamental properties of supercritical aqueous fluids. Recently, many studies have been conducted to provide a better understanding of SCW. These include studies of the kinetics and mechanisms of reactions of various compounds with water, including kinetic studies on the hydrolysis and oxidation of organic solutes, spectroscopic studies, theoretical and experimental investigations of the supercritical fluid structure, solubility measurements and modeling, and molecular dynamics simulations.

A major problem inhibiting the wide implementation of SCWO is the pronounced corrosion damage that occurs in regions of the process stream that are at temperatures around the critical temperature of water (350-450°C). Few materials (mostly, noble metals) are immune to

attack. Consequently, a better understanding of chemical conditions and corrosion processes that occur in SCWO is required if the technology is to be developed in a cost effective manner. In order to optimize the oxidation process and to monitor chemical conditions in SCWO reactors, it is necessary to develop various *in situ* monitoring techniques.

In this work, fundamental aspects of the chemistry of SCWO environments were explored via three principal techniques:

(i)   Theoretical analysis of the thermodynamics of metal-water systems (Pourbaix diagrams).

(ii)   Obtaining a better understanding of the chemical conditions that exist in SCWO systems through development of *in situ* monitoring techniques and chemistry modeling.

(iii) Experimental measurement of corrosion rates and corrosion modeling.

We explored several techniques for monitoring chemistry parameters and corrosion activity in SCWO reactors. The following sensors were developed: a differential resistance hydrogen sensor; an amperometric hydrogen sensor; a potentiometric hydrogen sensor; a potentiometric oxygen sensor; an oxygen, hydrogen, and redox potential combination sensor; pH sensors and reference electrodes; and an electrochemical noise sensor. We developed, as well, a new technique for assessing corrosion damage without the use of coupons.

Major theoretical and modeling results include the extension of potential-pH (Pourbaix) diagrams for metal-water systems into the supercritical temperature range, development of an approach to standardize pH scales in high subcritical and supercritical aqueous solutions, and development of a phenomenological model for describing corrosion processes in SCWO. The model takes into account the effects of electrolyte dissociation and water density, as influenced by temperature and pressure, upon the kinetics of corrosion of metals and alloys in supercritical water. Competing effects of temperature on the heterogeneous rate constant and on the concentrations of H^+ and O_2 leads to a pressure (and hence density) - dependent maximum in the

corrosion rate in the vicinity of the critical temperature. A new technique for calculating dissociation constants of electrolytes from conductivity data was also developed.

SUMMARY OF MAJOR ACCOMPLISHMENTS

The research described here has resulted in a number of major accomplishments, many of which may have a major impact on future work in this area. These accomplishments are as follows:

- Development of differential resistance and amperometric hydrogen sensors for use in supercritical water (ARO).

- Development of solid state potentiometric hydrogen and oxygen sensors for use in high temperature, subcritical aqueous systems (ARO).

- Development of pH sensors and reference electrodes for pH monitoring at temperatures up to 550°C (ARO).

- Development of a concept for pH standardization and pH scale for supercritical aqueous solutions (ARO).

- Demonstration of the viability of pH monitoring during the SCWO destruction of model waste (ARO).

- Development of combination hydrogen, oxygen, and redox potential sensors for use in SCW environments (ARO).

- Development of a reference electrodes for use in supercritical aqueous solutions (ARO).

- Development of new technique of the assessment of corrosion damage without the use of coupons (DOE).

- Development of potential-pH (Pourbaix) diagrams for metals in supercritical water (DOE).

- Development of a phenomenological model of metallic corrosion in supercritical solutions (DOE).

- Coupon tests of metals and alloys in supercritical HCl solutions (DOE).

- Demonstration of the use of electrochemical noise for the characterization of the corrosion processes in supercritical water (DOE).

- Polarization measurements in supercritical water (DOE, ARO).

- Development of a new technique for determination of the dissociation parameters of electrolytes in supercritical water from conductivity data (ARO).

- Development of new brazing techniques for metal/ceramic joining for fabricating high temperature *in situ* sensors (ARO).

The principal agency supporting the work that resulted in each accomplishment is identified in parentheses. In those instances where the support of both agencies contributed substantially to the success of the work, both agencies are listed.

TABLE OF CONTENTS

ix

LIST OF ILLUSTRATIONS

LIST OF TABLES

SECTION 1

INTRODUCTION

Supercritical Water Oxidation (SCWO) is now being actively developed as a means of destroying highly toxic organic waste (including physiological agents) and for reducing the volume of mixed waste (radioactive waste combined with RCRA hazardous waste). In this process, the waste is oxidized by molecular oxygen or hydrogen peroxide in water at temperatures in excess of the critical temperature (374°C). Oxidation is usually conducted at pressures of 3500-6000 psi (233-400 bar) and at temperatures over the range 400-600°C. The advantages of this process include: (i) Very high organic destruction factors (typically greater than 99.99%), (ii) high throughputs (500 gal/day), and (iii) closed cycle operation that minimizes uncontrolled emissions to the environment.

The major problem inhibiting the wide implementation of SCWO is the pronounced corrosion damage that occurs in regions of the process stream that are at temperatures around the critical temperature of water (350-450°C). Few materials (mostly, noble metals) are immune to attack. Consequently, better understanding of chemical conditions and corrosion processes in SCWO is required in order to select the most appropriate and cost-effective materials of fabrication. In order to optimize the oxidation process, and to monitor chemical conditions in SCWO reactors, it is necessary to develop various *in situ* monitoring techniques. The probes should be capable of withstanding the harsh operating conditions that are characteristic of SCWO process: high temperatures, high pressures, and the presence of aggressive chemical species. In Table 1-1 we summarize the most important chemical parameters relevant to the SCWO process.

The most important chemistry parameters to be monitored and controlled in the supercritical water waste treatment process are: pH, oxygen and hydrogen content, and redox potential. Two important corrosion parameters should be monitored as well, namely, the corrosion potential and the spontaneous fluctuations in potential and/or current (i.e., "noise"), which has been found to be an effective method for monitoring corrosion activity.

Table 1-1. Chemistry and Corrosion Parameters Relevant to SCWO reactors.

Parameter	T°C	P, psi	Important for optimizing
Chemical Parameters			
pH	300-500	750-7500	Corrosion mitigation
Redox parameters (Oxygen and Hydrogen content, Redox potential)	300-600	750-7500	Oxidation of waste, corrosion monitoring and mitigation
Conductivity	300-500	750-7500	Corrosion mitigation, oxidation of waste
Corrosion Activity Parameters		750-7500	
Electro-chemical potential	300-450	750-7500	Corrosion monitoring and mitigation
Electro-chemical noise	300-450	750-7500	Corrosion monitoring

In this work, chemical and electrochemical phenomena in SCWO were explored using four principal techniques:

(i) Theoretical analysis of the thermodynamics of metal/water systems, resulting in the derivation of potential/pH (Pourbaix) diagrams for metals in high subcritical and supercritical aqueous systems.

(ii) Development of a better understanding of the chemical conditions that exist in SCWO systems through the use of *in situ* chemical monitoring techniques and modeling.

(iii) Experimental measurement of the electrochemical conditions that exist in SCWO systems, and determination of corrosion rates *in situ*.

(iv) Modeling of corrosion processes, so as to provide a theoretical basis for metal/ solution interactions in SCWO systems.

Section 2 provides a short overview of the experimental techniques that we used in this work. Section 3 is devoted to the thermodynamics of metal-water systems, namely to the development of the potential-pH (Pourbaix) diagrams. In Sections 4-7 we present results of the development of *in situ* monitoring techniques and sensors for use in high subcritical and supercritical water. A new method for estimating dissociation constants of electrolytes at

supercritical temperatures from subcritical specific conductivity data is described in Section 8. Section 9 present the results of corrosion monitoring, measurements, and modeling, while Section 10 describes new metal-ceramic brazing techniques that have been used for making *in situ* sensors for use in SCW systems. Finally, Section 11 lists the publications that have resulted from this study. In those cases where manuscripts have been submitted but have not appeared in print, preprints may be obtained from the Principal Investigator, Prof. Digby Macdonald.

The work presented in this report was supported by both the Army Research Office and the Department of Energy/INEL (Contract No. C-88-101570) with emphasis on the work carried out under ARO sponsorship. We have included DOE-sponsored work in this report to provide the reader with a comprehensive account of the accomplishments that have been made in the Center for Advanced Materials over the past three years. Furthermore, many of the personnel involved were supported by both organizations. We emphasize, however, that the thrusts in the two programs, while being highly complementary, were different; that in the DOE-supported program being corrosion and that in the ARO-supported work being sensors.

SECTION 2

OVERVIEW OF
EXPERIMENTAL TECHNIQUES

SCWO systems are operated under conditions that present severe challenges when it comes to designing experimental facilities and specifying appropriate materials. The most important technical problems to overcome are: high temperatures (up to 600°C), high pressures (up to 7500 psi), and the very high corrosivity of the solution. Accordingly, it is useful to first briefly review some of the experimental techniques that have been employed during the course of this study so that the reader may appreciate the difficulties that are inherent in work of this type. Experimental details associated with specific techniques are discussed in the appropriate chapters throughout the report.

In this work, we designed and constructed several high temperature/high pressure loops capable of operating at temperatures up to 600°C and at pressures up to 6000 psi (400 bar). Water or aqueous solutions were pumped through the loops and cells via a HPLC (High Pressure Liquid Chromatography) pump. The pressure in the system was maintained via a relief valve. The cells for sensor development and/or corrosion studies were disposable and were replaced after extended operation in aggressive environments. This provided the necessary flexibility in the experimental equipment, and proved to be an economical solution to the corrosion of the equipment. The cells and pre-heaters were heated with heating tape. The sensing elements were incorporated into standard Conax fittings that were installed into the high pressure/high temperature test cells via cooled extensions. The cells and loops were generally fabricated from Types 316 and 304 stainless steels, although some Alloy C-276 components were employed, as needed. All parts that were exposed to high temperatures and pressures were replaced as needed.

We also developed a new and efficient way for the rapid and direct determination of corrosion rates in SCWO environments. This experimental technique measures the pH of the effluent of the highly acidic solution passing through the loop at the desired temperature and

pressure. The corrosion of the pipe walls affects the pH of the solution, according to the following reactions:

$$Me + 2H^+ = Me^{2+} + H_2$$

and

$$Me + 2\,HCl = MeCl_2 + H_2$$
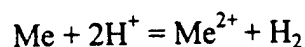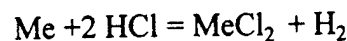
where Me stands for metal. It is clear that the consumption of the acid is proportional to the extent of corrosion., with the concentration of corrosion product being given by

$$C_{Me^{2+}} = \frac{1}{2}(C^\circ_{H^+} - C_{H^+}) = \frac{1}{2}(10^{-pH^\circ} - 10^{-pH})$$

We should note that this equation is valid for the test solution being much more acidic than the solution of corrosion products (metal salts). In this case, which is most important for SCWO applications, the change in the pH of the effluent provides direct information on the amount of the acid consumed by corrosion process. This technique has certain advantages over the traditional coupon tests. In particular, it does not require the disassembling of the equipment in order to measure weight loss, no insulators are necessary in order to prevent galvanic corrosion, and the data on corrosion are obtained in real time, with the possibility of changing the temperature, pressure, and the flow rate during the experiment. Hence, in one experiment we can obtain data corresponding to many different experimental conditions.

In this work, we also developed the following new sensors for use in SCWO systems:

- Reference electrodes

- pH sensors

- Oxygen and redox potential sensors

- Advanced differential resistance hydrogen sensors

- Amperometric hydrogen sensors

2-3

- Potentiometric oxygen and hydrogen sensors

- Electrochemical noise sensors

In Figures 2-1 through 2-3, we show photographically several sensors developed in this work for use in SCWO systems. These sensors were designed to monitor specific properties of the medium, including potential and pH. Many of these sensors represent "firsts" in the field, including the first measurements of pH, redox potential, electrochemical noise, and hydrogen at temperatures significantly above the critical temperature. These sensors hold significant promise as the bases for *in-situ* monitoring technologies.

The materials problems that are encountered in SCW cannot be over-emphasized. Thus, few of the "corrosion-resistant" alloys that are employed in subcritical systems, including the stainless steels and nickel-base alloys, are suitable for use in SCW under acidic, highly oxidizing conditions. Furthermore, the temperatures of interest (374°C-600°C) lie well above the useful range for polytetrafluoroethylene (PTFE or TEFLON®), and no elastomers are available for forming seals. Accordingly, seals often must be cooled, leading to greater complexity of the apparatus. These probes are compounded further in electrochemical studies because of the need to employ insulators that will operate under the conditions of interest and because of the existence of thermogalvanic effects and "ground loops" when using all-metal experimental systems.
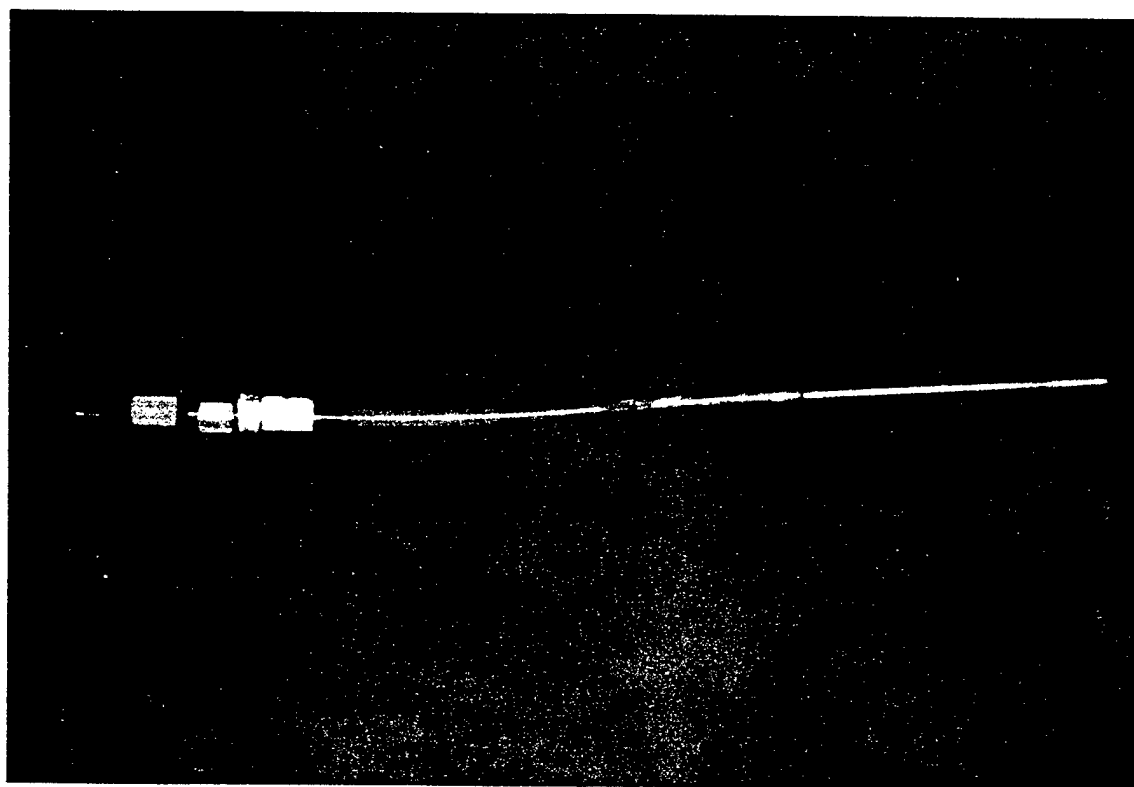
Figure 2-1. Reference electrode (external pressure-balanced reference electrode with silver/silver chloride internal element). Tested at temperatures up to 600°C.
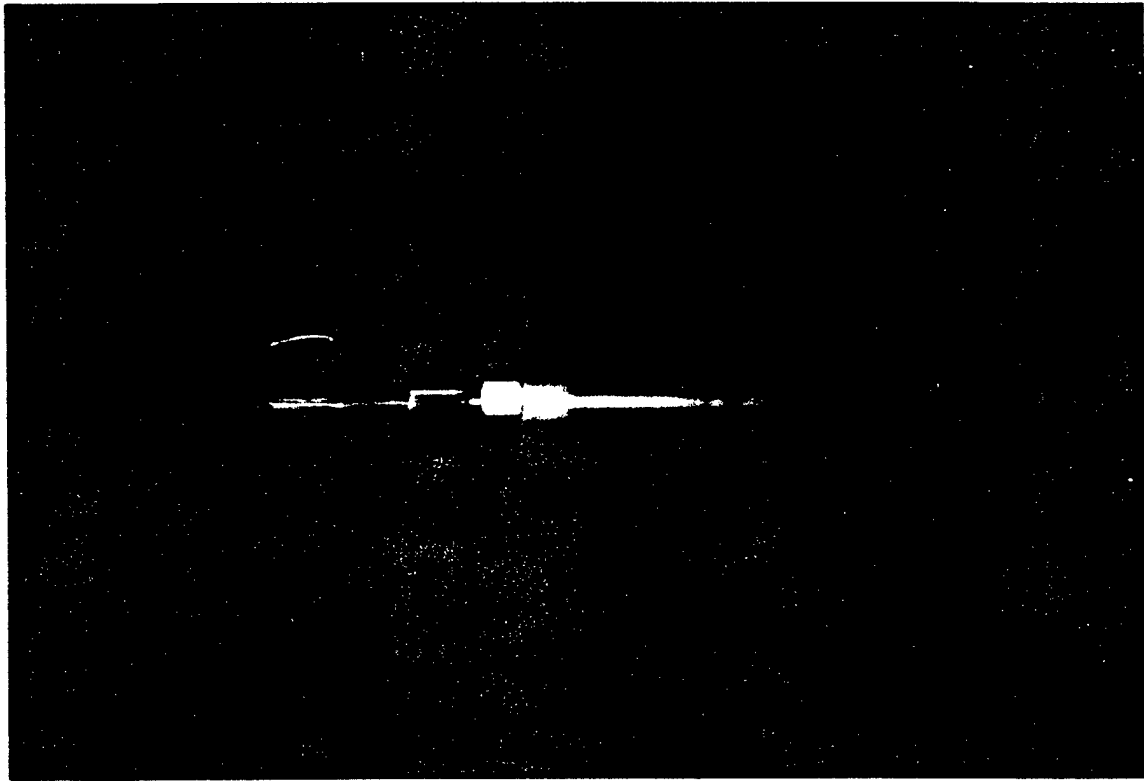
Figure 2-2.   pH sensor based on a yttria-stabilized zirconia membrane. Tested at temperatures up to 600°C.
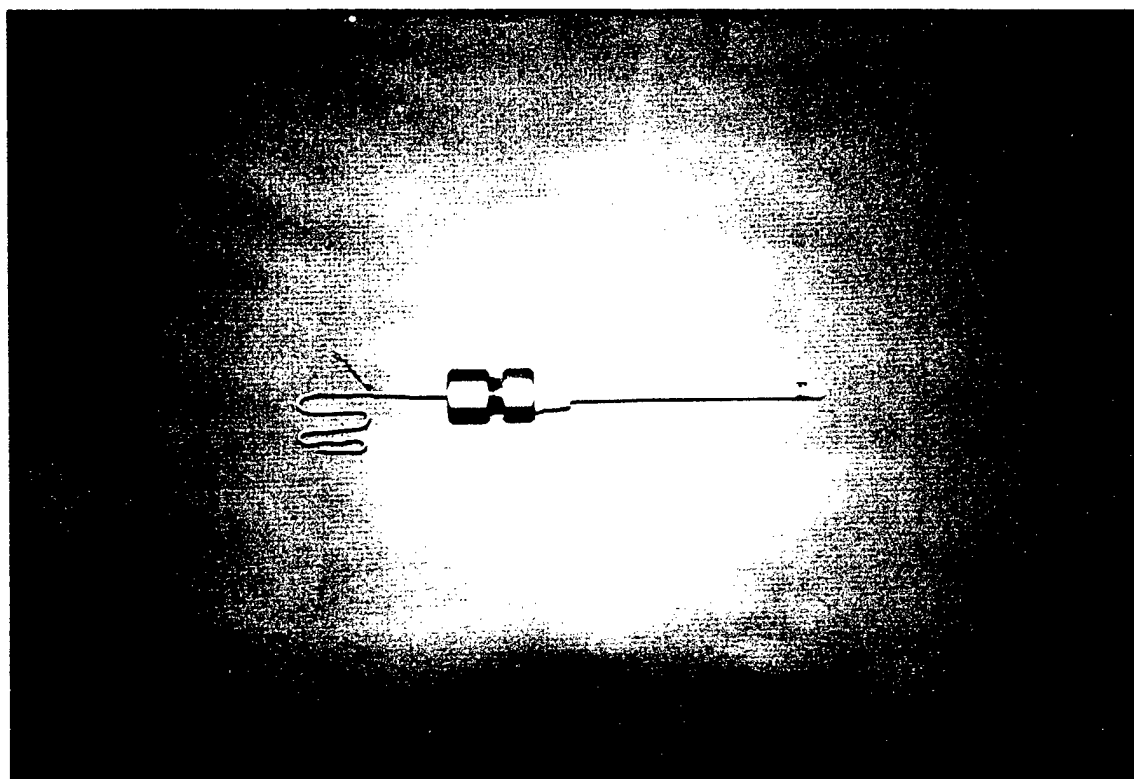
Figure 2-3. Oxygen, hydrogen, and redox potential sensor based on a yttria-stabilized zirconia membrane and a platinum electrode. Tested at temperatures up to 470°C.

SECTION 3

THERMODYNAMICS OF METAL-WATER SYSTEMS

3.1. THERMODYNAMICS OF METAL-WATER SYSTEMS

3.1.1 Introduction

Potential-pH (Pourbaix) diagrams are useful tools for summarizing the thermodynamic relationships in metal/water systems, and hence for interpreting equilibrium electrochemical data and, to a lesser extent, corrosion rate data. The diagrams provide important information on the regions of thermodynamic immunity, on the regions of possible corrosion, and on the domains of possible protection by passivation. In the most favorable cases, these diagrams enable one to predict the behavior of metals in corrosive media and to envisage ways of controlling or mitigating corrosion. The method of constructing Pourbaix diagrams is well established.[1]

Over the last 25 years, much attention has been paid to developing potential-pH diagrams for industrially-important metals and alloys at elevated temperatures, most often for the temperature range of 25 to 300°C. The first diagrams of this type appeared in the early 1970s, and were stimulated by the development of the "Entropy Correspondence Principle" by Criss and Cobble in 1964.[2] This principle allowed one to calculate entropies of ionic species over large temperature ranges. Potential-pH diagrams for many metals[3-13] in aqueous systems at elevated temperatures were constructed, and the reader is referred to the many reviews that have appeared in the literature on this subject (e.g., see References 14-16). Somewhat later, potential-pH diagrams were derived for alloys[17-19] and for adsorbed species[20] at elevated temperatures, and in one case[21] the diagrams were calculated at the temperature and pressure corresponding to the critical point of water.

Several industrial systems, such as the supercritical water oxidation (SCWO) of waste[22] and supercritical thermal power generation, involve metals and alloys exposed to supercritical

aqueous solutions. In the case of SCWO systems, particularly severe corrosion damage is observed at temperatures over the range 350-450°C, which has been attributed to the acid that is generated during the oxidation of halogenated waste. In this chapter, we report potential-pH diagrams calculated for the iron-water system over the temperature range from 100 to 500°C.

The construction of potential-pH diagrams requires knowledge of the thermodynamic parameters of reactions occurring in the metal/water system. Standard Gibbs energy changes for the reactions of interest can be obtained from literature data based on measurements or calculations using various methods of integrating (and perhaps extrapolating) Gibbs energy functions over the desired ranges of temperature and pressure. The data on standard Gibbs energies for solid species and water are, in most cases, readily available over the temperature range of interest. Unambiguous calculation of the thermodynamic functions for ionic species, however, is problematic, and involves extrathermodynamic models and extrapolations (see, e.g., References 2, 15, 23-25). These models and extrapolations were previously formulated for much narrower temperature ranges than that of interest here (100°C to 450°C), and it is expected that they may not yield reliable data at temperatures higher than 300°C.

3.1.2 Construction of Potential-pH Diagrams

As noted above, the principles of constructing potential-pH diagrams are well documented.[1,3-20] Standard Gibbs energy changes for the various reactions are required in order to define equilibrium relationships between the various components in the system. We should note here that the standard Gibbs energy change of a reaction (R) corresponds to that for the cell

SHE/R, where SHE designates the Standard Hydrogen Electrode and R represents the half cell of interest. Thus, the change in standard Gibbs energy for the half-cell reaction

$$Fe^{+2} + 2e^- = Fe$$
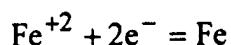
corresponds to the cell reaction

$$Fe^{+2} + H_2 = Fe + 2H^+$$
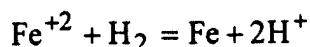
where all components are at unit activity. This full cell reaction is written in a form that satisfies the Isocoulombic Principle, or principle of balanced charges.[26,27] According to the Isocoulombic Principle, any errors in extrapolating thermodynamic data involving charged species to elevated temperatures are significantly decreased (due to compensation of errors) if the charge on both sides of the reaction is balanced.

In the present work, we have used the model developed by Helgeson and co-workers [28-31] to calculate standard Gibbs energy changes for the reactions of interest. The most complicated problem in aqueous thermodynamics is the determination of the thermodynamic functions of ionic species, whereas the thermodynamic parameters of solid species are usually readily available. The semi-empirical model developed by Helgeson et al.[31] considers any thermodynamic property of an ionic species as being a combination of an electrostatic contribution (modified Born equation) and a solvation contribution (corresponding equation of state), and incorporates most of the data that are currently available in the literature, with emphasis on high temperature/high pressure aqueous geochemical systems. This model appears to be the only one that is currently available that is capable of yielding reasonably reliable thermodynamic parameters for systems at supercritical temperatures. The model is incorporated into a computer program SUPCRT92, which is available from Professor Helgeson at the

3-4

University of California at Berkeley, and thus is ready for practical application. Although an unequivocal test of the model is difficult, within the context of the present work, the algorithm is capable of reproducing equilibrium constants for reactions of geochemical interest (e.g., oxide solubilities) at temperatures far in excess of the critical temperature of water. The thermodynamic data (Gibbs energies, enthalpies, etc.) predicted by this model are found to be in reasonable accord with those produced by other algorithms at temperatures from 25 to 300°C. The computer program, SUPCRT92,[31] based on this model, was used in the present work to calculate the standard Gibbs energy changes for reactions in the iron-water system.

The thermodynamic conventions for standard states used in SUPCRT92 are given in the corresponding paper of Helgeson et al.[31] We only note here that in SUPCRT92 the standard Gibbs energy of formation of the elements is zero at standard conditions (298°K, 1 bar) and the standard properties of the hydrogen ion are zero at any pressure and temperature. Because the potentials of all equilibria are referred to the same scale, the choice of the standard state presents no problem, provided that it is done consistently.

In deriving the diagrams for iron, we have considered four solid species (Fe, FeO, Fe_2O_3, Fe_3O_4) and two ionic species (Fe^{2+} and Fe^{3+}). We have not included hydrated forms of iron oxides and complex iron oxyanions, because of the great uncertainty in the extrapolated thermodynamic functions for those species in the supercritical region, and because low water densities in near-critical and supercritical systems at pressures below 500 bars favor decomposition of hydrated oxides to oxides and greatly decrease the stability of ionic species.

It should be noted that we have constructed the potential-pH diagrams under both subcritical and supercritical conditions for constant pressure, whereas in most previous works for

$T<T_c$, the diagrams refer to the saturated vapor pressure of water (221 bar at $T_c = 374°C$). A molal-based activity of 10^{-6} was selected for all ionic species, and we have assumed unit activity for water and solid species. In Table 3-1, we present the various reactions considered. In Table 3-2, we present the Gibbs energies for corresponding reactions.

Table 3-1. Reactions considered for construction of potential-pH diagrams.

(a) $H^+ + e^- = 1/2\,H_2$	$E = 0 - \dfrac{2.303RT}{F}pH$
(b) $O_2 + 4H^+ + 4e^- = 2H_2O$	$E = -\dfrac{\Delta G^o}{4F} - \dfrac{2.303RT}{F}pH$
(1) $Fe^{+2} + 2e^- \leftrightarrow Fe$	$E = -\dfrac{\Delta G^o}{2F} + \dfrac{2.303RT}{2F}\log a_{Fe^+_2}$
(2) $Fe^{+3} + 3e^- \leftrightarrow Fe$	$E = -\dfrac{\Delta G^o}{3F} + \dfrac{2.303RT}{3F}\log a_{Fe^{+3}}$
(3) $Fe^{+3} + e^- \leftrightarrow Fe^{+2}$	$E = -\dfrac{\Delta G^o}{F} + \dfrac{2.303RT}{F}\log a_{Fe^{+3}} - \dfrac{2.303RT}{F}\log a_{Fe^{+2}}$
(4) $FeO + 2H^+ + 2e^- \leftrightarrow Fe + H_2O$	$E = -\dfrac{\Delta G^o}{2F} - \dfrac{2.303RT}{F}pH$
(5) $FeO + 2H^+ \leftrightarrow Fe^{+2} + H_2O$	$pH = -\dfrac{\Delta G^o}{2.303RT2} - \dfrac{1}{2}\log a_{Fe^{+2}}$
(6) $Fe^{+3} + H_2O + e^- \leftrightarrow FeO + 2H^+$	$E = -\dfrac{\Delta G^o}{F} + \dfrac{2.303RT}{F}\log a_{Fe^{+3}} + \dfrac{2.303RT2}{F}pH$
(7) $Fe_2O_3 + 2H^+ + 2e^- \leftrightarrow 2FeO + H_2O$	$E = -\dfrac{\Delta G^o}{2F} - \dfrac{2.303RT}{F}pH$
(8) $Fe_3O_4 + 2H^+ + 2e^- \leftrightarrow 3FeO + H_2O$	$E = -\dfrac{\Delta G^o}{2F} - \dfrac{2.303RT}{F}pH$
(9) $Fe_2O_3 + 6H^+ + 6e^- \leftrightarrow 2Fe + 3H_2O$	$E = -\dfrac{\Delta G^o}{6F} - \dfrac{2.303RT}{F}pH$
(10) $Fe_2O_3 + 6H^+ + 2e^- \leftrightarrow 2Fe^{+2} + 3H_2O$	$E = -\dfrac{\Delta G^o}{2F} - \dfrac{2.303RT}{F}\log a_{Fe^{+2}} - \dfrac{2.303RT3}{F}pH$
(11) $Fe_2O_3 + 6H^+ \leftrightarrow 2Fe^{+3} + 3H_2O$	$pH = -\dfrac{\Delta G^o}{2.303RT6} - \dfrac{1}{3}\log a_{Fe^{+3}}$
(12) $3Fe_2O_3 + 2H^+ + 2e^- \leftrightarrow 2Fe_3O_4 + H_2O$	$E = -\dfrac{\Delta G^o}{2F} - \dfrac{2.303RT}{F}pH$
(13) $Fe_3O_4 + 8H^+ + 8e^- \leftrightarrow 3Fe + 4H_2O$	$E = -\dfrac{\Delta G^o}{8F} - \dfrac{2.303RT}{F}pH$
(14) $Fe_3O_4 + 8H^+ + 2e^- \leftrightarrow 3Fe^{+2} + 4H_2O$	$E = -\dfrac{\Delta G^o}{2F} - \dfrac{2.303RT3}{2F}\log a_{Fe^{+2}} - \dfrac{2.303RT4}{F}pH$
(15) $3Fe^{+3} + 4H_2O + e^- \leftrightarrow Fe_3O_4 + 8H^+$	$E = -\dfrac{\Delta G^o}{F} + \dfrac{2.303RT3}{F}\log a_{Fe^{+3}} + \dfrac{2.303RT8}{F}pH$

ΔG^o stands for change in the standard Gibbs energy for the corresponding full cell reaction.

Table 3-2.   Gibbs energy changes for various reactions (J/mol) at 500 bars, calculated using SUPCRT92 computer program.

REACTION

T,°C	1	2	3	4	5	6	7	8	9	10	11	12	13	14	15	b
100	92800.1	10881.4	-81919	21859.2	-70891	-10978	7625.57	25386.5	51348.5	-134252	29581.4	-27918	90977.5	-187423	-58333	-448330
125	92674.4	7642.56	-85032	24096.7	-68530	-16454	8078.82	25758	56275.9	-129073	40995	-27298	98067	-179961	-75139	-439950
150	92506.8	4223.52	-88283	26304.8	-66156	-22077	8484.4	26081	61094.4	-123915	52647.4	-26728	105010	-172511	-92335	-435760
175	92272.2	603.36	-91669	28479.4	-63750	-27876	8847.5	26364	65808.1	-118736	64601.4	-26204	111814	-165002	-110004	-427380
200	91957.9	-3243.1	-95205	30620.5	-61294	-33868	9172.3	26613	70421.3	-113499	76911.6	-25727	118497	-157381	-128231	-418581
225	91547.3	-7345.1	-98892	32732.3	-58772	-40077	9462.2	26834	74938.2	-108156	89624.1	-25299	125055	-149587	-147086	-411039
250	91023.6	-11707	-102730	34814.7	-56168	-46522	9719.7	27032	79358.6	-102689	102772	-24922	131495	-141572	-166620	-403916
275	90374.1	-16337	-106715	36863.6	-53474	-53200	9946.3	27209	83682.7	-97070	116356	-24595	137822	-133309	-186832	-396374
300	89599	-21227	-110826	38879	-50684	-60101	10143	27370	87906.2	-91292	130355	-24327	144023	-124774	-207698	-389251
325	88668.8	-26376	-115045	40856.7	-47779	-67233	10309	27516	92029.2	-85313	144781	-24122	150103	-115904	-229231	-382128
350	87378.3	-32154	-119532	42792.5	-44555	-74947	10443	27647	96034.8	-78726	160343	-23984	156044	-106095	-252502	-375005
375	89125.5	-31530	-120655	44682.2	-44410	-76212	10541	27761	99914.7	-78336	162974	-23917	161835	-105546	-256424	-368301
400	90374.1	-31429	-121803	46521.6	-43823	-77951	10597	27854	103648	-77104	166506	-23933	167437	-103686	-261724	-361597
425	94329.5	-24667	-118996	48289.8	-46005	-72960	10600	27915	107189	-81470	156526	-24046	172808	-110180	-246812	-354893
450	103296	-4944.2	-108240	49974.1	-53285	-54918	10530	27929	110486	-96110	120370	-24285	177870	-132023	-192702	-348608

3.1.3 Results and Discussion

In Figures 3-1 through 3-6, we present potential-pH diagrams for iron at temperatures over the range 100 to 450°C and at a pressure of 500 bar. We present similar diagrams in Figures 3-7 through 3-8 for temperature of 500°C and at pressures of 1000 and 2000 bars. For reference, we show schematically in Figure 3-5 the expected operating regions for SCWO systems and the corresponding region for the heat transport circuits of supercritical power plants. The region shown for SCWO systems is estimated for relatively high oxygen partial pressures, and for pH_T values ranging from 0 to 4. We should add that only a few direct measurements of pH in supercritical aqueous media have been attempted, although studies of this type are currently underway in our laboratory. Because of ion pairing, it is quite possible that high proton activities (corresponding to a low pH) may not be attainable, except at very high densities (i.e., at very high pressures). On the other hand, associated species (e.g., HCl) may themselves be very aggressive, in that they might participate directly in reactions of the type $Me + xHCl \rightarrow MeCl_x + (x/2)H_2$. If this were the case, "pH" may not be the most appropriate measure of solution aggressiveness. For reference, we present in Figure 3-9 the pH of pure water (neutral pH), calculated as $pH = \frac{1}{2}\log K_W$, where K_w is ionic product of water, $K_w = [H^+][OH^-]$.

Comparison of the Pourbaix diagrams derived in this work with those available in the literature for lower temperatures ($T \leq 300°C$) shows them to be in good agreement. The only diagram that we could find for the iron-water system at the critical temperature[21] was calculated using the Correspondence Principle of Criss and Cobble,[2] the use of which is absolutely not justified at temperatures above 250-300°C. The standard hydrogen electrode
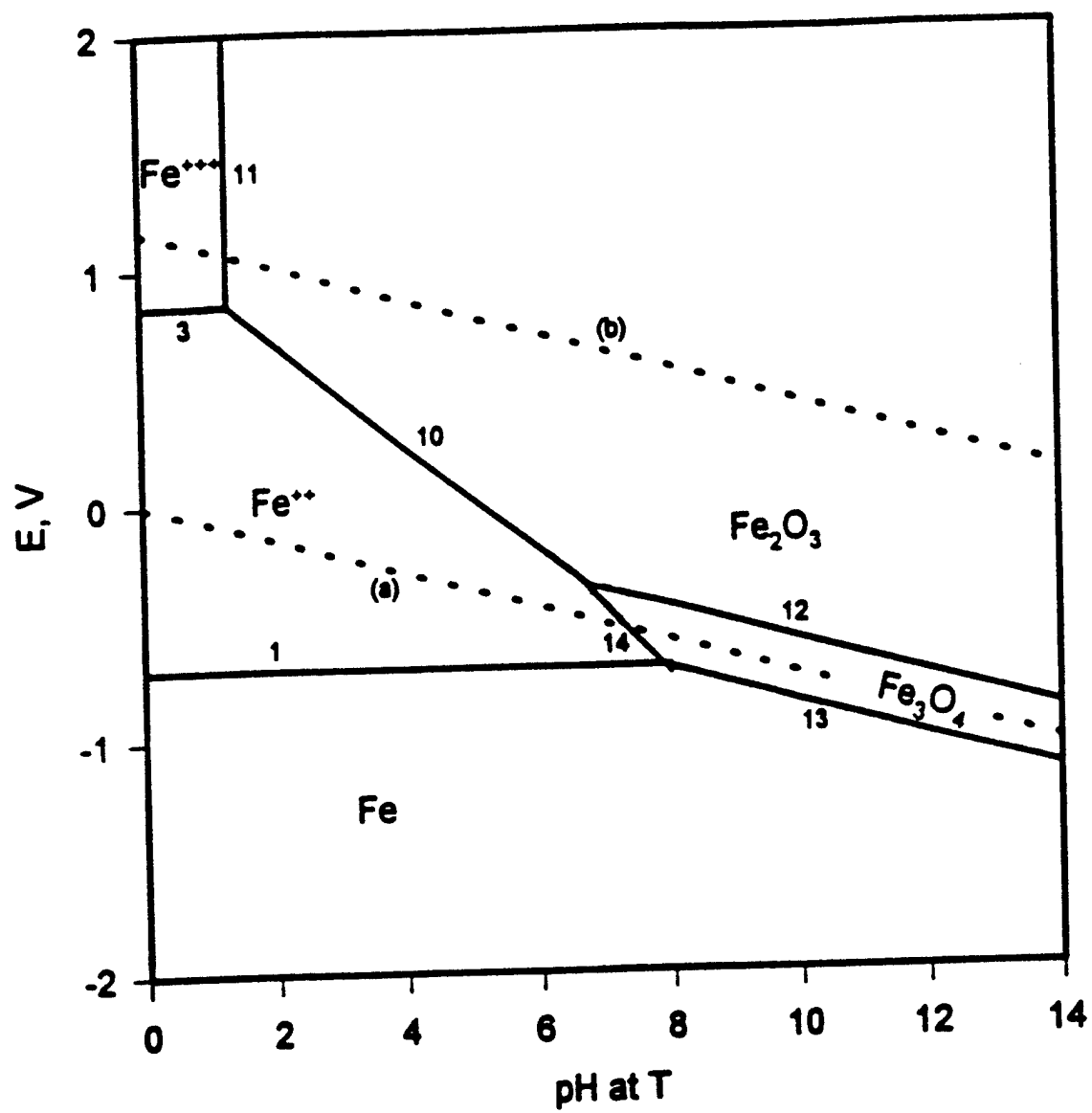
Figure 3-1.   Potential-pH diagram for Fe for 100°C and 500 bars.

200°C, 500 bar
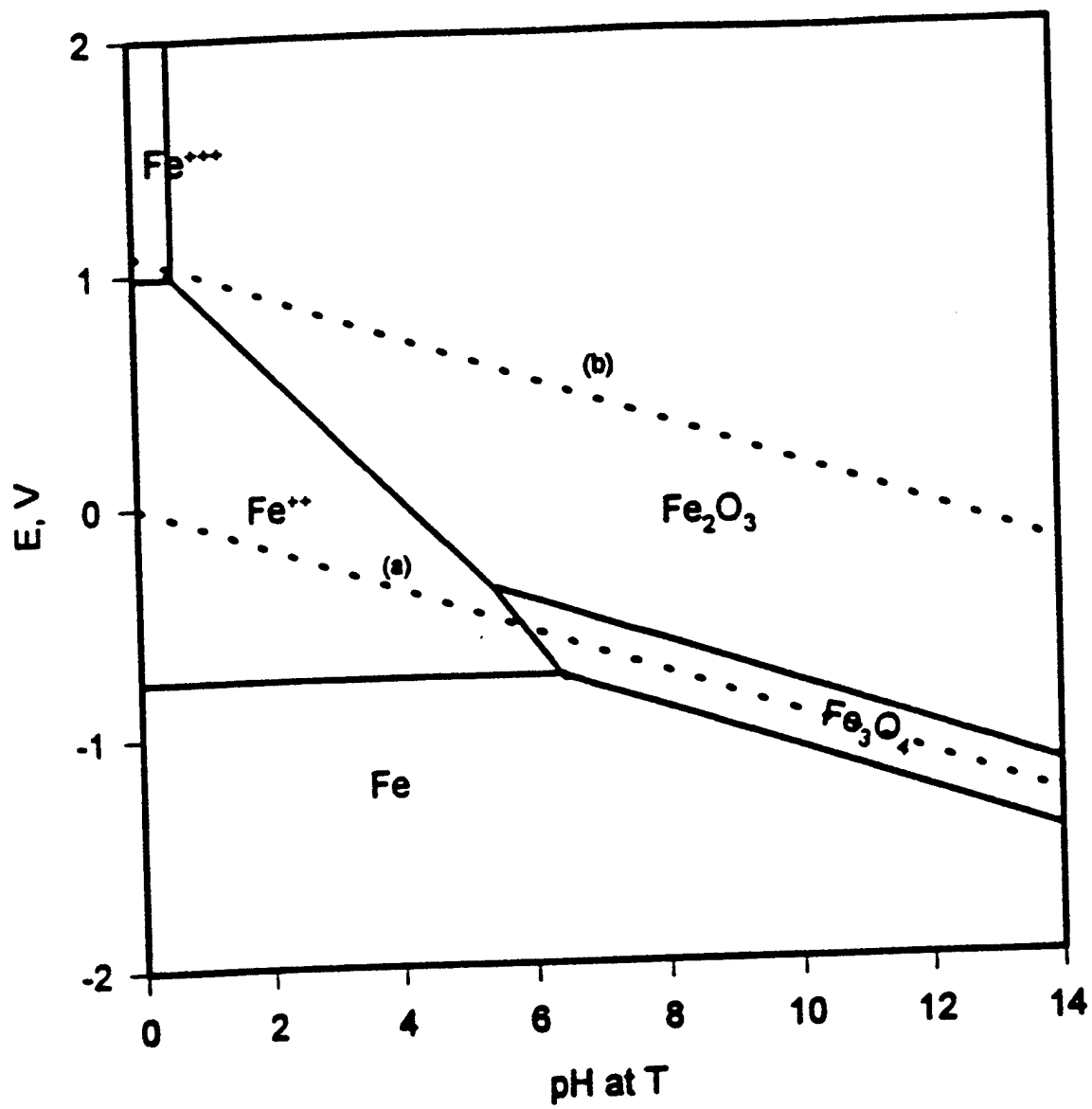
Figure 3-2.   Potential-pH diagram for Fe for 200°C and 500 bars.
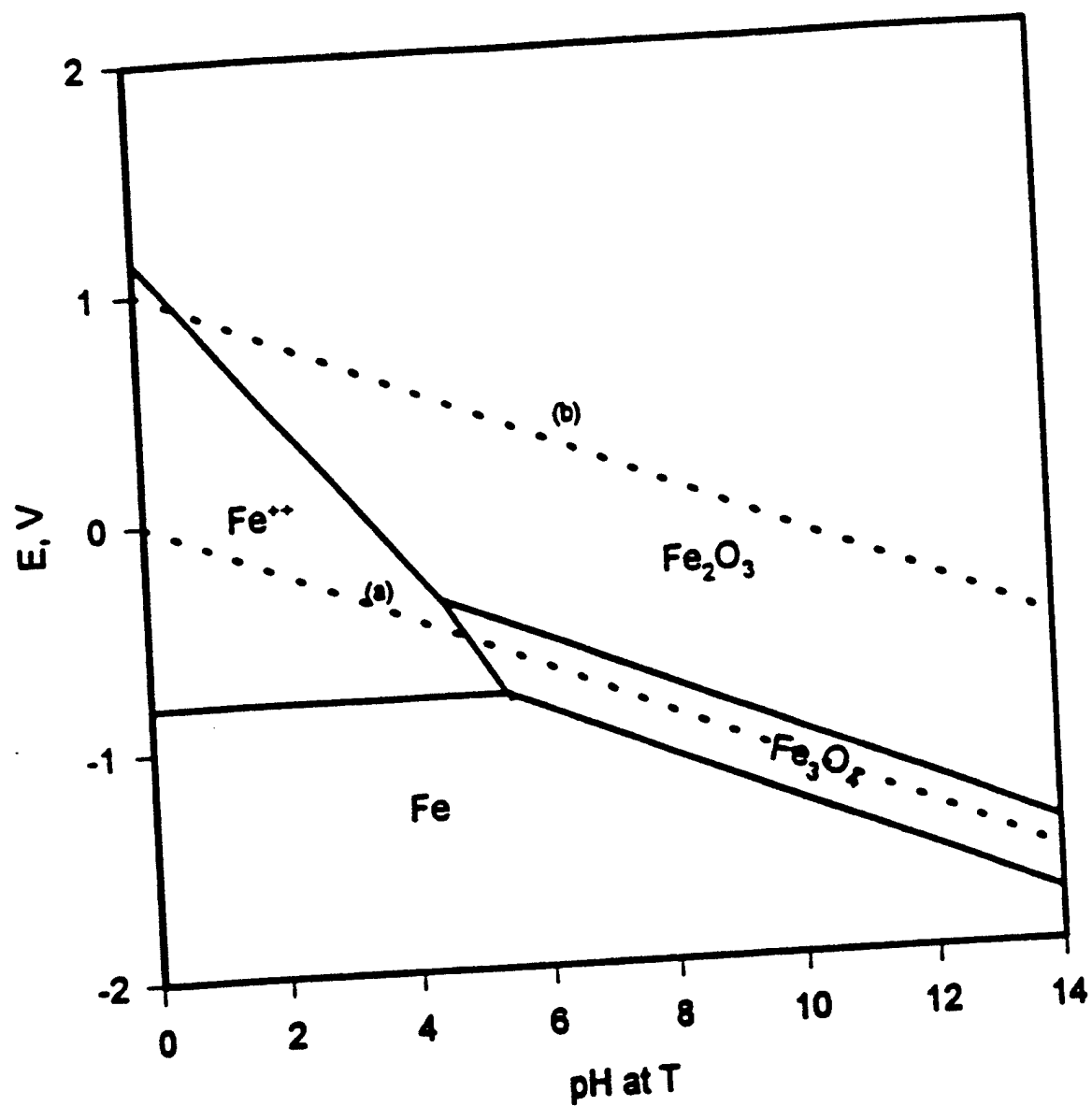
Figure 3-3.   Potential-pH diagram for Fe for 300°C and 500 bars.

350°C, 500 bar
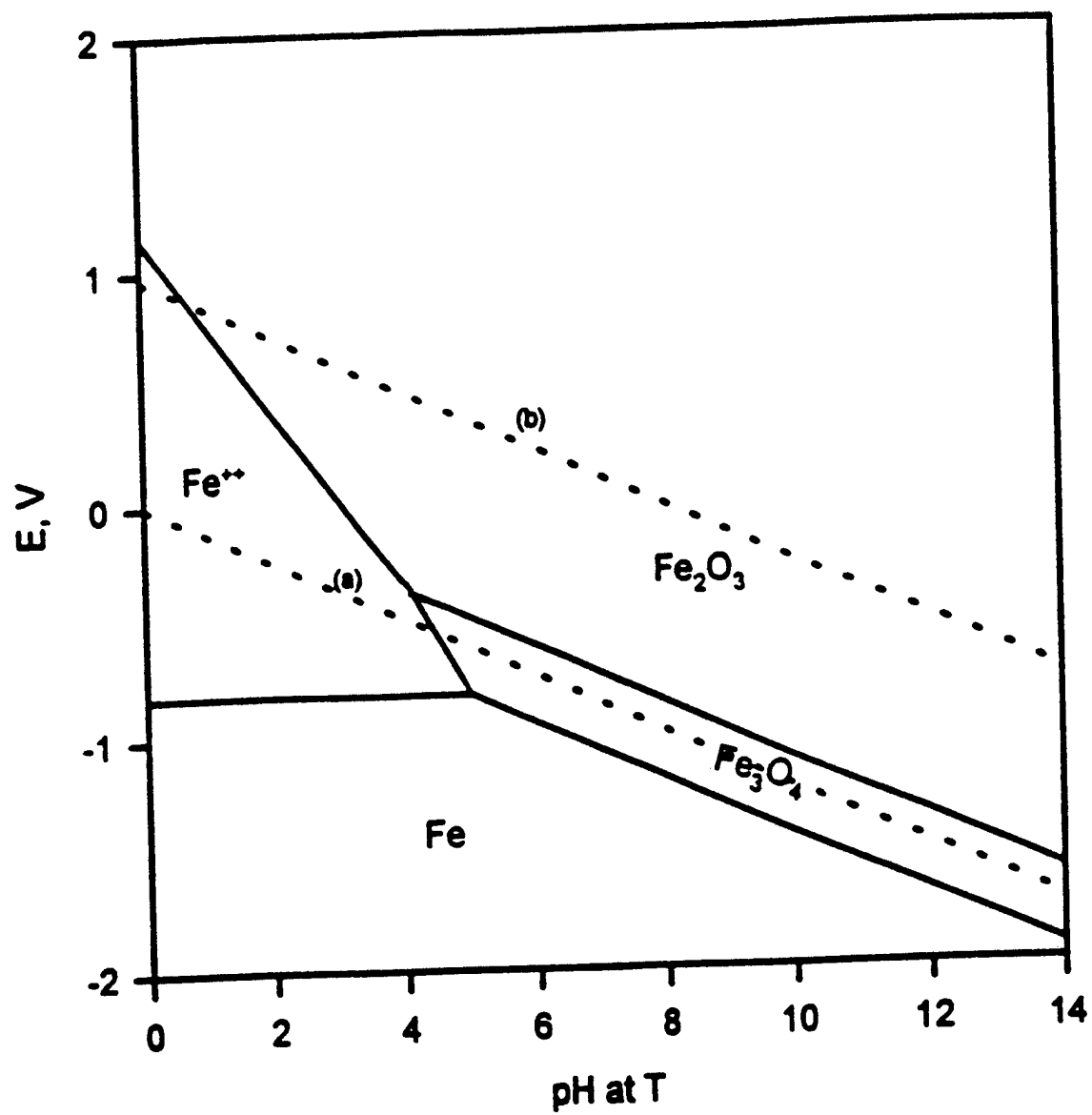
Figure 3-4.   Potential-pH diagram for Fe for 350°C and 500 bars.
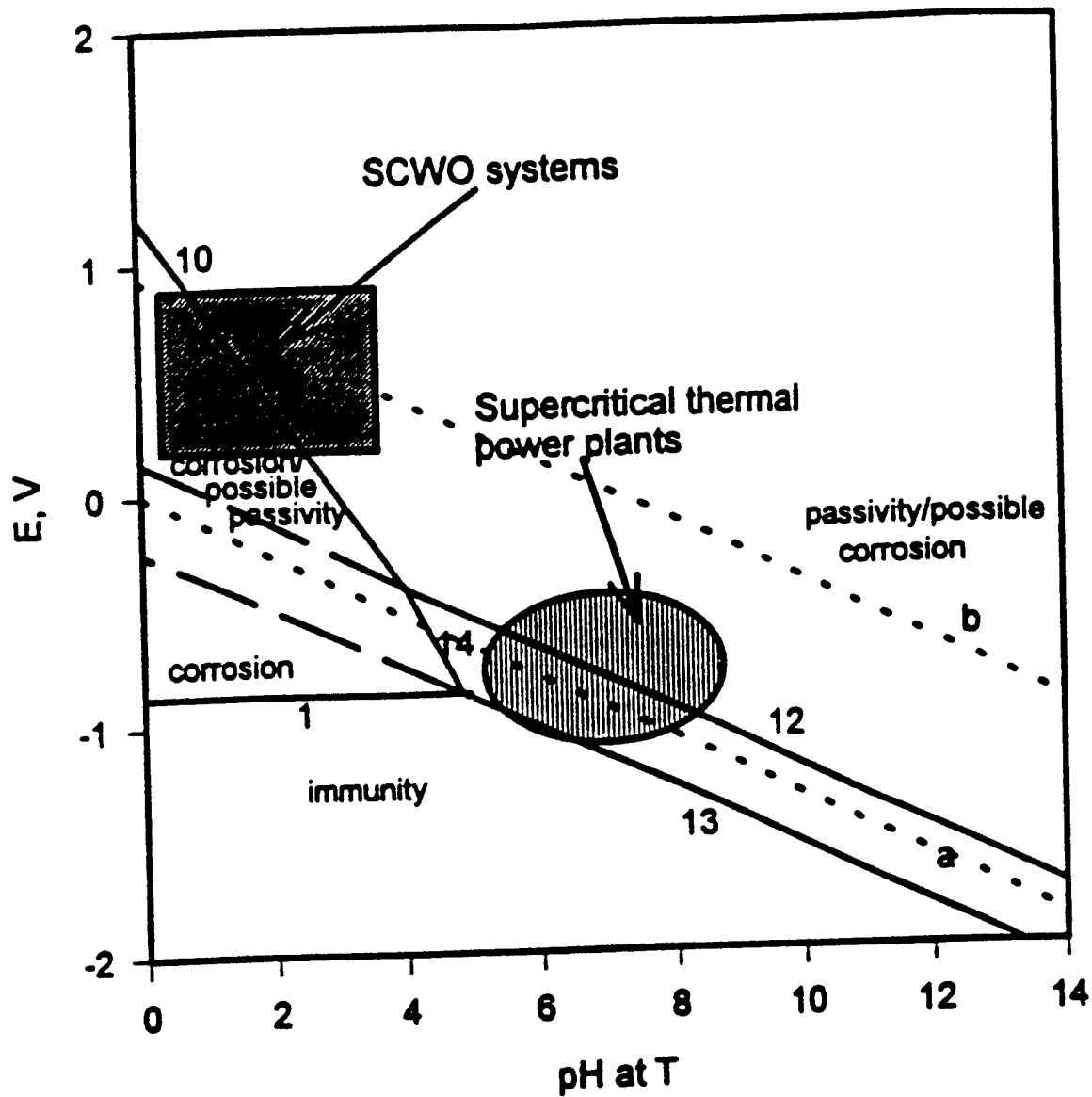
Figure 3-5.   Potential-pH diagram for Fe for 400°C and 500 bars.
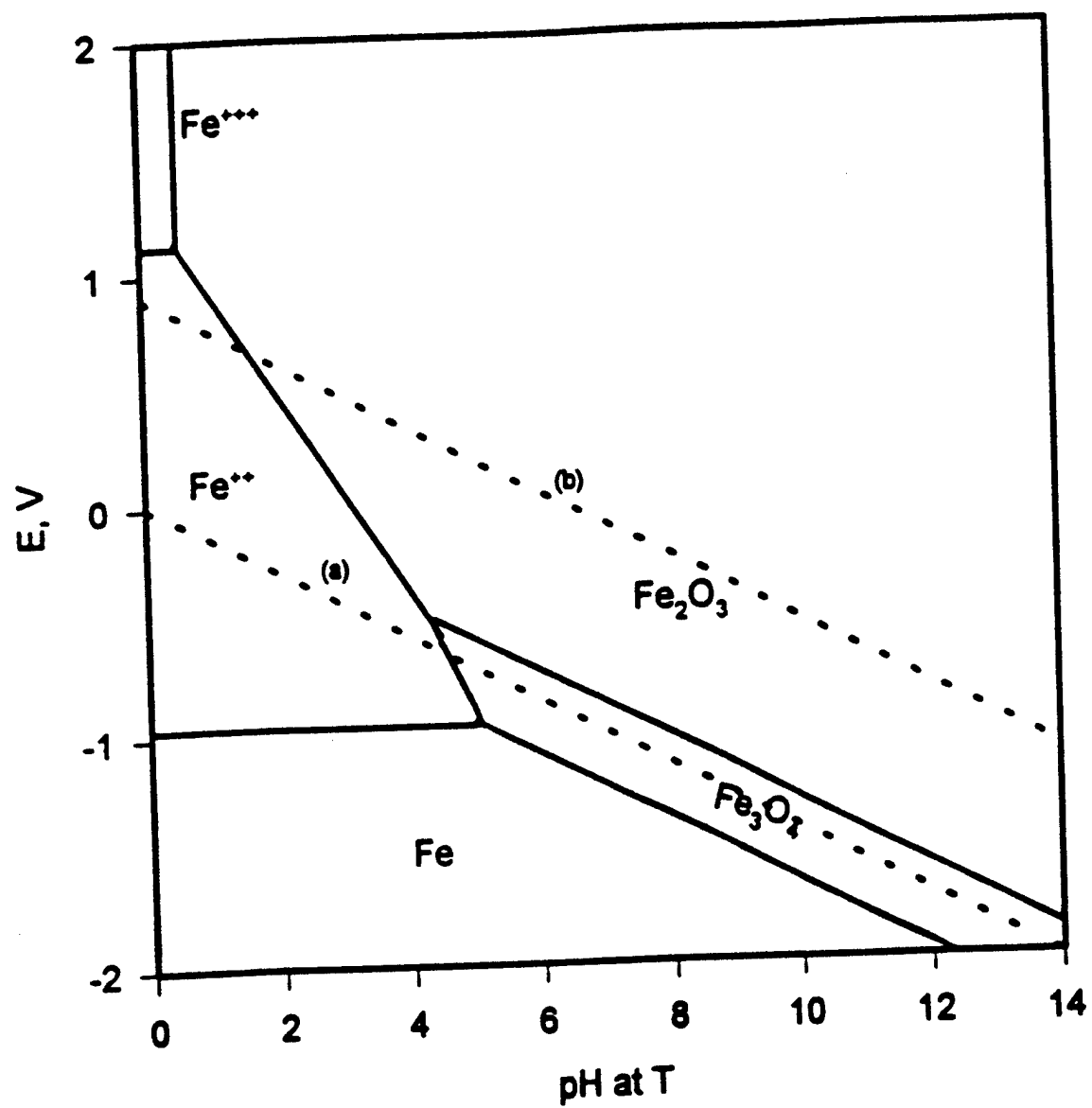
Figure 3-6.   Potential-pH diagram for Fe for 450°C and 500 bars.

500°C, 1000 bar
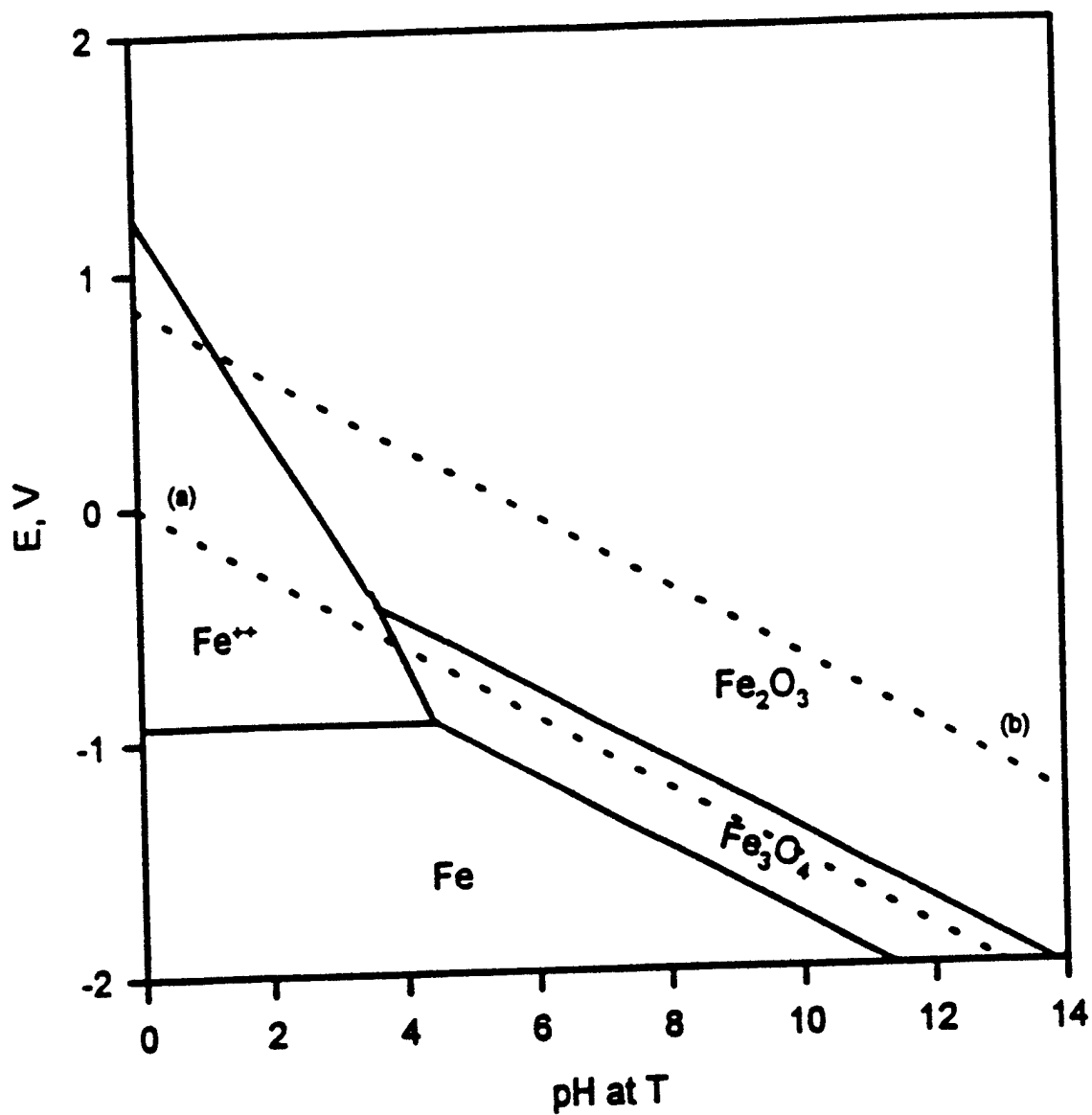
Figure 3-7.   Potential-pH diagram for Fe for 500°C and 1000 bars.

500°C, 2000 bar
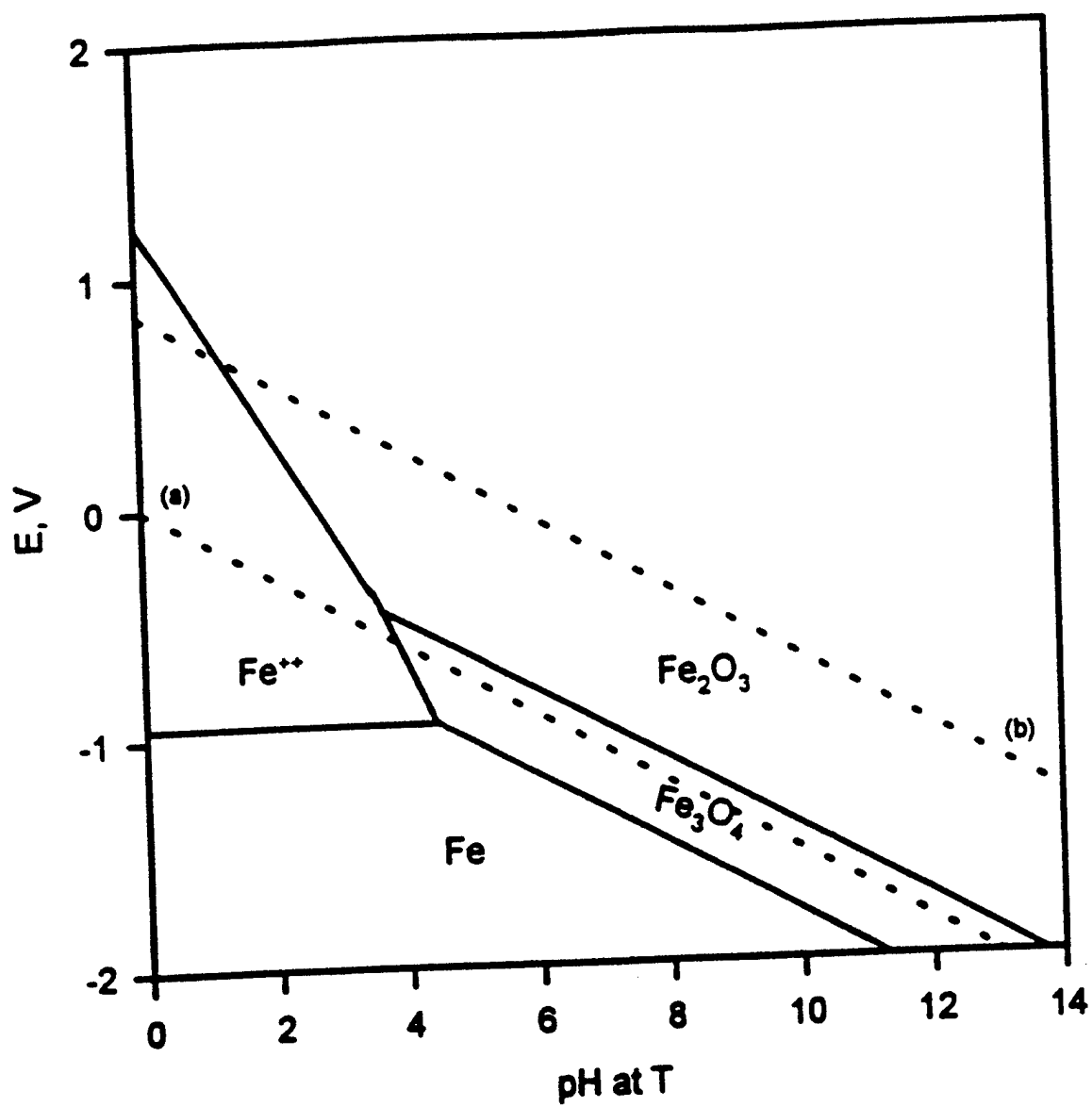
Figure 3-8.   Potential-pH diagram for Fe for 500°C and 2000 bars.
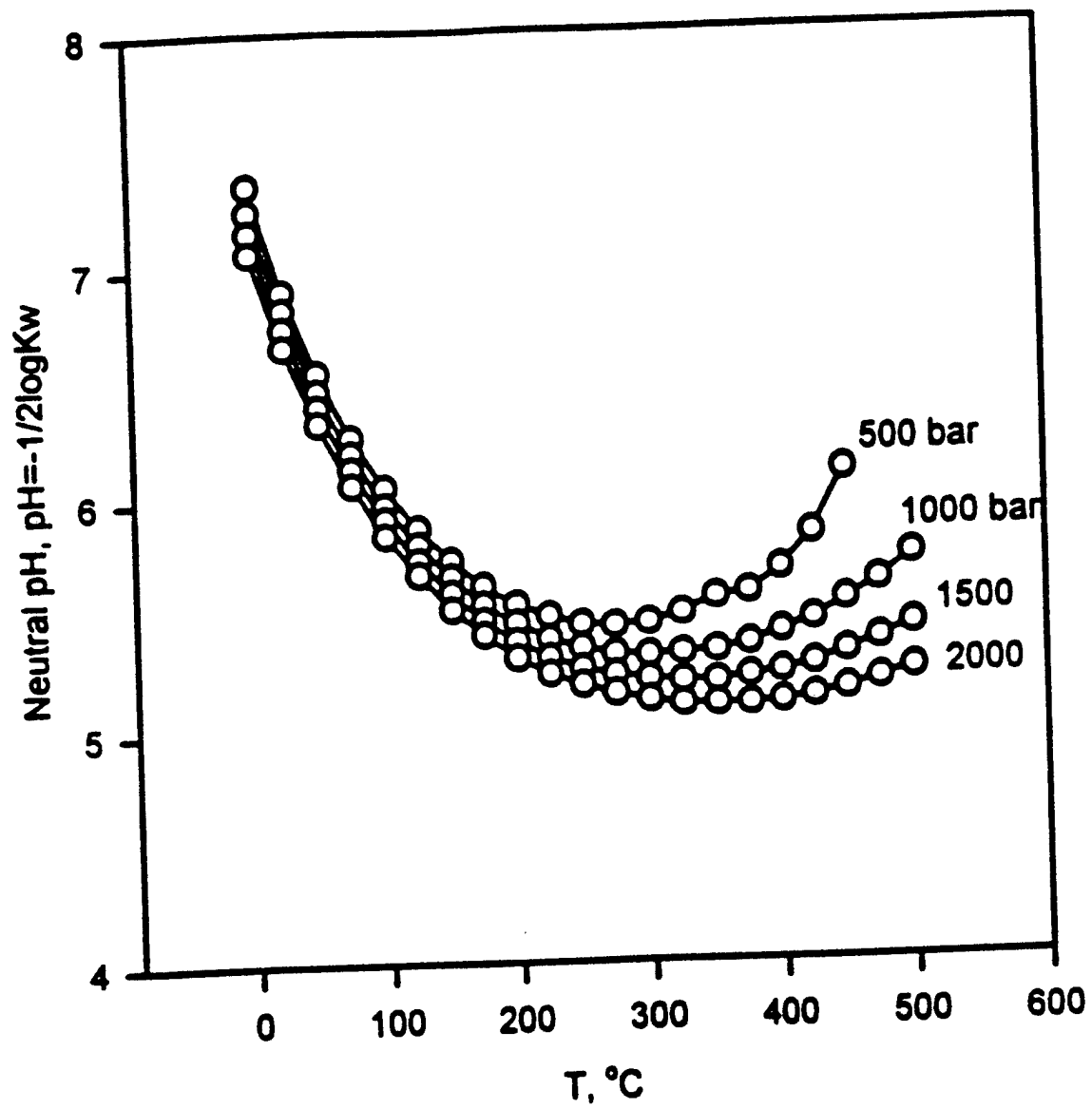
Figure 3-9. pH of pure water (neutral pH) at several pressures.

potential quoted for the critical temperature in Reference 21 is about +0.7 V, whereas according to the generally accepted convention it should be 0.0V.

The conditions for possible protection (passivity) of iron by the formation of metastable oxide layers are indicated in Figure 3-5 by the broken lines that represent extrapolations of the oxide equilibrium lines into the ion stability regions. Thus, at potentials above the extension of the equilibrium line for Fe/Fe_3O_4 into the Fe^{2+} stability field, it becomes possible to form Fe_3O_4 on the surface as a metastable phase, whereas at potentials above the extension of the equilibrium line for Fe_3O_4/Fe_2O_3 both Fe_3O_4 (magnetite) and Fe_2O_3 (hematite) can exist as meta-stable surface phases. Indeed, in this latter case, it is likely that the passive film on iron would possess a bilayer structure comprised of a magnetite inner layer and an outer hematite layer. However, at potentials below this line, but above that for Fe/Fe_3O_4, the passive layer is expected to consist of a single Fe_3O_4 layer. We have not included FeO in the diagrams, because this phase is unstable with respect to iron and magnetite at temperatures below about 560°C, but the conditions necessary for the formation of wurzite as a metastable phase are easily calculated from the information given in Tables 3-1 and 3-2.

Based on the above, we identify the region bounded by Fe/Fe^{2+} (Reaction 1) and the extension of Fe/Fe_3O_4 (Reaction 13) into the Fe^{2+} field as the unequivocal "corrosion field", where none of the oxides considered in this work could form, even as metastable phases. The region above the extension of Line 13, but bounded by Lines 10 and 11, is labeled "Corrosion/ Possible Passivity" to reflect the fact that Fe_3O_4, FeO, and Fe_2O_3 can form at different points (successively more positive potentials) within this region as metastable phases and hence may confer passivity on the surface. For similar reasons, we label the region bounded by Lines 13, 14,

10, and 11, representing the stability fields of Fe_3O_4 and Fe_2O_3, as "Passivity/Possible Corrosion" to reflect the fact the oxides form as stable phases, and hence are expected to passivate the surface, but passivity breakdown may lead to localized corrosion, such as pitting, erosion corrosion, stress corrosion cracking, and corrosion fatigue. Finally, the region below Lines 1 and 13 corresponds to the immune region for iron where corrosion of any kind to produce an iron activity $a_{Fe^{2+}} > 10^{-6}$ (for Line 1) is thermodynamically impossible. However, this region lies below the equilibrium line for H_2/H^+, so that the entry of hydrogen into iron (or steel) might reasonably be expected to give rise to hydrogen embrittlement at lower temperatures (T<200°C) and to hydrogen damage (due to the formation of CH_4) at higher temperatures (T>400°C). Note that the formation of metastable phases must be considered if one wishes to use potential/pH diagrams to explain the passivity of iron (for example) in highly acidic aqueous systems.

One of the principal findings of this work is the contraction of the area of thermodynamic immunity with increasing temperature, as illustrated in Figure 3-10, where diagrams calculated for 350 and 500°C at 1000 bars are superimposed. We should note, however, that the formation of possibly protective oxide layers at 500°C starts at a lower pH values than at 350°C. In basic solutions, we could expect iron to remain passive at all temperatures. The regions of stability of Fe^{2+} and Fe^{3+} decrease markedly with increasing temperature (see Figures 3-1 through 3-6) and, indeed, that for the latter (Fe^{3+}) disappears altogether at 300°C. (At 450°C, however, a small domain of Fe^{3+} again appears on the diagram). The decrease in the stability fields for ionic species, and in particular for highly charged species, has been previously noted,[10] and is attributed to the rapid decrease in the dielectric constant of water with increasing temperature.

350°C and 500°C, 1000 bar
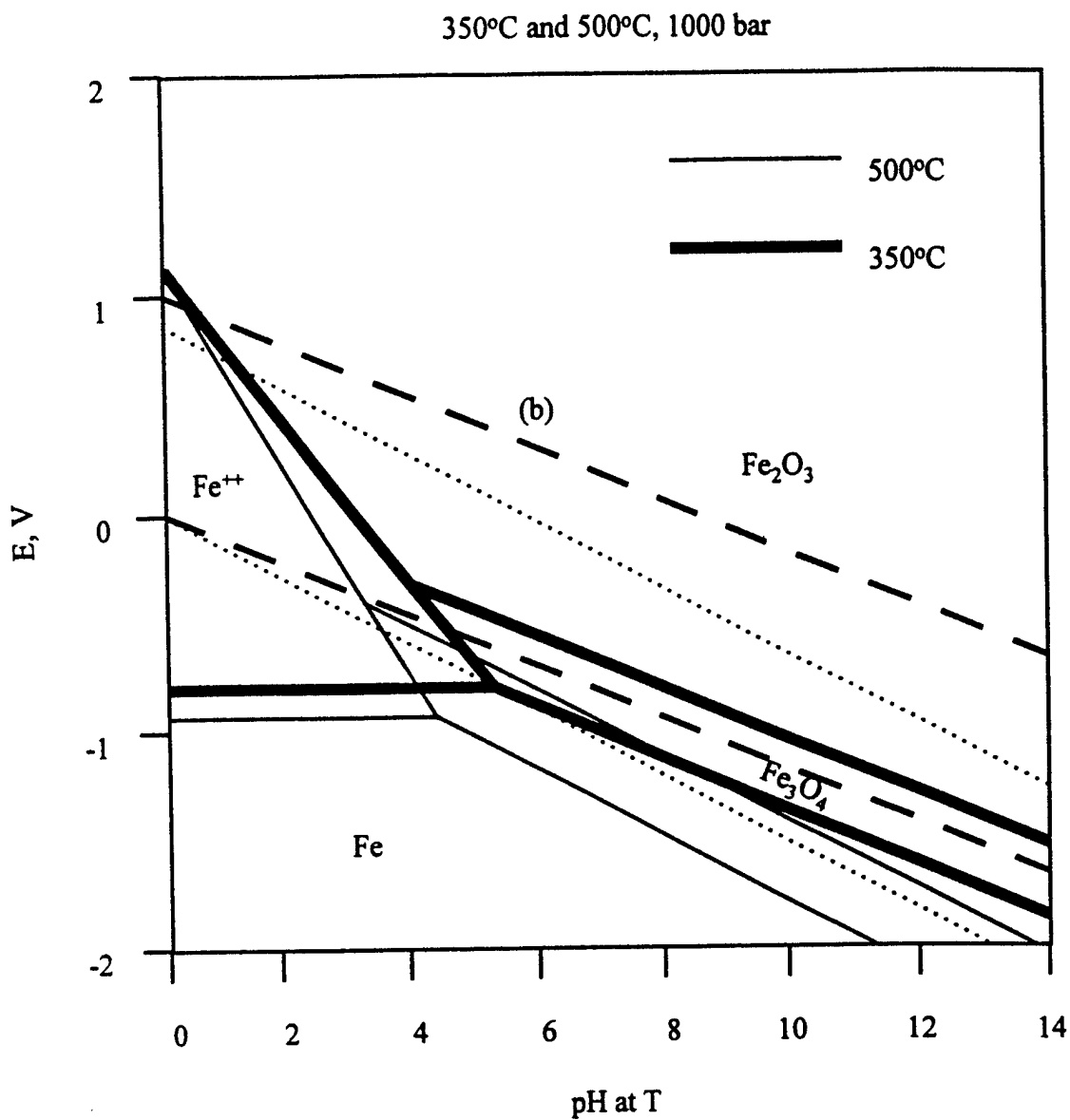
Figure 3-10. Comparison of potential-pH diagrams at 350 and 500°C, 1000 bars.

3-21

However, at temperatures above $T_c = 374°C$, the density (at a constant pressure) also drops precipitously with increasing temperature, which destabilizes highly charged ionic species even further (due to less effective solvation). We should note that highly charged species, such as Fe^{3+}, stabilize themselves in aqueous environments by decreasing their charge/radius ratios through hydrolysis (to form $Fe(OH)^{2+}$, $Fe(OH)_2^+$, $Fe(OH)_3^0$, for example) or by forming complex ions with anions in the solution (e.g., $FeCl^+$, $FeCl_2^+$, $FeCl_3^0$), as previously noted for iron at temperatures to 300°C.[9] These processes are expected to be even more important in supercritical systems but, due principally to the lack of reliable thermodynamic data, we have not included the hydrolyzed species or complex ions in the present work.

To our knowledge, the effect of pressure on the thermodynamic properties of iron in supercritical water has not been discussed previously. In Figure 3-11, we compare potential-pH diagrams at 400°C at pressures of 300 and 500 bar. The increase in the density of supercritical water with increasing pressure at a given activity of ionic species apparently favors an increase in the stability domain of iron. At still higher pressures (above 700-1000 bar), which are well above those envisaged for SCWO processes or that are experienced in supercritical thermal power plants, increasing pressure, on the contrary, results in the apparent stabilization of metal ions, and thus favors corrosion from a thermodynamic viewpoint. We note however, that changes in pressure (especially at the relatively low densities of water considered here) would result in significant changes in the standard chemical potentials of dissolved species, thus affecting the thermodynamic stability of iron.

At this point, it is necessary to caution the reader as to the accuracy of the calculated thermodynamic data for ionic species in low pressure supercritical media. As pointed out by

400°C, 500 bar and 300 bar
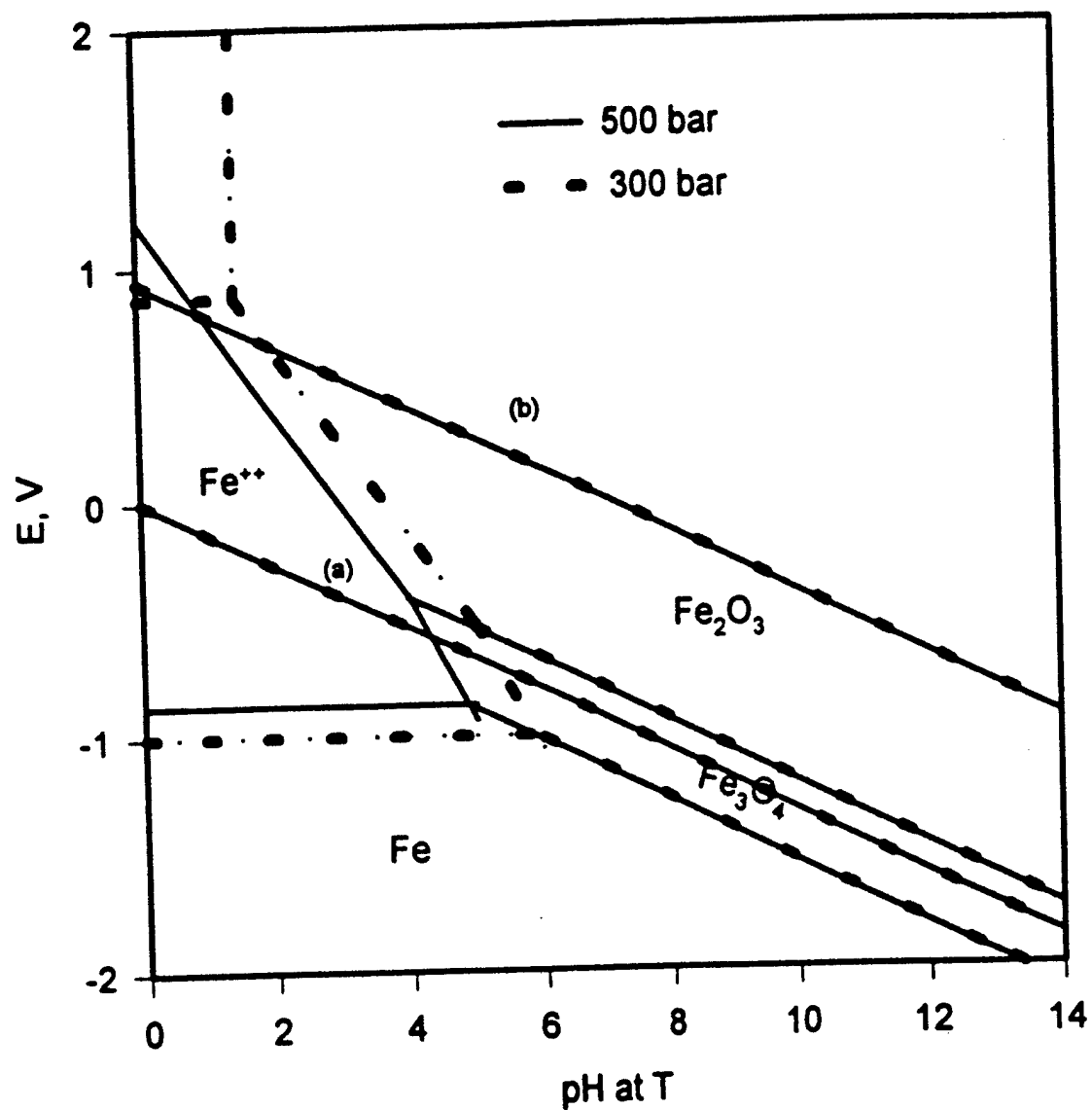
Figure 3-11. Comparison of potential-pH diagrams at a temperature of 400°C and at pressures of 500 and 300 bars.

Helgeson et al.,[31] the predictions of SUPCRT92 are not accurate at pressures below ≈ 500 bars for temperatures slightly above the critical temperature of water (374°C). This problem can be traced to the difficulties inherent in using a Born-type model for calculating the electrostatic contribution to the standard Gibbs energy of formation for an ion in a low density medium. On increasing the pressure, and hence on increasing the density, the Born model becomes increasingly more reliable. We illustrate the problem in Figure 3-12 by plotting the standard Gibbs energy change for the isocoulombic reaction $Fe^{+2} + H_2 = Fe + 2H^+$, calculated using SUPCRT92,[31] as a function of pressure and density for various temperatures. We see that for subcritical systems (in which the Born model is known to work quite well[24]), and for supercritical systems at high pressures and densities (Figure 3-13), the Gibbs energy change is an increasing monotonic function. However, for supercritical systems at low pressures and densities, ΔG° decreases with pressure and density over ranges that depend on the temperature. Thus, it would seem that the SUPCRT92 algorithm should be considered reliable for pressures greater than 500 bar, 1000 bar, and 1500 bar for temperatures of 400, 500, and 600°C, respectively. Thus, the diagrams that we present for 450°C and 500 bar, and that calculated for 400°C and pressure of 300 bar should be considered as being somewhat less precise. We should note that only those parts of the diagrams that involve ionic species are affected by these uncertainties. Clearly, the discussion presented above points to a pressing need to develop more accurate models for estimating thermodynamic functions in low density supercritical aqueous media.

Finally, we wish to emphasize here two most important drawbacks of potential-pH diagrams, which are general for any purely thermodynamic approach, for interpreting corrosion phenomena. First of all, Pourbaix diagrams show what reactions are possible or prohibited under
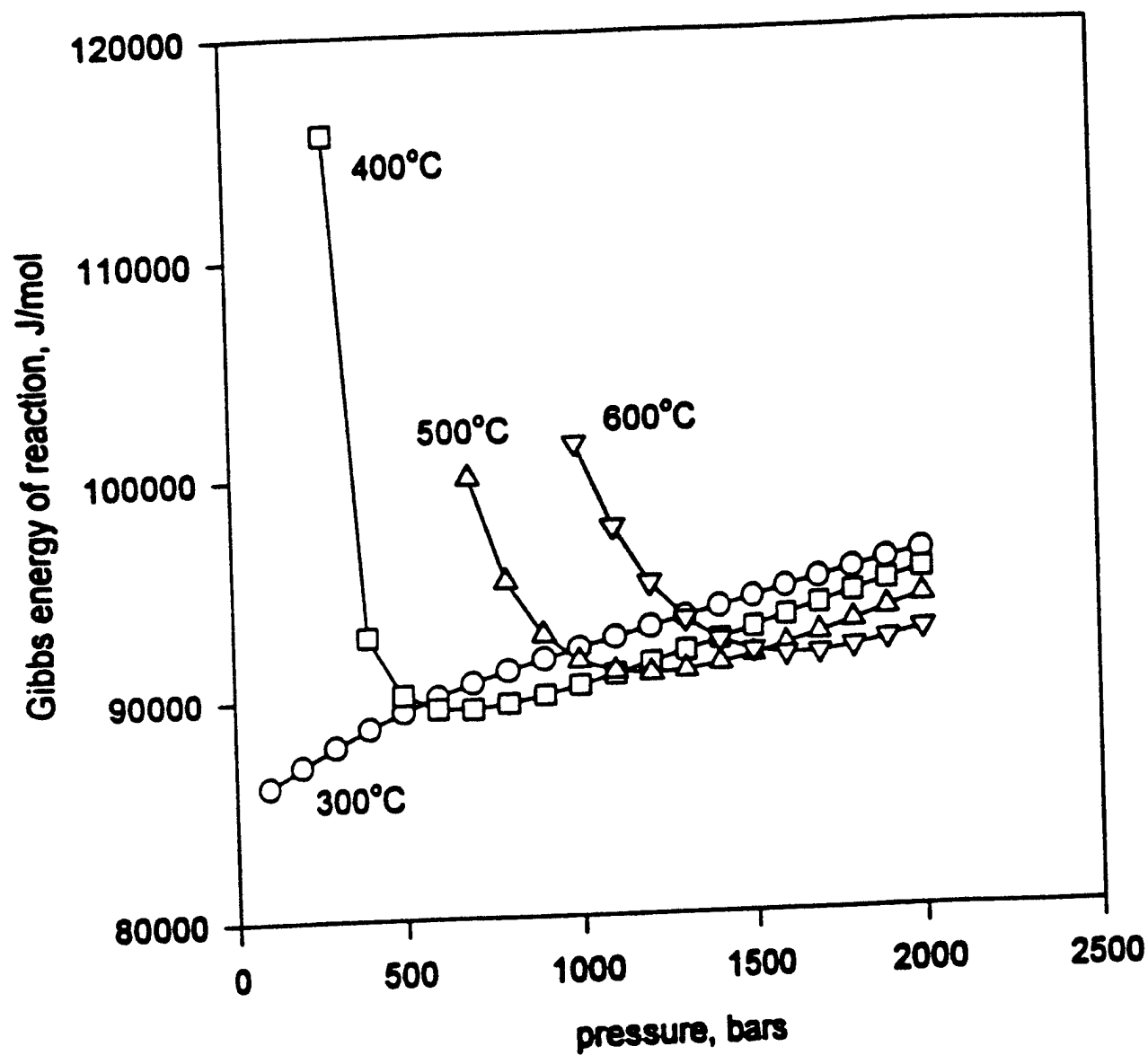
Figure 3-12.   Gibbs energy of Reaction (1), Table 3-1, as a function of pressure.

350°C, 1000 bar
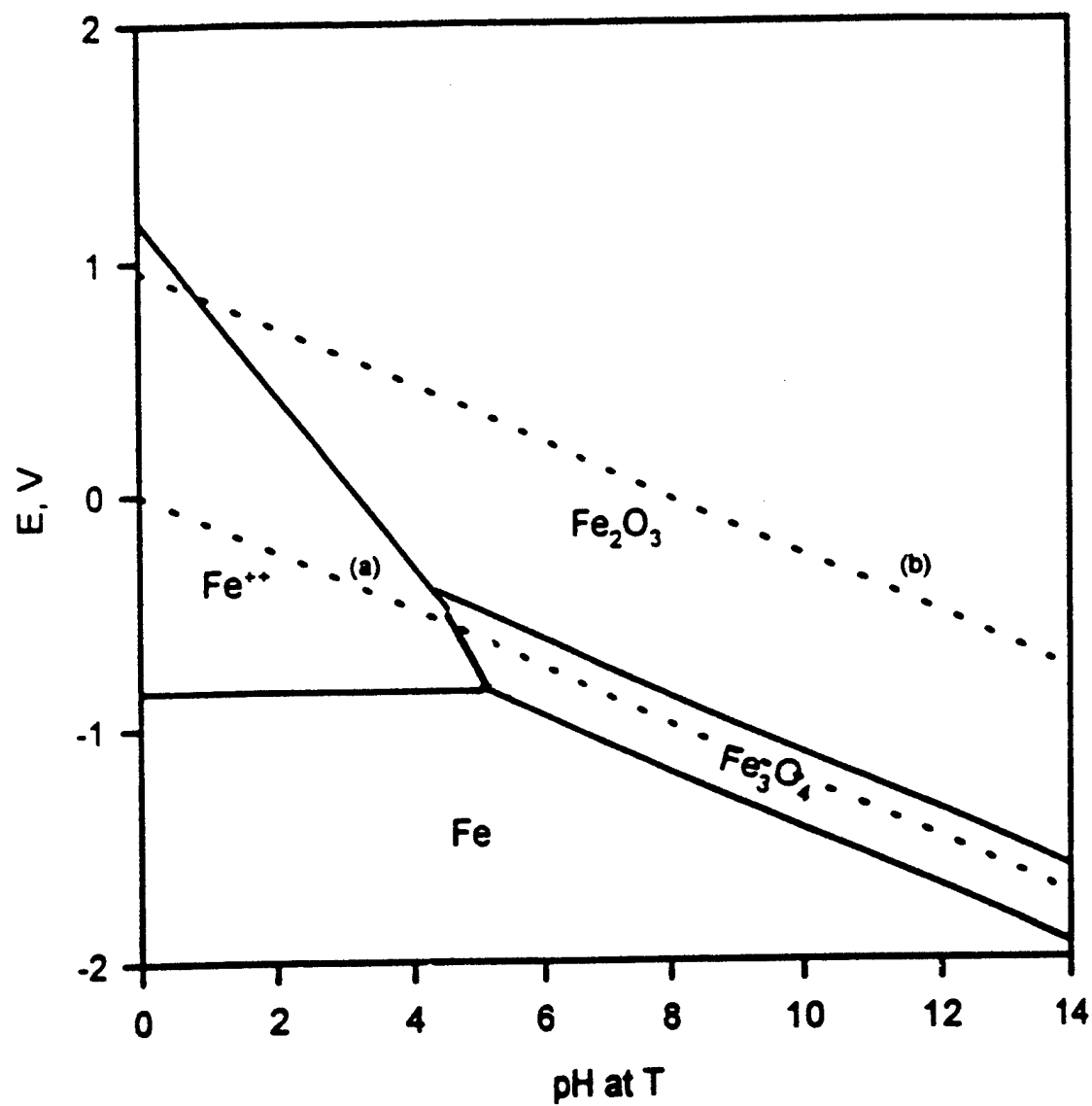
Figure 3-13.   Potential-pH diagram for Fe for 350°C and 1000 bars.

certain conditions; however, they say nothing about the rates of these reactions. Thus, the reaction rate of metal dissolution in the region of metal instability (for instance, at very low pH values and positive potentials) can be rather low at 100°C but may increase by several orders of magnitude as the temperature is raised to 400°C. At the same time, the predicted protection of the metal by the passive layer may be not realized because: (i) a low rate of formation of an oxide compared with its rate of dissolution may prevent its formation in the case of metastability or (ii) the passive film (regardless of whether it is stable or metastable) may be susceptible to breakdown by deleterious species in the environment. Thus, while metastable oxide layers, in many cases, can provide corrosion protection, their formation cannot be predicted, unequivocally, from equilibrium thermodynamics. The second major drawback of Pourbaix diagrams is that when they are constructed for the bulk metal, they cannot account for localized corrosion phenomena unless the conditions within the crevice can be specified, which is normally a kinetic problem. Thus, while the bulk metal may exist in the domain of thermodynamic immunity, the metal can be subject to significant corrosion damage due to localized corrosion, because conditions inside crevices are significantly different and lie outside of the immune region. Finally, we would like to emphasize the importance of comparing thermodynamic predictions with the actual field measurements of metallic corrosion, when interpreting corrosion phenomena.

3.1.4 Summary and Conclusions

In this work, potential-pH diagrams for the iron-water and nickel-water system (see Appendix) have been extended into the supercritical temperature region using thermodynamic

data generated by the computer program and model of Helgeson et al..[28-31] The following

conclusions can be drawn from an analysis of the diagrams:

1. The diagrams agree well with those available in the literature at subcritical temperatures (T

   < 300°C).

2. The domain of thermodynamic immunity of iron significantly decreases with increasing

   temperature, especially so at temperatures above 300°C.

3. The range of possible protection by passive oxide layers is shifted to lower pH values with

   increasing temperature.

4. Decreasing the pressure at supercritical temperatures is predicted to increase the domain of

   thermodynamic instability of iron (for the pressure range characteristic of SCWO systems).

3.1.5 References

1. M.Pourbaix, Atlas of Electrochemical Equilibria in Aqueous Solutions (Houston, TX: NACE, 1974).
2. C.M.Criss and J.W.Cobble, J.Amer.Chem.Soc. 86 (1964): p. 5385; p.5390.
3. H.E.Townsend, Corrosion Science, 10 (1970): p. 343.
4. R.J.Biernat and R.G.Robins, Electrochimica Acta 17 (1972): p. 1261.
5. D.Lewis, J.Inorg. Nucl. Chem. 33 (1971): p.2121.
6. R.L.Cowan and R.W.Staehle, J. Electrochem. Soc. 118, (1971): p.557.
7. D.D.Macdonald, G.R.Sherman, and P.Butler, Atomic Energy of Canada Ltd. Reports # 4136, 4137,4138,4139 (1972).
8. D.D.Macdonald and P.Butler, Corrosion Science, 13 (1973): p. 259.
9. D.D.Macdonald and B.C.Syrett, Corrosion 35 (1979): p.471.
10. D.D.Macdonald, Corrosion Science 16 (1976): p.461.
11. J.B.Lee, Corrosion 37 (1981): p.467.
12. H.S.Betrabet, W.B.Johnson, D.D.Macdonald, and W.A.T.Clark, in Equilibrium Diagrams, Proc. Int. Symp. Electrochem. Soc., Edited by R.P.Frankenthal and J.Kruger, 1984, p.83.
13. G.J.Theus et al., ibidem, p.95
14. J.T.N.Atkinson, ibidem, p.175.
15. P.Duby, in High Temperature High Pressure Electrochemistry in Aqueous solutions, NACE-4, p.353, 1976.
16. Diagrams of Chemical and Electrochemical equilibria, Proc. NATO Advanced Research Workshop, Edited by M.Pourbaix and A.Pourbaix, Brussels, Belgium, 1981.

17. D.Cubiccotti, Corrosion Scince, 44, (1988): p. 875.
18. D.Cubiccotti, Journal of Nuclear Materials, 167 (1989): p. 241.
19. D.Cubiccotti, Journal of Nuclear Materials, 201 (1993): p. 176.
20. P.Marcus and E.Protopopoff, J.Electrochem. Soc. 137(1990): 2709.
21. S.Huang, K.Daehling, T.E.Carleson, P.Taylor, C.Wai, A.Propp, in Supercritical Fluid Science and Technology, Edited by K.P.Johnston and J.M.L.Penninger, ACS Symposium Series 406, p.276, Washington D.C.,1989.
22. Proceedings of the First International Workshop on Supercritical Water Oxidation, Jacksonville, FL, 1995, in press.
23. D.F.Taylor, J.Electrochem.Soc. 125 (1978): p.808.
24. P.R.Tremaine and S.Goldman, J. Phys. Chem. 82 (1978): p.2317.
25. P.R.Tremaine, Int.Symp. Thermod. Nuclear Materials, Julich, 1979, p.47.
26. R.C.Murray and C.W.Cobble, 41 Internat. Water Conf. Engineers Soc. Western Pennsylvania, (1980): p. 295.
27. W.T.Lindsay, ibidem, p.284.
28. E.L. Shock and H.C.Helgeson, Geochim. et Cosmochim. Acta, 52 (1988): p. 2009.
29. H.C.Helgeson, K.D.H.Kirkham, and G.C.Flowers, Am.J.Sci. 281(1981): p.1249.
30. J.C.Tanger and H.C.Helgeson, Am. J. Sci. 288 (1988): p.19.
31. J.W.Johnson, E.H.Oelkers, and H.C.Helgeson, Computers & Geosciences 18 (1992): 899.

3.1.6 Appendix

Additional diagrams for the water-iron system and the nickel-water system are presented in this Appendix.
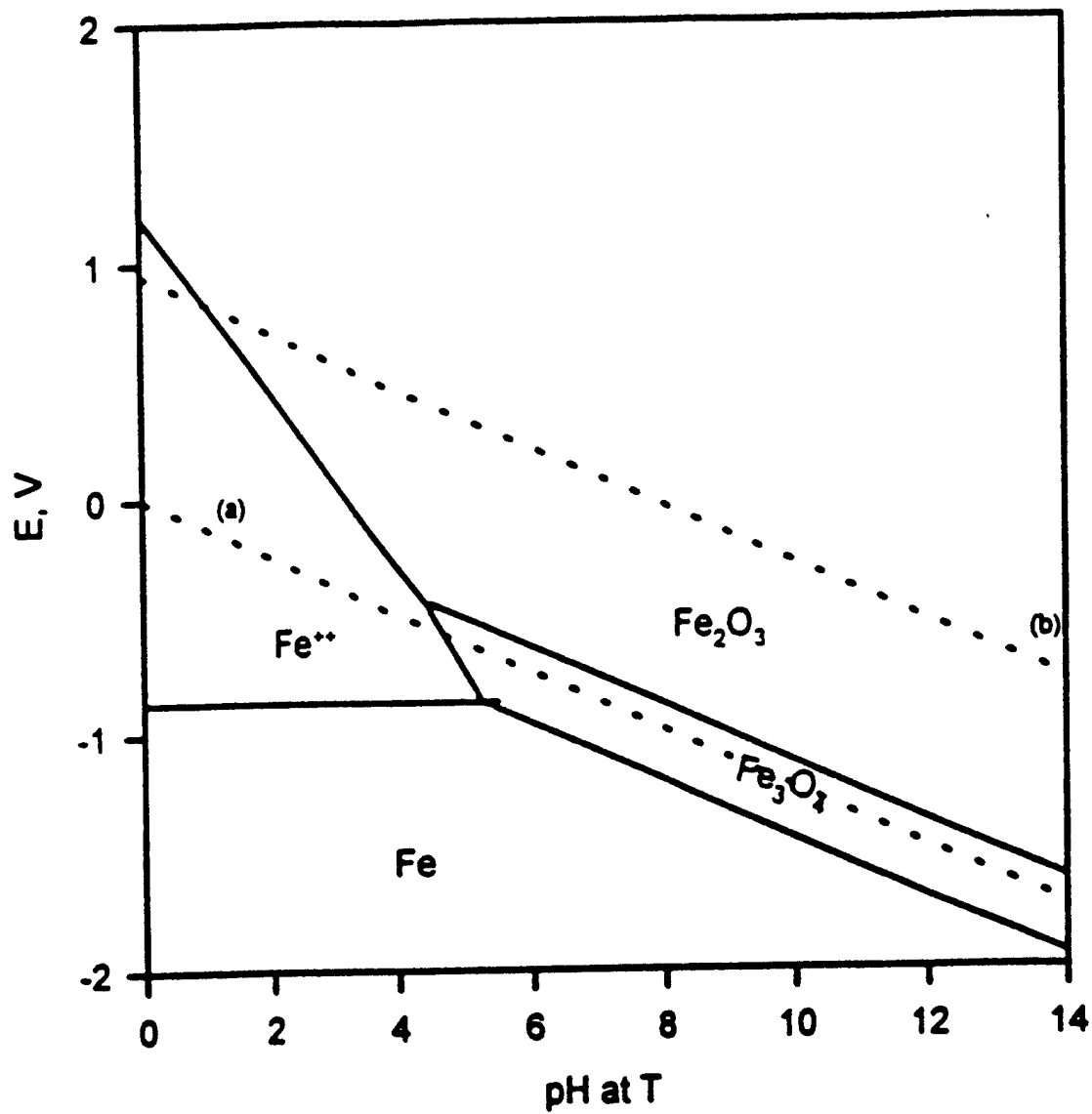
Figure 3-14.   Potential-pH diagram for Fe for 350°C and 2000 bars.

400°C, 1000 bar
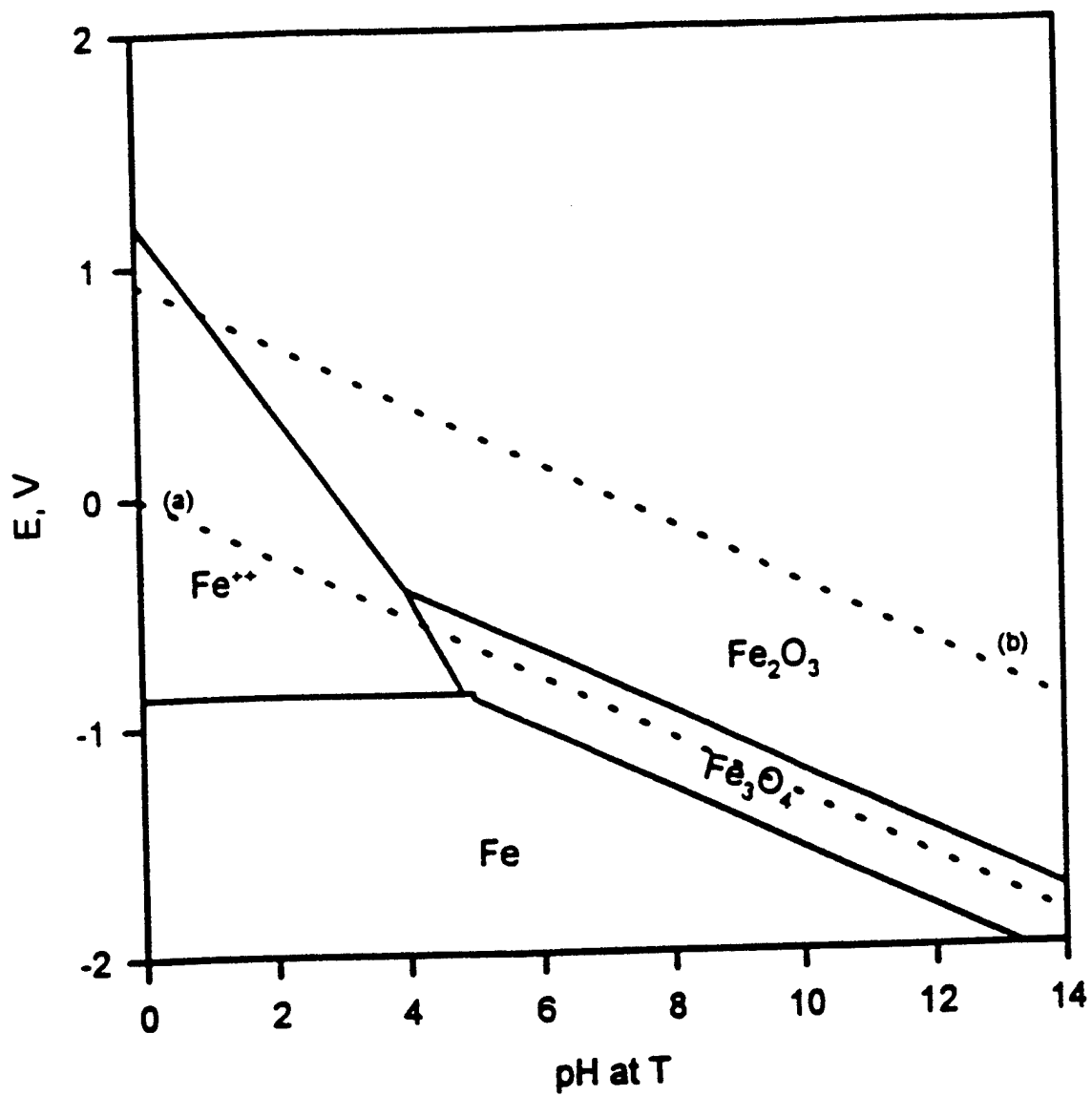
Figure 3-15.   Potential-pH diagram for Fe for 400°C and 1000 bars.

400°C, 2000 bar
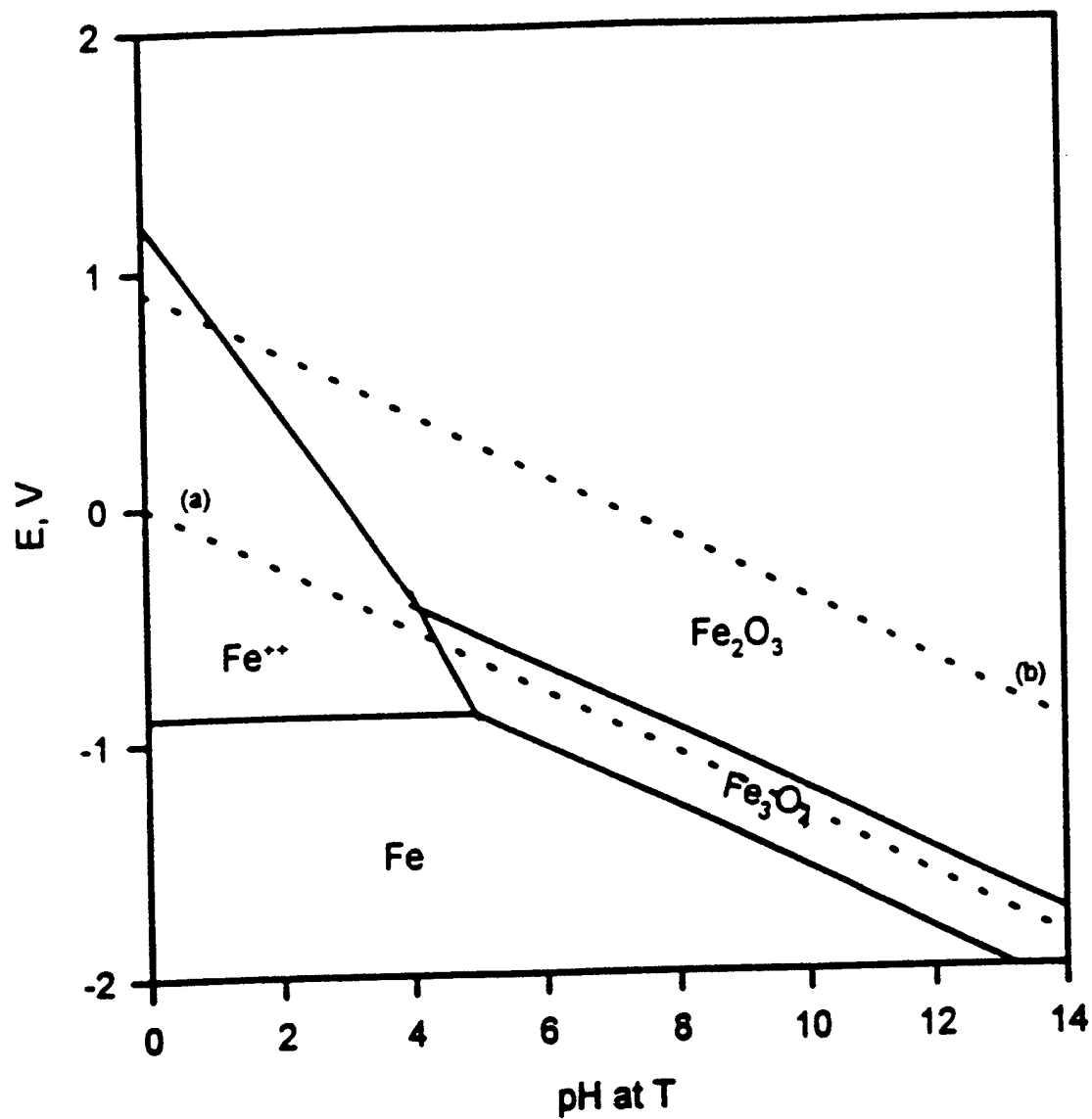
Figure 3-16.   Potential-pH diagram for Fe for 400°C and 2000 bars.

450°C, 1000 bar
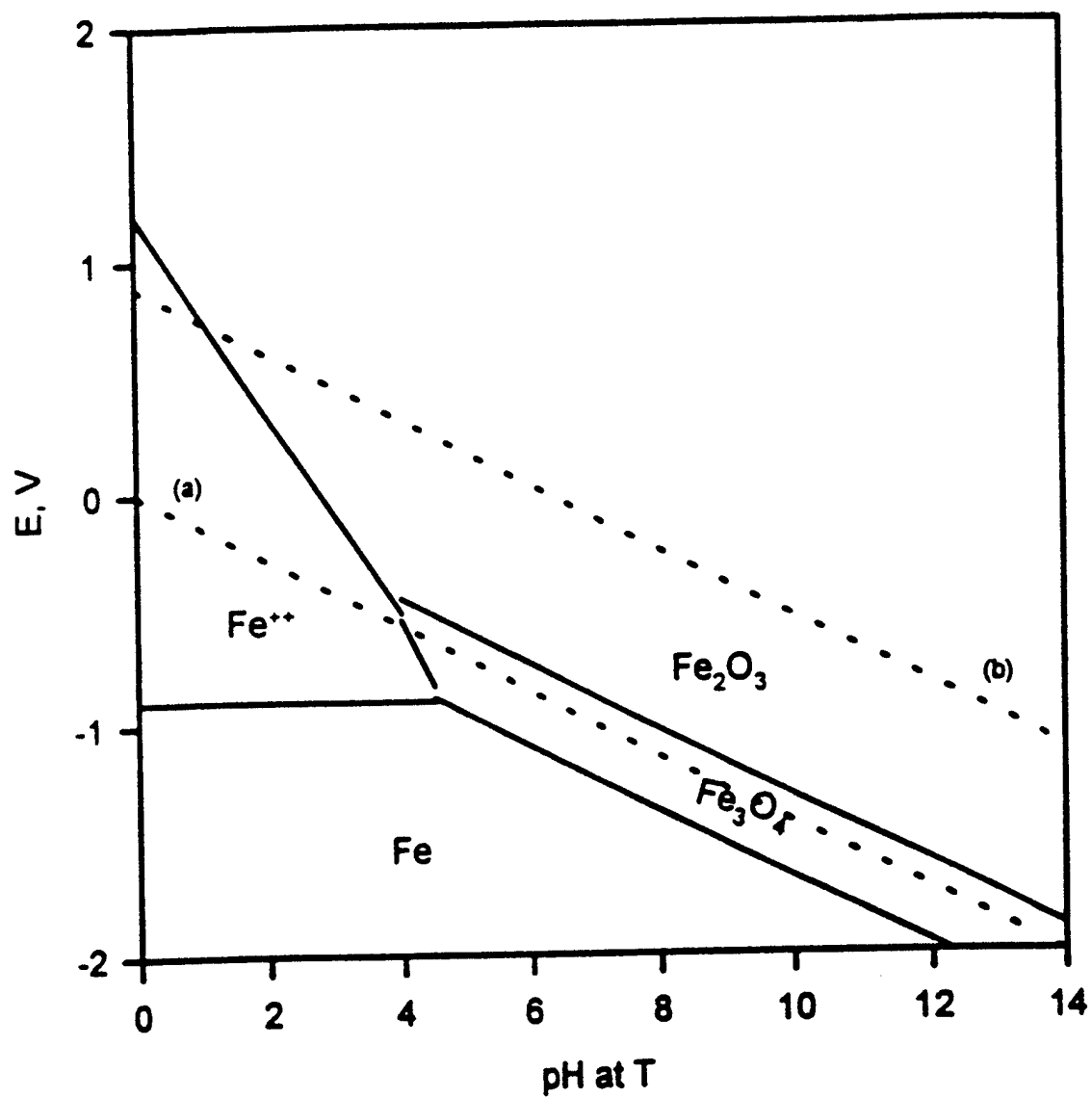
Figure 3-17.   Potential-pH diagram for Fe for 450°C and 1000 bars.

450°C, 2000 bar
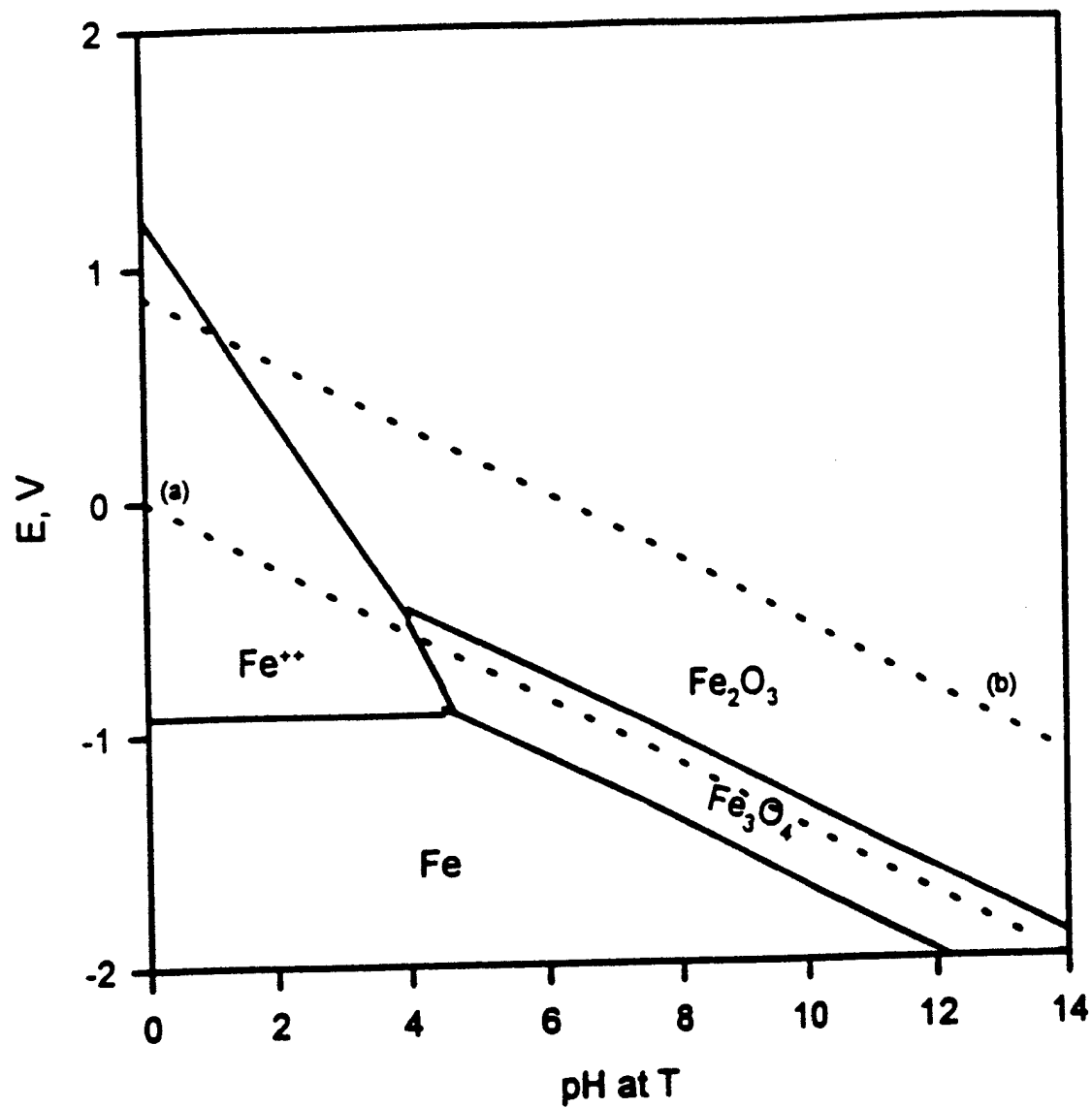
Figure 3-18. Potential-pH diagram for Fe for 450°C and 2000 bars.

100°C and 400°C, 500 bar
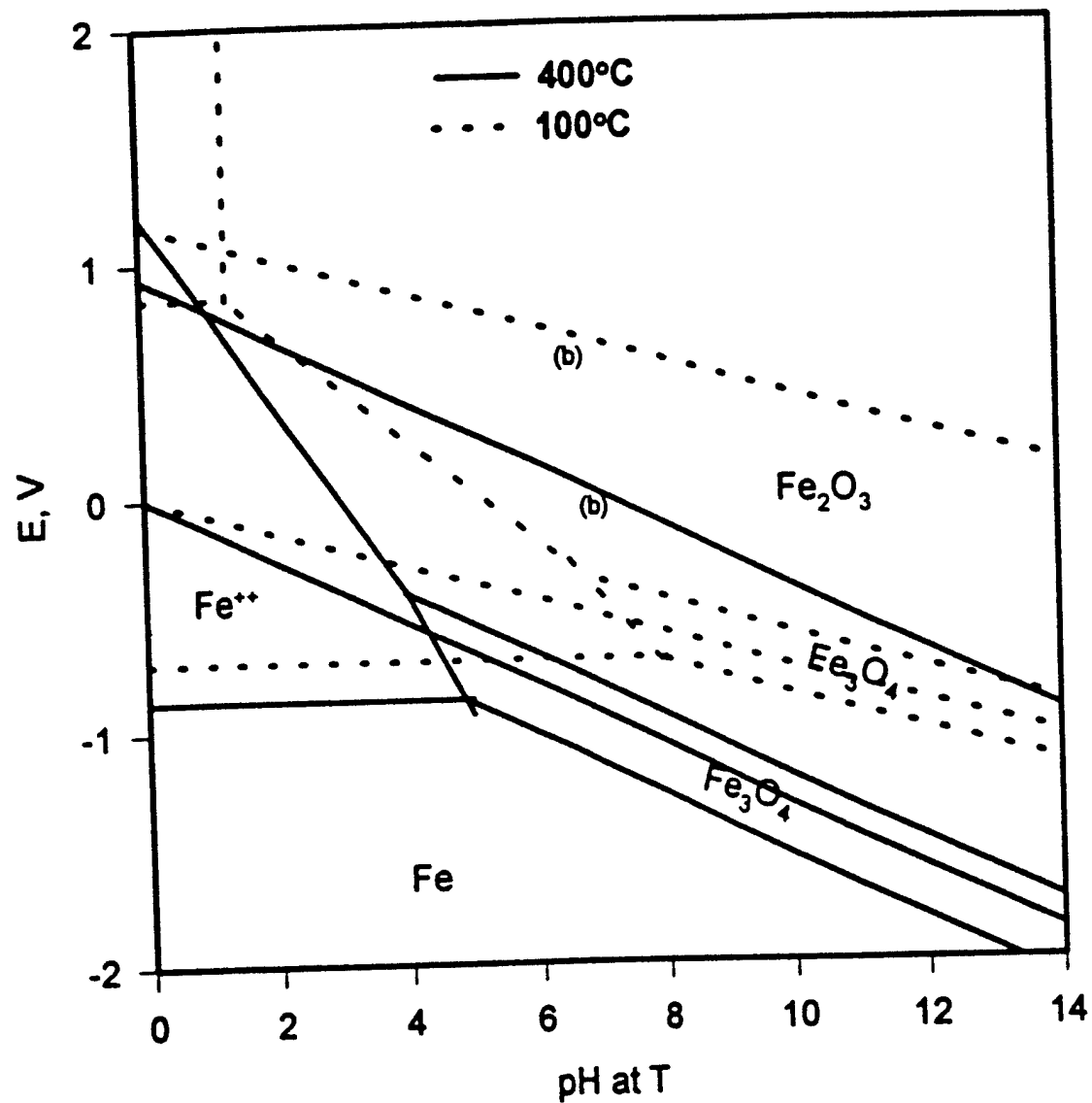
Figure 3-19.   Comparison of Potential-pH diagrams for Fe for 100 and 400°C at 500 bars.

100°C, 500 bar
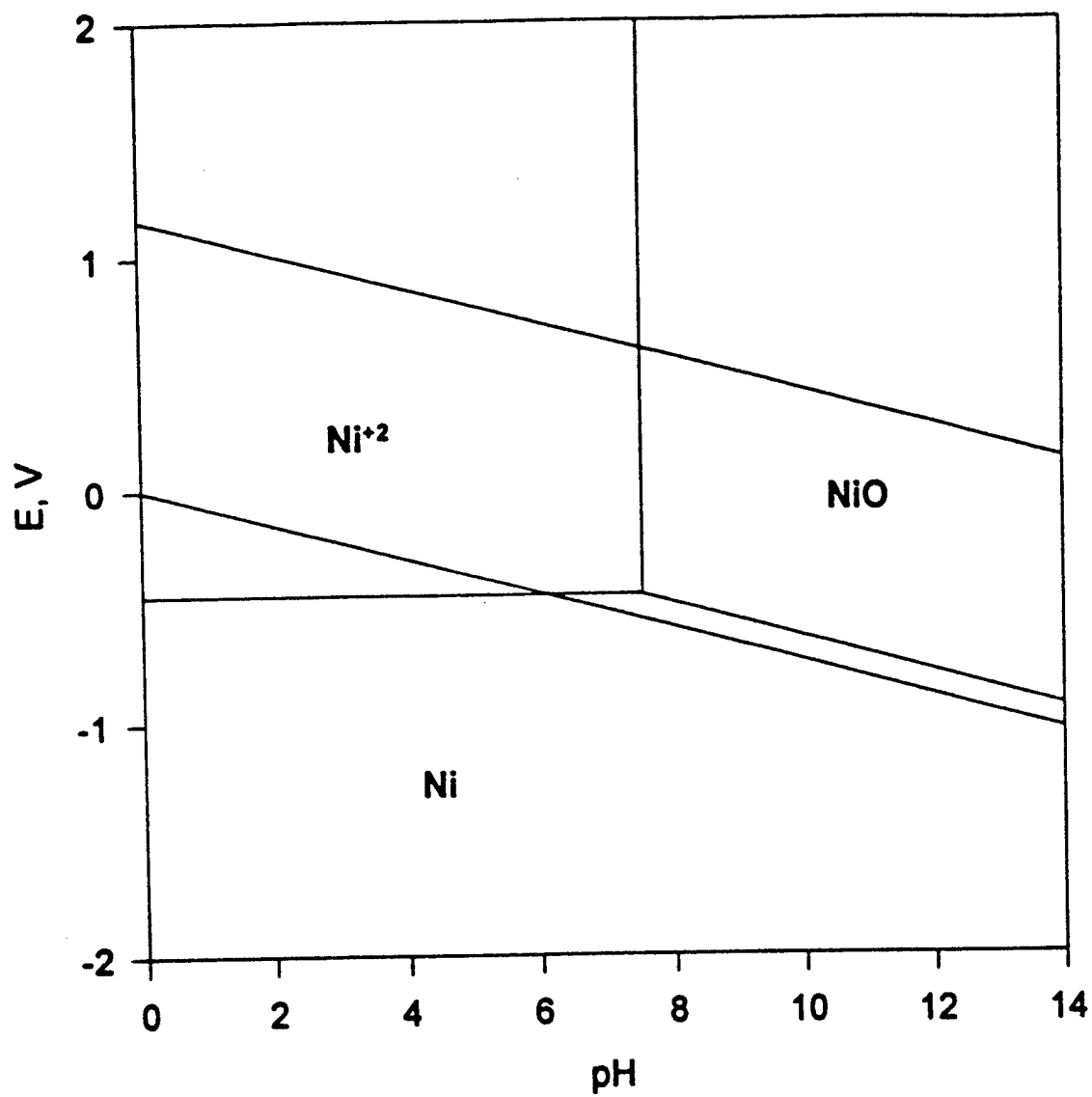
Figure 3-20. Potential-pH diagram for Ni at 100°C and 500 bars.

200°C, 500 bar
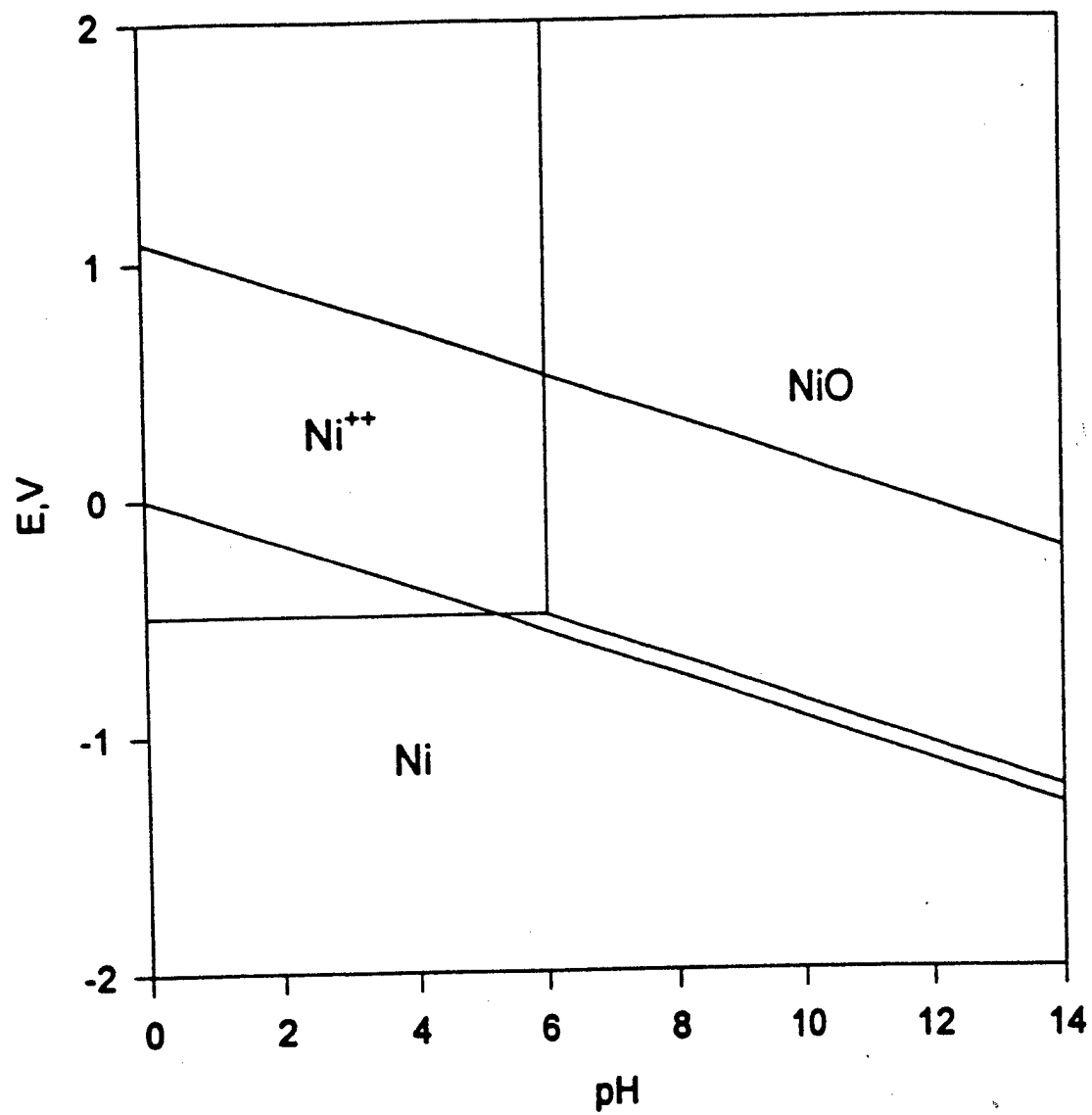
Figure 3-21.   Potential-pH diagram for Ni at 200°C and 500 bars.

300°C, 500 bar
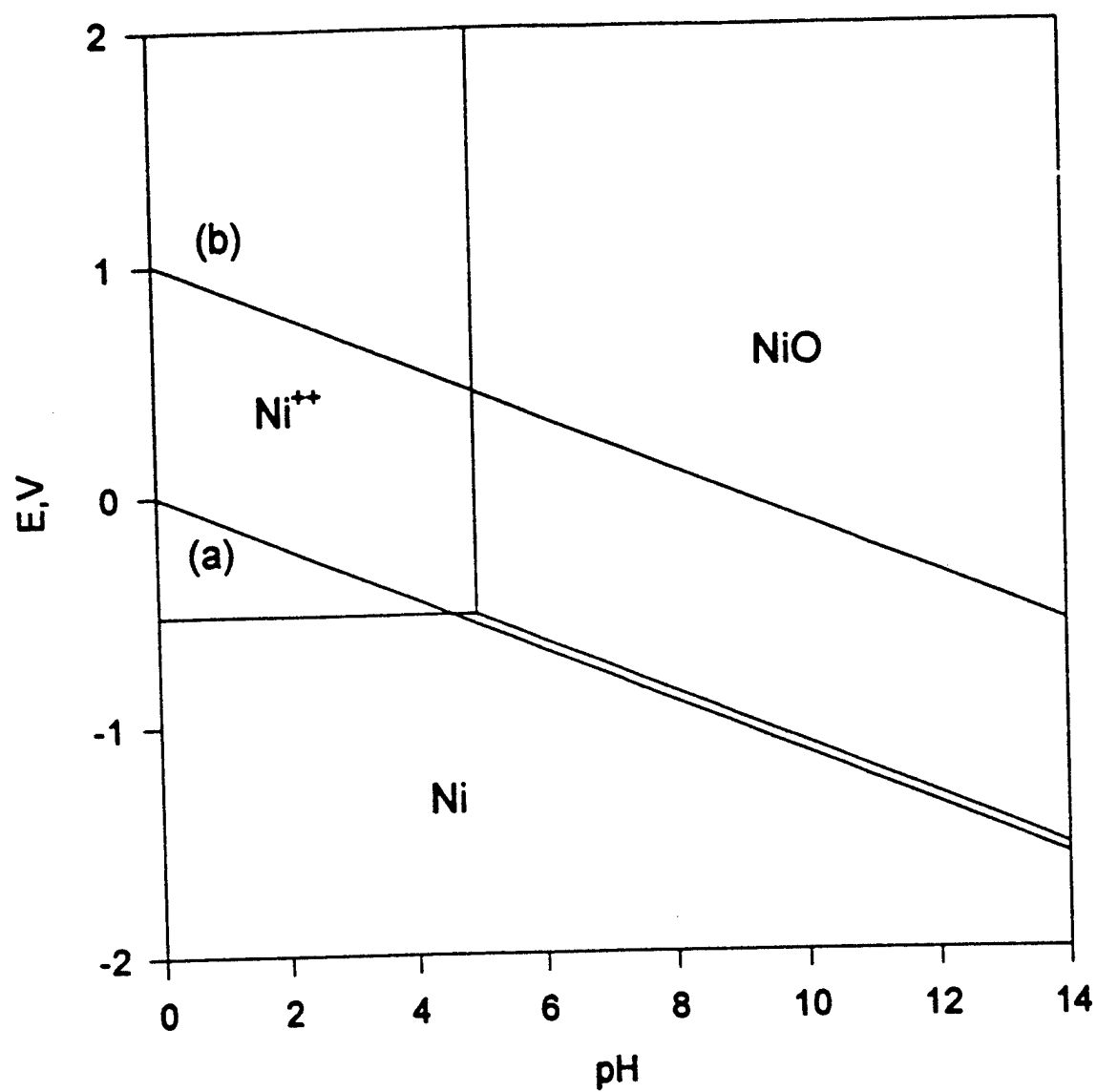
Figure 3-22.   Potential-pH diagram for Ni at 300°C and 500 bars.

400°C, 500 bar
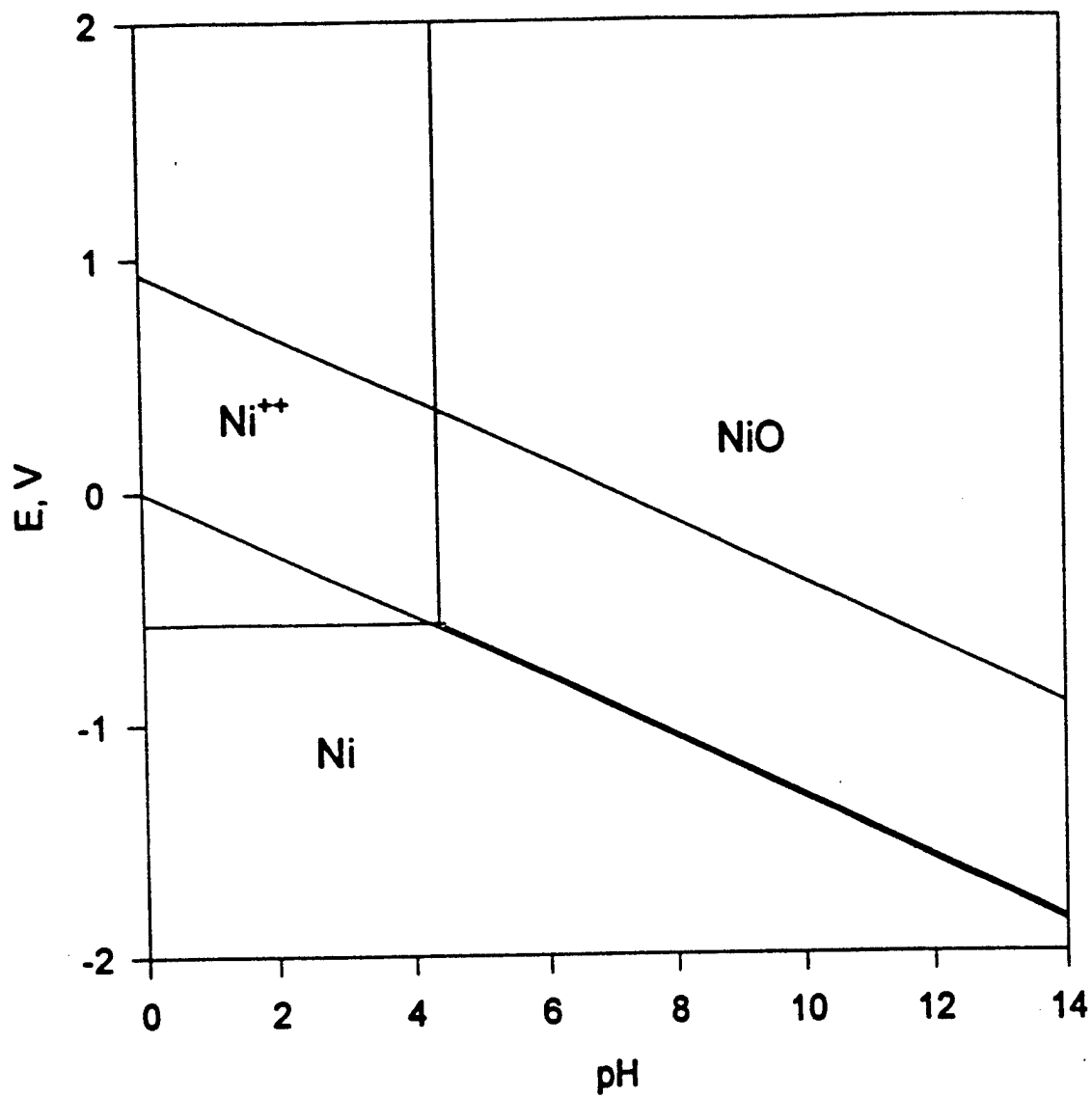
Figure 3-23.   Potential-pH diagram for Ni at 400°C and 500 bars.

450°C, 500 bar
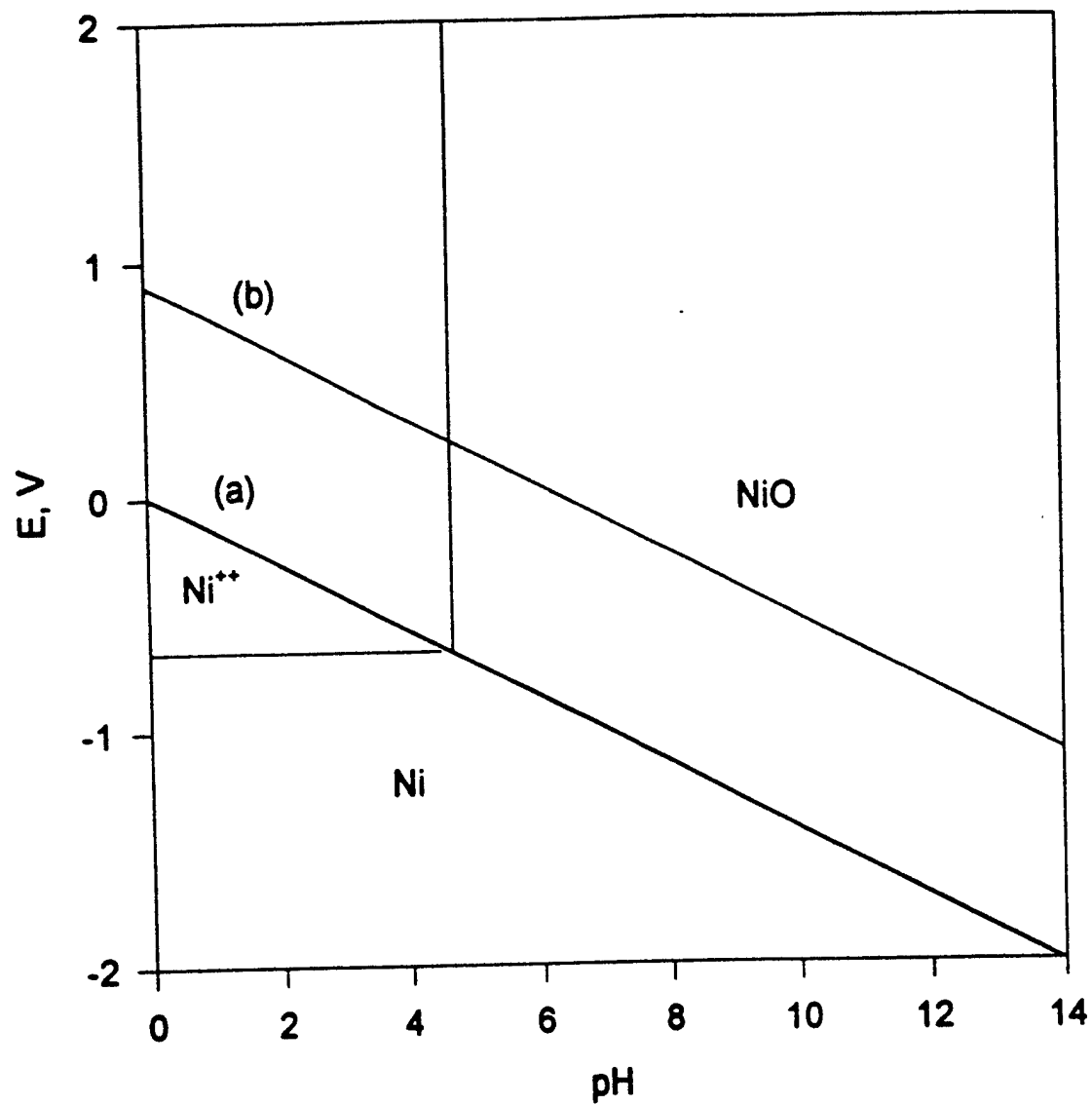
Figure 3-24. Potential-pH diagram for Ni at 450°C and 500 bars.

SECTION 4

HYDROGEN SENSORS

4.1. DEVELOPMENT OF DISSOLVED HYDROGEN SENSORS BASED ON YTTRIA-STABILIZED ZIRCONIA SOLID ELECTROLYTE WITH NOBLE METAL ELECTRODES

4.1.1 Abstract

A hydrogen sensor has been developed for *in situ* measurements of the concentration of hydrogen in aqueous solutions at elevated temperatures. The sensor was based on an electrochemical cell employing a yttria-stabilized zirconia (9% Y_2O_3) solid electrolyte, a $Ag-O_2$ (in air) reference electrode and a noble metal working electrode (Pt and Pd) covered with a PTFE membrane. The response of the sensor to hydrogen has been examined in gas mixtures and aqueous solutions at temperatures as high as 300°C, and for hydrogen concentrations ranging from 0.001 to 100% or 7.61×10^{-6} to 7.61×10^{-4} mol/kg, respectively. The sensor displayed rapid responses to changes in concentration of hydrogen in both gas mixtures and aqueous solutions. Linear relationships with Nernstian slopes (2.303RT/2F) were observed between the measured potential of the sensor and the logarithm of the hydrogen concentration. Oxygen in solution had little effect on the potential of the sensor when the concentration of oxygen was lower than that of hydrogen, while there was a significant change in the potential with oxygen concentration in gas mixtures. The potential of the sensor was not affected by the pH of the solution.

4.1.2 Introduction

To analyze and control the corrosion of metals and alloys in high temperature aqueous environments ranging from supercritical water oxidation (SCWO) systems to the heat transport systems of thermal power plants, it is necessary to monitor the chemical composition of the process fluid. Species such as H^+, dissolved oxygen, and dissolved hydrogen are particularly

important, because they determine the potential-pH regime of corrosion, and thus have a strong effect on the form of attack and on the rate of development of corrosion damage. Most thermal power plants are now equipped with water chemistry monitoring systems, which provide continuous analyses of conductivity, pH, and concentrations of oxygen, hydrogen, Cl⁻, and so forth. However, these analyses are carried out at ambient temperature, while the corrosion processes of interest occur at higher temperatures, and considerable doubt exists whether chemical parameters measured at ambient temperature accurately reflect water chemistry conditions at elevated temperatures. *In situ* monitoring of water chemistry at operating temperatures is therefore important.

Supercritical water oxidation (SCWO) is now being actively developed as a means of destroying toxic waste. The advantages offered by this technology are the high conversion factors (>99.999%, typically), the ability to handle even the most resilient waste materials (e.g., halogenated hydrocarbons), and the closed cycle nature of the operation (zero emissions). However, the oxidation of halogenated organics by oxygen in high subcritical and supercritical water results in the formation of highly corrosive conditions, to which few potential construction materials are immune. Although the environment may be highly oxidizing, suspicion exists that corrosion-induced hydrogen evolution may occur on active metals, such as iron, chromium, titanium, and zirconium, and on alloys containing these metals. The generation of hydrogen in SCWO systems could represent a significant hazard, and it is for this reason that rugged hydrogen sensors that are capable of operating at high subcritical temperatures are required.

The *in situ* measurement of hydrogen in high temperature aqueous systems has been previously described using differential resistance sensors consisting of Pd and Pt sensing

elements,[1,2] potentiometric combination sensors consisting of a yttria-stabilized zirconia (YSZ) membrane pH electrode and a Pt electrode,[3,4] and an amperometric sensor based on a two-electrode cell employing a proton-conducting solid electrolyte of zirconium phosphate, two Pt electrodes, and a PTFE diffusion membrane.[5] The differential resistance sensors can provide for the sensitive detection of hydrogen over a wide concentration range (0.01 to 11.25ppm) and can operate at high subcritical ($250<T<374°C$) and supercritical ($374<T<410°C$) temperatures.[1,2] The potentiometric sensors display good Nernstian response[4] and have been operated under supercritical conditions at temperatures as high as 455°C.[3] Because the YSZ pH electrode with a Hg-HgO internal reference element is rugged, and has been demonstrated to be free from interference from Cl$^-$ and S^{2-},[6-8] this sensor is particularly suited to monitoring process streams. However, the Pt electrode responds to changes in the redox potential of the system,[3] so that the unique determination of hydrogen concentration is difficult in the presence of other redox species. Finally, the amperometric sensor has been shown to respond rapidly to changes in hydrogen concentration in the range of 7.61×10^{-6} to 7.61×10^{-4} mol/kg,[5] with the output current being proportional to the square root of hydrogen concentration and with the current being almost independent of temperature within the range of 234 to 300°C.[5] The operation of the sensor in the region of the limiting current for the oxidation of hydrogen, where the current is proportional to the hydrogen concentration and therefore in the region of highest sensitivity, is difficult because of fast diffusion of hydrogen at elevated temperatures.[5] Thus, in order to monitor hydrogen *in situ* in high temperature aqueous systems, it will be necessary to develop other types of hydrogen sensors having different characteristics. In this study, we describe a new hydrogen sensor that can be used in aqueous solutions at temperatures up to 300°C. This sensor

is based on a two-electrode cell employing a silver-oxygen reference electrode and a noble metal working electrodes, a YSZ solid electrolyte, and a PTFE membrane.

4.1.3 Principles of Operation

The hydrogen sensor described in this study consists of a YSZ(ZrO_2-9mol%Y_2O_3) tube, a Ag powder internal reference electrode (inside the tube), and a hydrogen-sensitive working electrode (Pd, Pt) outside the tube. As shown in Figure 4-1, the working electrode is covered with a PTFE membrane to avoid direct contact with the environment. It is reasonable to assume that the PTFE membrane becomes rapidly saturated with hydrogen at the elevated temperatures of operation. We have also found that the Ag powder electrode in contact with the YSZ solid electrolyte works as a reversible oxygen electrode at temperatures above 250°C.[9] Accordingly, one can represent the sensor in the formal sense as

$$Ag - O_2(\text{in air}) \mid ZrO_2(Y_2O_3) \mid H_{ads}(\text{Pt or Pd}) \mid H_2(\text{in PTFE}) \mid H_2$$
$$\phi_{R,I} \quad ^I \phi_{Z,I} \quad \phi_{Z,II} \quad ^{II} \phi_{S,II}$$

(1)
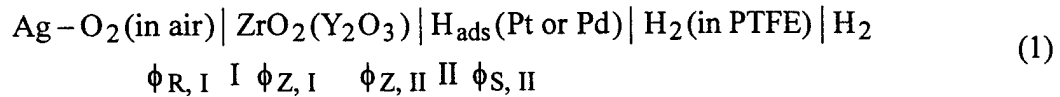
where H_{ads} is a hydrogen atom adsorbed at the YSZ-noble metal interface, ϕ is the electrical potential, and subscripts (R, I), (Z, I), (Z, II), and (S, II) denote the reference side of Interface I, the YSZ side of that interface, the YSZ side of Interface II, and the sensing side of that interface, respectively. Because YSZ is exclusively an oxygen ion conductor, the reactions that occur at Interfaces I and II can be written as

$$(1/2)O_2 + V_O^{\cdot\cdot} + 2e^- = O_O$$

(2)
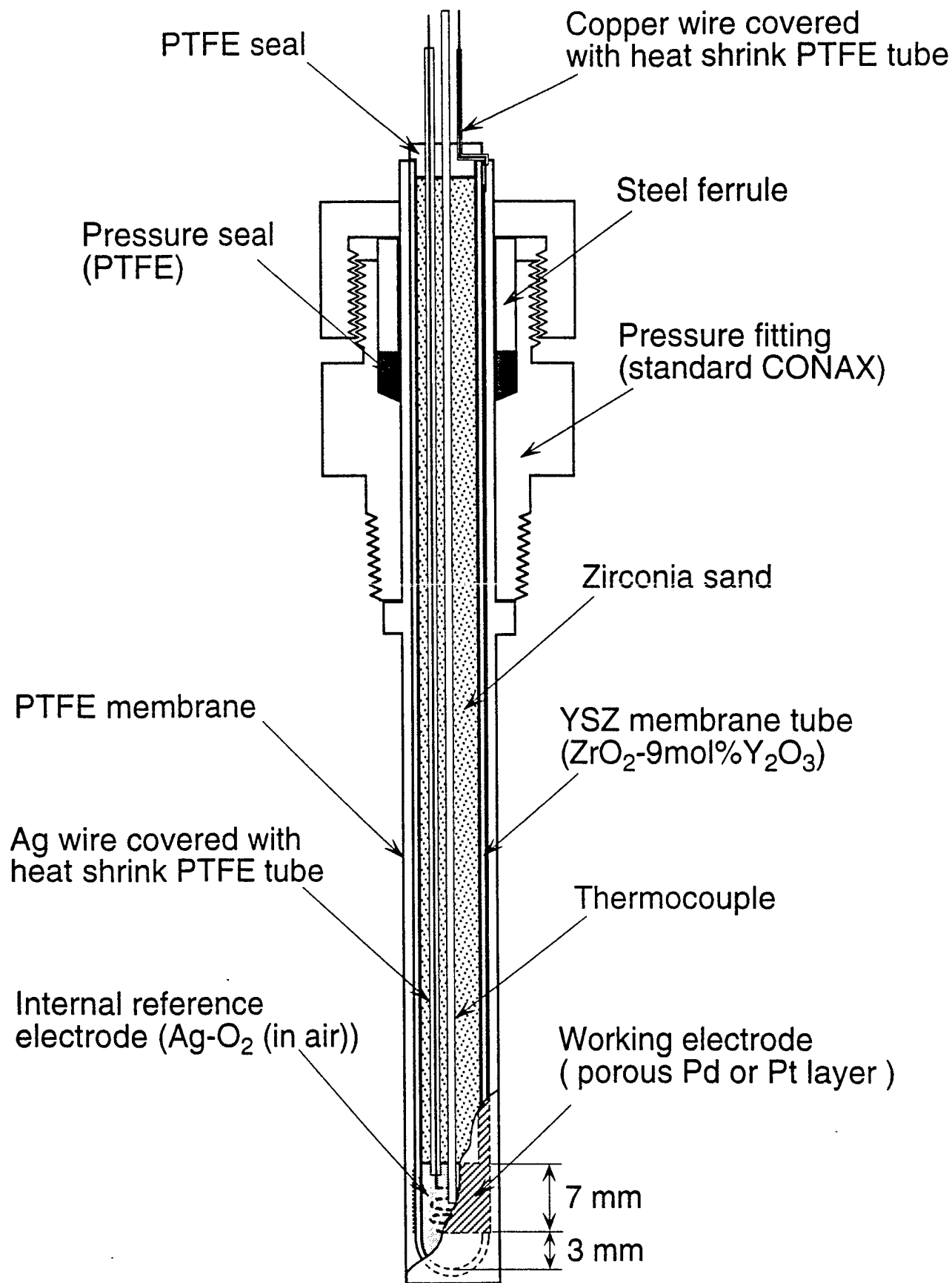
Figure 4-1. Schematic of YSZ-noble metal hydrogen sensor for use in high temperature aqueous solutions.

and

$$V_O^{..} + H_2O + 2e^- = O_O + 2H_{ads} \qquad (3)$$

respectively, where $V_O^{..}$ and O_O designate an oxygen vacancy with a formal double positive

charge and an oxide ion in a normal anion site in the YSZ lattice. The electrochemical potential

for each species in Reactions (2) and (3) is given by the following equation:

$$\mu_i = \mu_i^0 + RT \ln a_i + z_i F \phi \qquad (4)$$

where μ_i^0, a_i, and z_i are the standard chemical potential, the activity, and the charge on the

species i, respectively. At equilibrium, the sum of the electrochemical potentials for the species

on each side of Reactions (2) and (3) must be equal. This equilibrium condition leads to

potential differences at the two interfaces of

$$\phi_{R,I} - \phi_{Z,I} = \left(\mu_{O_2}^0 / 2 - \mu_{O_O}^0 + \mu_{V_O^{..}}^0 \right) \Big/ 2F + (RT/4F) \ln P_{O_2} + (RT/2F) \ln a_{V_O^{..},I} \qquad (5)$$

$$\phi_{S,II} - \phi_{Z,II} = \left(\mu_{H_2O}^0 - \mu_{H_2}^0 - \mu_{O_O}^0 + \mu_{V_O^{..}}^0 \right) \Big/ 2F + (RT/2F)(\ln a_{V_O^{..},I} + \ln a_{H_2O} - \ln a_{H_{ads}}^2) \qquad (6)$$

Subtracting Equation (6) from Equation (5) yields the potential of the noble metal working

electrode with respect to the reference Ag-O_2 ($P_{O_2} = 0.21$ atm) electrode as

$$\begin{aligned} E &= \left(\phi_{S,II} - \phi_{Z,II} \right) - \left(\phi_{R,I} - \phi_{Z,I} \right) \\ &= -E_1^0 - (RT/4F) \ln 0.21 + (RT/2F) \ln a_{H_2O} - (RT/F) \ln a_{H_{ads}} \end{aligned} \qquad (7)$$

where the standard potential, E_1^0, is related to the change in standard chemical potential for the

reaction

4-7

$$H_2 + (1/2)O_2 = H_2O \tag{8}$$

by

$$E_1^0 = -\Delta\mu^0 / 2F = -\left(\mu_{H_2O}^0 - \mu_{H_2}^0 - \mu_{O_2}^0 /2\right)\Big/ 2F \tag{9}$$

The water formed in Reaction (3) exists as a liquid or vapor, depending on the environment to which the sensor is exposed. Accordingly, the potential given by Equation (7) depends upon the activity or fugacity of water in the appropriate phase.

4.1.3.1 Gas Mixtures

In gaseous environments, the water formed by Reaction (3) equilibrates with water vapor in the atmosphere. The activity of water in Equation (7), therefore, must be replaced by the fugacity (or partial pressure, P_{H_2O}, to a good approximation). If the value of P_{H_2O} at the YSZ-noble metal interface is constant, the potential of the hydrogen sensor depends only on the activity, $a_{H_{ads}}$, of hydrogen adsorbed at the interface. The following adsorption-desorption reaction for hydrogen occurs on noble metal surfaces in a hydrogen-inert gas mixture:

$$H_2(g) \overset{k_1}{\underset{k_{-1}}{\longleftrightarrow}} 2H_{ads} \tag{10}$$

where k_1 and k_{-1} are the rate constants for forward and reverse reactions, respectively. The rate equation for Reaction (10) is given by

$$d[H_{ads}] / dt = k_1 P_{H_2} - k_{-1}[H_{ads}]^2 \tag{11}$$

where P_{H_2} is the partial pressure of hydrogen. At equilibrium $d[H_{ads}] / dt = 0$. Then, we have

$$[H_{ads}] = \sqrt{(k_1/k_{-1})P_{H_2}} \tag{12}$$

and Equation (7) becomes

$$E = -E_1^0 + (RT/2F)\ln P_{H_2O} - (RT/2F)\ln(k_1/k_{-1}) - (RT/2F)\ln P_{H_2} \tag{13}$$

If oxygen is present in the system, the oxidation of adsorbed hydrogen takes place on the noble metal surface. We assume that the following oxidation reactions occur:

$$O_2(g) + 2H_{ads} \overset{k_2}{\underset{k_{-2}}{\leftrightarrow}} 2OH_{ads} \tag{14}$$

and

$$OH_{ads} + H_{ads} \overset{k_3}{\underset{k_{-3}}{\leftrightarrow}} H_2O(g) \tag{15}$$

The rate equations for adsorbed species in Reactions (10), (14), and (15) are written as

$$d[H_{ads}]/dt = k_1 P_{H_2} - k_2 P_{O_2}[H_{ads}]^2 - k_3[OH_{ads}][H_{ads}] + k_{-3}P_{H_2O} \tag{16}$$

$$d[OH_{ads}]/dt = k_2 P_{O_2}[H_{ads}] - k_3[OH_{ads}][H_{ads}] + k_{-3}P_{H_2O} \tag{17}$$

In Equations (16) and (17), we have assumed that k_{-1} and k_{-2} are negligibly small, because the reverse reaction in Equation (10) is negligible in the presence of oxygen and the enthalpy of Reaction (14) is expected to be large.[10] At equilibrium, Equations (16) and (17) yield

$$[H_{ads}] = \sqrt{(k_1/2k_2)(P_{H_2}/P_{O_2})} \tag{18}$$

4-9

and Equation (7) becomes

$$E = -E_1^0 - (RT/4F)\ln 0.21 + (RT/2F)\ln P_{H_2O} - (RT/2F)\ln(k_1/2k_2)$$
$$-(RT/2F)\ln P_{H_2} + (RT/2F)\ln P_{O_2} \tag{19}$$

At 300°C we have $E_1^0 = 1.116$ V and $E_1^0 + (RT/4F)\ln 0.21 = 1.0968$ V.

4.1.3.2 Aqueous Solutions

In aqueous solutions, the water formed in Reaction (3) equilibrates with that in the solution. Both the noble metal electrode and the YSZ solid electrolyte are in contact with water after a significant amount of water is produced. For this situation, we can represent the sensor inside the PTFE membrane as

$$Ag - O_2(\text{in air}) \mid ZrO_2(Y_2O_3) \mid H_2O, H^+, H_2 \mid Pt \text{ or } Pd \tag{20}$$
$$\text{I} \qquad\qquad \text{II} \qquad\qquad \text{III}$$
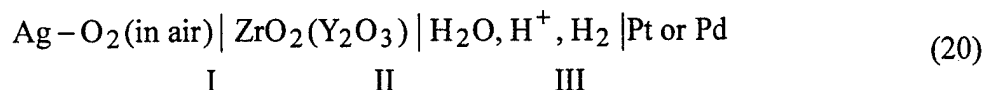
From this representation, one can find that the sensor is equivalent to an electrochemical cell that consists of a noble metal hydrogen electrode and a YSZ pH electrode in the same water. That is, the sensor is analogous to the potentiometric combination sensor consisting of a YSZ pH electrode with a Hg-HgO internal element and a Pt hydrogen electrode immersed in the same solution.[3,4] In contrast to the combination sensor, however, both the YSZ pH and noble metal hydrogen electrodes in Cell (20) are separated from actual solutions by the PTFE membrane, so that there is no redox species except for water-related species (H_2O, H_2, O_2, H^+, OH^-) in contact with the surface. The reactions at Interfaces II and III are written as

$$H_2O + V_O^{\bullet\bullet} = 2H^+ + O_O \tag{21}$$

and

$$2H^+ + 2e^- = H_2 \tag{22}$$

By combining Equations (2), (21), and (22), one can write the overall reaction of the sensor as

$$H_2 + (1/2)O_2 = H_2O\ (\ell) \tag{23}$$

The corresponding potential of the noble metal electrode with respect to the internal Ag reference electrode is given by the following equation:

$$E = -E_2^0 - (RT/4F)\ln 0.21 + (RT/2F)\ln a_{H_2O} - (RT/2F)\ln f_{H_2} \tag{24}$$

where f_{H_2} is the hydrogen fugacity in the water. The fugacity is defined as

$$f_{H_2} = \gamma_{H_2} \bullet m_{H_2} / K_H \tag{25}$$

where γ_{H_2} and m_{H_2} are the activity coefficient and molal concentration (mol•kg^{-1}) of dissolved hydrogen, and K_H is the Henry's constant for hydrogen (mol•kg^{-1}•atm^{-1}). At 300°C, we have $E_2^0 = 1.013\,V$ and $E_2^0 + (RT/4F)\ln 0.21 = 0.994\,V$. Equation (24) indicates that, at a given temperature, a linear relationship, with a unique Nernstian slope, should exist between the measured potential and the logarithm of the dissolved hydrogen concentration.

4.1.4 Experimental

Sensors were fabricated from YSZ tubes, closed at one end (9%Y$_2$O$_3$, Coors Ceramics Co.), that were 6.35 mm in diameter, 0.76 mm in wall thickness, and 101.6 or 152.4 mm in length. Materials used as working electrodes were Pt and Pd. A conventional painting method and an ion-beam-sputter (IBS) deposition technique were employed to prepare the electrodes. Pt and Pd paints (Ferro MSI Group) were applied to the appropriate position on the YSZ tubes, as

shown in Figure 4-1, and the coatings were fired at 1100°C for 12h in a pure Ar atmosphere. Before firing, organic binders in the paints were slowly burned out by increasing the temperature gradually from 250°C to 450°C in an Ar atmosphere followed by maintaining the temperature at 550°C for 30 min. in air. The thickness of the painted electrodes was about 0.02 mm. The preparation of thin IBS-Pt and -Pd electrodes was performed at Tohoku University, Japan. The ion-beam sputtering system used was equipped with a Kaufman type ion-source. Prior to sputter deposition, the vacuum chamber of the system was evacuated to a pressure lower than 2.2×10^{-4} Pa. Sputter deposition was then carried out at an Ar pressure of 3.5×10^{-2} to 3.7×10^{-2} Pa. The thicknesses of IBS-Pt and -Pd films were 150 nm and 110 nm, respectively. Silver powder (99.9%, 100 mesh, Alpha-Johnson Matthey) was used to prepare a reference electrode inside the YSZ tube. A silver wire and a thermocouple were embedded in the Ag powder to establish electrical contact and to measure the temperature of the sensor, respectively. The remaining part inside the tube was filled with ZrO_2 sand. For the experiments in high temperature aqueous solutions, the YSZ tube was covered with a PTFE sheath of 1mm thickness and fitted into a standard Conax fitting with a PTFE sealant. In the experiments in gas mixtures, a heat-shrink PTFE tube was adopted instead of using the PTFE sheath.

The response to changes in hydrogen concentration was examined at temperatures in the range of 250 to 300°C. Hydrogen-nitrogen mixtures (0.001 to 100% H_2) were used to change the concentration of hydrogen. A gas blending system, consisting of two mass flow meters and a gas mixing chamber, was used to obtain gas mixtures of appropriate compositions. The flow rate of the gas mixtures was adjusted to 200 sccm to keep the total pressure at 101.3 kPa, and a small test cell with a volume of 30cm^3 was used for the experiments with gas mixtures. The potential

of the working electrode of the sensor was measured with respect to the Ag-O$_2$ (in air) electrode by using a Keithley 617 electrometer having an input impedance of 2×10^{14} Ω.

The experiments in high temperature aqueous solutions were performed in a once-through flow system activated by a high pressure liquid chromatography pump as described elsewhere.[8] A single (liquid) phase was maintained in the system by adjusting the discharge pressure of the solutions to 11.7 MPa (1700 psig). The test solutions were pure water and 0.01M-NaOH. The hydrogen concentration in the solutions was controlled by sparging the solution reservoir with the gas mixtures having the appropriate composition. A solution flow rate of 0.0806 cm^3/s was employed, yielding a volume replacement time of approximately 1000s.

4.1.5 Results and Discussion

4.1.5.1 Hydrogen Response in Gas Mixtures

Figure 4-2 shows a typical response curve for the sensor equipped with a painted Pd working electrode in dry hydrogen-nitrogen gas mixtures at 300°C. Relatively rapid and reversible responses to changes in hydrogen concentration were observed: the 90% response time, which is defined as the time required to obtain 90% of the total potential variation, is about 1.5 ks. The steady state is reached within 3.6 ks after an increase in the hydrogen concentration. Although a longer time is required to reach the steady state when the concentration decreases, the steady state potential at a given hydrogen concentration is independent of the direction of change in the hydrogen concentration. Similar response characteristics were observed for the sensor with a painted Pt electrode. The sensors with IBS-Pt and -Pd electrodes showed fast responses compared with those with painted electrodes. To compare the response rates of the sensors, the

4-13
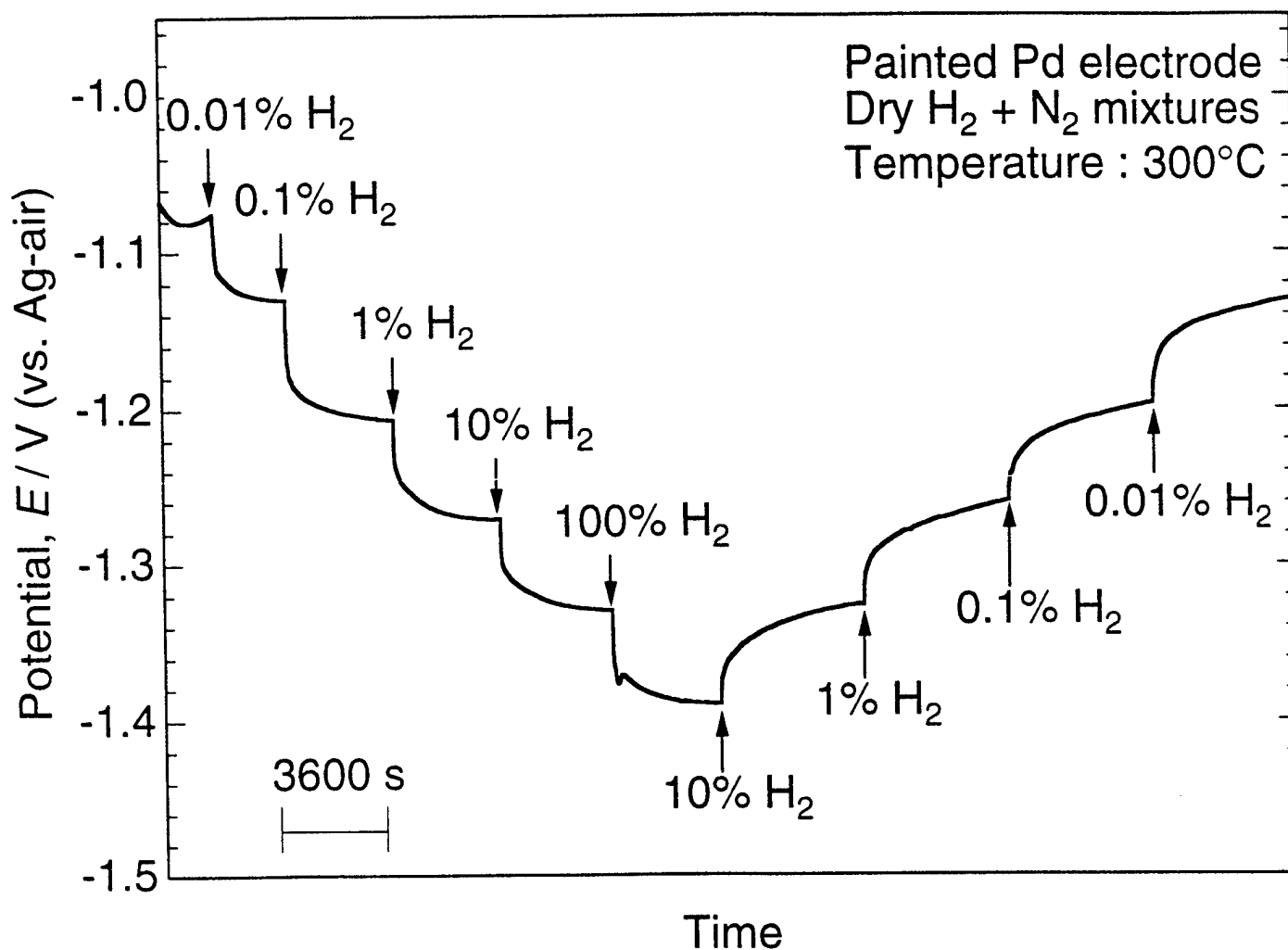
Figure 4-2. Response of the sensor with a painted Pd electrode to changes in hydrogen concentration in dry H_2- N_2 mixtures at 300°C and at total pressure of 101.3kPa.

90% response times were evaluated for a variation in the hydrogen concentration from 0.1 to 1% and from 1 to 0.1%, and are listed in Table 4-1. The data in Table 4-1 indicate that the response rate of the sensors with thin IBS film electrodes is faster than that of the sensors with thick painted electrodes by a factor of about ten. The observed fast response of sensors with thin IBS film electrodes is probably due to the larger surface area that is available for Reaction (3) at the gas-electrode-electrolyte interface.

The steady state potentials of four sensors with different working electrodes were measured in dry hydrogen-nitrogen mixtures at 300°C, and are plotted against the logarithm of the hydrogen concentration in Figure 4-3. Each sensor shows a linear correlation over the entire range of hydrogen concentration (0.001 to 100%). The slope of the correlation is in the range of -57 to -61 mV/decade, which agrees with the predicted slope of -56.9 mV/decade. At a given hydrogen concentration, differences exist in the measured potentials of the four sensors, which apparently arise from the different water vapor pressures.

The effect of water vapor was examined by using humidified hydrogen-nitrogen mixtures. In this experiment, test gas mixtures were equilibrated with water vapor at 25°C by passing the mixtures throughout pure water before they were introduced into the test cell. The results are shown in Figure 4-4, where the potentials of the sensor with a painted Pt electrode exposed to dry and wet hydrogen-nitrogen mixtures at 300°C are plotted as a function of hydrogen concentration. The potential of the sensor at a given hydrogen concentration is displaced in the positive direction in the presence of water vapor ($P_{H_2O} = 3.14 \, kPa$). The potentials measured in the wet gas mixtures are close to the theoretical values calculated from Equation (13) under the assumption that $k_1 = k_{-1}$.

Table 4-1. 90% response times for sensors with painted and IBS-deposited Pt and Pd electrodes at 300°C.

	90% response time / s	
Electrode	0.1% to 1% H_2	1% to 0.1%H_2
Painted Pt	1,820	2,280
Painted Pd	1,390	3,340
IBS-Pt	180	160
IBS-Pd	250	260
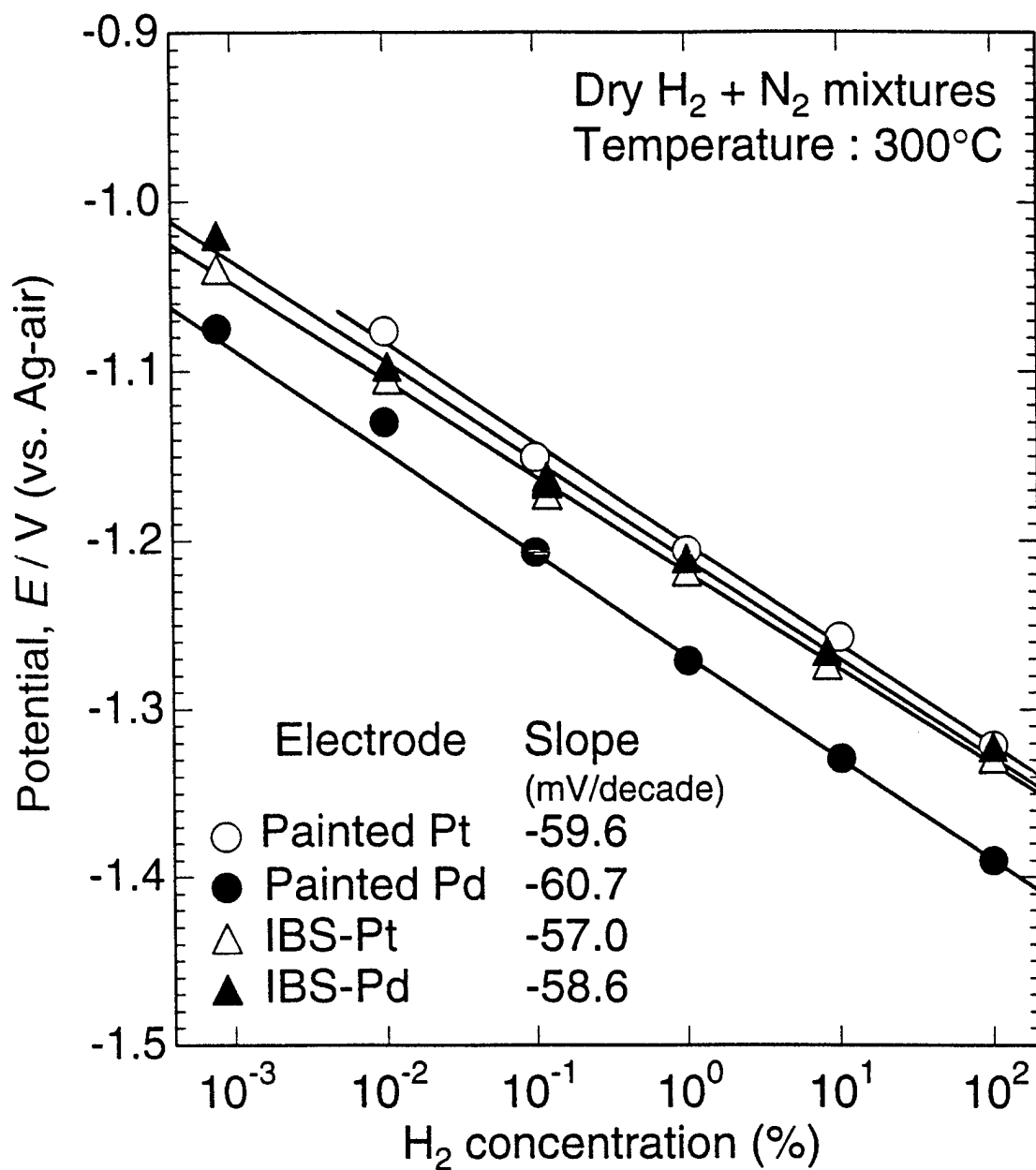
Figure 4-3. Potential of sensors with painted and IBS-deposited electrodes as a function of hydrogen concentration in dry H_2-N_2 mixtures at 300°C.
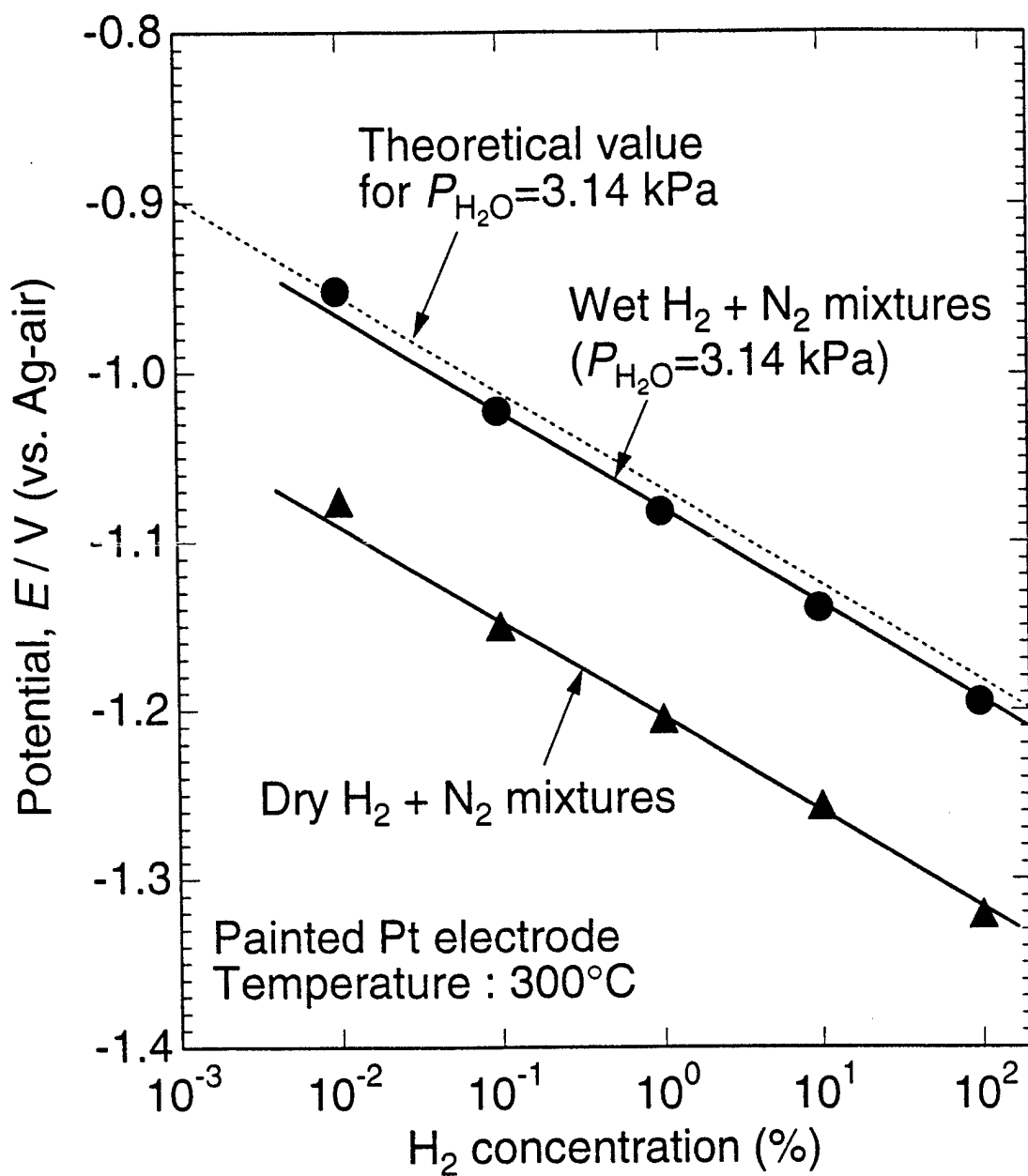
Figure 4-4. Potential of the sensor with a painted Pt electrode as a function of hydrogen concentration in dry and wet H_2-N_2 mixtures at 300°C.

Oxygen in the gas mixtures affected the potential of the sensor, as expected from Equation (19). Figure 4-5 exhibits the changes in potential for the sensor with an IBS-Pt electrode at 300°C as a function of the concentration of oxygen in dry H_2-O_2-N_2 mixtures having hydrogen concentrations of 0.1 and 1%. When the concentration of oxygen exceeds 0.002%, the potential of the sensor increases linearly with increasing logarithm of oxygen concentration. The slope of the straight line is 57 mV/decade, which is in good agreement with the predicted value of 56.9 mV/decade. The potential deviates from the Nernstian line when the concentration of oxygen becomes higher than that of hydrogen.

4.1.5.2 Hydrogen Response in Aqueous Solution

Figure 4-6 shows a typical response curve of the sensor with a Pt electrode when exposed to hydrogenated pure water at a temperature of 300°C and at a pressure of 11.7MPa. The concentration of dissolved hydrogen, m_{H_2}, shown in this figure was estimated from the following equation

$$m_{H_2} = 0.97 P_{H_2,25} K_{25} \tag{26}$$

where $P_{H_2,25}$ is the partial pressure of hydrogen in the gas mixtures used for sparging the solution reservoir at 25°C; the coefficient 0.97 is a correction factor for the vapor pressure of water in the reservoir, and K_{25} is Henry's constant for hydrogen at 25°C. In Equation (26), we assumed that the fugacity coefficient of hydrogen gas and the activity coefficient of dissolved hydrogen are both unity. To obtain the value of K_{25}, we used Battino's equation[11] for the solubility of hydrogen, which was derived from published data in the temperature range of 0 to 72°C. The calculated value of K_{25} is 7.85×10^{-4} mol•kg^{-1}•atm^{-1}. From Figure 4-6, we find that
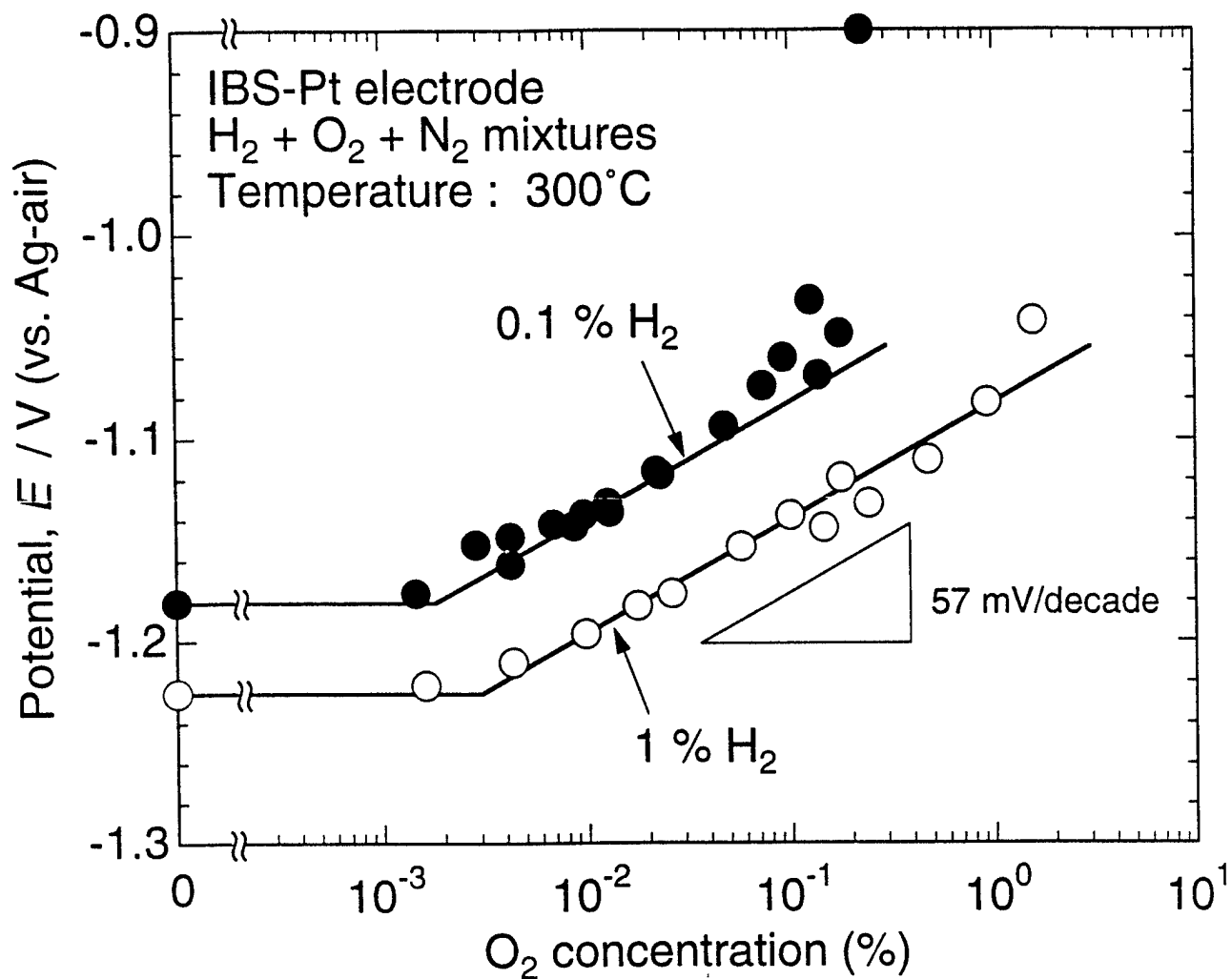
Figure 4-5. Potential of the sensor with an IBS-Pt electrode as a function of oxygen concentration in dry H_2-O_2-N_2 mixtures containing 0.1 and 1% H_2 at 300°C.
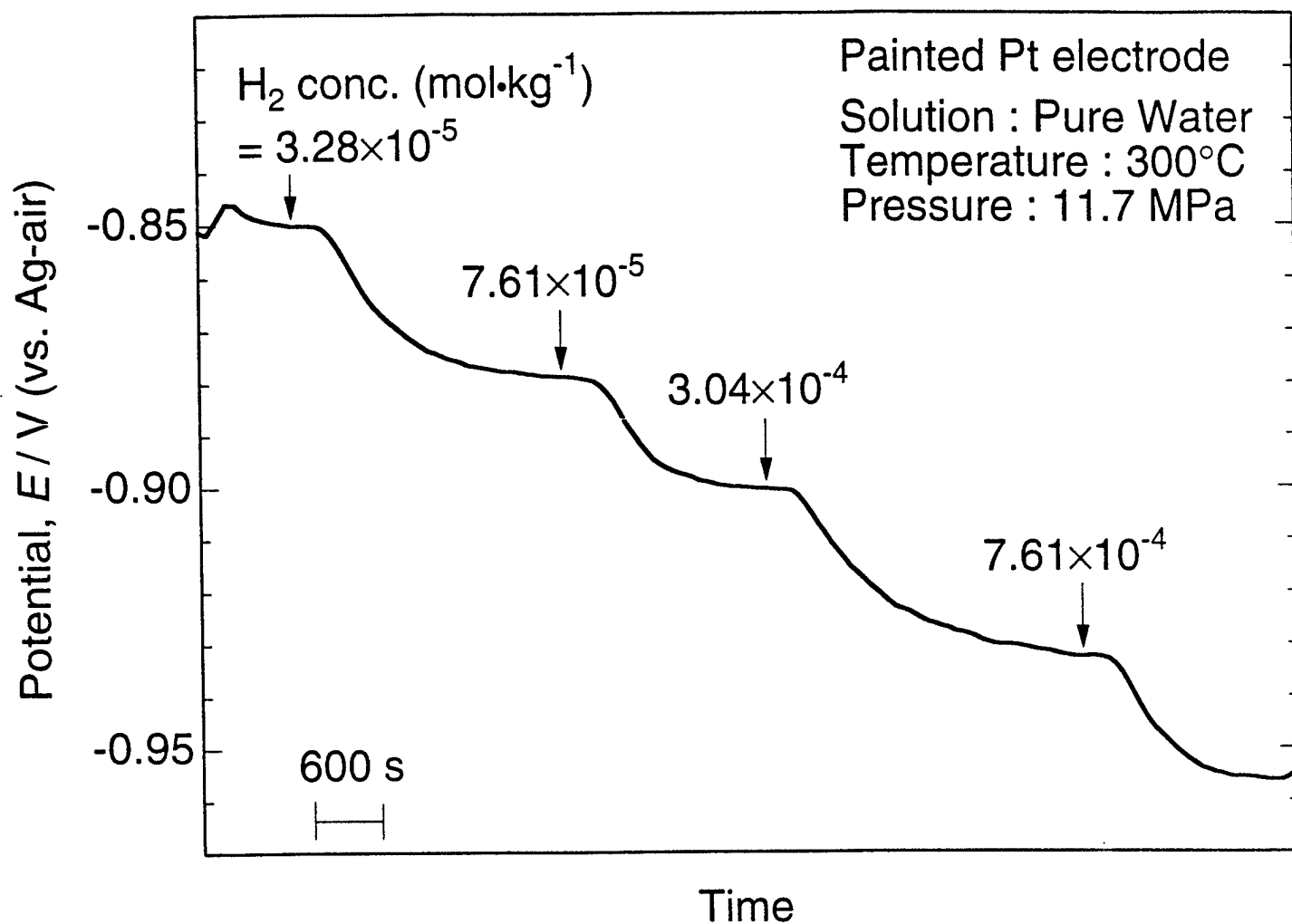
Figure 4-6. Response of the sensor with a painted Pt electrode to changes in hydrogen concentration in pure water at 300°C and 11.7 MPa.

the sensor responds to changes in dissolved hydrogen concentration, with the 90% response time being about 1.5 ks. We must note that the observed response time includes the mass transfer time in the once-through flow system used in the experiments, so that the actual response time of the sensor is probably shorter.

Similar response characteristics were observed for sensors with painted Pd electrodes, and with IBS-Pt and -Pd electrodes. In contrast to the experiments in gas mixtures, the response times of the sensors were independent of the type and preparation method of the working electrodes, as expected if the response time is determined by the replenishment time of the loop. Relationships between the steady state potentials of the sensors and the concentration of hydrogen in pure water at 250°C and 300°C are shown in Figure 4-7. The dashed lines in this figure indicate the theoretical values calculated from Equation (24). The fugacity of hydrogen, $f_{H_2, T}$, at a given temperature, T, was calculated from the following equation:

$$f_{H_2, T} = 0.97 P_{H_2, 25} \, K_{25} / K_T \tag{27}$$

To estimate the Henry's law constant at 250°C and 300°C, we used the regression equation based on the experimental data at temperatures between 46°C and 363°C.[12] The values of $K_{250}=2.48 \times 10^{-3}$ and $K_{300}=4.56 \times 10^{-3}$ mol·kg^{-1}·atm^{-1} were obtained from this source. The calculated E vs. $\log m_{H_2}$ relationships at 250°C and 300°C are given by

$$E = -1.166 - 0.0519 \log m_{H_2} \tag{28}$$

and

$$E = -1.127 - 0.0569 \log m_{H_2} \tag{29}$$

respectively.
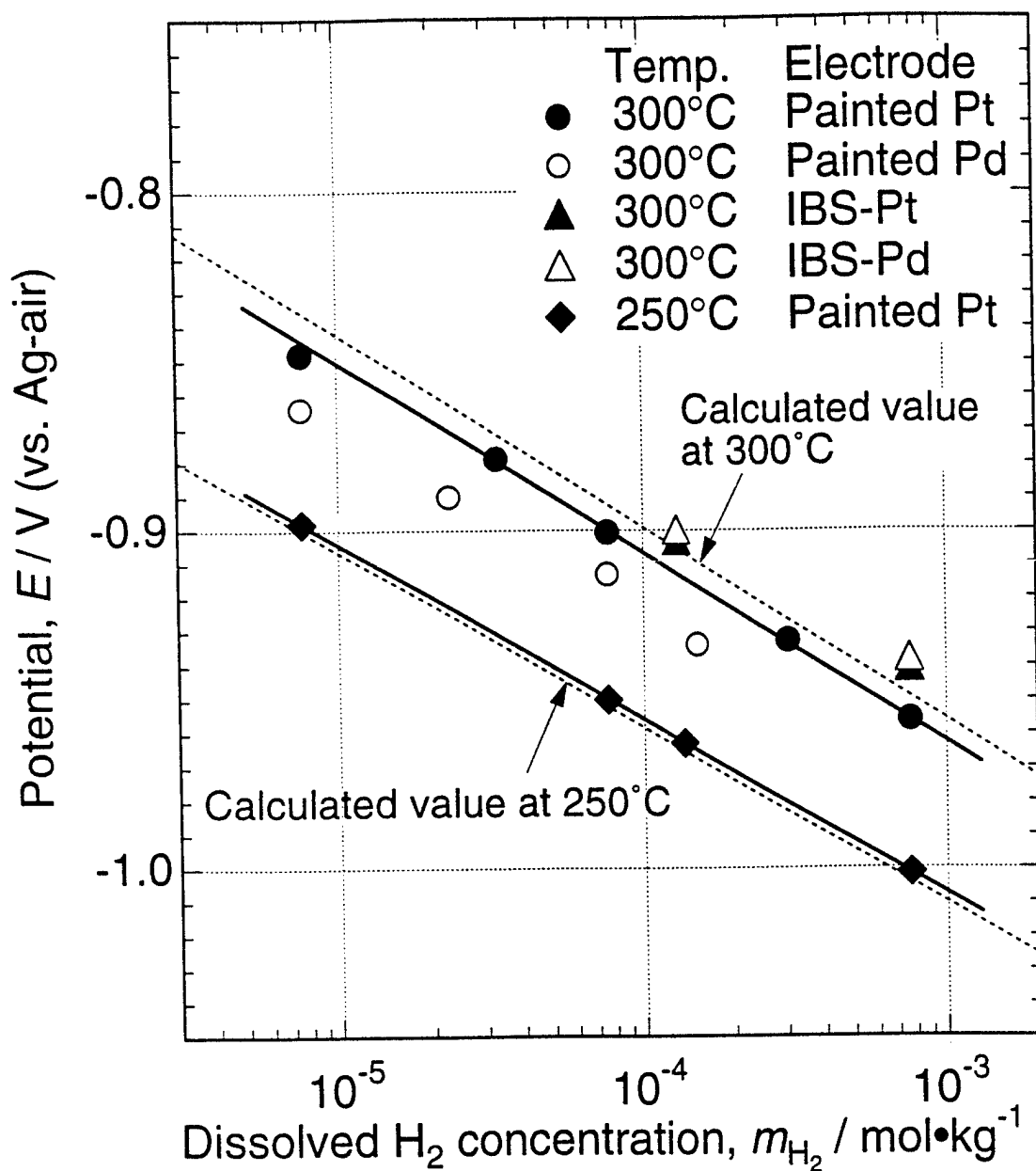
Figure 4-7. Potential of sensors with painted and IBS-deposited electrodes as a function of hydrogen concentration in pure water at 250 and 300°C and at 11.7 MPa.

In Figure 4-7, linear relationships between the potential and the logarithm of hydrogen concentration are observed for all working electrodes and at all temperatures examined. The relationships for the sensor with a painted Pt electrode at 250°C and 300°C are given by

$$E = -1.163 - 0.0517 \log m_{H_2} \tag{30}$$

and

$$E = -1.130 - 0.0560 \log m_{H_2} \tag{31}$$

respectively. These experimental relationships agree well with the theoretical expressions given by Equations (28) and (29).

Figure 4-8 shows the effect of solution pH on the potential of the sensor with an IBS-Pd electrode at 300°C. No change in potential of the sensor was observed when pure water was replaced by 0.01M-NaOH, indicating that the response of the sensor is independent of solution pH.

Oxygen in solution has little effect on the potential of the sensor, provided that the oxygen concentration is sufficiently low. Figure 4-9 exhibits the change in the potential with oxygen concentration in pure water containing 7.61×10^{-5} mol/kg hydrogen at 300°C. At oxygen concentrations lower than 6.50×10^{-5} mol/kg, the potential remained approximately constant. When the oxygen concentration exceeds 1.0×10^{-4} mol/kg, however, the potential increases abruptly, indicating that the oxygen electrode reaction becomes the predominant, potential-determining reaction. The data in Figure 4-9 reveal that if oxygen coexists with hydrogen, the potential of a noble metal electrode becomes a mixed potential that is determined by the reaction rates for the oxidation of hydrogen and the reduction of oxygen. When the concentration of
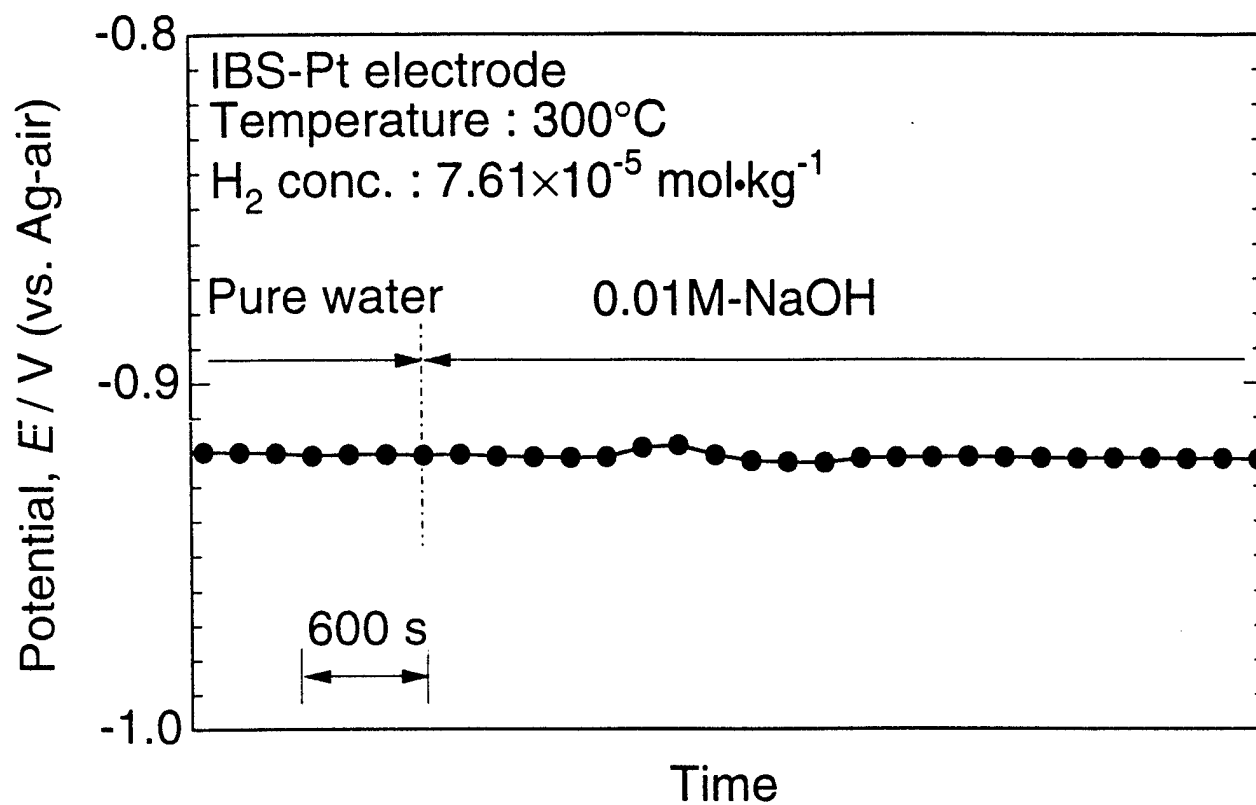
Figure 4-8. Potential vs. time curve after replacing pure water to 0.01M-NaOH. Dissolved hydrogen concentration was kept constant at 7.61×10^{-5} mol·kg^{-1} H$_2$.
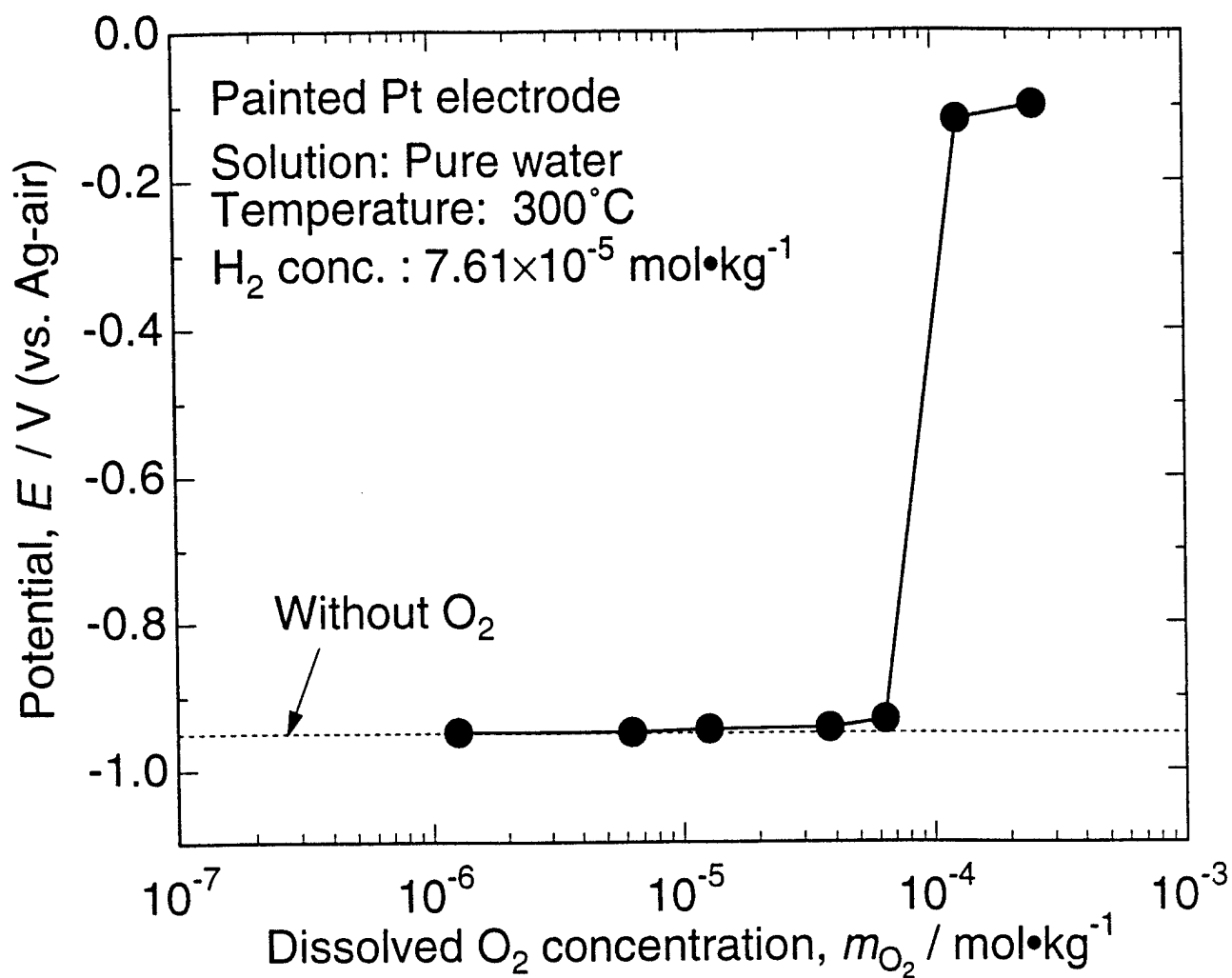
Figure 4-9. Potential of the sensor with a painted Pt electrode as a function of oxygen concentration in pure water containing 7.61×10^{-5} mol•kg^{-1} H$_2$ at 300°C and 11.7 MPa.

oxygen is lower than that of hydrogen, the mixed potential is determined primarily by the hydrogen electrode reaction and thus the effect of oxygen is negligibly small.

4.1.6 Conclusions

The principal findings of this work are summarized as follows:

(1) Hydrogen sensors based on a two-electrode cell employing a YSZ solid electrolyte membrane, a Ag-O_2 reference electrode, and a hydrogen-sensitive working electrode covered with a PTFE diffusion membrane have been developed.

(2) The sensors with Pt and Pd working electrodes displayed rapid and reversible responses to changes in hydrogen concentration in both gas mixtures and aqueous solutions at temperatures of 250°C and 300°C.

(3) The response rate in gas mixtures was faster for sensors employing thin IBS-Pt and -Pd electrodes compared with those employing thick painted electrodes. However, the responses in aqueous solutions was not affected by the difference in the preparation method of the electrodes.

(4) The measured potentials of the sensors varied linearly with the logarithm of hydrogen concentration, displaying Nernstian slopes (2.303RT/2F).

(5) Oxygen in solution has little effect on the potential of the sensor, when the concentration of oxygen is lower than that of hydrogen. However, a significant change was detected in the potential with increasing oxygen concentration in H_2-N_2 gas mixtures.

(6) The potential of the sensor is independent of the solution pH.

4.1.7 Acknowledgements

4.1.8 References

1. D.D. Macdonald, M.C.H. McKubre, A.C. Scott, and P.R. Wentrcek, *Ind. Eng. Chem. Fundam.*, **20**, 290 (1981).
2. C. Liu and D.D. Macdonald, *J. Supercritical Fluids*, **8**, 263 (1995).
3. L.B. Kriksunov, C.Liu and D.D. Macdonald, International Workshop on Supercritical Water Oxidation, Jacksonville, FL (1995).
4. K. Ding and W.E. Seyfried, Jr., *Geochim. Cosmochim. Acta*, **59**, 4769 (1995).
5. J. Mankowski and D.D. Macdonald, unpublished data (1993).
6. S. Hettiarachchi, P. Kedzierzawski, and D.D. Macdonald, *J. Electrochem. Soc.*, **132**, 1866 (1985).
7. D.D. Macdonald, S. Hettiarachchi, and S.J. Lenhart, *J. Solution Chem.*, **17**, 719(1988).
8. D.D. Macdonald, S. Hettiarachchi, H. Song, K. Makela, R. Emerson, M.B. Haim, *J. Solution Chem.*, **21**, 849 (1992).
9. N. Hara and D.D. Macdonald, unpublished data (1996).
10. I. Lundstrom, M.S. Shivaraman and C. Svensson, *J. Appl. Phys.*, **46**, 3876 (1975).
11. E. Wilhelm, R. Battino, and W.J. Wilcock, *Chem. Rev.*, **77**, 219 (1977).
12. J.Alvarez, R.Crovetto, and R.F. Prini, *Ber. Bunsenges. Phys. Chem.*, **92**, 935 (1988).

4.2 THE MEASUREMENT OF HENRY'S CONSTANT FOR HYDROGEN IN HIGH SUBCRITICAL AND SUPERCRITICAL AQUEOUS SYSTEMS

4.2.1 Abstract

Studies are reported on the $Hg/HgO/ZrO_2(Y_2O_3)/NaOH(aq)/H_2(Pt)$ cell at temperatures ranging from 298.15K (25°C) to 723.15K (450°C) and at a pressure of 275 bar, in order to assess the viability of ceramic sensors for measuring Henry's constant for hydrogen in high subcritical (473.15K<T<647.30K) and supercritical (T>647.30K) aqueous systems. Previous work has shown that this cell is thermodynamically well-behaved, in that the measured potential is in good agreement with that calculated from thermodynamic data for the cell components. Thus, the $Hg/HgO/ZrO_2(Y_2O_3)/H^+,H_2O$ ceramic membrane electrode, when combined with a platinum electrode, provides a convenient means of evaluating hydrogen activity and Henry's constant for hydrogen in high subcritical and supercritical aqueous systems. The apparent standard Gibbs energies of formation of $H_2(aq)$ at temperatures within the range 473 and 723 K and at a pressure of 275 bar have been obtained. The calculated Henry constants for dissolved molecular hydrogen in pure water were compared with the available literature data and good agreement was found over the entire temperature range explored in this work.

4.2.2 Introduction

One of the most challenging frontiers in chemistry is the study of high temperature aqueous solutions, principally because we lack many of the experimental probes that are standard for use at ambient or near ambient temperatures. Two important parameters are pH and hydrogen fugacity (f_{H_2}), because the former is a measure of hydrogen ion activity while the latter

is important for assessing the redox properties of the system. The ability to measure hydrogen ion activity (pH = -log a_{H^+}) is vital, because the chemistry of aqueous systems is dominated by protolytic processes, including acid/base equilibria, hydrolysis, and solubility reactions.[1-4] The accurate measurement of pH would permit the derivation of precise values for equilibrium constants that in turn would allow the direct evaluation of solution theories as well as the acquisition of accurate data for inclusion in current thermodynamic data bases. Likewise, the direct measurement of hydrogen fugacity is important for a variety of theoretical and practical reasons. Thus, from a practical viewpoint, corrosion in thermal power plant heat transport circuits (subcritical and supercritical) is frequently indicated by an increase in hydrogen concentration (fugacity) and a sensor capable of monitoring hydrogen at low fugacity would provide a direct method of monitoring corrosion rate *in situ*. From a more fundamental viewpoint, hydrogen is a strong reducing agent in high temperature aqueous solutions and hence it has a powerful influence on the redox potential of the system.

In previous papers,[6,7] we have demonstrated the thermodynamic viability of the YSZ/Pt cell at temperatures up to 400°C, and we published a rigorous thermodynamic analysis of the system for temperatures up to 300°C (but which is applicable to higher temperature with appropriate parameter changes). Importantly, we showed that the measured potential is determined by the metal/metal oxide couple on the dry side of the ceramic membrane, provided that the oxygen vacancy structure of the ceramic is at equilibrium. We have also shown[7,8] that the potential of the YSZ sensor responds sensibly to acids and bases at high supercritical temperatures (up to 798 K), but the lack of a thermodynamically-viable reference electrode has precluded a rigorous analysis of the data to date. While the present work was in progress, Ding

and Seyfried[9] reported the use of this cell to measure hydrogen at concentrations from 0.96×10^{-4} m to 5.75×10^{-3} m in pure water at a single temperature (400°C) and pressure (400 bars).

In this work, we explore the use of the $Hg/HgO/ZrO_2(Y_2O_3)/H^+$, H_2O, $H_2(Pt)$ cell for measuring hydrogen fugacity and for determining Henry's constant for hydrogen in high subcritical and supercritical sodium hydroxide solutions (0.1-0.001m) at temperatures ranging from 473K to 723K (200°C to 450°C) at a pressure of 275 bar. The viability of this cell for this purpose is made possible by virtue of the fact that the YSZ [$\equiv Hg/HgO/ZrO_2(Y_2O_3)/H^+$, H_2O] sensor is a pH primary electrode and hence displays a pH response that is identical to that of the H^+, $H_2O/H_2(Pt)$ electrode, but does not respond to hydrogen activity.

4.2.3 Thermodynamics of YSZ Ceramic Membrane Cells

Because the key to the present work is the Nernstian responses of the YSZ and the H^+, $H_2O/H_2(Pt)$ sensors, it is worthwhile to briefly review the work that has been reported to date on these electrodes, which is coincident with efforts to measure pH in high temperature aqueous systems. Thus, over the past 25-30 years, considerable progress has been made in developing practical techniques for measuring pH in subcritical aqueous systems, and most of these techniques are summarized in Table 4-2. Initial studies were centered on various hydrogen electrodes, including the Pd_xH/H^+ system[10,12,24] and hydrogen concentration cells.[13-21] Indeed, the latter system was used to great effect by Mesmer and co-workers[13-17] to measure the ionic product of water and the acid/base dissociation constants for NH_3, $B(OH)_3$, and H_3PO_4, and the hydrolysis constants for Al^{3+} at temperatures up to 300°C; and by Macdonald and co-workers[19-21]

Table 4-2. Summary of Methods Developed for Measuring pH in High Temperature Aqueous Systems.

Method	Authors	Restrictions
1. Hydrogen Concentration Cells (25°C-300°C)	See review, Mesmer et al.[14] Macdonald, Butler, & Owen[19,20] Macdonald & Owen (1973)[21]	Cannot be used for systems that are reduced by molecular hydrogen.
2. Pd_xH/H^+ (25°C-275°C)	Dobson[10] Macdonald, Wentrcek, & Scott[12] Tsuruta and Macdonald[24]	Cannot be used in the presence of species that are reduced by Pd(H).
3. $M_1M_xO_y/ZrO_2(Y_2O_3)/H^+$ (150°C-550°C)	Niedrach[22,23] Tsuruta & Macdonald[25] Hettiarachchi & Macdonald[31] Hettiarachchi, Kedzierzawski, Macdonald[26] Hettiarachchi & Macdonald[41] Bourcier et al.[3] Macdonald, Hettiarachchi, & Lenhart[6] Hettiarachchi, Lenhart, & Macdonald[27] Hettiarachchi, Makela, Song, & Macdonald[28] Makela, Hettiarachchi, Macdonald, Song, & Emerson[30] Kriksunov & Macdonald[7] Lvov et al.[32] Ding & Seyfried[9,33]	Primary pH sensor that does not need calibrating provided that a thermodynamically viable reference electrode is used. When used with a Hg/HgO internal element, the YSZ sensor is believed to be quite accurate with the currently observed uncertainties (±0.1-0.2 pH units) being attributed to errors in the reference electrode. The YSZ system has been used most extensively at T<300°C, but a few attempts to use it at higher temperatures, including supercritical temperatures.
4. Metal/Metal Oxide (100°C-550°C) a. $Pt-PtO_2$, $Ir-IrO_2$, $Zr-ZrO_2$, $Rh-Rh_2O_3$ b. Zr/ZrO_2 c. W/WO_3	Dobson et al.[11] Kriksunov & Macdonald[37] Kriksunov, Macdonald, & Millett[38]	W/WO_3 exhibits an essentially Nernstian response over a wide pH range, except in very acidic systems. This electrode has also been evaluated in supercritical systems (T≤550°C). Other metal/metal oxide electrodes generally do not exhibit satisfactory E/pH responses.
5. Glass Electrode	Le Peintre[34] Baes & Meyer[18] Krukov & Starostina[35] Dolidze[5] Kriksunov & Macdonald[36]	The fragility of glass has limited the use of thin-walled glass membranes at temperatures above 100°C. However, recent work by Kriksunov and Macdonald (1995) using a thick-walled tube suggests that glass electrodes may be serviceable, at least at temperatures up to 250°C.

to also measure K_w, to investigate the hydrolysis of Al^{3+} and the precipitation of boehmite (γ - AlOOH), and to measure transport numbers for H^+ and Cl^- in aqueous HCl solutions at temperatures up to 200°C. Although hydrogen concentration cells are capable of yielding precise data (±0.02 in pH) under ideal conditions at temperatures up to 300°C, and perhaps at temperatures up to T_c (374.15°C for pure water), particularly when a flowing cell is employed, they have three inherent disadvantages: (i) They cannot be used in systems that are inherently unstable in the presence of hydrogen (e.g., it cannot be used to study the hydrolysis of Cu^{2+}), (ii) they require the use of a buffer solution of accurately-known pH vs. temperature characteristics, and (iii) the liquid junction potential between the reference and test compartments must be suppressed by using a suitably-high background concentration of an indifferent electrolyte (e.g., KCl). Because of these limitations, a search was carried out for a more generally-applicable technique.

In the early 1980's, starting with the work of Niedrach et al.,[22,23] and shortly thereafter with the work of Macdonald and co-workers,[1,6,24-31] and others,[32,33] attention was focused on potentiometric sensors based on oxygen-ion conducting ceramics, such as yttria-stabilized zirconia. Niedrach et al.[22,23] focused their attention on the $Cu/CuO/ZrO_2(Y_2O_3)/H^+$, H_2O system, and then as a potential reference electrode for use in water-cooled nuclear reactor coolant circuits. However, its utility for this purpose depends entirely upon the pH remaining invariant with respect to changes occurring in the high temperature water coolant. For fundamental chemical studies, the YSZ electrode is better described as a pH sensor. In a series of papers, two of the present authors and their co-workers,[1,6,24-32] have explored the YSZ electrode for measuring pH in subcritical aqueous solutions. Over the past five years, some of these studies

have been extended to supercritical systems.[1,6,7,9,28] However, in only a few cases[6,9,28] was a rigorous thermodynamic analysis attempted to demonstrate that the potential of the cell YSZ/H$_2$ (Pt) was in acceptable agreement with thermodynamically-calculated potentials when proper allowance had been made for the non-ideal behavior of the solution (see Discussion). Good agreement was found between the measured and calculated potentials in subcritical systems,[6] regardless of the pH of the medium, and somewhat less rigorous analyses[1,28,33] indicated that the cell is thermodynamically well-behaved also at supercritical temperatures. These findings are important, because they demonstrate that the YSZ electrode exhibits the same pH response as does the H$^+$/H$_2$ (Pt) system, and hence it can be described as being Nernstian.

The search for an effective high temperature/high pressure pH-measurement technology has also resulted in the exploration of other systems. Thus, glass electrodes have been used with some success to measure pH at temperatures as high as 254°C,[34-36] and the W/WO$_3$ electrode has been explored at temperatures to 550°C (823K).[7,37,38] Both systems are secondary electrodes and, hence, unlike the YSZ electrode, they need to be calibrated using suitable pH buffers (which currently do not exist).

Finally, it is our opinion that the accuracy of potentiometric pH measurements is determined almost entirely (at least in the case of the YSZ sensor) by the accuracy of the reference electrode. While considerable progress has been made in developing both internal and external (pressure-balanced) reference electrodes,[39-42] particularly for use at subcritical temperatures, no reference electrode is currently available with sufficient accuracy (±5mV) that accurate thermodynamic data can be obtained. However, this is not an issue in the present work,

4-34

because both electrodes [YSZ and H$^+$/H$_2$ (Pt)] sense the same hydrogen ion activity, the activity of hydrogen is known, and no liquid junction potential exists in the system.

4.2.4 Experimental

4.2.4.1 YSZ Membrane pH Sensor

The YSZ-membrane pH sensor is shown in Figure 4-10. The YSZ tubes that were provided by Coors Ceramics Company (ZDY-4, nominal composition of 9 w% Y$_2$O$_3$) were 15.24 cm long with an outer diameter of 0.634 cm and a 0.0889 cm wall thickness. The rounded end of the tube was pre-conditioned by filling 5 cm of the inside with hydrofluoric acid (Baker Reagent 48%-51%), then immersing a similar length of the outer portion of the tube in boiling HF for ten minutes. This served to increase the effective surface area for the membrane for contact with the internal paste material and to remove any glassy phases formed by segregation of impurities to the outer surface during manufacture.

The Hg/HgO paste was prepared by combining a 50:50 volume ratio of Reagent Grade HgO and 99.9% Hg in a mortar and pestle until a paste of consistent texture was obtained. The rounded YSZ tip was filled with approximately 0.6 cm of the paste. An ASTM Grade 304 stainless steel wire provided electrical contact. One end was sanded and coiled to increase its effective surface area, then inserted into the paste. This wire was insulated with continuous heat shrink Teflon™, extending from very near the open end of the YSZ tube to approximately 5 cm from the end. The remainder of the tube was back-filled with fine (-325 mesh) ZrO$_2$ sand. The electrode was lightly tapped while adding the powder to ensure tight packing. Finally, the open end was filled with "J.B. Weld"™ epoxy to both seal the electrode and to provide some amount
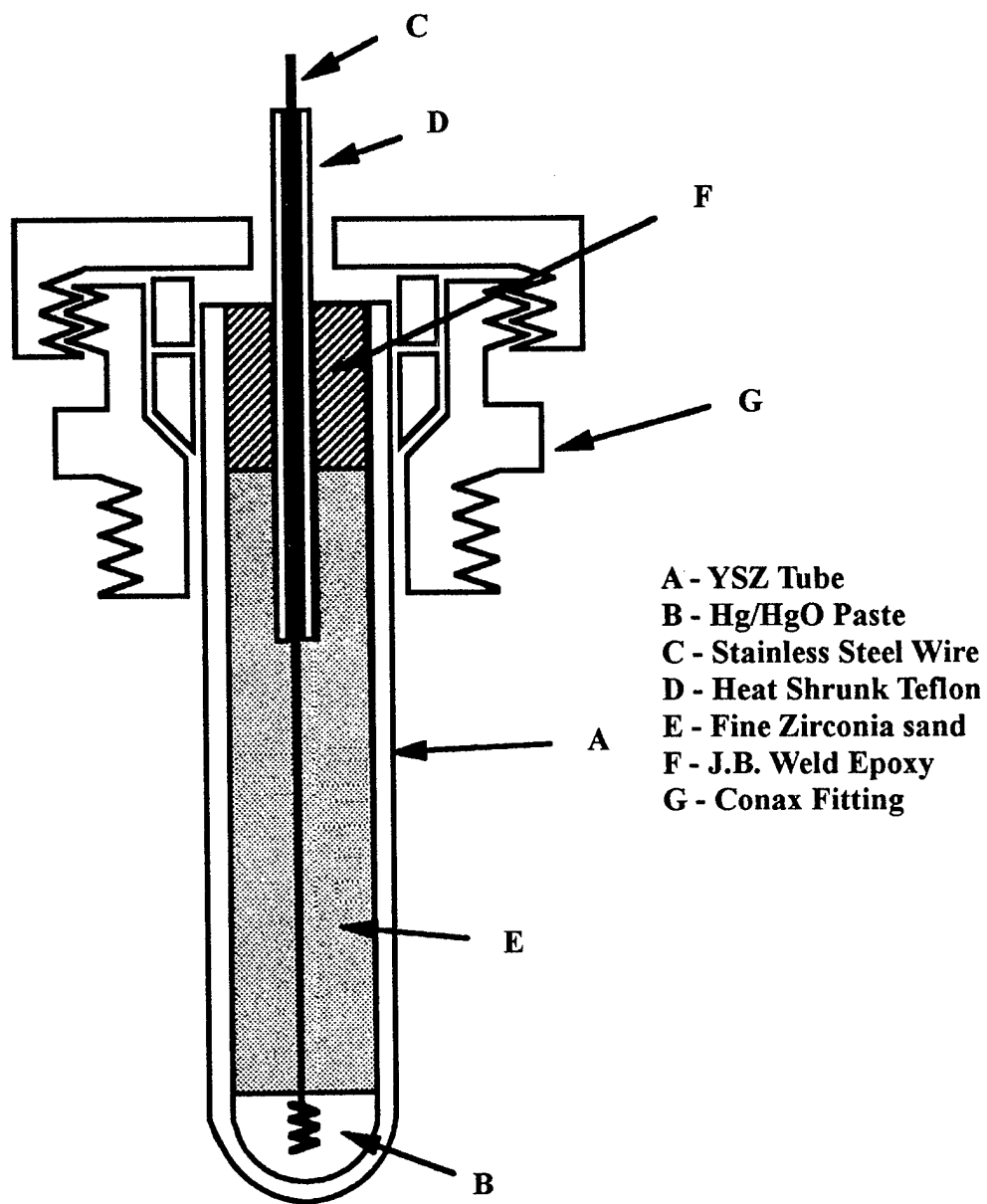
Figure 4-10. Diagram of the YSZ pH sensor, not to scale. The YSZ tube is 15.24 cm long, with a 0.634 cm outer diameter and 0.0889 cm wall thickness. A - YSZ Tube; B - Hg/HgO Paste; C - Stainless Steel Wire; D - Heat Shrunk Teflon; E - Fine Zirconia sand; F - J.B. Weld Epoxy; and G - Conax Fitting.

of mechanical support to the ceramic. The latter consideration was important for successful use in the CONAX compression fitting. The pressure fitting was cooled via a copper tubing water jacket.

4.2.4.2 Hydrogen Electrode

The hydrogen electrode, shown in Figure 4-11, consisted of a 0.5 mm diameter platinum wire (99.99% pure). The end of the electrode that was intended to be in contact with the high temperature test fluid was coiled and then lightly platinized by cathodic polarization in a solution of hexachloroplatinic acid. This produced a typical "Pt-black" film on the coil. The remainder of the electrode was insulated from the autoclave body with either high purity alumina tubing in the relatively hot regions (with an ID comparable to the wire diameter), or by heat shrink PTFE in the cooler portions of the autoclave. A tight PTFE sleeve, which was placed over the cooled end of the wire, was pinched by a high-pressure CONAX fitting to form the pressure seal. The wire outside the autoclave was again insulated from the walls by heat-shrink PTFE.

4.2.4.3 Autoclave/Circulation Loop/Solutions

A once-through flow loop, shown schematically in Figure 4-12, was used for all experiments. Solutions of 0.1m, 0.01m, and 0.001m NaOH were prepared by diluting an appropriate stock solution of Reagent Grade 1.0N NaOH with Millipore water (18.2 MΩ-cm). The solution was loaded into a four liter Nalgene™ reservoir and was then purged with pure H_2 gas for at least two days prior to use. Gas purging continued throughout the duration of the experiment. A High Pressure Liquid Chromatography (HPLC) pump provided flow of the
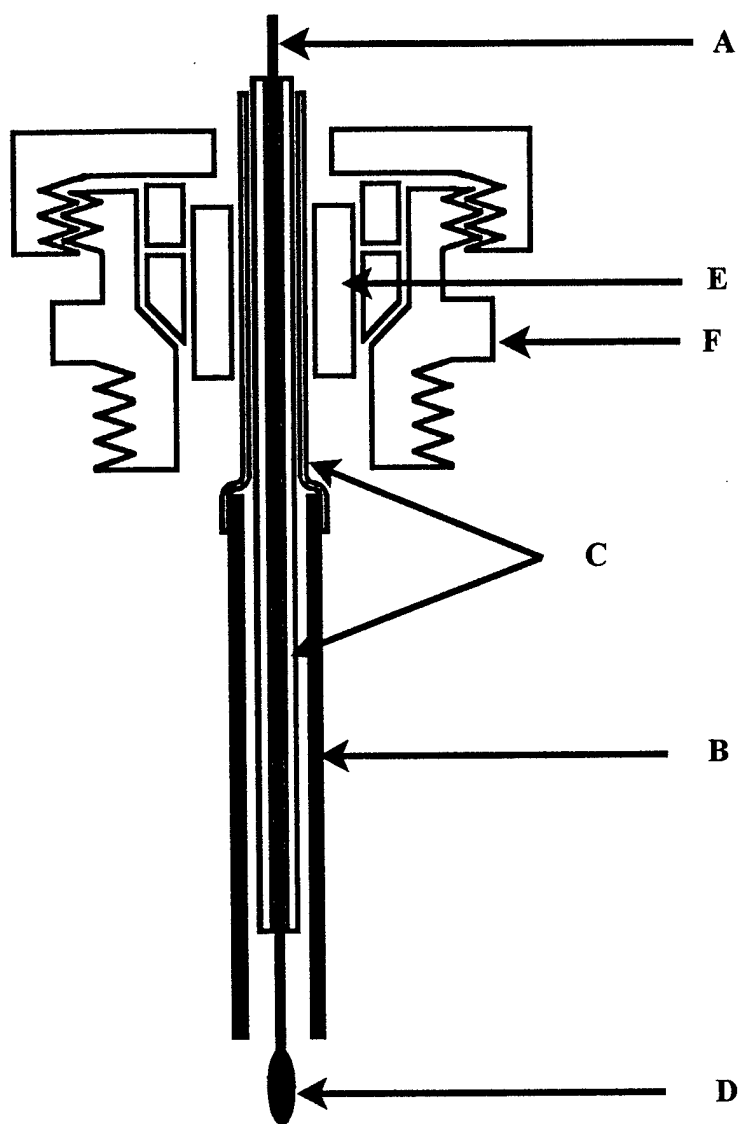
Figure 4-11. Schematic of the hydrogen electrode. Alumina sheath (B) shown in black, Teflon (C) in white: A - Pt Wire; B - Al_2O_3 Tubing; C - Heat Shrunk Teflon; D - Coiled, platinized end; E - Teflon gasket; and F - Conax fitting (stainless steel).
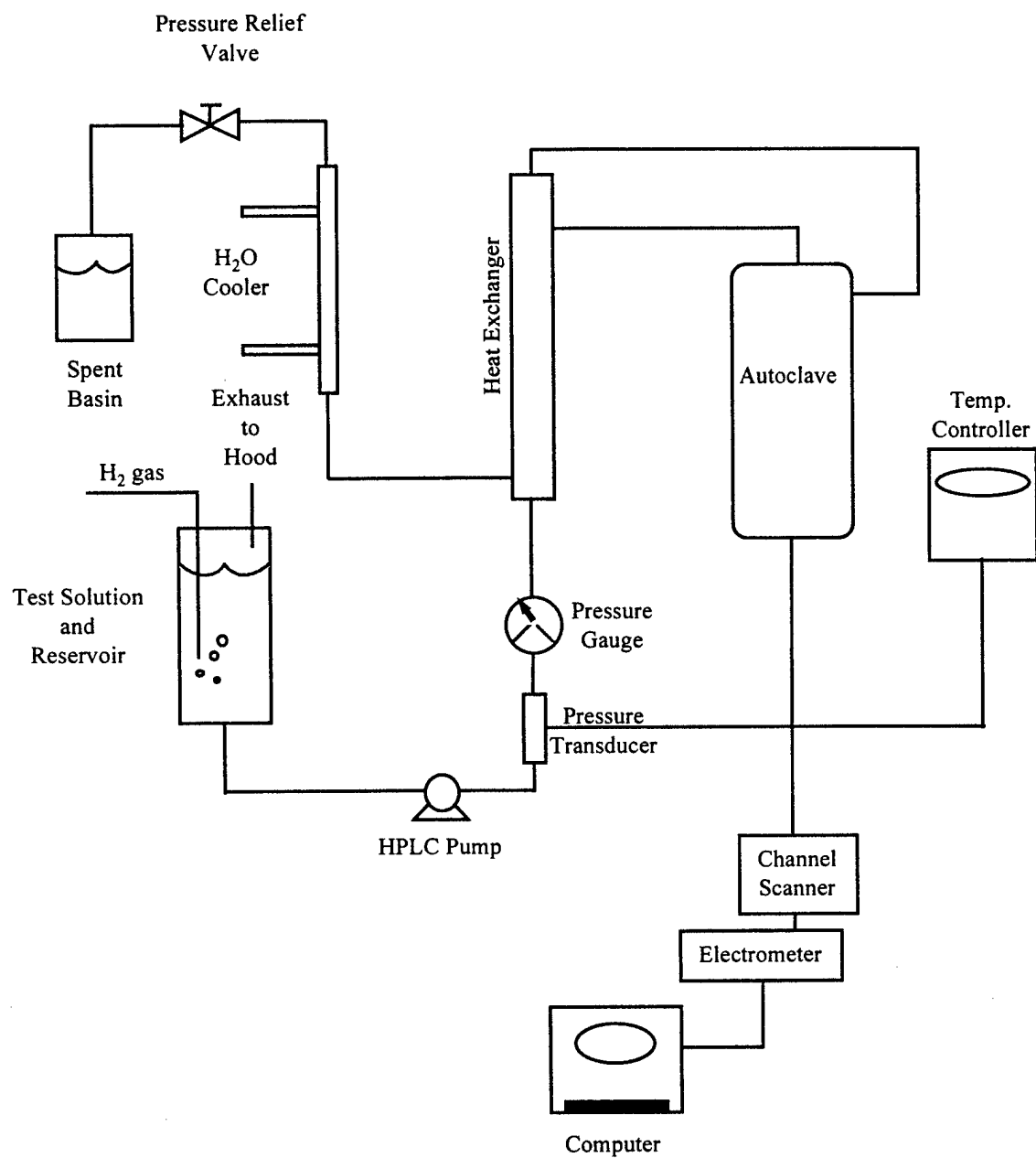
Figure 4-12. Schematic of the autoclave and once-through circulation loop, with data acquisition system.

solution through the test cell at a volume flow rate of 140 ml/hr, while simultaneously maintaining the pressure at 275 bar via a back pressure regulator. The pressure was monitored visually using a standard pressure gauge as well as electronically via a pressure transducer connected to the data acquisition system.

The solution was preheated by passing it through the inner channel of a regenerative heat exchanger, from which the solution flowed directly to the measurement cell. A commercially-available Type 316 Stainless Steel Cajon™ union cross served as the autoclave (Figure 4-13), with modifications to accommodate the hydrogen and YSZ electrodes (and an External Pressure Balanced Reference Electrode, which is not discussed in this paper) in the one unit. Primary heating was provided by overlapping wraps of 313W Omegalux™ heating tape. The test cell was insulated from the external environment by fibrous alumina. The slight tilt of the autoclave, as depicted in Figure 4-13, was important for cooling the EPBRE seal. The temperature was measured using an Inconel-sheathed, K-type thermocouple, and was controlled with a Jenco Model 377 controller. Once through the autoclave, the test solution was utilized on the outer channel of the regenerative heat exchanger, cooled in a water-jacket chiller, and finally sent to the spent reservoir.

Experiments were conducted at a constant pressure of 275 bar. Fresh solution was pumped through the autoclave until the potential between the YSZ electrode and the hydrogen electrode attained a steady value typically within ±3mV. The autoclave has heated in 50°C steps to a maximum of 450°C, resting at each interval until the potential attained a steady-state value. The temperature was then decreased in 50°C steps and the cell potential was recorded in the descending direction. The time required to achieve stability in the potential between the YSZ
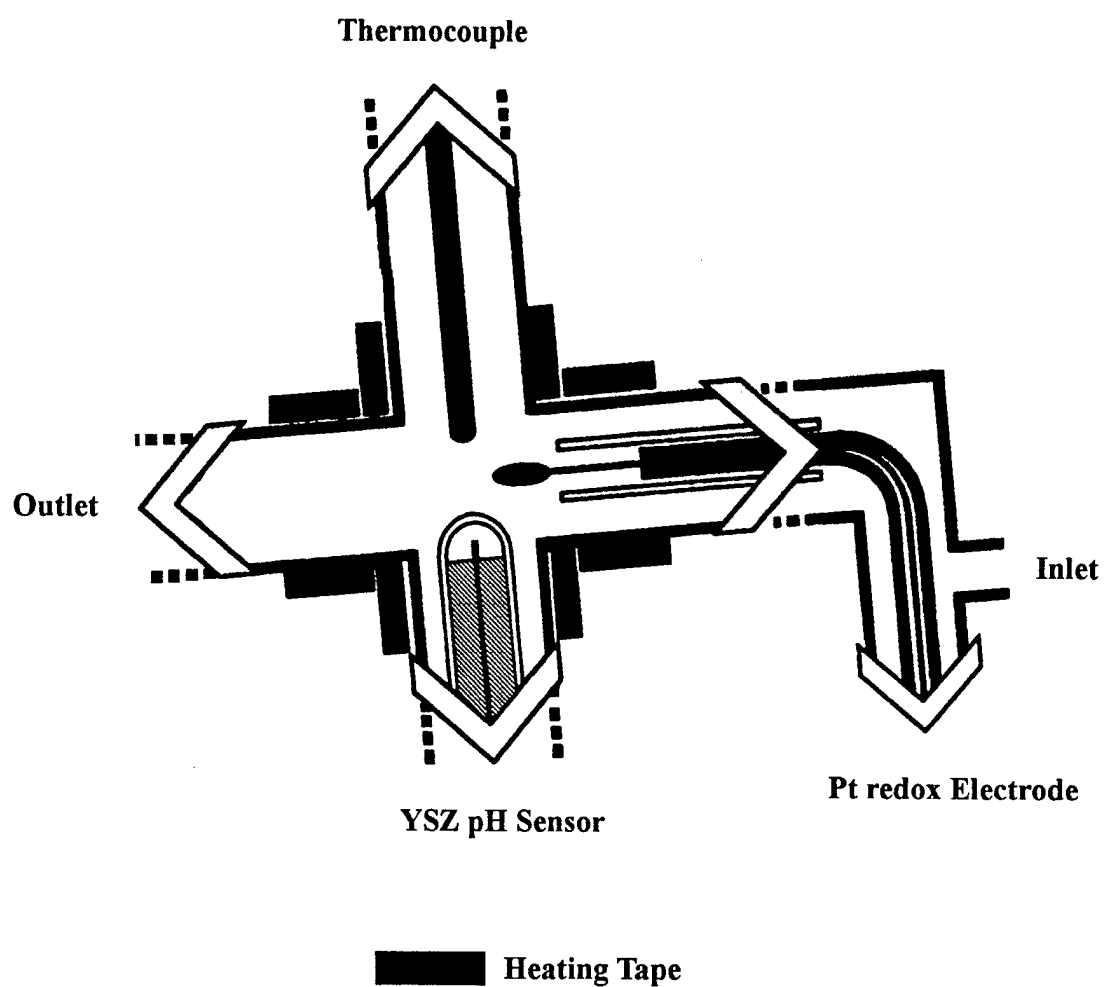
Figure 4-13. Cross section of autoclave showing approximate orientations and location of electrodes.

electrode and to the hydrogen electrode and up to one hour. Duplicate runs were performed on each solution.

All potentials (including the thermocouple readings) were measured using a Keithley 617 Programmer Electrometer, having an input impedance of 200TΩ. Separate inputs were chosen via a Keithley 705 Scanner. All data were collected by the acquisition system over a standard IEEE-488 bus using a Borland Turbo Pascal program.

4.2.5 Results and Discussion

The cell for the potentiometric measurements can be represented formally as two half cells, $Hg/HgO/H^+,H_2O$ and $H_2/H^+,H_2O$, that are separated by a yttria-stabilized zirconia (YSZ) membrane. For our specific conditions, recognizing that the Hg/HgO couple is maintained at the system temperature but at ambient pressure, whereas the hydrogen electrode is maintained at both the system temperature and pressure, the cell is best written as

$$|\!\!<\!\!\text{------} P_0 \text{------}\!\!>\!|\!\!<\!\!\text{------} P \text{------}\!\!>\!|\!\!<\!\!-P_0 -$$
$$\text{Cu} \mid \text{Fe} \mid \text{Hg} \mid \text{HgO} \mid \text{YSZ} \mid \text{NaOH(aq)} \mid \text{Pt(H}_2) \mid \text{Cu} \qquad \text{(I)}$$
$$\varphi_L \qquad\qquad\qquad\qquad\qquad\qquad \varphi_R$$
$$|\!\!<\!\!\text{------} E = \varphi_R - \varphi_L \text{------}\!\!>\!|$$
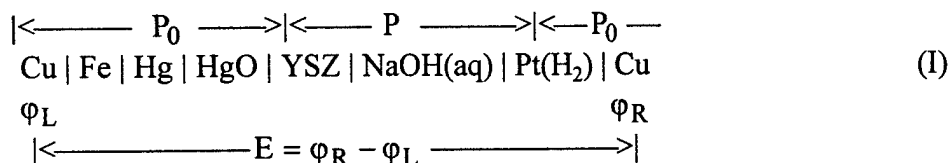
where E is the electromotive force (e.m.f.) observed at temperature T and pressure P, φ_L and φ_R are the electrostatic potentials of the left and right terminals, and P and P_0 are, respectively, the working (275 bar) and ambient (1 bar) pressures. The experimental values of E obtained for temperature, T, between 473 and 723 K and for three molal concentrations of NaOH(aq) m, (0.1, 0.01, and 0.001 mol/kg), are presented in Table 4-3. In thermodynamic terms, E can be regarded

4-42

Table 4-3. Measured potentials, E , of the HgO/Hg/YSZ/NaOH(m)/H$_2$(Pt) Cell (I) as a function of NaOH(aq) concentration for temperatures between 473 and 723 K and at a pressure P=275 bar.

T = 473 K		T = 523 K		T = 573 K	
m, mol/kg	E, mV	m, mol/kg	E, mV	m, mol/kg	E, mV
10^{-3}	-853	10^{-3}	-846	10^{-3}	-819
10^{-3}	-860	10^{-3}	-843	10^{-3}	-815
10^{-3}	-855	10^{-3}	-843	10^{-3}	-804
10^{-2}	-852	10^{-3}	-871	10^{-3}	-839
10^{-2}	-884	10^{-2}	-859	10^{-2}	-842
10^{-2}	-874	10^{-2}	-876	10^{-2}	-852
10^{-2}	-888	10^{-2}	-880	10^{-2}	-853
10^{-2}	-877	10^{-2}	-879	10^{-2}	-854
10^{-1}	-894	10^{-2}	-885	10^{-2}	-855
10^{-1}	-881	10^{-2}	-881	10^{-2}	-855
10^{-1}	-835	10^{-1}	-873	10^{-1}	-842
10^{-1}	-904	10^{-1}	-893	10^{-1}	-857
-	-	10^{-1}	-884	10^{-1}	-846
E^0 = -872±6		E^0 = -870±5		E^0 = -841±5	

T = 623 K		T = 673 K		T = 723 K	
m, mol/kg	E, mV	m, mol/kg	E, mV	m, mol/kg	E, mV
10^{-3}	-792	10^{-3}	-751	10^{-3}	-715
10^{-3}	-773	10^{-3}	-753	10^{-2}	-720
10^{-3}	-775	10^{-2}	-761	10^{-2}	-715
10^{-3}	-809	10^{-2}	-769	10^{-2}	-712
10^{-2}	-806	10^{-2}	-763	10^{-1}	-729
10^{-2}	-822	10^{-2}	-765	-	-
10^{-2}	-815	10^{-2}	-765	-	-
10^{-2}	-825	10^{-2}	-764	-	-
10^{-2}	-818	10^{-1}	-774	-	-
10^{-2}	-824	10^{-1}	-802	-	-
10^{-1}	-802	10^{-1}	-805	-	-
10^{-1}	-821	-	-	-	-
E^0 = -807±5		E^0 = -770±5		E^0 = -718±3	

as the difference between the reversible potentials of the $H_2(Pt)$, $E_{H^+/H_2(aq)}$, and Hg/HgO,

$E_{HgO/Hg}$, couples as:

$$E = E_{H^+/H_2(aq)} - E_{Hg/HgO} =$$

$$E^0_{H^+/H_2(aq)} + \frac{RT}{2F} \ln \frac{a^2_{H^+}}{a_{H_2(aq)}} - E^0_{Hg/HgO} - \frac{RT}{2F} \ln \frac{a^2_{H^+}}{a_{H_2O}} = E^0 + \frac{RT}{2F} \ln \left(\frac{a_{H_2O}}{a_{H_2}} \right) \quad (1)$$

where it is assumed that the oxygen vacancy structure in the YSZ ceramic membrane is in

equilibrium and hence that the electrochemical potential of an oxygen vacancy on the internal

reference side of the membrane is the same as that on the test environment side of the membrane

(Macdonald et al.[1]). In Equation (1), $E^0_{H^+/H_2(aq)}$ and $E^0_{HgO/Hg}$ are, respectively, the standard

electrode potentials of the right [$H^+/H_2(aq)$] half cell and the left (HgO/Hg) half cells; and a_{H^+},

$a_{H_2(aq)}$, and a_{H_2O}, are the activities of $H^+(aq)$, molecular hydrogen $H_2(aq)$ dissolved in the

solution, and water, respectively. Note that we use a standard state of unit activity of $H_2(aq)$ in a

hypothetical one molal solution referenced to infinite dilution at any temperature and pressure

rather than the customary unit fugacity. The activity of molecular hydrogen in Equation (1), can

be calculated from

$$a_{H_2} = (m^0_{H_2} 10^{-k_s c}) \gamma_{H_2} \quad (2)$$

if the solubility of molecular hydrogen in pure water, $m^0_{H_2}$, as well as the Sechenov (salting-

in/salting-out) coefficient, k_s, for dissolved H_2 in NaOH(aq) solutions is known. For all further

calculations, we take $m^0_{H_2} = 7.84 \times 10^{-4}$ mol/kg (at 298.15 K and 1 bar)[43] and $k_s = 0.140$

liters/mol.[44] In Equation (2), c is the molar concentration of NaOH(aq) at 298.15 K and 1 bar,

and γ_{H_2} is the activity coefficient of the dissolved molecular $H_2(aq)$, which is assumed to be 1 at such a low (hydrogen) concentration. Note that the calculated Thomson potentials in platinum and iron wires were found to be a small positive numbers and were neglected in this study.

In dilute (0.001-0.1m) NaOH(aq) solutions at high temperatures (473-723K), the activity of water, a_{H_2O}, in Equation (1) can be calculated using the second-order approximation to the Debye-Huckel theory (Robinson and Stokes[45]):

$$\ell n\, a_{H_2O} = -\frac{m_{tot}}{55.51} \times$$
$$\left\{ 1 - \frac{A_m}{B_m^3 \mathring{a}^3 (\sqrt{I_m})^3}[(1 + B_m \mathring{a}\sqrt{I_m}) - 2\ell n(1 + B_m \mathring{a}\sqrt{I_n}) - (1 + B_m \mathring{a}\sqrt{I_m})^{-1}] + \frac{\log\left(1 + \frac{m_{tot}}{55.51}\right)}{\frac{m_{tot}}{55.51}} \right\} \quad (3)$$

where m_{tot} is the sum of the molalities of all of the solute species in solution, I_m is the ionic strength of the NaOH(aq) solution on the molal concentration scale, and A_m, B_m, and $\mathring{a}$ are the Debye-Huckel theory parameters. $\mathring{a}$ was taken as a constant equal to 0.45 nm. A_m and B_m were calculated[45] using density and dielectric constant data for water taken from Klein and Harvey.[46] For calculating m_{tot} and I, it was first necessary to solve the speciation problem for the NaOH-H₂O system for the appropriate temperature and density. In doing so, we considered four dissolved species, $H^+(aq)$, $OH^-(aq)$, $Na^+(aq)$, and $NaOH^0(aq)$, and two ionic equilibria in describing the system:

$$H_2O(l) \leftrightarrow H^+(aq) + OH^-(aq) \quad (4)$$

and

$$Na^+(aq) + OH^-(aq) \leftrightarrow NaOH^0(aq) \tag{5}$$
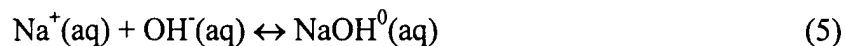
From this speciation model, I and m_{tot} can be calculated by:

$$I_m = \frac{1}{2}(m_{OH^-} + m_{Na+} + m_{H^+}) \tag{6}$$

and

$$m_{tot} = m_{OH^-} + m_{Na+} + m_{H^+} + m_{NaOH^0} \tag{7}$$

The concentrations of the species were calculated from the following system of non-linear

Equations (8)-(11):

$$m_{OH^-} = \frac{m}{1 + K_{NaOH}m_{OH^-}\gamma_{\pm}^2} + \frac{K_w a_{H_2O}}{m_{OH^-}\gamma_{\pm}^2} \tag{8}$$

$$m_{H^+} = \frac{K_w a_{H_2O}}{m_{OH^-}\gamma_{\pm}^2} \tag{9}$$

$$m_{Na^+} = \frac{m}{1 + K_{NaOH}m_{OH^-}\gamma_{\pm}^2} \tag{10}$$

$$m_{NaOH^0} = m - \frac{m}{1 + K_{NaOH}m_{OH^-}\gamma_{\pm}^2} \tag{11}$$

where m is the analytical concentration of NaOH(aq), K_{NaOH} is the association constant of

NaOH(aq) [Reaction (5)], and K_w is the dissociation constant of water [Reaction (4)]. K_{NaOH}

and K_w values were taken, respectively, from the papers of Ho and Palmer[47] and Marshall and

Franck.[48] The mean activity coefficient, $\gamma_{\pm}$, in Equations (8)-(11) was calculated using the

second-order approximation of the Debye-Huckel theory:[45]

$$\log\gamma_{\pm} = -\frac{A_m\sqrt{I_m}}{1 + B_m \dot{a}\sqrt{I_m}} - \log\left(1 + \frac{m_{tot}}{55.51}\right) \tag{12}$$

In Figure 4-14, we present a comparison of the calculated [Equation (3)] and observed (Simonson et al.[49]) data for a_{H_2O} at temperatures of 473 and 523 K. This comparison clearly demonstrates the good accuracy of our calculations of a_{H_2O} at subcritical temperatures, and allows us to use Equations (3) and (12) to describe the solution non-ideality at temperatures up to 723 K.

Using the experimental data for E given in Table 4-3, and calculating a_{H_2O} and a_{H_2} as described above, we calculated the E^0 values for all temperatures and NaOH concentrations employed. Average values for E^0 for each temperature, as well as the standard deviations, were then calculated and are presented in Table 4-3. It is important to note that the E^0 values correspond to the following cell reaction:

$$Hg(l,T,P=1bar) + H_2O(l,T,P=275\ bar) = H_2(aq,T,P=275\ bar) + HgO(s,T,P=1bar) \tag{13}$$
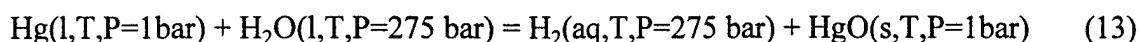
where each component is specified at a particular temperature and pressure. The standard Gibbs energy change, $\Delta_r G^0(T,P)$, is given by

$$\Delta_r G^0(T,P) = -2FE^0 =$$
$$\Delta_f G^0_{H_2(aq)}(T,P) - \Delta_f G^0_{H_2O(l)}(T,P) - \Delta_f G^0_{Hg(l)}(T,P_0) + \Delta_f G^0_{HgO(s)}(T,P_0) \tag{14}$$

where $\Delta_f G^0_i$ represents the apparent standard Gibbs energy of formation for the ith species of Reaction (13) at the given temperature and pressure. Note that the $\Delta_f G^0_i$ values can be calculated, in the general case, from
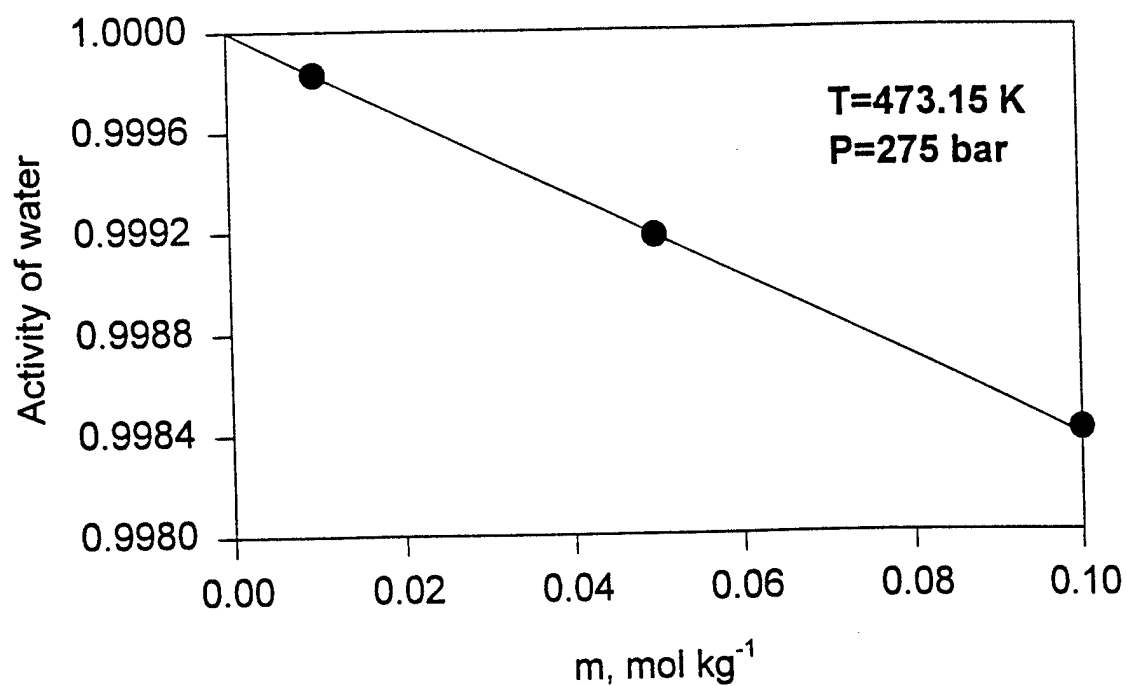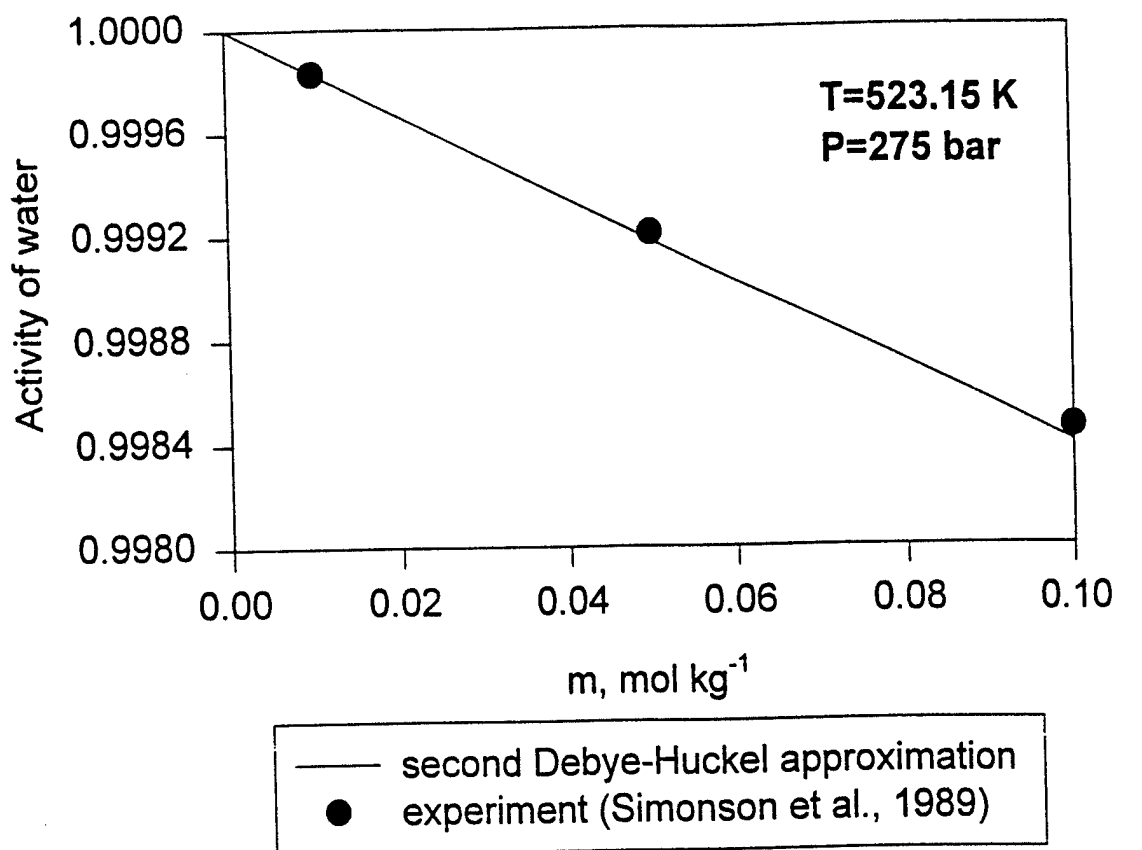
Figure 4-14. Comparison of calculated by [Equation (3)] and observed[49] data for the activity of water, a_{H_2O}, at temperatures of 473.15 and 523.15K and at a pressure of 275 bar.

$$\Delta_f G_i^0(T,P) =$$

$$\Delta_f G_{i,T_0,P_0}^0 + \int_{P_0}^{P} V_{i,T_0}^0(P)dP - S_{i,T_0,P_0}^0(T-T_0) + (T-T_0)\int_{P_0}^{P} \frac{\partial[V_{i,T_0}^0(P)]}{\partial T}dP + \qquad (15)$$

$$\int_{T_0}^{T} C_{P,i}^0(T)dT - T\int_{T_0}^{T} \frac{C_{P,i}^0(T)}{T}dT,$$

if the temperature dependence of the standard molal isobaric heat capacity $C_{P,i}^0(T)$ at pressure P, as well as the temperature and pressure dependencies of the standard molal volume $V_{i,T_0}^0(P)$ of the ith species are known. In Equation (15), $\Delta_f G_{i,T_0,P_0}^0$ is the standard molal Gibbs energy of formation of the ith species from its elements in the their stable phase at the reference temperature T_0 and pressure P_0, and S_{i,T_0,P_0}^0 is the standard molal entropy of the ith species also at the reference temperature T_0 and pressure P_0. Note that the electrochemical Cell (I) is not under isobaric conditions, in that the YSZ membrane is the pressure boundary. Thus, the left part of the cell is at the reference pressure, P_0, and the right part is at a working pressure, P. Because of that, the apparent standard Gibbs energy of formation for Hg(l) and HgO(s) must be calculated from the following expression:

$$\Delta_f G_i^0(T,P_0) = \Delta_f G_{i,T_0,P_0}^0 - S_{i,T_0,P_0}^0(T-T_0) + \int_{T_0}^{T} C_{P_0,i}^0(T)dT - T\int_{T_0}^{T} \frac{C_{P_0,i}^0(T)}{T}dT, \qquad (16)$$

which is a simplified form of Equation (15) for the case when $P = P_0$. The values of $C_{P_0,i}^0(T)$ employed in Equation (16) are commonly expressed as functions of the form

$$C_{P_0,i}^0(T) = a_i + b_i + c_i T^{-2} \qquad (17)$$

where a_i, b_i, and c_i are empirical regression coefficients. The values of $\Delta_f G^0_{i,T_0,P_0}$, S^0_{i,T_0,P_0}, and a_i, b_i, and c_i for Hg(l) and HgO(s) used in our calculations are given in Table 4-4 (Johnson et al.,[50] Naumov et al.[54]). The thermodynamic properties of water at elevated temperatures were calculated using the NIST/ASME Steam Properties Formulation for General and Scientific Use (Klein and Harvey[46]). The calculated $\Delta_f G^0_i(T, P = 275 \text{ bar})$ for water and $\Delta_f G^0_i(T, P_0)$ values for Hg(l) and HgO(s) at temperatures between 473 and 723 K are presented in Table 4-5.

In Table 4-5, we also present the apparent standard Gibbs energy of formation of H_2(aq), $\Delta_f G^0_{H_2(aq)}(T, 275 \text{ bar})$, calculated from the experimental data for E^0 by using Equation (14).

Henry constants, K_H, for dissolved molecular hydrogen in pure water have been reported in the literature for wide ranges of temperatures and pressures. The apparent standard Gibbs energy of formation of H_2(aq), $\Delta_f G^0_{H_2(aq)}(T, 275 \text{ bar})$, obtained in this work can be used to calculate K_H ($= f_{H_2}/a_{H_2}$) values as

$$RT \ln K_H = \Delta_f G^0_{H_2(aq)}(T, 275 \text{ bar}) - \Delta_f G^0_{H_2(g)}(T, 1 \text{ bar}) \tag{18}$$

at temperatures within the range 473 and 723 K and at a pressure of 275 bar for further comparison with the available literature data. In Equation (18), $\Delta_f G^0_{H_2(g)}(T, 1 \text{ bar})$ is the apparent standard Gibbs energy of formation of the H_2(g) in the ideal gas state (Johnson et al.[50]). Figure 4-15 shows a comparison of the $\ln K_H$ values obtained in this work (Table 4-5) with the experimental data of Fernandez-Prini and Crovetto[51] and of Kishima and Sakai.[52] Good agreement is obtained over the whole range of temperature, although our measurements appear to

Table 4-4. Thermodynamic properties of the chemical components in the electrochemical cell.

Components	$\Delta_f G^0_{i,T_0,P_0}$ kJ/mol	S^0_{i,T_0,P_0} J/mol/K	a_i J/mol	$b_i\, 10^3$ J/mol/K	$c_i\, 10^{-5}$ J K^2/mol
Hg(l)	0	76.023	26.945	0	-0.795
HgO(s)	-58.409	70.291	34.853	30.836	0
H$_2$(aq)	17.723	57.739	-	-	-
H$_2$O(l)	-237.183	69.923	-	-	-

Table 4-5. Apparent standard Gibbs energies of formation of the cell components and ln K_H at temperatures from 473 to 723 K and at a pressure P=275 bar.

T, K	$\Delta_f G^0_{H_2O}$(T,275 bar) kJ/mol	$\Delta_f G^0_{Hg(l)}$(T,1 bar) * kJ/mol	$\Delta_f G^0_{HgO(s)}$(T,1 bar) kJ/mol	$\Delta_f G^0_{H_2(aq)}$(T,275 bar) kJ/mol	ln (K_H/bar kg mol^{-1})
473	-252.1	-14.4	-72.6	2.4	6.7
523	-257.5	-19.0	-77.4	-0.2	7.2
573	-263.4	-23.6	-82.3	-8.3	6.4
623	-269.6	-28.3	-87.5	-17.6	5.5
673	-276.4	-37.4	-92.9	-28.1	4.6
723	-284.4	-47.0	-98.5	-42.4	3.2

* At temperatures above 623 K a pressure of 5 bar was used for the calculation because of the phase transition from Hg(l) to Hg(g) at T=630 K.

H$_2$ - H$_2$O
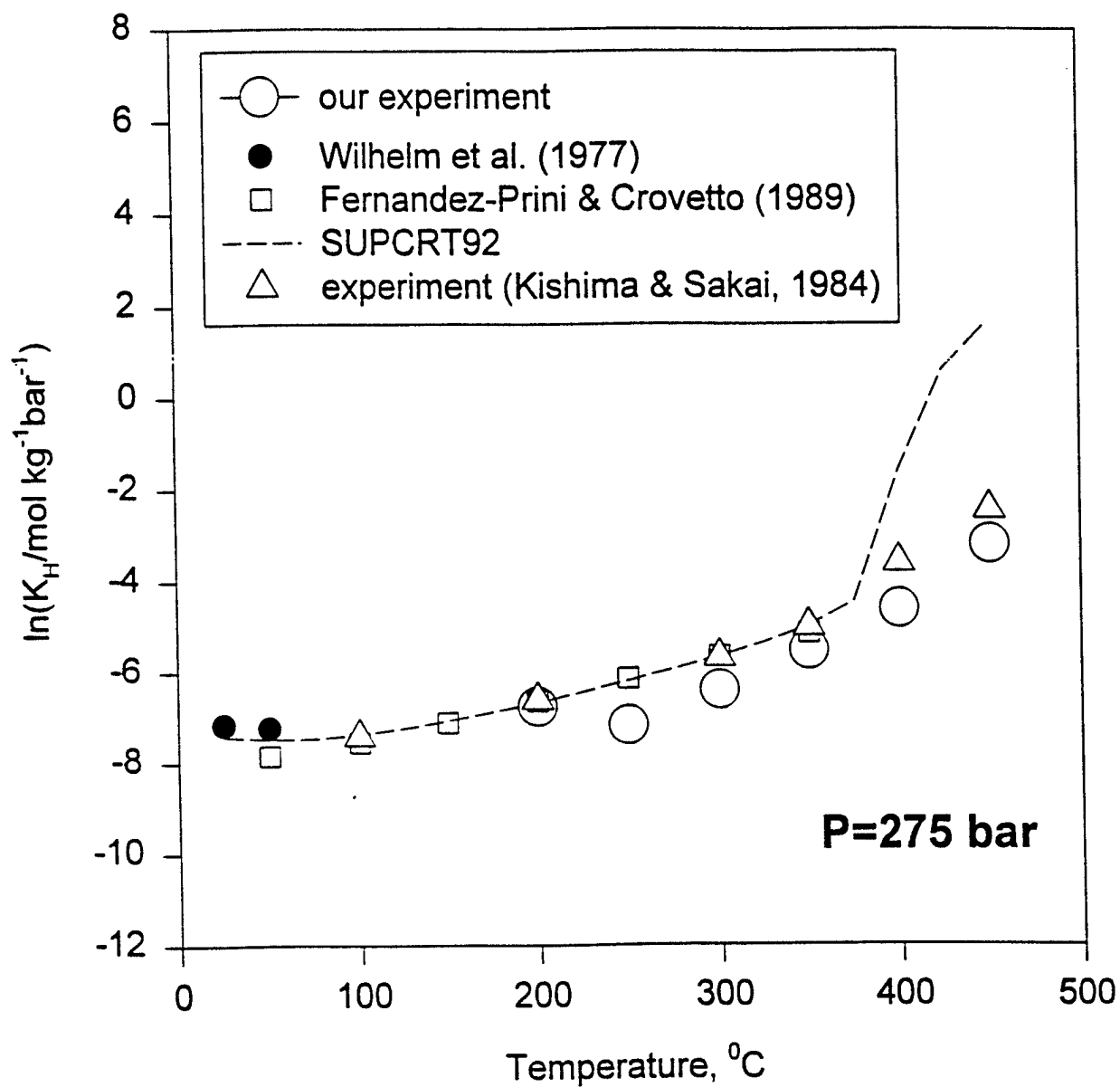
Figure 4-15. Comparison of the $\ln K_H$ values for H$_2$(aq) obtained in this work with other literature data[49,50,51] at temperatures up to 723K and pressure 275 bar.

be slightly lower than those of both groups of workers. Note than our $\ln K_H$ vs. temperature data pass through the critical region smoothly, as do the data of Kishima and Sakai, who used an entirely different experimental technique. Finally, we also plot in Figure 4-15 values for $\ln K_H$ obtained from the thermodynamic code, SUPCRT92 (Johnson et al.[50]). Good agreement is observed for subcritical, but not for supercritical, temperatures.

Contrariwise, the close agreement that is observed between the Henrys law constants measured in this work and those reported by Fernandez-Prini and Crovetto[51] for temperatures up to 350°C and by Kishima and Sakai[52] at temperatures up to 450°C demonstrates that the YSZ/H_2(Pt) cell is thermodynamically well-behaved at high subcritical and supercritical temperatures. This finding confirms the earlier work of Hettiarachchi et al.,[1,28] and the more recent studies of Ding and Seyfried.[9,33] Thus, when used with a suitable reference electrode, the YSZ electrode is a primary pH sensor (as previously noted[1,26]) with pH ($=-\log a_{H+}$) being readily obtained from

$$pH = \frac{F}{2.303RT}(E^o_{Hg/HgO} - E + E_J) - \frac{1}{2}\log a_{H_2O} \qquad (19)$$

where E is the measured potential of the YSZ electrode on the SHE scale, E_j is the isothermal liquid junction potential (if any) associated with the practical reference electrode, a_{H2O} is the activity of water, and $E^o_{Hg/HgO}$ is the standard potential of the Hg/HgO reference couple of the YSZ electrode, which is given by

$$E^o_{Hg/HgO} = 1.11178 - 1.2617 \times 10^{-3} \times T + 3.1347 \times 10^{-6} \times T^2 - 4.3130 \times 10^{-9} \times T^3 + 2.2915 \times 10^{-12} \times T^4 \qquad (20)$$

Equation (20) fits the available thermodynamic data[50,53] with a precision of ±0.3mV over the temperature range from 298K to 723K.

We end this section by briefly reviewing other methods that have been devised to measure hydrogen *in situ* in high temperature aqueous solutions. Thus, Macdonald et al.[54] made use of the effect of H on the resistance of a palladium wire together with temperature compensation via a platinum wire to devise a sensor that was both rugged and sensitive. Under optimal conditions, about 5×10^{-6} mol/kg of dissolved hydrogen could be measured at 275°C. In a later study, Liu and Macdonald[55] extended the technique to supercritical conditions and demonstrated the ability of the sensor to measure hydrogen at temperatures as high as 410°C. The sensor output was found to vary with $\sqrt{p_{H_2}}$, and hence with $\sqrt{m_{H_2}}$, as had been found for the lower temperature study, in agreement with Sievert's law. Recently, Ding Seyfried,[9] building on earlier work by Hettiarachchi et al.,[28] employed a $(Pt)H_2/H^+$, $H_2O/ZrO_2(Y_2O_3)/HgO/Hg$ cell to measure hydrogen in water at a single temperature and pressure of 400°C and 400 bars, respectively. They showed that the potential of the cell using Pt as the hydrogen electrode varied linearly with $\log m_{H2} = 0.096\text{-}5.75$ mmol/kg with a slope of 0.054 V^{-1}. The slope is significantly lower than the theoretical value of 0.067 V^{-1}, which the authors attribute to sampling errors. More recently,[9] the same authors report similar measurements using gold as the hydrogen electrode and have found an E vs. $\log m_{H2}$ slope at 400°C of 0.0668V, which is in good agreement with theory. A solid-state amperometric hydrogen sensor has also been devised[56] and has been evaluated at temperatures up to 300°C. The steady-state current was found to vary with the square root of the hydrogen concentration in accordance with an adsorption/charge transfer mechanism at the platinum sensing electrode. Finally, very recently, Hara and Macdonald,[57] have described the use of a H_2, $H_2O/PTFE/(Pt$ or $Pd)/ZrO_2(Y_2O_3)/Ag/O_2(Pt)$ cell for measuring hydrogen in high temperature aqueous solutions, with the theoretical response being obtained

over a wide range of hydrogen concentration (7.61×10^{-6} to 7.61×10^{-4} mol/kg). The use of a PTFE (polytetrafluoroethylene) diffusion membrane in the present design limits the upper temperature of the operation to about 300°C. In all of the studies outlined above, the objective was to measure hydrogen concentration as opposed to Henry's constant, which is the more important thermodynamic quantity. The present work extends the use of equilibrium electrochemical cells to measure K_H for hydrogen in aqueous solutions at high subcritical and supercritical aqueous solutions.

4.2.6 References

1. D. D. Macdonald, S. Hettiarachchi, H. Song, K. Makela, R. Emerson, and M. Haim, *J. Solut. Chem.*, **21**, 849 (1992).
2. G. C. Ulmer and H. L. Barnes, *Hydrothermal Experimental Techniques*, Wiley-Interscience, New York (1987).
3. W. L. Bourcier, G. C. Ulmer, and H. L. Barnes, "Hydrothermal pH Sensors of ZrO_2, Pd Hydrides, and Ir Oxides", *Hydrothermal Experimental Techniques*, by G. C. Ulmer and H. L. Barnes (eds.), Wiley-Interscience, New York, p. 157-188 (1987).
4. H. L. Barnes, "Buffers for pH and Redox Control of Hydrothermal Systems", *Hydrothermal Experimental Techniques*, Ed. by G. C. Ulmer and H. L. Barnes (eds.), Wiley-Interscience, New York, p. 507-514 (1987).
5. V. A. Dolidze, "Electrodes for Potentiometric High - Temperature Determination of pH", *Ion-selective Electrodes*, E. Pungor and I. Buzas (eds.), Elsevier, Amsterdam, p. 57-97 (1978).
6. D. D. Macdonald, S. Hettiarachchi, and S. J. Lenhart, *J. Soln. Chem.*, **17**, 719 (1988).
7. L. B. Kriksunov and D. D. Macdonald, "Advances in Measuring Chemistry Parameters in High Temperature Aqueous Systems", *Physical Chemistry of Aqueous Systems*, H. J. White, J. V. Sengers, D. B. Neumann, J. C. Bellows (eds.), Begell House, p. 432- 440 (1995).
8. L. B. Kriksunov and D. D. Macdonald, "Electrochemical Sensors for High Temperature Aqueous Environments", *Proc. 187th Mtg. of the Electrochemical Society*, Extended Abstracts 95-1, p. 694 (1995a).
9. K. Ding and W. E. Seyfried, Jr., *Geochim. Cosmochim. Acta*, **59**, 4769 (1995): *J. Soln. Chem.*, **25**, 421 (1996).
10. J. V. Dobson, *J. Electroanal. Chem.*, **35**, 129 (1972).
11. J. V. Dobson, P. R. Snodin, and H. R. Thirsk, *Electrochim. Acta*, **21**, 527 (1976).
12. D. D. Macdonald, P. R. Wentrcek, and A. C. Scott, *J. Electrochem. Soc.*, **127**(8), 1745 (1980).
13. R. E. Mesmer, W. L. Marshall, D. A. Palmer, J. M. Simonson, and H. F. Holmes, *J. Solut. Chem.* **17**, 699 (1988).

14. R. E. Mesmer, D. A. Palmer, and D. J. Wesolowski, "Potentiometric Studies at ORNL with Hydrogen Electrode Concentration Cell", *Physical Chemistry of Aqueous Systems*, H. J. White, J. V. Sengers, D. B. Neumann, J. C. Bellows (eds.), Begell House, p. 423-431 (1995).

15. F. H. Sweeton, R. E. Mesmer, and C. F. Baes Jr., *J. of Phys. E. Scientific Instruments*, **6**, 165 (1973).

16. D. J. Wesolowski, D. A. Palmer, and R. E. Mesmer, "Measurements and Control of pH in Hydrothermal Solutions", *Water-Rock Interaction*, Y. K. Kharaka, O. V. Chudaev, Balkema (eds.), p. 51-55. (1995).

17. R. E. Mesmer, C. F. Baes, and F. W. Sweeton, *J. Phys. Chem.*, **74**, 1937 (1970).

18. C. F. Baes and N. J. Meyer, *Inorg. Chem.*, **1**, 780 (1962).

19. D. D. Macdonald, P. Butler, and D. Owen, *J. Phys. Chem.*, **77**(20), 2474 (1973).

20. D. D. Macdonald, P. Butler, and D. Owen, *Can. J. Chem.*, **51**, 2590 (1973).

21. D. D. Macdonald and D. Owen, *Can. J. Chem.*, **51**(16), 2747 (1973).

22. L. W. Niedrach, *J. Electrochem. Soc.*, **127**, 2122 (1980).

23. L. W. Niedrach and W. H. Stoddard, *J. Electrochem. Soc.*, **131**, 1017 (1984).

24. T. Tsuruta and D. D. Macdonald, *J. Electrochem. Soc.*, **128**, 1199 (1981).

25. T. Tsuruta and D. D. Macdonald, *J. Electrochem. Soc.*, **129**, 1221 (1982).

26. S. Hettiarachchi, P. Kedzierzawski, and D. D. Macdonald, *J. Electrochem. Soc.*, **132**(8), 1866 (1985).

27. S. Hettiarachchi, S. J. Lenhart, and D. D. Macdonald, "Electrochemical Techniques for Monitoring pH in High Temperature Aqueous Systems", *Proc. 3rd Int'l. Symp. Envir. Degrad. Mat. Nucl. Power Systs.-Water Reactors*, G. J. Theus and J. R. Weeks (eds.), NACE, Houston, TX (1988).

28. S. Hettiarachchi, K. Makela, H. Song, and D. D. Macdonald, *J. Electrochem. Soc.*, **139**(1), L3 (1992).

29. L. B. Kriksunov and D. D. Macdonald, "Study of the Zirconium/Zirconium Oxide Electrode as a pH Sensor at Temperatures up to 300°C" *Proc. 186th Mtg. of the Electrochem. Soc.*, Extended Abstracts 94-2 (1994).

30. K. Makela, S. Hettiarachchi, D. D. Macdonald, H. Song, and R. Emerson, "Development of Reference and pH Sensors for Monitoring High Temperature Water Chemistry Parameters in Nuclear Power Plants", *Proc. 12th Scandinavian Corrosion Congress & Eurocorr '92*, Tech. Res. Cent., Espoo, Finland (1992).

31. S. Hettiarachchi and D. D. Macdonald, *J. Electrochem. Soc.*, **131**(9), 2206 (1984).

32. S. N. Lvov, G. Perboni, and M. Broglia, "High Temperature pH Measurements in Dilute Aqueous Ammonia Solutions", *Physical Chemistry of Aqueous Systems*, H. J. White, J. V. Sengers, D. B. Neumann, J. C. Bellows (eds.), Begell House, p. 441-448 (1995).

33. K. Ding and W. E. Seyfried, *Science*, **272**, 1634 (1996).

34. M. Le Peintre, *Bull.Sos.Fr. Electr.*, **1**, 582 (1960).

35. P. A. Kryukov and L. I. Starostina, *Izv. Sibir. Otdel. Akad. Nauk SSSR, Ser. Khim. Nauk*, **7**, 27 (1969).

36. L. B. Kriksunov and D. D. Macdonald, *Sensors and Actuators B (Chemical)*, **22**, 201 (1994).

37. L. B. Kriksunov and D. D. Macdonald, "Tungsten/Tungsten Oxide pH Sensing Electrode for High Temperature Aqueous Environments", *Proc. 185th Mtg. of the Electrochem. Soc.*, Extended Abstracts 94-1, p. 1597-1598 (1994).

38. L. B. Kriksunov, D. D. Macdonald, and P. J. Millett, *J. Electrochem. Soc.*, **141**(11), 3002 (1994).
39. D. D. Macdonald, *Corrosion*, **34**(3), 75 (1978).
40. D. D. Macdonald, A. C. Scott, and P. R. Wentrcek, *J. Electrochem. Soc.*, **126**, 908 (1979).
41. D. D. Macdonald, A. C. Scott, and P. R. Wentrcek, *J. Electrochem. Soc.*, **126**(9), 1618 (1979).
42. S. Hettiarachchi and D. D. Macdonald, *J. Electrochem. Soc.*, **134**(5), 1307 (1987).
43. H. Wilhelm, R. Battino, and R. J. Wilcock, *Chem. Rev.*, **77**(2), 219 (1977).
44. F. A. Long and W. F. McDevit, *Chem. Rev.*, **51**, 119 (1952).
45. R. A. Robinson and R. H. Stokes, *Electrolyte Solutions*, Butterworths, London (1959).
46. S. A. Klein and A. H. Harvey, "Formulation for General and Scientific Use", PC Software Package, Department of Commerce/NIST (1996).
47. P. C. Ho and D. A. Palmer, *J. Soln. Chem.*, **25**, 711 (1996).
48. W. L. Marshall and E. U. Franck, *J. Phys. Chem. Ref. Data*, **10**, 295 (1981).
49. J. M. Simonson, R. E. Mesmer, and P. S. Z. Rogers, *J. Chem. Thermod.*, **21**, 561 (1989).
50. J. W. Johnson, E. H. Oelkers, and H. C. Helgeson, *Computers and Geosciences*, **18**, 899 (1992).
51. R. Fernandez Prini and R. Crovetto, *J. Phys. Chem. Ref. Data*, **18**(3), 1231 (1989).
52. N. Kishima and H. Sakai, *Earth and Planetary Science Letters*, **67**, 79 (1984).
53. G. B. Naumov, B. N. Ryzhenko, and I. L. Khodakovsky, *Handbook of Thermodynamic Data*. U.S. Geological Survey, Menlo Park, California (1974).
54. D. D. Macdonald, M. C. H. McKubre, A. C. Scott, and P. R. Wentrcek, *Ind. Eng. Chem. Fundam.*, **20**, 290 (1981).
55. C. Liu and D. D. Macdonald, *J. Supercrit. Fluids*, **8**, 263 (1995).
56. L. B. Kriksunov and D. D. Macdonald, *Sensors and Actuators B*, **32**, 57 (1996).
57. N. Hara and D. D. Macdonald, "Development of Dissolved Hydrogen Sensors Based on Yttria-Stabilized Zirconia Solid Electrolyte with Noble Metal Electrodes", *J. Electrochem. Soc.*, submitted (1996).

4.3 ADVANCED DIFFERENTIAL RESISTANCE HYDROGEN SENSOR

Three dissolved gas sensors were developed during the course of this project. This Chapter will address the second sensor of the group, the differential resistance hydrogen sensor. This advanced sensor has been developed for monitoring hydrogen in aqueous environments over wide ranges of temperature and pressure.[1-3] The technique is based on the well-known fact that the electrical resistance of palladium varies with the amount of hydrogen absorbed into the lattice.[4] Because of their ability to reversibly absorb hydrogen, and because of their relatively large coefficients of electrical resistivity with respect to hydrogen concentration in the lattice, palladium and palladium alloys have been previously used in many types of hydrogen sensors, and related devices.[5-9] However, the harshness of high temperature aqueous environments renders many of these sensors unsuitable for an SCWO system. Furthermore, while hydrogen sensors for use in high temperature aqueous environments have been fabricated previously,[8-9] they were limited to subcritical temperatures, because of the use of organic material (e.g., PTFE) for electrical insulation. These materials cannot withstand the harsh aqueous environments that exists at temperatures in excess of 320°C.[9] The advanced hydrogen sensor described here uses a zirconium mandrel, whose surface has been oxidized to form a thin and continuous zirconia layer, as the support for the Pd and Pt sensing elements. The sensor can be used at supercritical temperatures, because zirconia is particularly immune to corrosion in high temperature aqueous solutions. The sensor has been fabricated using a palladium wire for sensing hydrogen, a platinum wire for temperature compensation, and a high precision resistometer to measure and compare the differential resistance between the palladium and platinum probes. To our

knowledge, this is the first time that dissolved hydrogen has been measured, in situ, in aqueous environments above the critical point of water.

The design of the sensor is shown schematically in Figure 4-16, and the sensor was fabricated at the Pennsylvania State University. As noted above, the main mandrel is a 6.35 mm (OD) zirconium tube, which was covered with a thin, continuous zirconia film after threads were
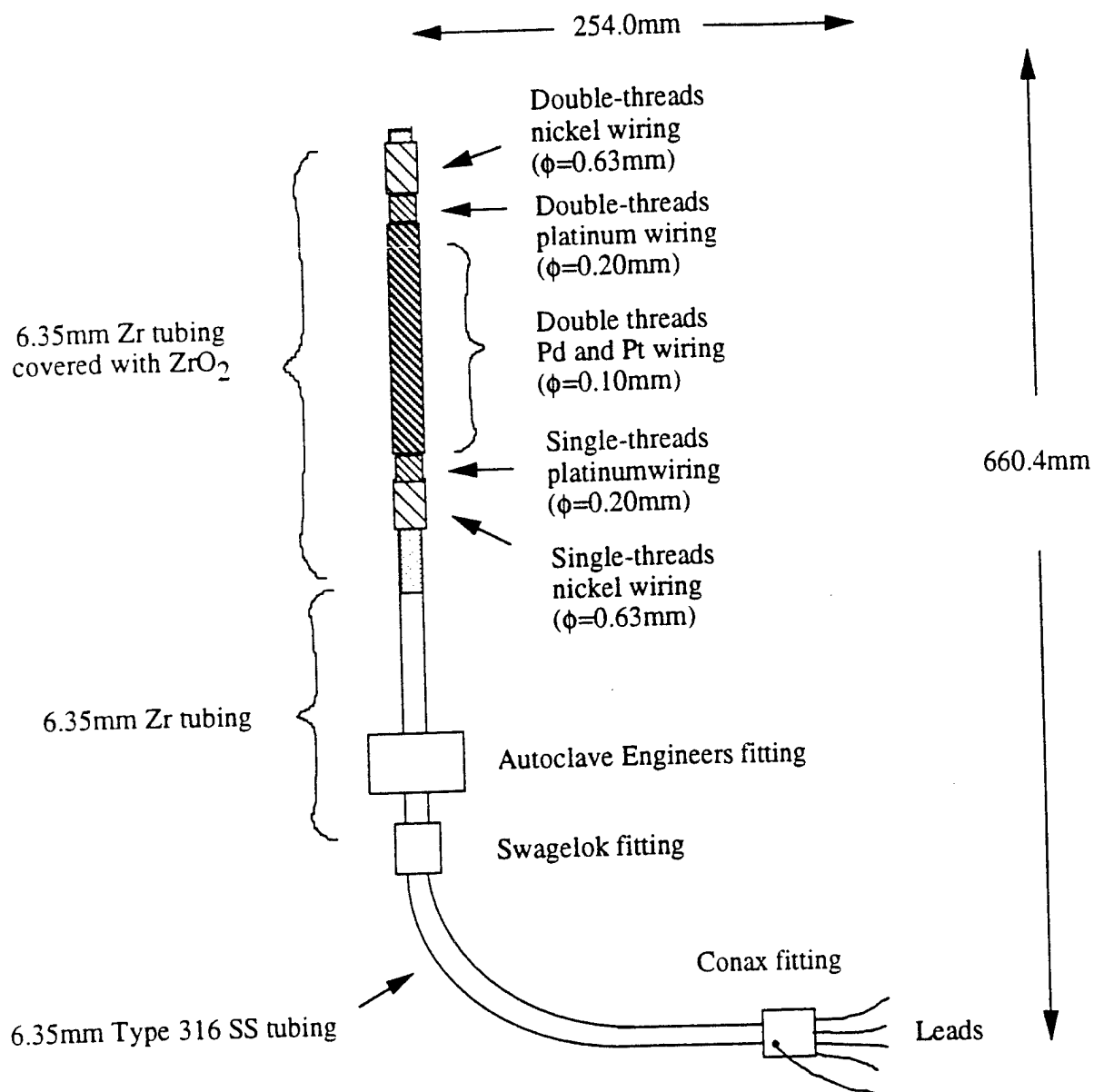
Figure 4-16. Schematic of the hydrogen sensor assembly.

4-59

machined down part of its length to accommodate the palladium and platinum wires. The thin zirconia layer on the zirconium mandrel was formed by high temperature oxidation, in such a way that only the end exposed to the high temperature solution was fully covered with oxide. A four-wire configuration was used to ensure high precision resistance measurements. Pure nickel wire of 0.63 mm diameter was chosen as the leads, because of its resistance to corrosion in this type of application. The leads are arranged inside the zirconium tube and are guided by a four-channel alumina tube in order to avoid mutual electrical contact and contact with the zirconium tube. The outer diameter of the alumina tube is 4.0 mm, and each channel has a diameter of 0.7 mm. The palladium and platinum sensing elements are connected together at one end (common) and are spot-welded to the zirconium mandrel. The graded profile of the zirconium oxide ensures that the zirconium tube is available for a metal-to-metal seal using an Autoclave Engineers high pressure fitting (AE 6MX94K2 316SS). The zirconium tube was then connected through a Swagelok fitting to a 6.35 mm Type 316 SS tube, which was then sealed, with the multi-channel alumina tube, by a Conax fitting utilizing a PTFE sealant (Gland MHC2-020-B4). The tube is bent to a 90° angle to avoid extrusion of the leads under pressure. The body of the loop is used as the common lead, and the electrical continuity is assured by the spot-weld of the common lead to the zirconium tube and by the metal-to-metal fittings.

The sensing elements are 0.10 mm diameter palladium and platinum wires, with the later being used to compensate for the effect of temperature fluctuations. Short lengths of pure nickel wire, with a diameter equal to 0.5 mm, were connected to both ends of the sensing elements, via an intermediate platinum wire (0.20 mm diameter), to enhance the ruggedness of the sensor. The electrical resistances of the palladium and platinum sensing elements were measured using a high precision resistometer (Automatic Systems Laboratories Inc., Model F250). The resistometer is essentially a 4 wire, autobalancing, AC resistance ratio bridge, which uses a 1 mA square wave

current excitation at 375 Hz to make comparative resistance measurements. The resolution of the resistometer is 0.001Ω.

Assuming that the resistance of the palladium wire is a function of temperature, T, and hydrogen concentration, C, the following can be stated:

$$dR_{Pd} = (\frac{\partial R_{Pd}}{\partial T})dT + (\frac{\partial R_{Pd}}{\partial C})dC \qquad (1)$$

For a finite change in T and C, we get,

$$\delta R_{Pd} = (\frac{\partial R_{Pd}}{\partial T})\delta T + (\frac{\partial R_{Pd}}{\partial C})\delta C \qquad (2)$$

where $\delta R_{Pd} = R_{Pd} - R_{Pd}^0$, $\delta T = T - T_0$ and $\delta C = C - C_0$, and R_{Pd}^0, C_0, T_0 refer to a reference state. Thus,

$$R_{Pd} = R_{Pd}^0 + (\frac{\partial R_{Pd}}{\partial T})(T - T_0) + (\frac{\partial R_{Pd}}{\partial C})(C - C_0) \qquad (3)$$

Defining

$$\gamma_T^{Pd} = \frac{\partial Ln(R_{Pd})}{\partial T} = \frac{1}{R_{Pd}}\frac{\partial R_{Pd}}{\partial T} \approx \frac{1}{R_{Pd}^0}\frac{\partial R_{Pd}}{\partial T} \qquad (4)$$

and

$$\gamma_C^{Pd} = \frac{\partial Ln(R_{Pd})}{\partial C} = \frac{1}{R_{Pd}}\frac{\partial R_{Pd}}{\partial C} \approx \frac{1}{R_{Pd}^0}\frac{\partial R_{Pd}}{\partial C} \qquad (5)$$

gives

$$R_{Pd} = R_{Pd}^0[1 + \gamma_T^{Pd}(T - T_0) + \gamma_C^{Pd}(C - C_0)] \qquad (6)$$

Likewise, for platinum,

$$R_{Pt} = R_{Pt}^0[1 + \gamma_T^{Pt}(T - T_0)] \qquad (7)$$

If no hydrogen exists in the palladium, we may define a differential resistance as,

$$R_{Pd}^{nh} = R_{Pd}^0 + R_{Pd}^0 \gamma_T^{Pd}(T - T_0) \tag{8}$$

where R_{Pd}^{nh} is the resistance of a palladium wire at temperature T, with no hydrogen absorbed.

The difference between Equations (7) and (8) gives,

$$\Delta R^{nh} = (R_{Pd}^0 - R_{Pt}^0) + [R_{Pd}^0 \gamma_T^{Pd} - R_{Pt}^0 \gamma_T^{Pt}](T - T_0) \tag{9}$$

This is a constant for any given sensor. Consequently,

$$\Delta R = R_{Pd} - R_{Pt} = \Delta R^{nh} + R_{Pd}^0 \gamma_C^{Pd}(C - C_0) \tag{10}$$

Rearranging Equation (10), and by choosing the reference state with $C_0=0$, gives,

$$C = (\Delta R - \Delta R^{nh}) / R_{Pd}^0 \gamma_C^{Pd} \tag{11}$$

4.3.1 Sensitivity

Let $\Delta R - \Delta R^{nh} = D_R$, as being the experimentally measured quantity. However, the sensitivity

also depends on the resistance of the palladium wire R_{Pd}^0; thus, from Equation (11), we have,

$$\delta C = \frac{1}{\gamma_C^{Pd}}[\frac{R_{Pd}^0 \delta D_R - D_R \delta R_{Pd}^0}{(R_{Pd}^0)^2}] \tag{12}$$

and hence,

$$\delta = \frac{\delta C}{C} = \frac{1}{D_R}[\frac{R_{Pd}^0 \delta D_R - D_R \delta R_{Pd}^0}{(R_{Pd}^0)}] \tag{13}$$

or,

$$\delta = \frac{\delta D_R}{D_R} - \frac{\delta R_{Pd}^0}{R_{Pd}^0} \tag{14}$$

Because $\delta R_{Pt}^0 = 0$ for any given sensor, the sensitivity of the hydrogen sensor is expressed as,

$$\delta = \frac{\delta D_R}{D_R} \qquad\qquad (15)$$

Accordingly, the sensitivity of the hydrogen sensor is predicted to depend on the resistance of palladium with no hydrogen absorbed.

4.3.2 Stability and Response Time

Figure 4-17 illustrates the stability of the hydrogen sensor, at 360°C, in terms of the differential resistance, as a function of time for a constant hydrogen concentration. The data show that for continuous monitoring of up to 10 hours, the sensor yields a constant and stable output. The hydrogen concentration in the solution was calculated from the saturation pressure in the reservoir using Henry's law.[10]

The response time of a sensor is a very important factor in industrial monitoring applications. We have observed that the change in the differential resistance to 90% of full scale, in response to a change in the partial pressure of hydrogen in the reservoir, occurs in about 30 minutes (Figure 4-18 insert). However, the real response of the sensing element to a change in hydrogen concentration is, in fact, much faster, since the observed response can be attributed to the use of a HPLC pump, which has a limited pumping capacity, to refresh the solution in the test cell. At a pumping rate of 4.0ml/min, which was used in the experiment, the time required to refresh the test loop prior to the exit of the cell (which has a volume of approximately 70ml) is approximately 20 min. Tests conducted at ambient temperature, by introducing hydrogen gas directly into the test cell, show that the sensor responds to a change in hydrogen concentration within a few minutes. Literature data indicate that the rate at which the palladium resistance

changes due to hydrogen absorption, expressed in terms of $\frac{dR}{Rdt}$ (hr^{-1}), increases significantly

with elevating temperature. Thus, the available data show that, from 25 to 180°C, the rate at

which the resistance changes increases by a factor of 6, in the case of hydrogen absorption, and

by a factor of 4, in the case of hydrogen desorption. [11] Because of this increase in diffusivity of

hydrogen in palladium with increasing temperature, we believe that the actual response time of

the sensor at 360°C is, at the most, of the order of a few tens of seconds.
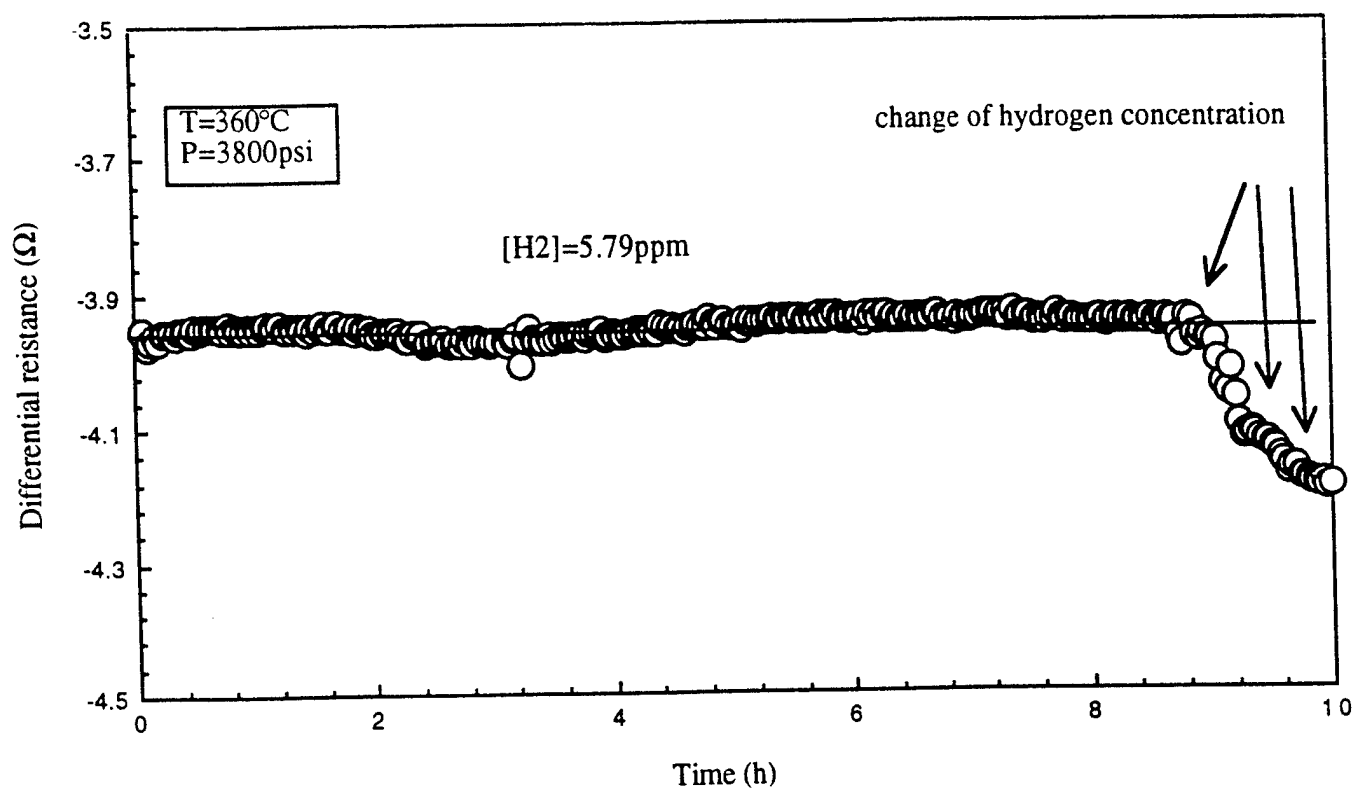
Figure 4-17. The differential resistance as a function of time at 360°C for a constant hydrogen
concentration.

4.3.3 Effect of Hydrogen Cycling

The variation of the differential resistance as a function of time during hydrogen cycling is shown in Figure 4-18. Data obtained at 360°C indicate that the output correlates uniquely with the hydrogen concentration, in that the same output is observed for the same hydrogen concentration after hydrogen cycling. Because the mechanism of hydrogen absorption is presumably different from that of desorption, because each process involves different reactions, the absorption rate is different from that of desorption.[12] Hence a hysteresis phenomenon may develop when the sensor is used to monitor variation of hydrogen concentration in a dehydrogenating process. However, the literature data
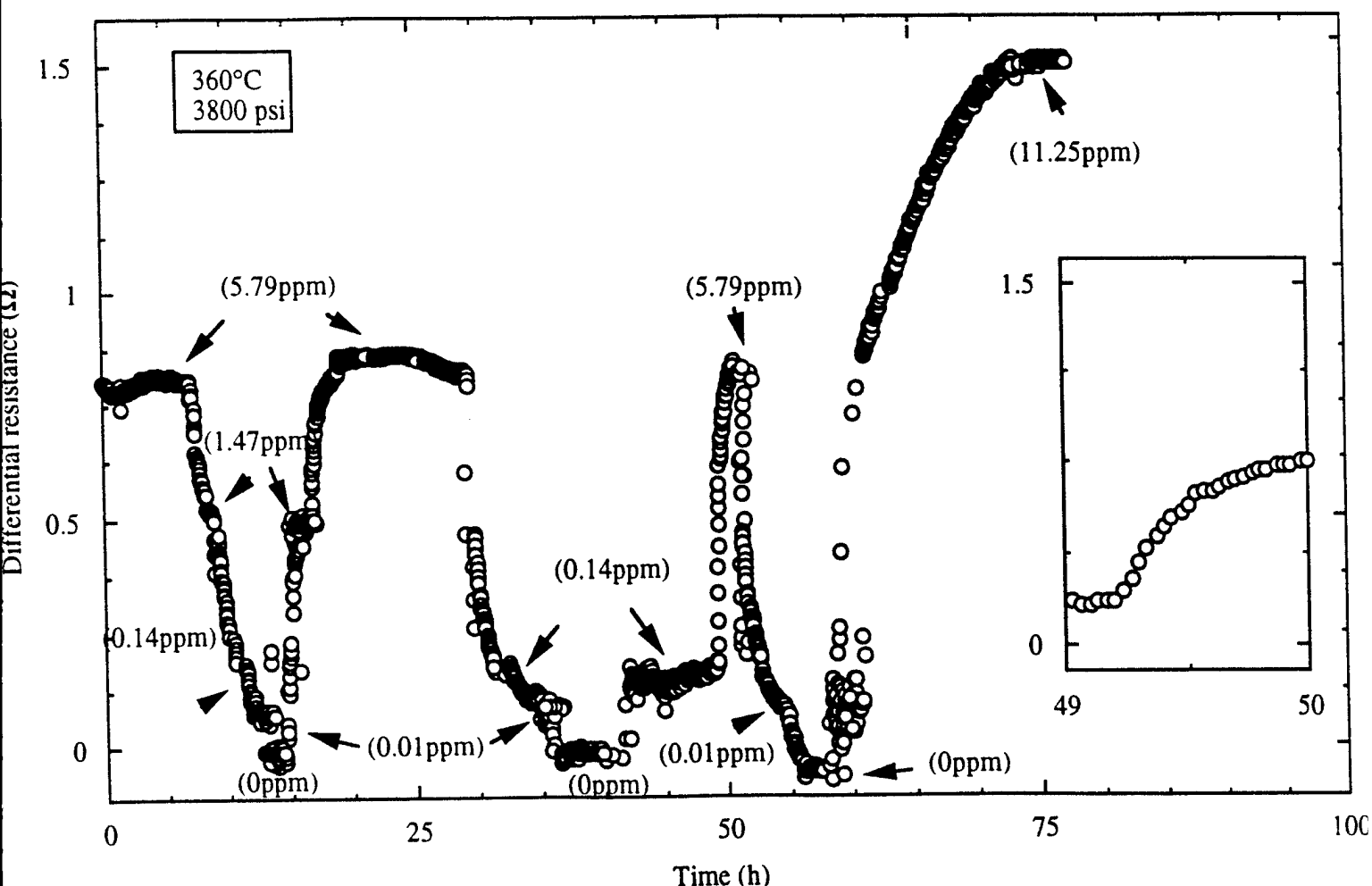
Figure 4-18. The normalized differential resistance at 360°C (with respect to the differential resistance with no hydrogen) as a function of time during hydrogen cycling.

indicate that the difference in absorption and desorption rates tends to diminish as the temperature increases. Thus, it was found that, at room temperature, a factor of 3.6 exists between desorption and absorption rates for hydrogen in palladium, while at 180°C, this factor becomes 2.3.[12] This indicates that at higher temperatures (such as in supercritical aqueous environments), the hydrogen sensor described in this paper should become equally responsive to decreases and increases in the hydrogen concentration in the immediate environment. Finally, the data that we have obtained in this study indicate that the sensor is reversible to the hydrogen concentration.

4.3.4 Effect of Hydrogen Concentration

The variation of the differential resistance with respect to hydrogen concentration and temperature is shown in Figure 4-19. The data indicate that, within the temperature range investigated (from 250 to 410°C), the output increases linearly with $C^{0.5}$, where C is the hydrogen concentration in the bulk environment. This is an important feature for on-line monitoring, in that once the sensor is calibrated for a specific set of conditions (temperature, solution, pressure, range of hydrogen concentration, etc.), it can be used to monitor dissolved hydrogen accurately under other conditions (but at the same temperature).

As stated previously, the resistometer has a limited precision, which, in our case, is 0.001Ω. Therefore, it is always advantageous that the sensing elements have as high an electrical resistance as possible, so as to produce a large change in the absolute value of the resistance for a given hydrogen concentration. In our case, physical and mechanical ruggedness considerations limit the maximum electrical resistance that can be achieved. The resolution for this sensor can
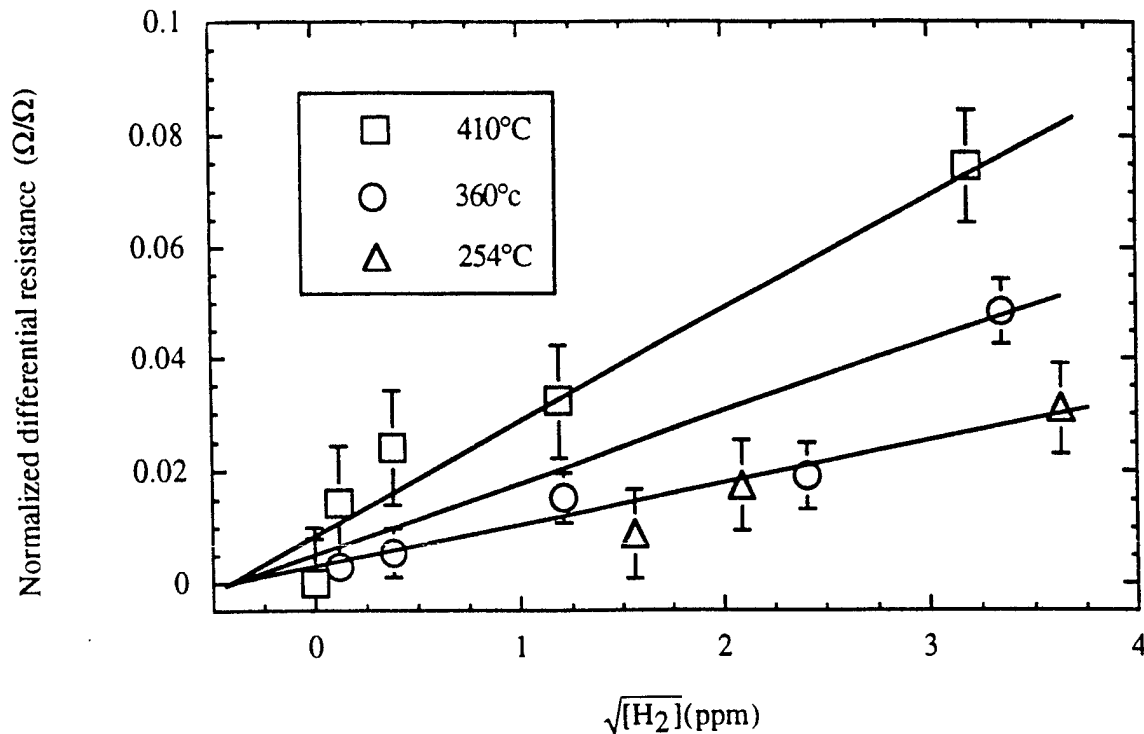
Figure 4-19. The normalized differential resistance (with respect to the average resistance of the palladium and platinum wires at room temperature) as a function of hydrogen concentration and temperature.

be readily estimated from Figure 4-19, by calculating the equivalent hydrogen concentration corresponding to the precision of the resistometer. This calculation yields a resolution of 4.3ppb (which corresponds to a resistance change of 0.001Ω) at 410°C and 7.4ppb at 360°C. However, we see no reason why the resolution cannot be reduced to the sub-ppb level by appropriate changes in the design.

4.3.5 Possible Application of the Sensors in SCWO Reactors

The sensor described here should operate at supercritical temperatures for extended periods of time without significant deterioration. However, in very aggressive environments, when a large concentration of HCl is present, it may be necessary to use the sensors in a "pseudo in situ" mode (Figure 4-20). In this case, the sensor would be located in a side-arm at somewhat lower temperature than the actual reactor temperature. Due to the temperature gradient and the corresponding density gradient, the solution in the sensor compartment will be effectively exchanged with the solution in the reactor. Because of the lower temperature, the sensors should operate over much longer periods of time.

Utilizing a design similar to that presented in Figure 4-20, it should be possible to employ PTFE-based sensors in SCWO reactors provided that the temperature of the monitoring location is maintained below ~320°C.
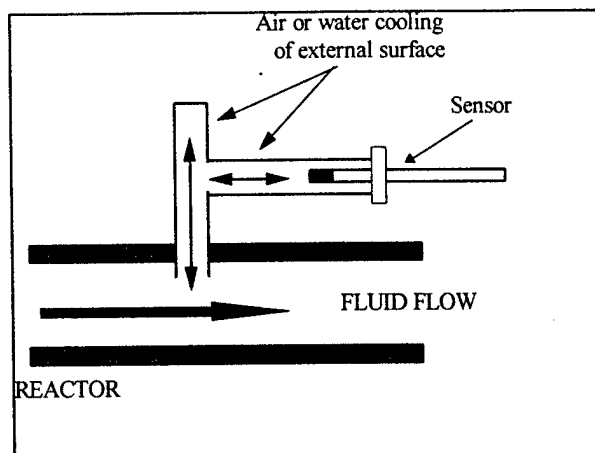
Figure 4-20. Position of the sensor in the case of "pseudo *in situ*" operation.

4-68

4.3.6 References

1. L.B.Kriksunov, C.Liu, and D.D.Macdonald, "Oxygen, hydrogen, and redox potential combination sensor for supercritical aqueous systems", I International Workshop on supercritical water oxidation, Jacksonville, FL (1995).

2. C.Liu and D.D.Macdonald, "Monitoring dissolved hydrogen in supercritical aqueous environments", Extended Abstracts, 187 Meet. Electrochem. Soc., Reno, Nevada (1995).

3. C. Liu and D. D. Macdonald, "An Advanced Pd/Pt Relative Resistance Sensor for the Continuous Monitoring of Dissolved Hydrogen in Aqueous Systems at High Subcritical and Supercritical Temperatures", Submitted to J. Supercritical Fluids.

4. F. A. Lewis, "The Palladium-Hydrogen System," Academic Press, London (1967).

5. R. C. Hughes, R. J. Reynolds, M. W. Jenkins, and J. L. Rodriguez, "Wide Range H_2 Sensor Using Catalytic Alloys," Extended Abstract, 183th Meeting of the Electrochemical Society, Vol. 93-1, pub. The Electrochemical Society, Inc., Pennington, NJ, p.1597 (1993).

6. A. J. Howard, M. Lovejoy, M. A. Butler, R. F. Carson, M. B. Sinclair, J. P. Hohimer, S. A. Casalnuovo, G. A. Vawter, R. J. Shul and R. P. Schneider, "A Novel H_2 Sensor on GaAs," Extended Abstract, 185th Meeting of the Electrochemical Society, Vol. 94-1, pub. The Electrochemical Society, Inc., Pennington, NJ, p.1603 (1994).

7. G. W. Hunter, P. G. Neudeck, G. D. Jefferson and G. C. Madzsar, "Research into Hydrogen Sensor Technology at NASA Lewis," Extended Abstract, 183th Meeting of the Electrochemical Society, Vol. 93-1, pub. The Electrochemical Society, Inc., Pennington, NJ, p.2761 (1993).

8. J. M. Wright and D. J. Stiteler, "The Bettis Technical Review," WAPD-BT-&, Office of Technical Service, Department of Commerce, Washington, DC (1958).

9. D. D. Macdonald, M. C. H. McKurbre, A. C. Scott and P. R. Wentrcek, Ind. Eng. Chem. Fundam., 20, 290 (1981).

10. G. B. Naumov, B. N. Ryzherko and I. L. Knodakovsky, "Handbook of Thermodynamic Data", National Technical Service, Department of Commerce, Springfield, VA, p.247 (1974).

11. J. V. Dobson, M. N. Dagless and H. R. Thirsk, J. Chem. Soc., Faraday Trans-1, 68, 764 (1972).

12. J. V. Dobson, B. R. Chapman, and H. R. Thirsk, "The Palladium-Hydride Reference Electrode in Hydrogen-Free Electrolyte Solutions at Elevated Temperatures," in "High Temperature, High Pressure Electrochemistry in Aqueous Solutions," Proc. Int. Corros. Conf., University of Surrey, England, Jan. 1973, Eds. D. de G. Jones, J. Slater and R. W. Staehle, pub. NACE, Houston, TX, p. 341 (1975).

4.4 AMPEROMETRIC HYDROGEN SENSOR

This section will address the third sensor developed in this project. Here we report results on the development of a relatively simple and inexpensive amperometric sensor, that can be used at temperatures up to 300°C (and, with some modifications, at even higher temperatures) for monitoring hydrogen *in situ* in aqueous systems that are typical of SCWO environments. The sensor is based on a two-electrode cell employing platinum electrodes, a proton-conducting solid electrolyte, and a PTFE diffusion membrane.

The sensing element of the hydrogen sensor (Figure 4-21) was fabricated from a thin-wall heat shrinkable PTFE tube and employs zirconium phosphate (acid form, Magnesium Electron Inc.) as a solid state proton conductor. Two identical platinum wires (diameter 0.5 mm) were used as electrodes. The sensing element was incorporated into a standard 1/4" Conax fitting,
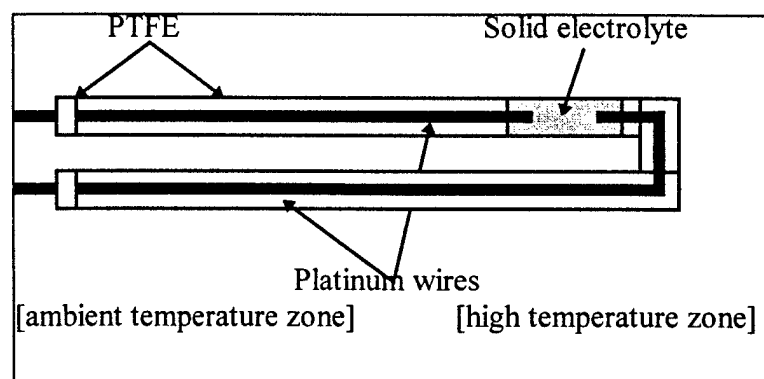
Figure 4-21. Schematic of the amperometric hydrogen sensor.

which was installed into the high pressure/high temperature test cell. The cell comprised of 1/4" O.D. Type 316 SS tubing, and incorporated feedthroughs for a thermocouple, the hydrogen sensor, and the solution input and output. Water was pumped through the cell via a HPLC pump. The pressure in the system was maintained via a relief valve, and was always higher than the

4-70

saturated vapor pressure of water at the operating temperature. The cell was heated with heating tape. We used water saturated at room temperature and at 1 atm pressure with gas mixtures containing 100%, 10%, and 1% hydrogen (balance - argon) or with laboratory air. The hydrogen content of the hydrogenated solutions was estimated using Henry's constant for hydrogen at 25°C.

The cell was polarized potentiostatically using a potentiostat in a two-electrode mode at a potential of 0.1 V. The reference electrode cable of the potentiostat was connected together with the counter electrode to one of the sensor poles, whereas the working electrode cable was connected to another pole. The cell current was recorded as a function of the hydrogen content and the temperature.

The sensor developed in this study is a symmetric electrochemical cell of the type

$$(Pt) \, H_2 \, / \, HX \, / \, H_2 \, (Pt) \tag{1}$$

where HX represents the proton-conducting electrolyte. On imposing a voltage difference between the two platinum electrodes, hydrogen is oxidized at the positive electrode

$$H_2 \rightarrow 2 \, H^+ + 2 \, e^- \tag{2}$$

but is evolved at the negative electrode

$$2 \, H^+ + 2 \, e^- \rightarrow H_2 \tag{3}$$

However, the supply of hydrogen to the anode is limited by mass transfer, by dissociation/adsorption of hydrogen on the Pt surface, or by oxidation of the adsorbed hydrogen atoms.

The zirconium phosphate (acid form) solid electrolyte employed in this sensor is stable at high temperatures [5] and hence is ideally suited for use in sensors that are designed to operate in

high temperature aqueous systems. However, aqueous electrolytes can be used in this kind of sensor as well. The disadvantage of aqueous systems is their large coefficients of expansion and the large saturation pressures of water and aqueous solutions. Accordingly, the sensor could be damaged during heating or during sudden decompression of the system.

Typical data measured at temperatures of 234°C and 300°C are presented in Figure 4-22 in logarithmic coordinates . Note that points corresponding to the air-saturated water are shown separately.
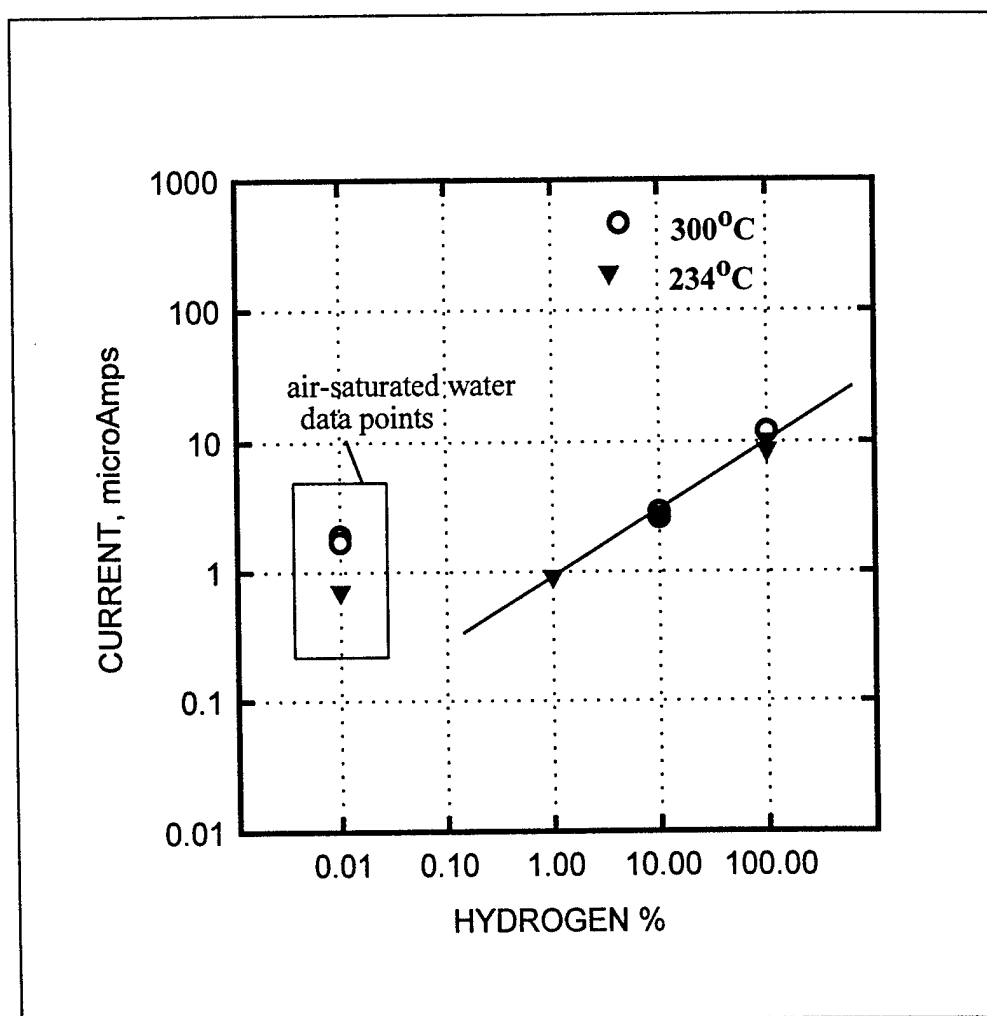
Figure 4-22. Cell current vs. hydrogen content at 234 and 300°C.

Interestingly, the cell current does not change significantly when the temperature is raised from 234 to 300°C. In Figures 4-23 and 4-24 the cell current is shown as a function of time during a change in the concentration of hydrogen (Figure 4-23) or on replacing the hydrogen with air (Figure 4-24). The response time, which is determined principally by the rate of replacement of the solution in the test cell, is of the order of 5-10 minutes and is significantly dependent upon the solution pumping rate. During the transition from hydrogenated to air-saturated water, we observed non-stationary behavior with large fluctuations in the current. (Figure 4-24). This behavior is possibly due to the concurrent O_2-H_2 adsorption-desorption phenomena on the surface of the electrodes.
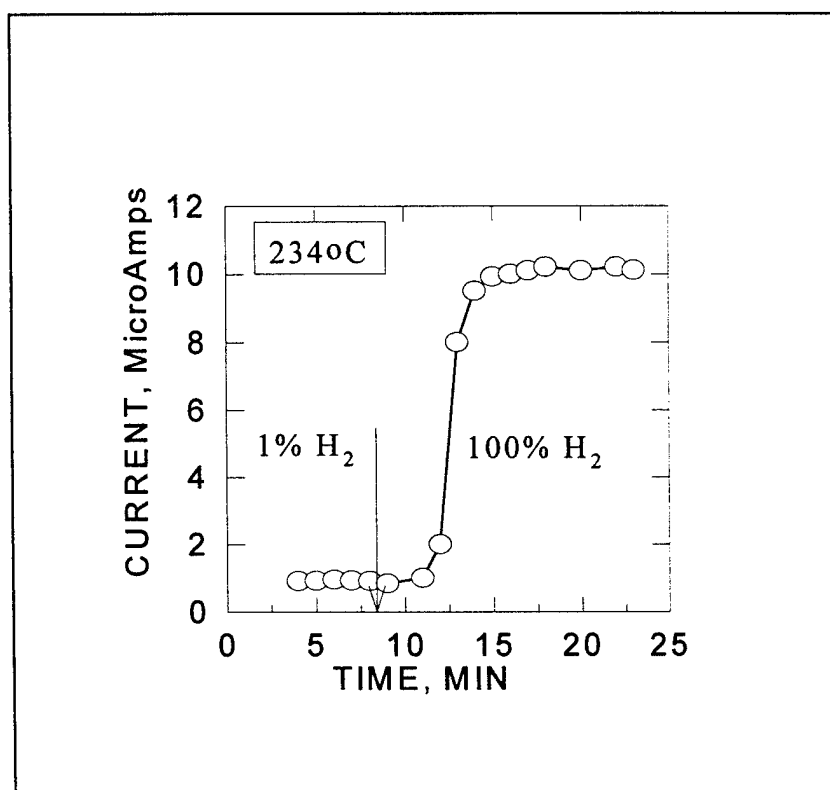
Figure 4-23. Cell current vs. time during change from water saturated with 1% hydrogen to water saturated with 100% hydrogen. Time of the solution change at the inlet of the HPLC pump is indicated by the arrow.
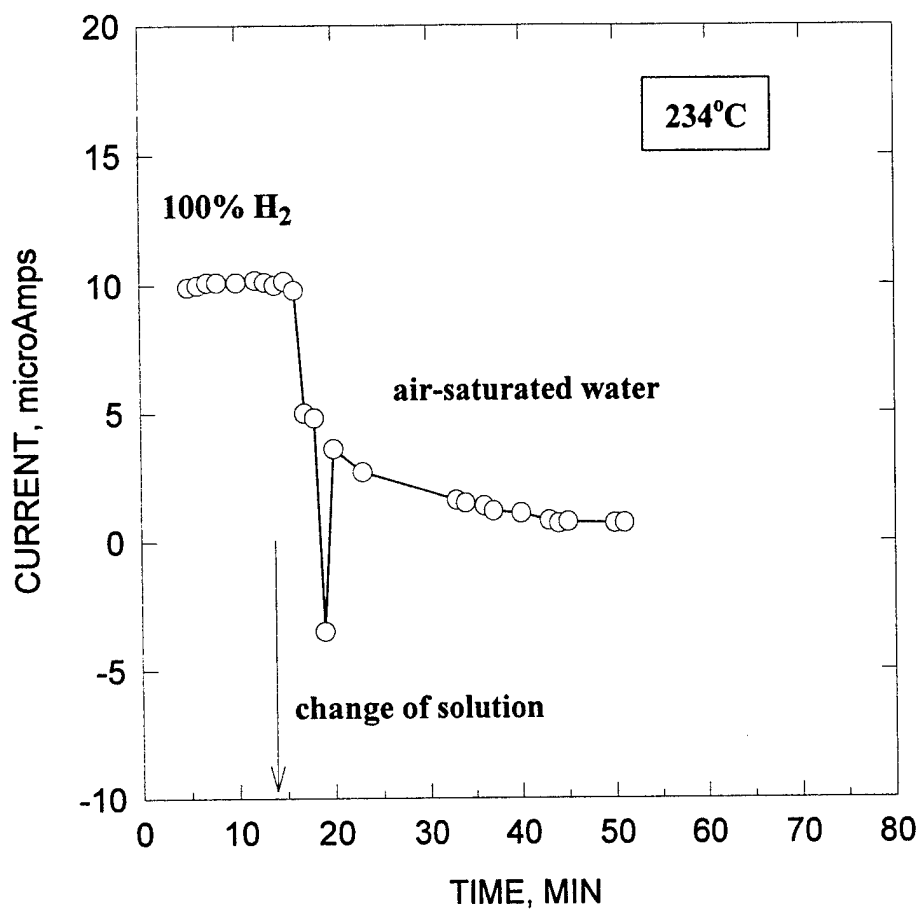
Figure 4-24. Cell current vs. time during change from water saturated with 100% hydrogen to air-saturated water. Time of the solution change at the inlet of the HPLC pump is indicated by the arrow.

We now return to the data shown in Figure 4-22. The correlation between the sensor current and

the concentration of hydrogen can be represented as

$$\log i = \text{constant} + 1/2 \log [H_2\%] \qquad (4)$$

where [H$_2$%] represents the percentage of hydrogen in the sparging gas and i is the current in microamperes. Taking inverse logarithms of both sides shows that the current has the form

$$i = \text{constant}*[H_2]^{1/2} \tag{5}$$

where [H$_2$] is the concentration of hydrogen in the fluid, related to [H$_2$%] through Henry's law. It is reasonable to assume that the PTFE becomes rapidly saturated with hydrogen, in which case the concentration of hydrogen at the surface of the platinum anode should also be proportional to [H$_2$]. Accordingly, the empirically established relationship between the current and [H$_2$] [i.e., Equation (5)] would seem to be consistent with the notion that the rate determining step at the anode (which is assumed to control the current) is the oxidation of adsorbed atomic hydrogen that is produced by the dissociation of molecular hydrogen on the surface of platinum. Thus, we envisage a mechanism that includes three pre-equilibrium steps and one rate-determining step (RDS), and which occurs at the anode, as follows

$$\overset{K\ 1}{H_2(\text{solution}) \Leftrightarrow H_2(\text{PTFE})} \tag{6}$$

$$\overset{K2}{H_2(\text{PTFE}) \Leftrightarrow H_2(\text{Pt})} \tag{7}$$

$$\overset{K3}{H_2(\text{Pt}) \Leftrightarrow 2H_{ads}} \tag{8}$$

$$\overset{k4}{H_{ads} \Rightarrow H^+(\text{solid electrolyte}) + e^-} \quad \text{(RDS)} \tag{9}$$
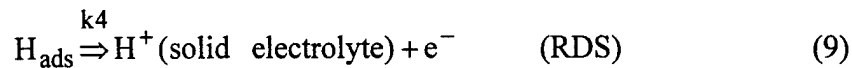
For the equilibrium Reactions (6)-(8) and for the rate-determining Reaction (9), we write:

$$[H_2(\text{PTFE})] = K_1[H_2] \tag{10}$$

$$[H_2(\text{Pt})] = K_2[H_2(\text{PTFE})] \tag{11}$$

$$[H_{ads}] = \sqrt{K_3[H_2(\text{Pt})]} \tag{12}$$

$$i = k_4[H_{ads}] \tag{13}$$

Substituting Equations (10)-(12) into (13) we obtain:

$$i = k_4[H_{ads}] = k_4\sqrt{K_3[H_2(Pt)]} = k_4\sqrt{K_3K_2[H_2(PTFE)]} = k_4\sqrt{K_3K_2K_1[H_2]} \tag{14}$$

or

$$i = constant*[H_2]^{1/2} \tag{15}$$

which has the same form as the experimental correlation Equation (5).

Higher sensitivity might be achieved by operating in the region of the limiting current for the oxidation of H_2, where the current is proportional to the concentration and not to the square of the concentration of the reacting species, in the aqueous phase. Thus, the majority of gas sensors of this type that are available commercially (e.g., Clark cell oxygen sensors) operate in the diffusion-limited current regime. We note, however, that if the kinetics of the oxidation reaction are slow, it is difficult to achieve a mass-transfer limited current, especially at elevated temperatures, where diffusion is rather fast. We made measurements at higher cell potentials, in an attempt to operate the sensor in the diffusion-controlled mode. The measurements, however, indicated, that at higher potentials the sensor did not respond to changes in the hydrogen concentration. The major problem with measurements at higher potentials, in systems that employ both solid or liquid electrolytes, is the occurrence of interfering reactions. In the case of anodic processes, we can envisage the following interfering reactions: (i) electrolyte decomposition through various mechanisms, and/or (ii) anodic electrode dissolution. The first mechanism appears to be the most probable reason for the absence of a response of the sensor at high cell potentials. Additional work is clearly needed to elucidate this point.

For the measurement of hydrogen in SCWO systems, it is necessary to monitor hydrogen in water at somewhat higher temperatures (300-550°C), where PTFE cannot be used. For those applications, we have developed a "pseudo *in situ*" modification of the hydrogen sensor, which is described elsewhere in this report. According to this design, the sensor is located at a somewhat lower temperature, and the monitored solution is continuously exchanged with the bulk solution due to convection induced by the temperature gradient.

4.4.1 Conclusions

In summary, we have developed and tested a sensor for *in situ* monitoring of hydrogen in high temperature/high pressure water. The advantages of this sensor include:

1. The sensor is relatively simple and inexpensive;

2. No reference electrode is required;

3. No complicated electronic equipment is necessary;

4. The sensor displays a relatively fast response time;

5. The sensor provides for *in situ* or "pseudo *in situ*" operation;

6. The PTFE membrane enables the use of the sensor in practically any aggressive environment; and

7. The sensor can be used in steam as well as in water.

SECTION 5

OXYGEN SENSOR

5.1 OXYGEN RESPONSE OF YTTRIA-STABILIZED ZIRCONIA SENSORS IN GASEOUS AND AQUEOUS SYSTEMS

5.1.1 Abstract

A simple zirconia sensor equipped with Ag powder electrodes was fabricated, and the response to oxygen in gaseous and aqueous environments was examined at temperatures over the range of 200°C to 330°C. The sensor showed a fast, Nernstian response to changes in oxygen partial pressure in gaseous systems. In aqueous systems at 300°C, the sensor also responded to changes in the dissolved oxygen concentration in a Nernstian manner.

5.1.2 Introduction

Oxygen sensors based on yttria-stabilized-zirconia (YSZ) solid electrolytes have been well developed and widely applied to the measurement of oxygen activity in gas mixtures and metals above 600°C. The YSZ oxygen sensors are also potentially applicable to the measurement of dissolved oxygen in high temperature aqueous systems, but to our knowledge they have never been developed for this purpose, although they have been used to measure oxygen in steam.[1] The lack of success in the use of these sensors for measuring oxygen concentration in aqueous systems is due to the fact that conventional YSZ oxygen sensors equipped with painted porous Pt electrodes show a slow response, and exhibit significant deviations from ideal Nernstian behavior, at temperatures below 450°C. Recently, the use of several types of oxide electrodes has succeeded in lowering the temperature of operation down to 300°C,[2-4] and the lowest reported temperature of 183°C was realized by using $Bi_3Ru_3O_{11}$ electrodes subject to chemical gaseous pre-treatments.[5] Some of these studies suggest that the

5-2

electrode microstructure, as well as the electrocatalytic activity of the electrode materials, plays an important role in determining the low temperature performance.[2-4] Even for the same electrode materials, a decrease in the firing temperature after painting improves the oxygen response of the electrodes at low temperatures. Thus, electrodes having a fine grain size have large surface areas available for oxygen exchange reactions at the gas-electrode-electrolyte interface. From such a microstructual point of view, purely powder-like electrodes seem to be the most suitable. Kaneko et al.[6] showed that Ag electrodes made by painting and firing at 500°C provided for a Nernstian response at temperatures as low as 347°C. Danielson et al.[7] used Ag powder as the internal reference electrode in a YSZ pH sensor, and suggested that the Ag powder electrode, which was seasoned initially at 300°C before use, worked as a reversible oxygen electrode even at temperatures lower than 200°C.

In this study, we have fabricated YSZ sensors equipped with Ag powder electrodes and have examined their performance for measuring oxygen in gas mixtures over the temperature range of 200 to 330°C. A preliminary examination of the use of the sensor for measuring dissolved oxygen in water at 300°C is also reported.

5.1.3 Experimental

Two types of sensors, A and B, having different structures of the internal reference electrode, were fabricated from YSZ tubes that were closed at one end (9%Y$_2$O$_3$, Coors Ceramics Co.). The tubes were 6.35 mm in diameter, 0.76 mm in wall thickness, and 101.6 or 152.4 mm in length. Silver powder (99.9%, 100 mesh, Alpha-Johnson Matthey) was used for both the internal reference and working electrodes. As shown in Figure 5-1, the reference electrode in the Type A
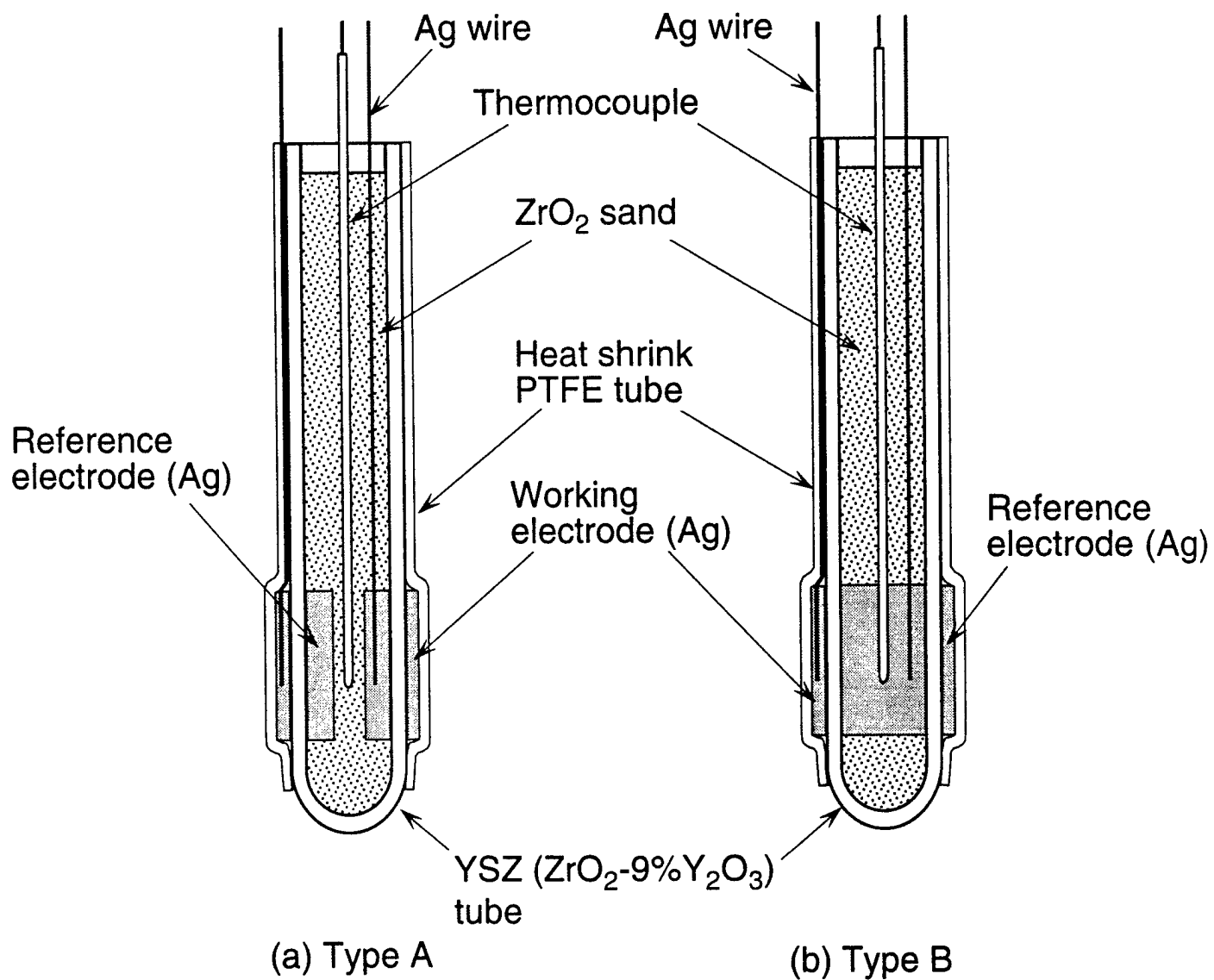
Figure 5-1.   Schematic of YSZ oxygen sensor with Ag powder electrodes.

sensor was in the form of cylinder attached to the inner wall of the tube. This reference electrode was constructed by the following method. The space, in which the Ag powder is located, was formed by using ZrO_2 sand and a PTFE rod. After filling about 5 mm of the space with Ag powder and the remaining space with ZrO_2 sand, the tube was heated at 340°C for 30s. This resulted in an adherent Ag powder electrode attached to the inner wall of the tube after the removal of the ZrO_2 sand and the PTFE rod. A thermocouple was placed at an appropriate position and the tube was filled with ZrO_2 sand to ensure contact of the reference electrode and the thermocouple. In the Type B sensor, the active region corresponding to the outer working electrode was filled with Ag powder. The working electrode was made by first filling the space between the YSZ tube and a heat shrinkable PTFE tube with Ag powder and then heating at 340°C for 30s. The thickness of the working electrode was about 0.3 mm. Ag wires were embedded in both the working and reference electrodes to make electrical contact.

The newly-fabricated sensors were heated at 300°C in air for more than 3h prior to testing. The oxygen response was then examined over the temperature range of 200°C to 330°C, with oxygen-argon mixtures (0.1 to 100%O_2) being used to control the oxygen partial pressure. The flow rate was adjusted to 100 sccm to maintain the total pressure of the test cell at 101.3kPa. The electromotive force (EMF) of the sensor was measured using a Keithley 617 electrometer having an input impedance of 2×10^{14} Ω. The measurement of EMF was made with respect to the internal Ag reference electrode exposed to air. Thus, the theoretical EMF values are given by the Nernst equation,

$$EMF = (RT / 4F)\ln(P_{O_2} / 0.21) \qquad (1)$$

The experiments in high temperature water were performed in a once-through flow system activated by a high pressure liquid chromatography pump. In these experiments, the sensor was covered with a PTFE sheath of 1mm thickness and was introduced into the high temperature/high pressure environment using a standard Conax fitting with a PTFE sealant.

5.1.4 Results and Discussion

Figure 5-2 shows a typical response curve for the Type A sensor (No.) at 250°C. This sensor had the same electrode structure as shown in Figure 5-1. Fast and reversible responses to changes in oxygen partial pressure were observed: the time required to obtain 90% of the total EMF variation was about 60s, and the steady state EMF was attained within 5 minutes after increasing the oxygen partial pressure. Although a longer time is required to reach the steady state when the oxygen pressure decreases than when P_{O_2} increases, the steady state value of EMF at a given oxygen pressure is independent of the direction of the oxygen pressure change.

The steady state EMF values obtained from Figure 5-2 are plotted in Figure 5-3 as a function of oxygen pressure, P_{O_2}. The dashed line indicates the theoretical values calculated from Equation (1). The experimental EMF increases linearly with increasing logarithm of P_{O_2}, over the range of P_{O_2} =0.1013 to 101.3 kPa. The slope of the experimental EMF vs. $\log P_{O_2}$ plot, 26.1mV/decade, agrees well with the theoretical value, 25.95 mV/decade. There is only a slight shift of the experimental plot from the theoretical line (about 1.5mV).

The same experiments, as described above, were carried out at temperatures ranging from 200°C to 330°C. The response was reversible, even at temperatures as low as 200°C, while the response rate became slow at low temperatures as shown in Figure 5-4, where the 90% response
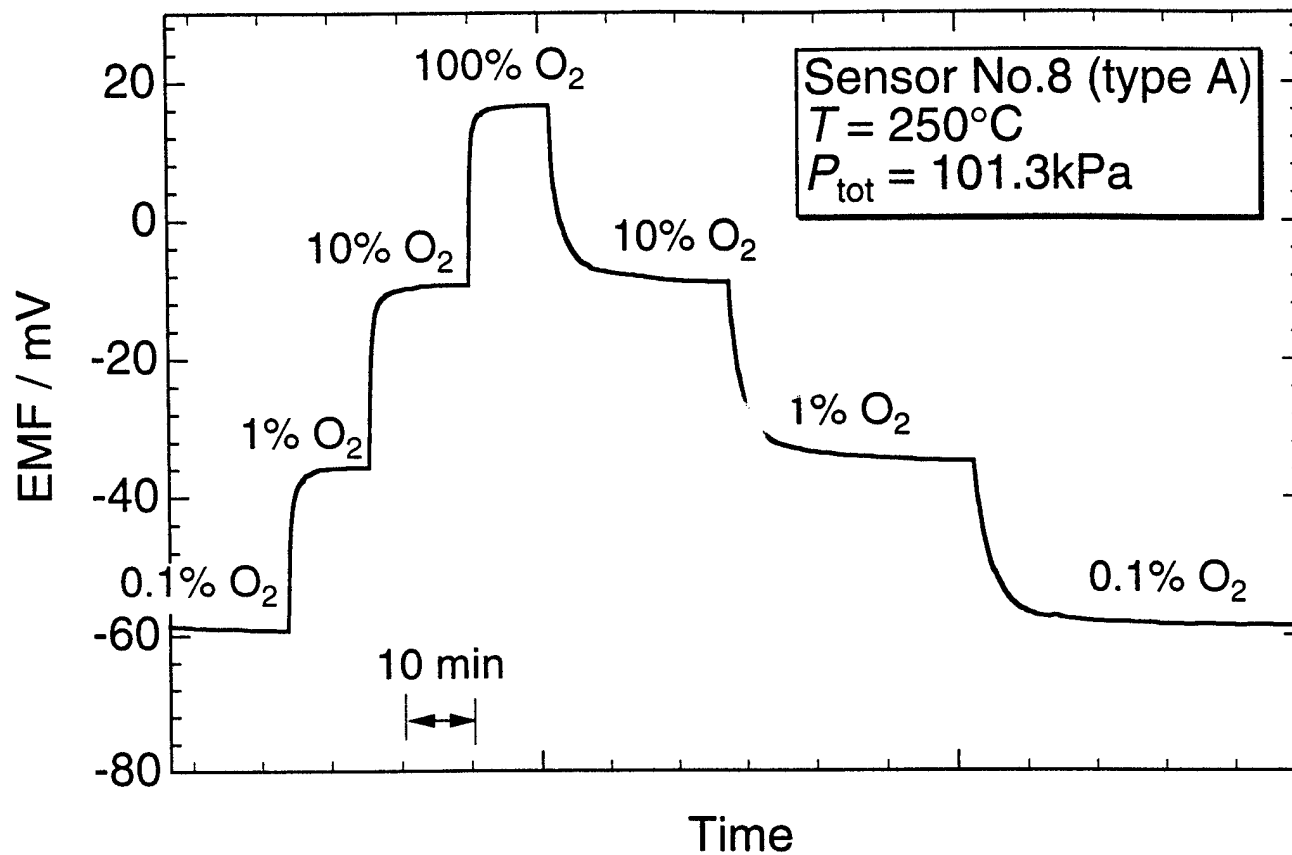
Figure 5-2. Response of the YSZ sensor to changes in composition of O_2-Ar mixtures at 250°C and at a total pressure of 101.3kPa.
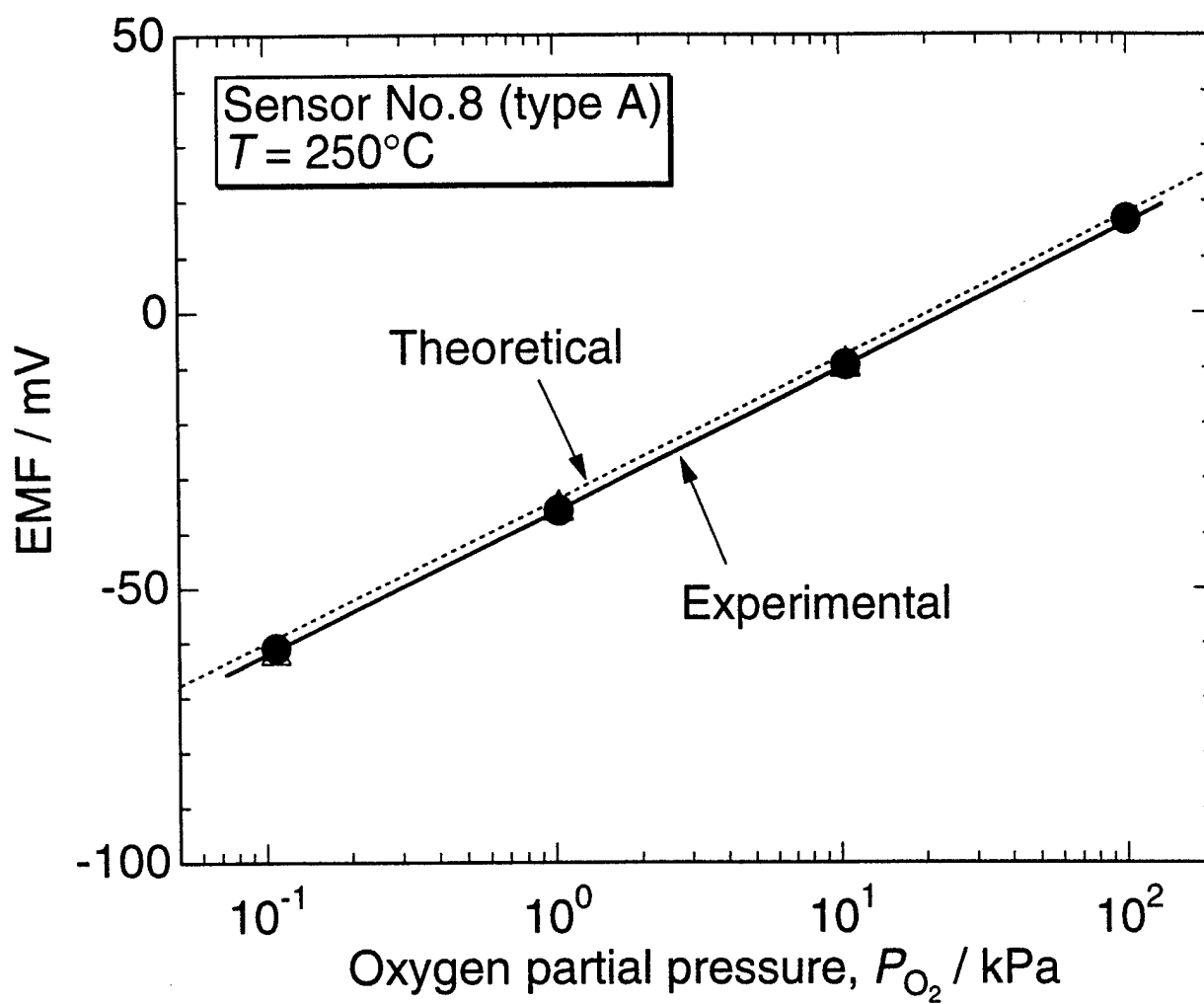
Figure 5-3. Change in EMF as a function of oxygen partial pressure, P_{O_2}, at 250°C.
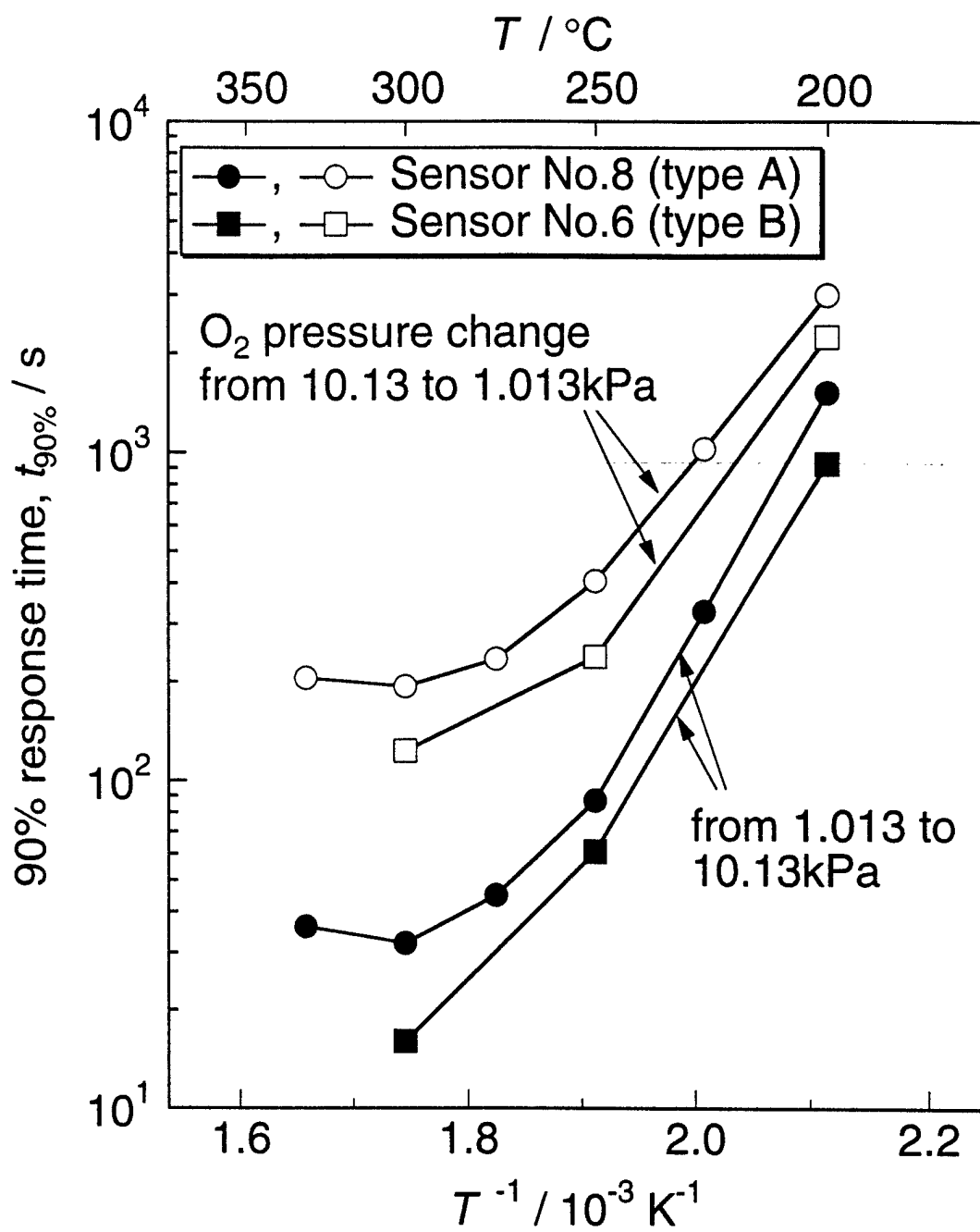
Figure 5-4. Changes in the 90% response time, $t_{90\%}$, as a function of inverse temperature, $1/T$.

time, $t_{90\%}$, for changes in oxygen pressure from 1.013kPa to 10.13kPa and 10.13kPa to 1.013kPa are plotted as a function of inverse temperature, 1/T. The sensor labeled No. 6 in Figure 5-4 had a reference electrode of Type B. There was no marked difference between the response rates of the two types of sensors.

Linear relationships were observed in EMF vs. $\log P_{O_2}$ plots at all temperatures examined. Figures 5(a) and (b) show the changes in the slopes of the EMF vs. $\log P_{O_2}$ plot and the EMF obtained at an oxygen pressure of 1.013kPa, respectively, as a function of temperature. The dashed lines in these figures indicate the theoretical values calculated from the Equation (1). The experimental slope of the EMF vs. $\log P_{O_2}$ plot is in good agreement with the theoretical value at every temperature. At temperatures above 250°C, the EMF value at a given oxygen pressure falls on the theoretical line, indicating that the sensor works as a potentiometric oxygen sensor. The deviation of the experimental EMF from the theoretical value becomes significant at temperatures below 225°C. Some sensors of Type B showed a more significant deviation at temperatures below 250°C, while the deviation of the EMF at 300°C was always less than 3mV.

The preheat-treatment of the sensor at 300°C was indispensable for obtaining a fast response at temperatures below 250°C. When the sensors were kept at room temperature for a couple of days before testing, and then heated directly at 200°C and 225°C, the steady state EMF was not observed, even after 24 hours.

To examine the applicability of the sensor to the measurement of the dissolved oxygen in high temperature aqueous solutions, EMF measurements were carried out in pure water at 300°C and at a total pressure of 11.7MPa. Figure 5-6 shows the change in EMF as a function of dissolved
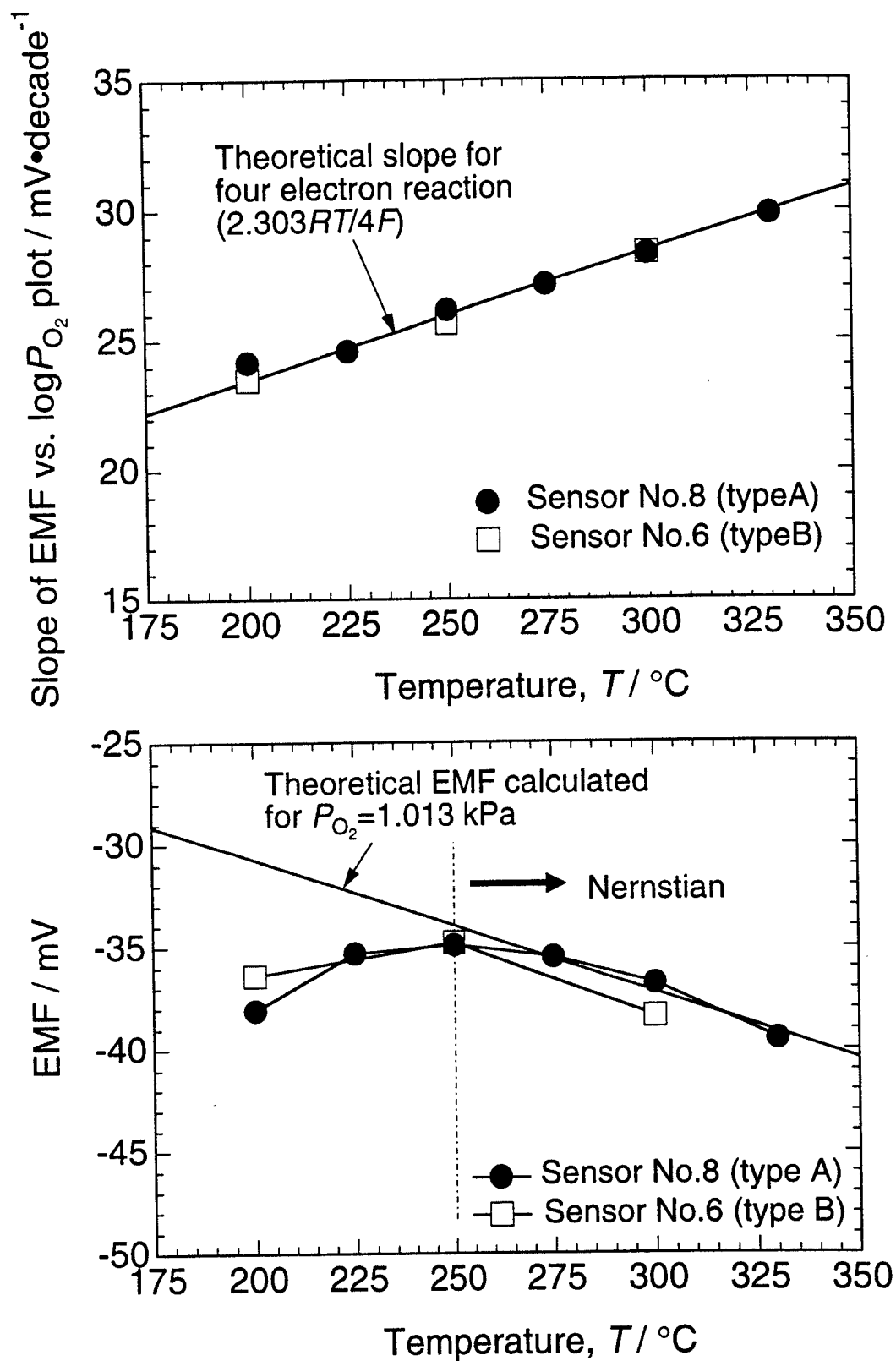
Figure 5-5. Changes in slope of EMF vs. log P_{O_2} plot (a) and EMF value at P_{O_2} =1.013 kPa (b) as a function of temperature, T.
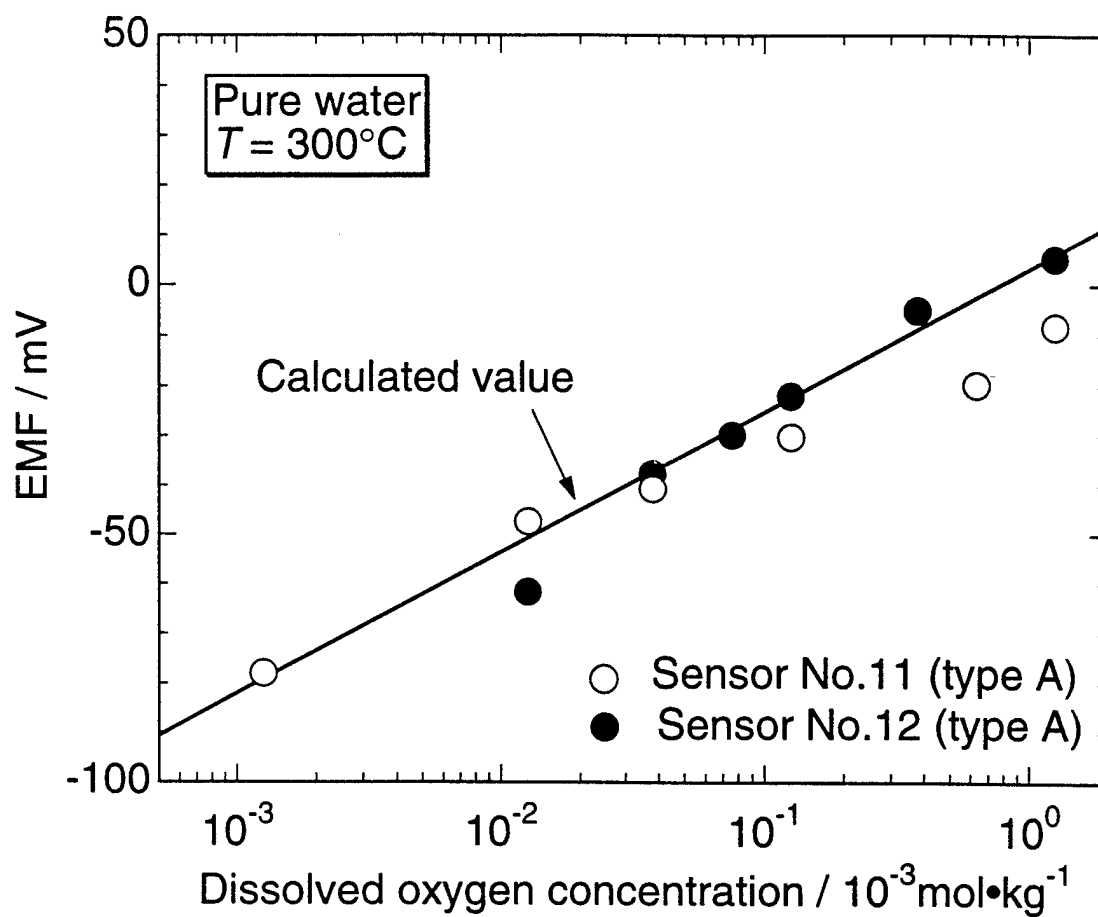
Figure 5-6.   Changes in EMF with dissolved oxygen concentration in water at 300°C.

oxygen concentration, m_{O_2}, in the water. The value of m_{O_2} was estimated from the partial

pressure of oxygen in the solution reservoir at 25°C, $P_{O_2,25}$, using the following equation:

$$m_{O_2} = 0.97 P_{O_2,25} K_{25} \qquad (2)$$

where the coefficient 0.97 is a correction factor for the vapor pressure of water in the reservoir

and K_{25} is Henry's constant for oxygen at 25°C. The solid line in Figure 5-6 indicates the

theoretical values calculated using the effective partial pressure of oxygen at 300°C, $P_{O_2,300}$,

which is given by

$$P_{O_2,300} = 0.97 P_{O_2,25} K_{25} / K_{300} \qquad (3)$$

Henry's constant for oxygen in water at 300°C was estimated using the regression equation

derived by Clever and Han.[8] As shown in Figure 5-6, the EMF values for sensors No. 11 and 12

are very close to the calculated line over the oxygen concentration range of 1.2×10^{-6} to 1.2×10^{-3}

mol/kg. Although a more detailed examination of this sensor is warranted, which should include

modification of the sensor structure to enhance long term stability and reproducibility, the

present results suggest that the YSZ sensor equipped with Ag powder electrodes is a useful solid-

state device for measuring dissolved oxygen in high temperature aqueous solutions.

5.1.5 References

1. D.D. Macdonald, unpublished work (1978-79).
2. S.P.S. Badwal and F.T. Ciacchi, *J. Appl. Electrochem.*, **16**, 28 (1986).
3. S.P.S. Badwal, F.T. Ciacchi, and J.W. Haylock, *J. Appl. Electrochem.*, **18**, 232 (1988).
4. K. Eguchi, T. Inoue, M. Ueda, J. Kamimae, and H. Arai, *Sensors and Actuators B*, **13-14**, 38 (1993).
5. M. Kleitz, T. Iharada, F. Abraham, G. Mairesse, and J. Fouletier, *Sensors and Actuators B*, **13-14**, 27 (1993).
6. H. Kanaeko, H. Taimatsu, Y. Miyoshi, K. Kawanaka, and T. Kusano, *Sensors and Actuators B*, **13-14**, 151 (1993).
7. M.J. Danielson and O.H. Koski, *J. Electrochem. Soc.*, **132**, 296 (1985).
8. H.L. Clever and C.H. Han, "Thermodynamics of Aqueous Systems with Industrial Application", Ed. S.A. Newman, ACS Symposium Series 133, p. 513, Amer. Chem. Soc., Washington, D.C. (1980).

SECTION 6

COMBINATION OXYGEN, HYDROGEN, AND REDOX POTENTIAL SENSORS

6.1. OXYGEN, HYDROGEN, AND REDOX POTENTIAL COMBINATION SENSORS

The monitoring of oxygen and hydrogen, as well as the redox potential in supercritical water and in high subcritical aqueous solutions is important for corrosion prevention and process control in Supercritical Water Oxidation (SCWO) systems. In particular, oxygen excess/deficiency is a most important control parameter in the SCWO process, and *in situ* monitoring of the oxygen level will be required for accurate control of the oxidation process. At the same time, monitoring of hydrogen content, as well, can be important in the SCWO environments. The source of hydrogen in SCWO systems is metallic corrosion, where hydrogen is produced by the reactions:

$$Me + 2\,H^+ = Me^{++} + H_2 \tag{1}$$

and/or

$$Me + 2\,HCl = MeCl_2 + H_2 \tag{2}$$

Even relatively low corrosion rates produce large concentrations of dissolved hydrogen. As an example, the dissolution of 1 gram of iron by mechanisms (1) and/or (2) in 20 kg of supercritical water produces $1/56*22.4/20 = 0.4/20=0.02$ liters H_2/kg H_2O, corresponding approximately to a solution saturated with hydrogen at 1 atm pressure and at room temperature. The redox potential in the solution is strongly affected by the presence of hydrogen and in extreme cases a net oxidation process may convert to a net reduction process. The hydrogen concentration is, as well, indicative of the extent of corrosion in the reactor.

A sensor for measuring oxygen, hydrogen, and redox potential has been developed during the course of this project. This sensor is based on a combination of two electrodes structurally combined into one unit: a yttria-stabilized zirconia (YSZ) membrane pH electrode

and a Pt electrode, which is sensitive to oxygen and hydrogen concentrations and to pH (Figure

6-1). The potential of the YSZ membrane can be represented as

$$E = E^o_{YSZ} - \frac{2.303RT}{F}pH - \frac{2.303RT}{2F}\log a_{H_2O} \qquad (3)$$

where a_{H2O} is the activity of water and E^o_{YSZ} is the standard potential for the internal couple used

in the YSZ membrane. The potential of the platinum electrode in a hydrogenated environment

can be written as

$$E = -\frac{2.303RT}{F}pH - \frac{2.303RT}{2F}\log f_{H_2} \qquad (4)$$

where f_{H_2} is the fugacity of hydrogen.
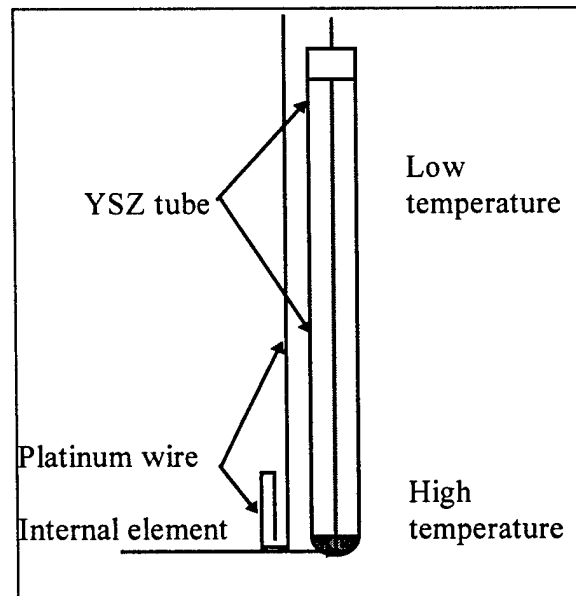
Figure 6-1.   Oxygen, hydrogen, and redox potential combination sensor.

Similarly, the potential of the platinum electrode, when it is working as a reversible oxygen

electrode, can be written as follows:

$$E = E_{OX}^o - \frac{2.303RT}{F}pH - \frac{2.303RT}{4F}\log f_{O_2} - \frac{2.303RT}{2F}\log a_{H_2O} \tag{5}$$

where E_{ox}^o is the standard potential for the O_2/H_2O couple and f_{O_2} is the fugacity of oxygen.

Importantly, both Equations (3), (4), and (5) contain the same dependence of the electrode potential on pH. Hence the potential difference between the YSZ electrode and Pt electrode in both hydrogenated and oxygenated environments will be pH-independent. For a hydrogenated environment, we obtain the potential difference by subtracting Equation (4) from (3):

$$\Delta E = E_{YSZ}^o + \frac{2.303RT}{2F}\log f_{H_2} - \frac{2.303RT}{2F}\log a_{H_2O} \tag{6}$$

From this last equation, it is apparent that we can estimate the hydrogen fugacity in the solution, independently of the solution pH:

$$\log f_{H_2} = 2F(\Delta E - E_{YSZ}^o)/2.303RT + \log a_{H_2O} \tag{7}$$

Likewise, subtracting Equation (5) from Equation (3) we obtain for oxygenated environments:

$$\Delta E = (E_{YSZ}^o - E_{OX}^o) + \frac{2.303RT}{4F}\log f_{O_2} \tag{8}$$

and hence

$$\log f_{O_2} = 4F(\Delta E - E_{YSZ}^o + E_{OX}^o)/2.303RT \tag{9}$$

Because all of the quantities on the right hand sides are known or can be measured, the sensors are primary sensors and, in principle, do not need calibrating. Note that the sensor is the same in both cases. We should emphasize that Equation (7) for hydrogenated environments contains the activity of water, which can be estimated for dilute solutions from the PVT properties of water.

6-4

Another important issue is that both Equations (7) and (9) contain thermodynamic fugacities (activities) of dissolved gases. Fugacity coefficients might significantly differ from unity and, because of this, the practical determination of the concentration of dissolved gas may require precalibration of the sensor in solutions of known gas concentrations.

Experiments were performed at temperatures in excess of 500°C and at pressure of 3500-4000 psi. Several different designs of the sensor were explored. The sensors were found to respond to changes in oxygen and hydrogen concentrations in the solution, as determined by saturating the feed solution with the corresponding gas (Figures 6-2 through 6-6). The response time of the sensor is mostly determined by the solution replacement time in the high temperature/high pressure loop and cell. The time required for the solution of a new concentration to reach the measurement zone determines the sensor response time.
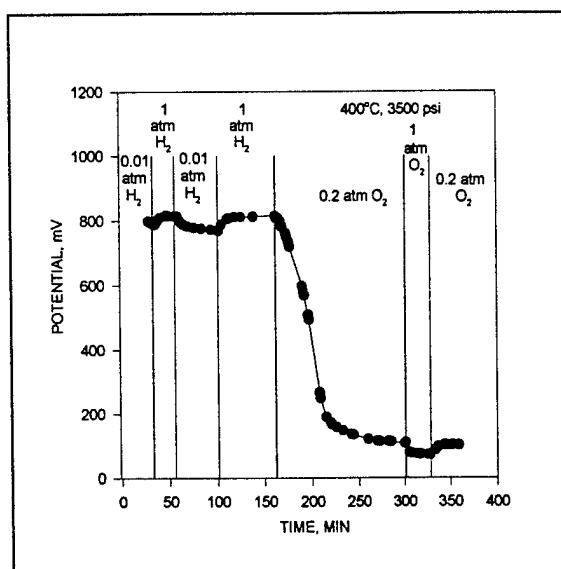
Figure 6-2.   Response of the sensor to change in oxygen and hydrogen concentrations at 400°C in the solution of 0.002 m NaOH.
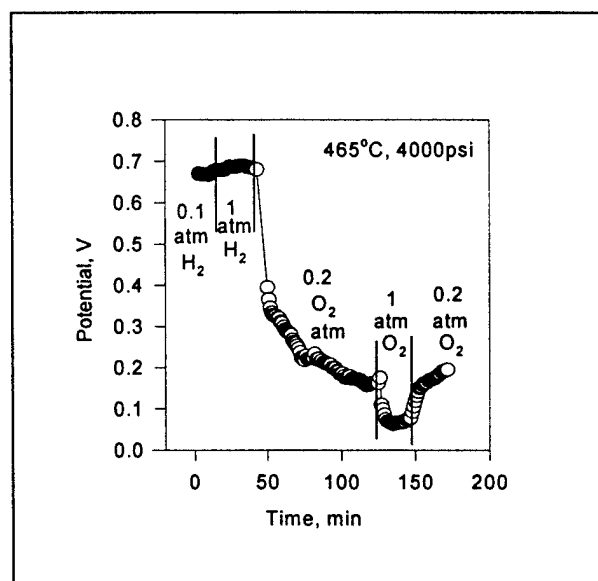
Figure 6-3.   Response of the sensor to change in oxygen and hydrogen concentrations at
465°C in the solution of 0.002 m NaOH.
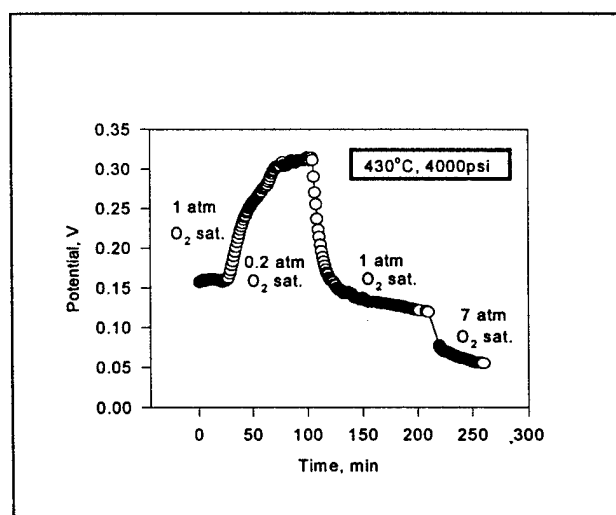
Figure 6-4.   Response of the sensor to changes in oxygen concentration in 0.002 m NaOH at
430°C.
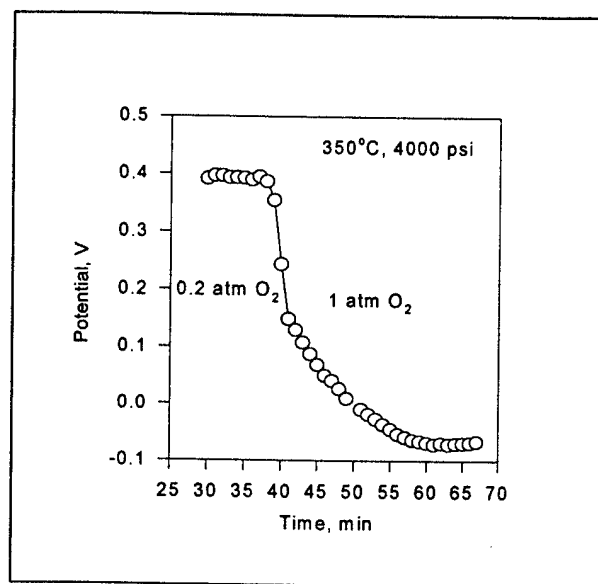
Figure 6-5.   Response of the sensor to changes in oxygen concentration in 0.002 m NaOH at 350°C.
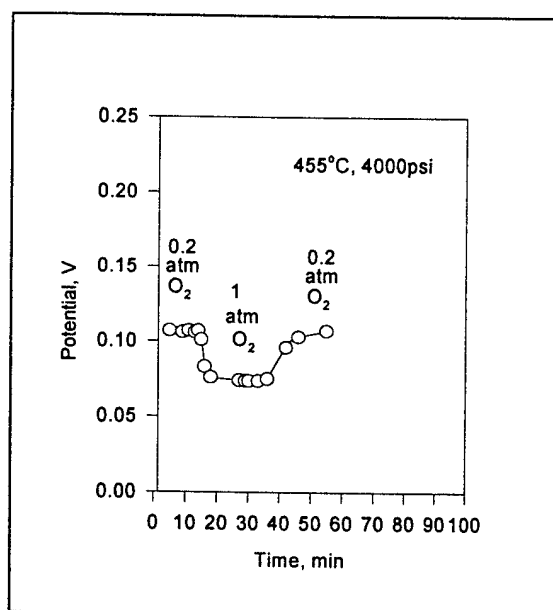
Figure 6-6.   Response of the sensor to changes in oxygen concentration in 0.002 m NaOH at 455°C.

From Figures 6-2 through 6-6, it is apparent that the sensor responds rapidly to changes in the oxygen and hydrogen concentrations and, correspondingly, to the redox potential in the solution. Additional measurements are necessary in order to establish a calibration function $E=f(P, T, C_{OX}, C_{H2})$, but because the sensor is a non-equilibrium sensor a calibration (in principle) should be determined for each system.

In Figure 6-7 we show the potential of the sensor measured in a stainless steel cell at a low pH, which was established by the addition of HCl. Due to the considerable corrosion of the cell, according to Reactions (1) and (2), a high hydrogen concentration was established in the solution. As one can see from the Figure 6-7, the sensor did indeed indicate the presence of a large amount of hydrogen (potential above 0.9 V) and did not respond to the change of the solution from oxygen-saturated to argon-saturated. Thus, when the sensor is used as an oxygen sensor, hydrogen must be considered to be a strongly interfering species. Even in the presence of hydrogen, however, the sensor operates as a redox sensor, thus providing information on the redox conditions in the reactor.
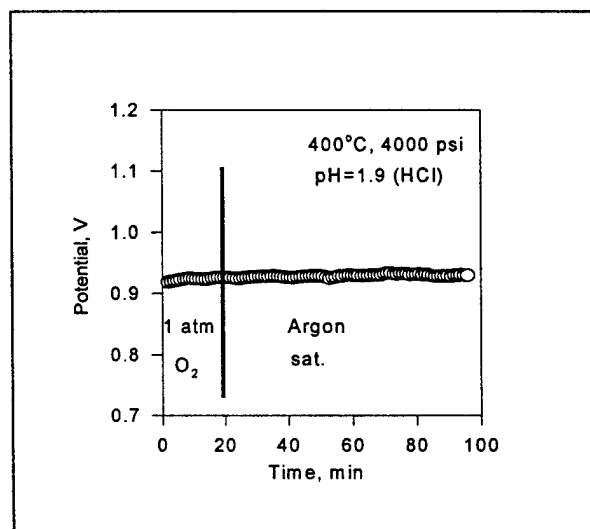
Figure 6-7.   Response of the sensor to changes in oxygen concentration at 400°C in a HCl solution of pH=1.9.

We also tested a modification of this sensor, in which the yttria-stabilized zirconia tube was replaced by a tungsten/tungsten oxide electrode. Elsewhere we have shown that this electrode is pH-sensitive, and is practically insensitive to oxygen and hydrogen. In Figure 6-8, we present preliminary data on the response of this sensor to the changes in the gas concentration in the solution. This tungsten/tungsten oxide-platinum combination sensor clearly responds to changes in the redox conditions in the solution.
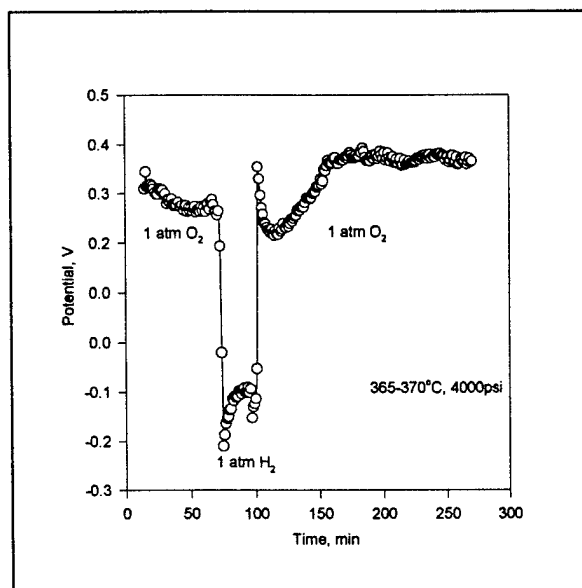
Figure 6-8.   Response of the tungsten/tungsten oxide - platinum combination sensor to changes in oxygen and hydrogen concentrations in pure water at 365-370°C.

The major advantages of the combination sensors described here include: (i) Absence of a traditional reference electrode (such as a Ag/AgCl external pressure-balanced reference electrode); (ii) the possibility of employing the sensor up to very high temperatures (YSZ membranes are routinely used in fuel cells and oxygen sensor applications at temperatures in excess of 700°C in the gas phase); (iii) the fact that this is a universal oxygen, hydrogen, and redox combination sensor, autocorrected for the pH of the solution; and (iv) the sensor is very

resistant to corrosion (YSZ and Pt are probably the most corrosion resistant materials for use in high subcritical and supercritical aqueous solutions).

Applications of the sensor include monitoring oxygen and hydrogen concentration, and redox potential, in SCWO systems, as well as for monitoring the chemistry of the heat transport fluid (water) in supercritical thermal power plants. Because the sensor contains an independent pH-sensitive electrode, it can be used, as well, in conjunction with a suitable reference electrode, for simultaneous pH monitoring. If the value of pH in the system is kept constant, the YSZ membrane electrode of the sensor could also be utilized as a reference electrode in order to monitor corrosion potentials of structural components.

We believe that building an optimized sensor of this type for testing in pilot plant or in industrial applications would be of tremendous value for on-line process monitoring and for improving our understanding of the reactions that occur in SCWO reactors.

SECTION 7

DEVELOPMENT OF pH AND REFERENCE ELECTRODES

7.1. DEVELOPMENT OF REFERENCE AND pH ELECTRODES FOR USE IN SUPERCRITICAL WATER

7.1.1 Introduction

7.1.1.1 pH Electrodes

Any pH electrode intended for use in SCWO systems must obviously endure very high temperatures and pressures, and must not degrade chemically or thermally. The chemistry of the waste streams could vary significantly, so a response to a wide range of pH is desired. This response must not be adversely affected by redox species in the solution (most notably here, oxygen). Preferably, the sensor should be a primary electrode. That is, its overall electrochemical potential should be dependent upon completely thermodynamic arguments only. Otherwise, the electrode would require calibration, and current buffer solutions with known pH for this task are limited to roughly 275°C.[1]

In the search for a viable pH sensor, many candidate electrodes may be disregarded on the basis of the above criteria. Fiber optic pH sensors have only been tested at room temperature, and even then respond to a limited range of pH.[2,3] The change in the capacitance of semiconducting materials to solution pH has been investigated by Hara and Sugimoto.[4] The Nb-doped TiO_2 electrode displayed a completely Nernstian behavior in a wide range of pH only to 250°C. The electrode apparently suffered interference from redox species K^+ and Na^+. Palladium-hydride electrodes[5] rely upon the difference in the chemical potential of hydrogen in solution with that in the $\alpha+\beta$ phase of palladium. However, the formation of this phase is thermodynamically impossible above 300°C.

Metal/ metal-oxide electrodes such as Hg/HgO and Ag/Ag$_2$O in direct contact with the solution respond to pH via reactions involving the metal and its sparingly soluble oxide (or hydroxide).[1] Excessive solubility, however, limits the lifetime of the electrode and would likely be a problem in the SCWO environment. Both Hg/HgO and Ag/Ag$_2$O are also susceptible to interference from halides. Tungsten-tungsten oxide electrodes have shown distinct promise up to 300°C[6] and provide reasonably reproducible responses to changes in pH up to 600°C.[7] Unfortunately, the potential-determining reaction in either case could not be unequivocally resolved; hence, the sensor is not a primary electrode. The calibration of glass electrodes in buffer solutions is accurate only for a limited range of pH and temperature outside that of the buffer itself.

The platinum-hydrogen electrode and the Yttria Stabilized Zirconia (YSZ) membrane pH electrodes are primary electrodes with no need for extra-thermodynamic calibrations.[8] Briefly, the potential of a platinum wire in an aqueous solution containing hydrogen is governed by the Hydrogen Electrode Reaction (HER)

$$H^+ + e^- \Leftrightarrow \frac{1}{2}H_2 \tag{1}$$

with a potential that is dependent upon pH and hydrogen fugacity (f_{H2}) being given by

$$E = E^\circ_{H^+/H_2} - \frac{2.303RT}{F}\log f_{H_2}^{1/2} - \frac{2.303RT}{F}pH \tag{2}$$

where the first term is the standard potential of Reaction (1), R is the universal gas constant, T is absolute temperature, and F is Faraday's constant. If one can then determine hydrogen fugacity through experiment or calculation, the potential is strictly a function of pH. It is important to note that the presence of oxidizing agents in actual SCWO environments precludes the HER as the

dominant redox reaction at the Pt wire. However, experimental conditions in this research were imposed such that this electrode still provides an invaluable electrochemical reference point.

The YSZ membrane pH sensor, first introduced by Niedrach,[9] demonstrated better than 90% Nernstian behavior in aqueous solutions with pH between 3 to 8 at 285°C. Essentially, the reference material (in this case Cu/Cu$_2$O paste) is in equilibrium with the inner surface of the YSZ membrane. Likewise, there exists an equilibrium between the solution pH and the outer surface. The two reactions are electrochemically connected via oxygen vacancies in the membrane. Therefore, pH shifts in the solution cause a change in the potential of the overall electrode which may be measured against a known reference point.

The YSZ membrane pH sensor has been used to very high subcritical temperatures, and even briefly to 380°C.[10] Internal pastes such as Ag and graphite (in the presence of oxygen), and Cu/Cu$_2$O have been studied.[11] Hettiarachchi et al.[12] later found that the Cu/Cu$_2$O and Ag/Ag$_2$O internal pastes each degraded with time at 275°C (to CuO and Ag, respectively), prompting them to explore the Hg/HgO couple. It has proven to be an excellent alternative, thermodynamically speaking.[10,13] Tsuruta and Macdonald have shown that the sensor exhibits a Nernstian response at temperatures only above 200°C, and that there is somewhat of an "acid error" for pH levels below 4 in borate buffer solutions.[14] The acid error was possibly due to the presence of SiO$_2$ in the tubes, used by the specific supplier as a sintering agent. Hettiarachchi et al.[14] found no adverse effects from redox species, such as oxygen or hydrogen gas, and from chloride or sulfide ions, nor was the pressure of the electrolyte (up to 1000 psi tested) a factor. For these reasons, the YSZ membrane electrode with a Hg/HgO internal paste was considered the best choice for this research.

7.1.1.2 Reference Electrodes

There are several choices for reference electrode designs, though all should meet several key requirements. Its potential should be stable and reproducible with changes in pressure or temperature, insensitive to the presence of redox species or poisons, and to changes of solution pH. Ideally, the potential should provide a reasonable connection to a thermodynamic scale, either by calculation or calibration. Reference electrodes generally fall into two categories: internal and external. With internal electrodes, the electroactive element is maintained at the same temperature and pressure as the test solution. It may be directly immersed in the test electrolyte or contained in a separate solution compartment of known composition, with electrochemical connection then provided via a junction permeable to the solution ions.

An example of an internal electrode, which has proven useful at high temperatures, is described below.[15] The electrode potential is set by the equilibrium between the element material (AgCl) and the reference solution (usually HCl or KCl). There is also a perturbation in the potential of the electrode arising from the diffusion of ions across the junction (porous Zirconia frit in this case). This is referred to as the Isothermal Liquid Junction Potential,[16] or E_{ILJ}. It is important to note here that it is a function of the temperature of the junction, as well as the activity and mobilities of all ions involved in the junction. Internal references of this kind are not generally used for very high temperature applications, since most reference elements undergo some degree of hydrolysis at high temperatures.[17] Also, hydrogen ingress into the bridge may reduce the AgCl to HCl, inducing drift in the electrode.[15] From Equation (2), the platinum wire may be used as a reference electrode provided one knows the pH of the solution (thus the electrode is not strictly a reference), as well as the hydrogen fugacity. Furthermore, one must be

careful to exclude organic materials and redox species in solution (such as oxygen, Fe^{3+}, or CrO_4^{2-}), since they will poison the electrode. In aqueous solutions which meet these criteria, the platinum/ hydrogen electrode is still considered to be one of the best thermodynamic reference points.[18]

External electrodes overcome the problem of hydrolysis by locating the element remote to the heated portion of the apparatus. Electrochemical connection to the test solution is then made via a non-isothermal bridge. The most well-developed form of this electrode is the External Pressure-Balanced Reference Electrode (EPBRE), wherein the electroactive element is at the same pressure as the test solution.[15] In addition to the E_{ILJ} effect, there is a potential formed due to the thermal gradient along the bridge solution, referred to as the Thermal Liquid Junction, or E_{TLJ}.[19,20] Generally, when the autoclave is heated, the concentration of the electrolyte in the hot region will be lower than that in the cooler portion of the bridge. Mass transfer tends to occur towards the cold end due to irreversible thermodynamic processes. With time, the system approaches a steady state in which there is a balance between the forces that tend to establish and dissipate the concentration gradient. This is known as the Soret steady state.[21] It is important to note that the rate at which steady state is attained is a complex function of mobility and entropy of transport for various ions, and convective heat flow characteristics of the salt bridge. The steady state may not be achieved for a very long time, and may be a substantial portion of the overall cell voltage.

7.1.2 Experimental Approach and Apparatus

7.1.2.1 YSZ Membrane pH Sensor

The YSZ tubes provided by Coors Ceramics Company (ZDY-4, nominal 9 w% Y_2O_3) were six inches long with an outer diameter of 0.25" and a 0.035" wall thickness. The rounded end of the tube was pre-conditioned by filling two inches of the inside with hydrofluoric acid (Baker reagent 48%-51%), then immersing a similar length of the outer portion of the tube in boiling acid for ten minutes. This served to increase the effective surface area of the membrane for contact with the internal paste material.

The Hg/HgO paste was prepared by combining a 50:50 volume ratio of reagent grade HgO and 99.9% Hg in a mortar and pestle until a paste of consistent texture was obtained. The rounded YSZ tip was filled with approximately ¼" of the paste. An ASTM grade 304 stainless steel wire provided electrical contact. One end was sanded and coiled to increase its effective surface area, then inserted into the paste. This wire was insulated with continuous heat shrink Teflon, extending from very near the open end of the YSZ tube to approximately two inches inside. The remainder of the tube, except for ¼", was back filled with fine (-325 mesh) ZrO_2 sand. The electrode was lightly tapped while adding this powder to ensure tight packing. Finally, the open end was filled with "J.B. Weld"™ epoxy to both seal the electrode and to provide some amount of mechanical support to the ceramic. The latter consideration was important for successful use in the CONAX compression fitting. The fitting was cooled via a copper tubing water jacket.

7.1.2.2 External Pressure-Balanced Reference Electrode (EPBRE)

The high-temperature region of the External Pressure-balanced Reference Electrode was made from a five inch piece of 1/4" OD, 0.035" wall 99.2% zirconium tubing (ASTM grade B-523). One end was pinched to a slit approximately 0.5 mm wide. To make the tubing electrically insulating, it was initially heated in a Bunsen burner while purging the inside with a constant flow of pure oxygen gas. This created a black oxide. The tube was then placed into an ambient atmosphere furnace at 700°C for seven hours. This produced an even, yellow-white oxide film.

The oxidized zirconium tube was then filled with coarse (150 mesh) ZrO_2 sand to minimize diffusion of solution through the tube. The remainder of the electrode was constructed from heat shrinkable Teflon as shown. This tubing was shrunk first around the oxidized zirconium, then around a solid piece of glass coated in saturated KCl solution. Minute KCl crystals thus formed between the Teflon and the glass. This created a frit between the test and reference solutions, sufficiently "loose" to allow ionic contact between the reference and test solutions, while allowing minimal diffusion. The Teflon tube was then filled with saturated KCl solution. Fine ZrO_2 powder was added to the majority of the reference solution chamber to reduce diffusion of KCl.

The Ag/AgCl element was prepared by sintering silver powder onto the tip of a 0.5 mm silver wire (both 99.9% pure) using a Bunsen burner. AgCl crystals (99.9% pure) were then similarly sintered onto the Ag tip until a purple/ brown color. The element was then lightly electrolyzed in HCl acid. The potentials of elements thus constructed were checked against a Saturated Calomel Electrode (SCE) and found to be within ± 2mV of the theoretical value of -0.045V_{SCE}. The silver wire was wrapped with shrink Teflon to prevent shunting to the autoclave

body. Extension of the Teflon walls of the reference solution chamber to a point outside the CONAX fitting also helped to prevent shunting of the electrode in the event of leaks. The necessary pressure seal was achieved by pinching the Ag/AgCl assembly, a Teflon gasket, and the Teflon reference chamber in a CONAX fitting. This area of the reference chamber was cooled with a copper tubing water jacket soldered to the fitting. Once constructed, the Ag/AgCl element was eight inches from the center of the autoclave, while the glass frit was positioned five inches from the same point.

7.1.2.3 Redox/Reversible Hydrogen Electrode

The redox electrode is a 0.5 mm diameter platinum wire (99.99% pure). The end of the electrode in contact with the high temperature test fluid was coiled and then lightly platinized by cathodic polarization in a solution of hexachloroplatinic acid. This produced the typical "Pt-black" film on the coil. The remainder of the electrode was insulated from the autoclave body with either high purity alumina tubing in the relatively hot regions (with an ID comparable to the wire diameter), or by heat shrink Teflon in the cooler portions of the autoclave. As with the EPBRE, a tight Teflon sleeve placed over the cool end of the wire was pinched by a high-pressure CONAX fitting. The wire outside the autoclave was again insulated from the walls by shrink Teflon.

7.1.2.4 Autoclave/Circulation Loop/Solutions

A once-through circulation loop was used for all experiments. Test solutions of 0.1m, 0.01m and 0.001m NaOH were prepared by diluting an appropriate stock solution of reagent

grade 1.0N NaOH with Millipore water (18.2 MΩ-cm). Solutions were loaded into a four liter Nalgene reservoir and purged with pure H_2 gas for at least two days prior to use. Gas purging continued throughout the duration of the test. A High Pressure Liquid Chromatography (HPLC) pump provided circulation of the solution at 140 ml/hr, while system pressure was sustained at a constant 275 bar (~4000 psi) via a back pressure regulator. Pressure was monitored visually using a standard pressure gauge as well as electronically via a pressure transducer connected to the data acquisition system.

Test solutions were preheated by passing through the inner channel of a heat exchanger, from which the solution flowed directly to the autoclave. A commercially available 316 stainless steel Cajon® union cross served as the autoclave. Two overlapping wraps of 313W Omegalux™ tape provided primary heating. The central portion of the autoclave was surrounded in several layers of fibrous alumina insulation. Autoclave "A" had room for only the redox and EPBRE, while "B" was slightly modified to accept the redox, EPBRE, and YSZ electrodes simultaneously. The slight tilt of the autoclaves as pictured was important for cooling the EPBRE seal. Temperature was measured by an Inconel-sheathed K-type thermocouple, and controlled with a Jenco Model 377 thermometer controller. Once through the autoclave, the test solution was utilized on the outer channel of the heat exchanger, cooled in a water-jacket chiller, and finally sent to the spent reservoir.

Tests were conducted with each autoclave design at a constant pressure of 4000 psi (275 bar). Fresh solution was pumped through the autoclave until the potential between the redox and EPBRE attained a steady value (±1 mV, typically). The autoclave was heated in 50°C intervals to a maximum of 450°C, resting at each interval until the electrodes reached apparent steady state

values. In the case of autoclave "B", stability was considered on the basis of the potential between the redox and YSZ pH electrodes. Time to stability was within 10 to 15 minutes for the YSZ electrode relative to the redox, and up to an hour for the EPBRE relative to the redox. The autoclave was then cooled, again stopping at 50°C intervals. Any given solution run was repeated a couple of times to attain some indication of system reproducibility. For brevity, the individual tests will be referred to as either "A#" or "B#", depending on the autoclave arrangement and the numerical order in which the test was conducted.

All potentials were measured using a Keithley 617 Programmable Electrometer, having an input impedance of 200TΩ. Separate inputs were chosen via a Keithley 705 Scanner. All data were collected by the acquisition system over a standard IEEE-488 bus using a Borland Turbo Pascal program written by this author. In addition to measuring potentials between electrodes, the acquisition system monitored the outputs of the temperature controller and the pressure transducer. Regular checks of the resistance between a given electrode and the autoclave, once filled with solution, gave no indications of electrode shunting.

7.1.2.5 Estimation of pH at High Temperature and Pressure

The estimates of expected pH are required to calibrate the EPBRE and to assess a relative accuracy of this system in measuring pH. Such calculations can be made for the dilute NaOH solutions used in this test in the following manner.[22]

The equilibrium composition of a homogenous aqueous solution can be calculated by minimizing the Gibbs energy G

$$G \to \min \sum_j \mu_j n_j \qquad (3)$$

where μ_j is the chemical potential and n_j is the number of moles of the j-th component of the solution including aqueous species (j=i) and water molecules (j=w). The chemical potential μ_j can be presented as

$$\mu_i = \mu_i^0 + RT\ln(m_i\gamma_i) \tag{4}$$

for any dissolved species, and as

$$\mu_w = \mu_w^0 + RT\ln(x_w\gamma_w) \tag{5}$$

for the water molecules. In Equation (4), m_i is the molality of the i-th species, γ_i is its molal activity coefficient, and μ_i^0 its standard chemical potential. In Equation (5), x_w is the mole fraction of water and γ_w is the rational activity coefficient, each of which are considered unity for the dilute solutions used in this study. μ_w^0 is the standard chemical potential of water. While the absolute values for μ_j^0 cannot be derived, one can calculate the Gibbs energy of formation $\Delta_f G_j^0$, which can be used instead of μ_j^0 for minimizing the G function. In this case, Equation (3) may be rewritten as

$$G \rightarrow \min\left[\sum_i n_i \, (\Delta_f G_i^0 + RT\ln(m_i\gamma_i)) + n_w(\Delta_f G_w^0)\right] \tag{6}$$

The Debye-Hückel approach can be applied to calculate the activity coefficients of the ions γ_i in dilute solutions up to approximately 0.1m concentrations:[23]

$$\ln\gamma_i = -\frac{z_i A\sqrt{I}}{1 + aB\sqrt{I}} \tag{7}$$

where z_i is the ion charge, $I = 0.5 \sum_i m_i z_i^2$ is the ionic strength. The terms A, B, and a are the

Debye-Hückel parameters. Values for A and B depend upon the density, temperature, and

dielectric constant of pure water by the following formulations[24]

$$A = \frac{1.8248 \times 10^{-6}}{(\varepsilon\ T)^{3/2}} \rho^{1/2} \quad \text{in} \quad \text{mole}^{-1/2}\ l^{1/2}\ K^{3/2} \tag{8}$$

$$B = \frac{50.29 \times 10^8}{(\varepsilon\ T)^{1/2}} \rho^{1/2} \quad \text{in} \ \text{cm}^{-1}\ \text{mole}^{-1/2}\ l^{1/2}\ K^{1/2} \tag{9}$$

where ε is the dielectric constant, T is the absolute temperature, and ρ is the density in g/cm^3.

Values for the dielectric constant and density of pure water at various temperatures and pressures

are available in the NBS/NRC steam tables.[25] The ion size parameter "a" varies between 0.25 nm

and 1.1 nm in general, and is 0.45 nm for Na^+, 0.35 nm for OH^-, and 0.9 nm for H^+.[26] In these

calculations, a value of 0.45 nm was used for all ions. Considering that B is on the order of 0.3-

0.5 for all conditions of these tests and the ionic strength is at most 0.1, one can see that the

denominator of Equation (7) will not deviate significantly from unity regardless of the specific

ion size parameter chosen.

The minimization procedure, provided by S. Lvov and colleagues,[22] then seeks a

composition of the solution (all m_i) at given values of n_i, $\Delta_f G_i^0$ and γ_i which minimizes G.

There is a paucity of experimental $\Delta_f G_i^0$ data for charged aqueous species in the supercritical

region, but the SUPCRT92 program provided by Johnson, Oelkers, and Helgeson[27] may be

applied to calculate them. The solution pH was then determined from the concentration of H^+

corresponding to the lowest energy configuration of the system. The code algorithms for charged

aqueous species are limited to a water density of at least 0.35g/cm^3 at T $\leq$ 350°C, and to

pressures greater than 500 bar for T $\geq$ 400°C. Under the conditions of this research, then, pH

could be estimated only up to 350°C. Note that γ_i is a function of the composition, and the

minimization is necessarily an iterative procedure.

7.1.3 Important Thermodynamic Relationships

7.1.3.1 Formalisms for Subcritical Conditions

Consider the electrochemical cell consisting of a YSZ membrane pH sensor and a

reference electrode in an aqueous solution as given by Macdonald and co-workers[28]

$$\text{Ref} \mid \text{H}_2\text{O}, \text{H}^+ \mid \text{ZrO}_2(\text{Y}_2\text{O}_3) \mid \text{HgO} / \text{Hg} \tag{10}$$

with a cell potential of

$$E^Y - E^{ref} = E^\circ_{Hg/HgO} - \frac{2.303RT}{2F} \log a_{H_2O} - \frac{2.303RT}{F} \times pH \tag{11}$$

$E^\circ_{Hg/HgO}$ is the temperature-dependent standard potential of the Hg/HgO half cell

$$\text{HgO} + 2\text{H}^+ + 2\text{e}^- \Leftrightarrow \text{Hg} + \text{H}_2\text{O} \tag{12}$$
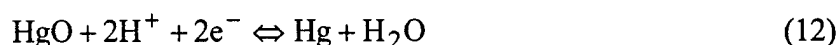
with a dependence upon absolute temperature of

$$E^\circ_{Hg/HgO} = 1.054 - 4.177 \times 10^{-4} T_K + 9.193 \times 10^{-5} T_K \ln\left(\frac{T_K}{298.15}\right)$$
$$+ 3.5 \times 10^{-8} T_K^2 - 1.7996 / T_K \tag{13}$$

E^Y and E^{Ref} are equivalent to E^{YSZ} and E^{EPBRE} in this work, respectively. From the same paper,

the following potential relationship between the Pt-hydrogen electrode and the EPBRE was also

presented

$$E^H - E^{Ref} = -\frac{2.303RT}{2F}\log\left[\left(\frac{K^\circ_{H_2}}{K_{H_2}}\right)\left(\frac{\gamma^\circ_{H_2}}{\gamma_{H_2}}\right)f^\circ_{H_2}\right] - \frac{2.303RT}{F}pH \tag{14}$$

where K is Henry's constant of hydrogen, γ its activity coefficient, and f its fugacity. The superscripts T and ° indicate values at the system temperature and the standard state temperature of 298.15K, respectively. The E^H term is equivalent to the E^{Pt} in this work. It is implicitly stated that, in Equations (11) and (14), the E^{Ref} term contains within it all necessary corrections to the SHE scale, both from thermodynamic (E_{TLJ}) and irreversible origins (E_{TLJ}). Finally, the subtraction of Equation (14) from Equation (11) leaves

$$E^Y - E^H = E^\circ_{Hg/HgO} + \frac{2.303RT}{2F}\log\left[\left(\frac{K^\circ_{H_2}}{K_{H_2}}\right)\left(\frac{\gamma^\circ_{H_2}}{\gamma_{H_2}}\right)\left(\frac{f^\circ_{H_2}}{a_{H_2O}}\right)\right] \tag{15}$$

While the above relationships are derived from an electrochemical cell very similar to the one used in this study, two important modifications were made for use in the supercritical region. First, the concept of Henry's constant used to describe the solubility of hydrogen in liquid water is somewhat awkward when used for $T>T_C$ where water is a fluid with properties varying from "liquid-like" to "gas-like". Secondly, Equation (13) affords no direct method to account for changes in $E^\circ_{Hg/HgO}$ if the mercury liquid undergoes a transition to mercury gas. Such a phase change is thermodynamically feasible above 357°C, and in fact is a practical concern for the sensor used in these tests.

The next section therefore describes a more rigorous treatment of this system, recently presented by Lvov and Macdonald.[29] It will then be demonstrated how the SUPCRT92 code may again be used to provide the necessary thermodynamic treatment for many species of interest;

this includes the formation energy of aqueous hydrogen beyond the critical point, and the effects of the mercury transition on $E_{Hg/HgO}^{\circ}$. The nuances of the EPBRE and YSZ pH sensor potentials are also more directly outlined.

7.1.3.2 Modifications for Supercritical Applications

Lvov and Macdonald[29] consider the cell consisting of the YSZ sensor and the EPBRE

$$|\leftarrow ------ T_1 -----\rightarrow|\leftarrow -----------T_2 ----------\rightarrow|\leftarrow T_1 \rightarrow$$

$$\text{Cu} \mid \text{Ag} \mid \text{AgCl} \mid \text{MCl}_n \text{ (aq)} \mid \text{H}^+\text{(aq)} \mid \text{YSZ} \mid \text{HgO(s)} \mid \text{Ag} \dots \text{Ag} \mid \text{Cu} \qquad (16)$$
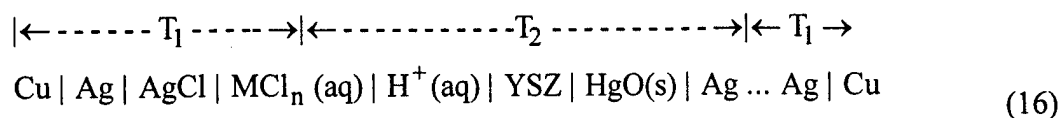
$$\varphi_L \leftarrow ------------ \quad E = \varphi_R - \varphi_L \quad ------------\rightarrow \varphi_R$$

for which they obtain the following potential relationship between the right and left hand electrodes $(E^{YSZ}-E^{EPBRE})$

$$E^{YSZ} - E^{EPBRE} = -\frac{1}{F}\int_{T_2}^{T_1} \bar{S}_{e^-,Ag}\, dT + E_{TLJ} + E_D(T_2) +$$

$$\frac{1}{F}\left(\begin{array}{c} \mu_{H^+}(T_2)+\mu_{Cl^-}(T_1)-\frac{1}{2}\mu_{Hg}(T_2)-\frac{1}{2}\mu_{H_2O}(T_2) \\ +\frac{1}{2}\mu_{HgO}(T_2)-\mu_{AgCl}(T_1)+\mu_{Ag}(T_1) \end{array}\right) \qquad (17)$$

The first term represents the potential difference arising from the temperature gradient across the contact wire of the pH sensor (in this work, actually stainless steel). This is called the Thomson (or Kelvin) effect. While typically neglected, it may be a few milivolts when the autoclave is at 450°C, depending upon material. E_{TLJ} is the thermal liquid junction term, and E_D is the quoted notation for the isothermal liquid junction (E_{ILJ}). The last term contains all chemical potentials of

the species involved, which will be demonstrated in the following sections to have terms comparable to Equation (11).

A full derivation of this relationship is beyond the scope of this text. However, consideration of each term is worthwhile to appreciate those factors which affect the overall potential of the cell in Equation (16).

7.1.3.3 Details of YSZ Membrane pH Sensor

Consider a portion of the cell in Equation (16)

$$
\begin{array}{c}
|\leftarrow \text{------------} T_2 \text{------------} \rightarrow| \\
H_2O(\,H^+(aq))\,|\quad YSZ\quad |\,HgO(s)\,|\,Hg(l) \\
1\qquad\quad 2\qquad\;\; 3\qquad 4\qquad 5 \\
\leftarrow\text{--------} E = \varphi^{\,5} - \varphi^{\,1} \text{--------}\rightarrow
\end{array}
\tag{18}
$$
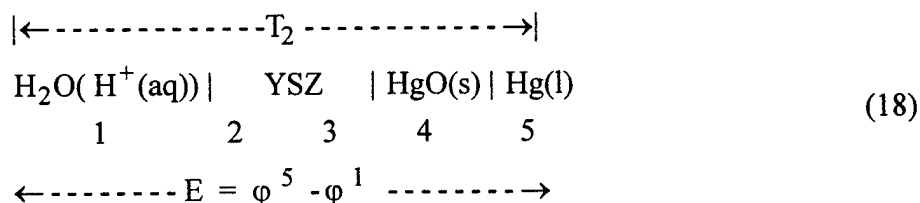
Each phase is numbered, with the YSZ tube being split in two, essentially an inner and outer region in contact with the paste and the test solution, respectively. The electrochemical potential of any species shared between two adjoining phases must be the same in each phase. For example, the electrochemical potential of Hg^{2+} in liquid mercury and in $HgO(s)$ must be the same, so one may write

$$
\tilde{\mu}^{(5)}_{Hg^{2+}} = \tilde{\mu}^{(4)}_{Hg^{2+}}
\tag{19}
$$

or by inserting the definition of electrochemical potential

$$
\mu^{(5)}_{Hg^{2+}} + 2F\phi^{(5)} = \mu^{(4)}_{Hg^{2+}} + 2F\phi^{(4)}
\tag{20}
$$

where μ is the chemical potential and ϕ is the electrostatic potential. Equations such as these for

all species in the cell may be written, and having solved for the electrostatic potential term, the

following obtained

$$F\left(\phi^{(5)} - \phi^{(4)}\right) = -\frac{1}{2}\left(\mu^{(5)}_{Hg^{2+}} - \mu^{(4)}_{Hg^{2+}}\right) \tag{21a}$$

$$F\left(\phi^{(4)} - \phi^{(3)}\right) = \frac{1}{2}\left(\mu^{(4)}_{O^{2-}} - \mu^{(3)}_{O^{2-}}\right) \tag{21b}$$

$$F\left(\phi^{(3)} - \phi^{(2)}\right) = -\frac{1}{2}\left(\mu^{(3)}_{V_O^{\bullet\bullet}} - \mu^{(2)}_{V_O^{\bullet\bullet}}\right) \tag{21c}$$

$$F\left(\phi^{(2)} - \phi^{(1)}\right) = -\frac{1}{2}\left(\mu^{(2)}_{O^{2-}} - \mu^{(1)}_{O^{2-}}\right) \tag{21d}$$

In Equation (21c), $V_O^{\bullet\bullet}$ is standard Kroger-Vink notation for an oxygen vacancy within the YSZ

crystal lattice having a requisite charge of positive two. Relationships for species within any

given phase above may be written as

$$\mu^{(5)}_{Hg^{2+}} = \mu^{(5)}_{Hg} - 2\mu^{(5)}_{e^-} \tag{22a}$$

$$\mu^{(4)}_{Hg^{2+}} = \mu^{(4)}_{HgO} - \mu^{(4)}_{O^{2-}} \tag{22b}$$

$$\mu^{(3)}_{O^{2-}} = \mu^{(3)}_{O_O} - \mu^{(3)}_{V_O^{\bullet\bullet}} \tag{22c}$$

$$\mu^{(2)}_{V_O^{\bullet\bullet}} = \mu^{(2)}_{O_O} - \mu^{(2)}_{O^{2-}} \tag{22d}$$

$$\mu^{(1)}_{O^{2-}} = \mu^{(1)}_{H_2O} - 2\mu^{(1)}_{H^+} \tag{22e}$$

The term O_O appearing in Equations (22c) and (22d) indicates an oxygen species on an oxygen

site in the YSZ lattice, having no net charge. At this point, some assumptions concerning the

YSZ membrane must be made. First, if the sensor is used under potentiometric conditions as it is in these studies, then $\phi^{(3)} = \phi^{(2)}$. The overall potential of the cell portion in Equation (18) may then be written as

$$\phi^5 - \phi^1 = \left(\phi^5 - \phi^4\right) - \left(\phi^4 - \phi^3\right) - \left(\phi^3 - \phi^2\right) - \left(\phi^2 - \phi^1\right) \qquad (23)$$

Further, the defect structure is assumed to be the same across the YSZ tube such that

$$\mu_{V_O^{\bullet\bullet}}^{(3)} = \mu_{V_O^{\bullet\bullet}}^{(2)} \quad \text{and} \quad \mu_{O_O}^{(3)} = \mu_{O_O}^{(2)} \qquad (24)$$

Substituting Equations (21) and (22) into (23), with the condition in Equation (24), generates the final potential relationship

$$\left(\phi^5 - \phi^1\right) = \frac{1}{2F}\left[\mu_{Hg} + \mu_{H_2O} - 2\mu_{e^-} - 2\mu_{H^+} - \mu_{HgO}\right] \qquad (25)$$

many of the terms of which we can see in Equation (17). (Note that what may be considered a somewhat arbitrary species of Hg^{2+} in Hg(l) cancels in the final analysis.) This treatment provides the same final result as those previously published,[15,30] with a slightly more explicit consideration of the defect structure of the YSZ membrane.

7.1.3.4 Standard Potential of Hg/HgO

The form of Equation (17) is not immediately useful since individual chemical potentials cannot be measured. However, substituting the definition of chemical potential ($\mu_i = \mu_i^{\circ} + RT\ln a_i$) and remembering that the standard chemical potential may be written as

$$\mu_i^{\circ} = \Delta_f G_i^{\circ} \qquad (26)$$

then Equation (17) becomes

$$E^{YSZ} - E^{EPBRE} = -\frac{1}{F} \int_{T_2}^{T_1} \bar{S}_{e^-,Ag} dT + E_{TLJ} + E_D(T_2) + \tag{27a}$$

$$\frac{1}{2F}\left(2\Delta_f G^{\circ}_{Cl^-}(T_1) + 2\Delta_f G^{\circ}_{Ag}(T_1) - 2\Delta_f G^{\circ}_{AgCl}(T_1) - 2\Delta_f G^{\circ}_{e^-}\right) \tag{27b}$$

$$+ \frac{1}{2F}\left(-\Delta_f G^{\circ}_{Hg}(T_2) - \Delta_f G^{\circ}_{H_2O}(T_2) + \Delta_f G^{\circ}_{HgO}(T_2) + 2\Delta_f G^{\circ}_{H^+} + 2\Delta_f G^{\circ}_{e^-}\right) \tag{27c}$$

$$- \frac{RT}{2F}\left(\ln a_{H_2O}\right) + \frac{RT}{F}\left(\ln a_{H^+}\right) \tag{27d}$$

The activities of all solid species are taken as unity. From the Nernst equation, $\Delta_f G^{\circ}_i = -nFE^{\circ}$, one can see that the terms in Equations (27b) and (27c) constitute the standard potential of the Ag/AgCl electrode,

$$2Ag + 2Cl^- \Leftrightarrow 2e^- + 2AgCl^- \tag{28}$$
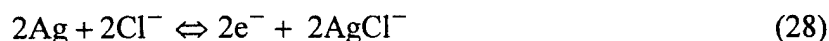
and the Hg/HgO couple (Equation 12), respectively. The standard potential of the Ag/AgCl couple in saturated KCl solution is a constant of $0.197V_{SHE}$ provided the element remains at $25°C$. Note in Equation (27) that the electron terms were added just to illustrate the origin of the standard potential terms; in the overall equation they cancel.

The Gibbs formation energies for all species in Equations (27c) and (27d) may again be calculated using the SUPCRT92 software. Two points concerning its use should be made. First, calculation of Gibbs energies for water, solids, liquids, and non-charged aqueous species are not limited for the conditions of this work. Secondly, the standard state of the software is such that the Gibbs energy of the half cell reaction in Equations (12) and (28) are not on the SHE scale directly. One must subtract the formation energy for hydrogen gas

$$2H^+ + 2e^- \Leftrightarrow H_2(g) \tag{29}$$

from Equation (27c) and add it to Equation (27d) to put each of the half cell reactions on the

SHE scale. (A full discussion of this scale change is provided elsewhere.[31]) Note that in the

overall Equation (28), this operation causes no net change in the overall potential. Rather, it

simply allows for consistency when comparing the standard potentials of the Hg/HgO paste by

this method to that of Macdonald. Since by definition $\ln(x) = 2.303\log(x)$, and $pH \equiv -\log a_{H^+}$,

the modified relationship is then

$$E^{YSZ} - E^{EPBRE} = -\frac{1}{F}\int_{T_2}^{T_1}\bar{S}_{e^-,Ag}\,dT + E_{TLJ} + E_D(T_2) + E_{Ag/AgCl}^{\circ,SUP}(T_1) \qquad (30a)$$

$$+ E_{Hg/HgO}^{\circ,SUP}(T_2) - \frac{2.303RT}{2F}\left(\log a_{H_2O}\right) - \frac{2.303RT}{F}pH \qquad (30b)$$

where the superscript "SUP" indicates the standard potentials calculated using the SUPCRT92

software. Equation (30) is essentially identical in form to that of Macdonald [Equation (11)]. By

using the SUPCRT92 software, one may account for the possible transition of mercury liquid to

gas.

According to Table 7-1, the transition of mercury liquid to gas is thermodynamically

feasible at 357°C and one atmosphere of pressure. Unfortunately, the pressure on the paste side

of the sensor is neither monitored nor imposed on the present electrode design. Therefore, two

conditions of the mercury deserve consideration, each dependent upon the integrity of the epoxy

seal at the cool end of the electrode. First, if the epoxy remains intact, then the pressure in the tip

of the sensor at the maximum test temperature of 450°C could reach the equilibrium vapor

pressure of 4.7 bar indicated in Table 7-1. This corresponds to a pressure of approximately 75

psi. It is reasonable to imagine that the sealant might endure such a pressure. However, if the

epoxy seal cannot hold the vapor pressure of liquid mercury at temperature, then the paste is effectively under atmospheric conditions, and the transition to mercury gas can occur above 357°C.

The pressure and temperature variables input to the SUPCRT92 code for mercury then took two paths. First, the transition temperature of Hg(l) was temporarily increased in the SUPCRT92 database to suppress the liquid to gas transition. The assumed pressure under this state was taken as approximately 5 bar. Calculations to reflect possible transition were made using one bar as the input pressure to the code (slightly less than one atmosphere). All species on the solution side of the YSZ were calculated at 275 bar, roughly the system pressure of 4000 psi. Gibbs formation energies for all species were calculated from 25°C to 500°C.

The results of these calculations are shown in Table 7-2. The values from Equation (13) are calculated for comparison, extrapolated to 500°C. One can see that $E^{\circ}_{Hg/HgO}$ is nearly the same (within 5 mV) regardless of technique up to the mercury boiling temperature. It is apparent that boiling of mercury results in a very abrupt positive shift in the standard potential which continues to higher temperatures. Even assuming the mercury remains liquid, the standard potential as calculated in this study deviates from the extrapolated equation of Macdonald by nearly +15 mV at 450°C. As will be discussed later, this corresponds to a possible error in pH measurements of approximately 0.1 pH units at that temperature. For convenience in calculations, the results for the Hg(l) case were fitted to the following polynomial.

$$E^{\circ,SUP}_{Hg/HgO} = 0.9313 - 3.049 \times 10^{-4} T_c + 3.852 \times 10^{-7} T_c^2$$
$$- 9.692 \times 10^{-10} T_c^3 + 1.376 \times 10^{-12} T_c^4 \tag{31}$$

Table 7-1. Vapor Pressure of Liquid Mercury.

T (C)	v.p. (mm Hg)	v.p. (bar)[c]
[a] 126.2	1	0.002
[a] 184.0	10	0.015
[a] 228.8	40	0.058
[a] 261.7	100	0.145
[a] 232.0	400	0.581
[b] 357	760	1.103
[b] 400	1576	2.287
[b] 425	2294	3.330
[b] 450	3254	4.723
[b] 475	4508	6.545
[b] 500	6117	8.880

a) CRC Hnd. Chem Phys. Vol. 66, pg. D-194
b) CRC Hnd. Chem Phys. Vol. 66, pg. D-213
c) calculated from 1 bar = 689mm Hg

Table 7-2. Comparison of Hg/HgO standard potentials.

T(C)	$E^{\circ,SUP}_{Hg/HgO}$	$E^{\circ,SUP}_{Hg/HgO}$ (Hg(l) $\Rightarrow$ Hg(g))	$E^{\circ}_{Hg/HgO}$ Macdonald
25	0.924	0.924	0.927
50	0.917	0.917	0.917
100	0.904	0.904	0.906
150	0.892	0.892	0.893
200	0.880	0.880	0.880
250	0.870	0.870	0.869
300	0.860	0.860	0.857
350	0.851	0.851	0.847
400	0.843	0.865	0.836
450	0.841	0.887	0.827
475	0.840	0.898	0.822

7.1.3.5 Isothermal Liquid Junction Potential

The magnitude and sign of E_{ILJ} of the cell representing the junction between the KCl and NaOH solutions

$$
\begin{array}{c}
|\!\leftarrow\!----T_2-----\!\rightarrow\!| \\
\mathrm{KCl\,(aq)} \mid \mathrm{NaOH(m)} \\
\alpha \qquad\quad \beta
\end{array}
\tag{32}
$$

may be calculated by the general expression for the junction potential[16]

$$
E_{ILJ} = \phi^{\beta} - \phi^{\alpha} = -\frac{RT}{F}\sum_{\alpha}^{\beta}\frac{t_i}{z_i}\,d\ln a_i
\tag{33}
$$

where t_i is the transfer number of an ion in the junction, z_i its charge, and a_i its activity. The transference number may be obtained by dividing the equivalent ionic conductivity of a given species (λ_i) by the total ionic conductivity of all species involved in the junction

$$
t_i = \frac{\lambda_i}{\sum_{j=1}^{n}\lambda_j}
\tag{34}
$$

In this specific study, K^+, Na^+, Cl^-, and OH^- are the ions of interest. As a first estimate, it is convenient to assume that the concentration of ions in the junction closely approximates their activities. If it is further assumed that the concentration of each ion follows a linear gradient between opposite ends of the junction, one obtains the Henderson equation

$$
E_{ILJ} = \frac{\sum_i \dfrac{|z_i|u_i}{z_i}\left[C_i(\beta)-C_i(\alpha)\right]}{\sum_i |z_i|u_i\left[C_i(\beta)-C_i(\alpha)\right]} \times \frac{RT}{F}\ln\frac{\sum_i |z_i|u_i\,C_i(\alpha)}{\sum_i |z_i|u_i\,C_i(\beta)}
\tag{35}
$$

where $u_i = \lambda_i / F$ (here, u_i is the mobility). Values for λ_i have been published by Quist and Marshall[32] for all ions pertinent to this work up to 400°C. Calculations herein are limited to 350°C since they found that λ_{OH^-} approaches infinity at higher temperatures. One obtains a junction potential varying from 0 to -25 mV$_{SHE}$ as the autoclave temperature varies from room to 350°C. Since the KCl is saturated, the effect of activity was also considered, using the same values for ionic mobilities in an integration program provided by co-workers in the author's Department of study.[33] The results indicate very little effect of activity coefficient, expected since the working solution is so dilute.

The disadvantage to the EPBRE at hand is that the actual junction resides at a point physically removed from the center of the autoclave. The author's experience with the autoclave indicates the junction is not likely above 300°C even with the autoclave at 450°C, so an estimate for E_{ILJ} between 0 and -25 mV$_{SHE}$ seems reasonable.

7.1.3.6 Thermal Liquid Junction Potential

The thermal diffusion potential is given by non-equilibrium thermodynamics[29] as

$$E_{TLJ} = -\frac{1}{F} \int_{T_1}^{T_2} \sum_i \left(\frac{t_i\, S_i^*}{z_i} \right) dT \tag{36}$$

where S_i^* is the transported entropy of a given ionic species and all other terms are as defined previously. Note that in the specific EPBRE used in this study, there would be another term, for the thermal diffusion of the NaOH solution between the glass frit and the high temperature region of the autoclave. Calculation of E_{TLJ} in both cases is difficult for several reasons. First, values for the transported entropy of ions for high temperatures is limited, and even then for only

very dilute solutions. Also, Equation (36) applies strictly to the initial state of the system, before significant thermal diffusion occurs. It is impossible to predict the concentration gradient that will arise when the Soret steady state is reached. In fact, one can't even generally be sure even if the Soret steady state has been reached.

There is some literature available concerning the magnitudes of potential offsets expected, both from calculations and experiment. Lvov and Macdonald[29] have calculated E_{TLJ} for very dilute bridge solutions (up to 0.01m) in the initial state from irreversible thermodynamics. They found E_{TLJ} could be substantial. For an infinitely dilute HCl solution in a bridge with ends at room temperature and 350°C, a shift of -150mV is expected. For KCl solutions, the effect is far less pronounced, only about +25 mV shift for the same conditions. At a constant autoclave temperature of 300°C, calculations showed that E_{TLJ} varied a great deal with concentration for HCl, not more than 10mV for KCl. To apply these calculations to the saturated KCl bridge used in this study, effects of ion-ion and ion-dipole interactions would have to be taken into account in the entropy of transport. This author infers from Lvov and Macdonald's discussion that these data are not generally available. Even if they were, one could still only calculate the initial value of the thermal junction. The other alternative is to measure the E_{TLJ} in an appropriate cell. E_{TLJ} was found to be substantial, on the order of 180mV with a gradient of 250°C.

The intention of this study is to calibrate these thermal effects against the Pt-hydrogen electrode. Hopefully, with well-behaved diffusion characteristics within the coupled bridge compartments, fairly reproducible results may be achieved.

7.1.3.7 Summary of Working Relationships/Expectations

Similar applications were applied in the work of Lvov and Macdonald[29] on another system pertinent to this research, E^{Pt}-E^{EPBRE}

$$|\leftarrow \text{------} T_1 \text{-----} \rightarrow| \leftarrow \text{-------} T_2 \text{---} \text{----} \rightarrow| \leftarrow T_1 \rightarrow$$

$$Cu \mid Ag \mid AgCl \mid MCl_n \ (aq) \mid H^+(aq) \mid H_2(Pt) \mid Pt \dots Pt \mid Cu \qquad (37)$$
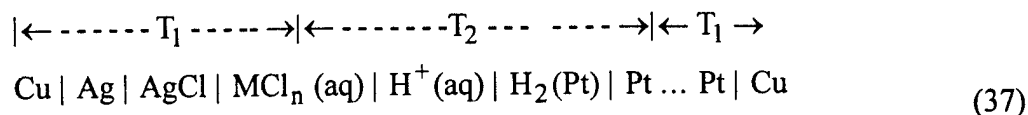
$$\varphi_L \leftarrow \text{---------} \quad E = \varphi_R - \varphi_L \quad \text{--------} \rightarrow \varphi_R$$

with the potential relationship given as

$$E = -\frac{1}{F}\int_{T_2}^{T_1} \bar{\bar{S}}_{e^-,Pt} \, dT + E_{TLJ} + E_D(T_2) +$$

$$\frac{1}{F}\left(\mu_{H^+}(T_2)+\mu_{Cl^-}(T_1)-\frac{1}{2}\mu_{H_2}(T_2)-\mu_{AgCl}(T_1)+\mu_{Ag}(T_1)\right) \qquad (38)$$

Making similar modifications to this relationship and changing to the notation of this text,

$$E^{Pt}-E^{EPBRE} = -\frac{1}{F}\int_{T_2}^{T_1} \bar{\bar{S}}_{e^-,Pt} \, dT + E_{TLJ} + E_D(T_2) + E^{\circ,SUP}_{Ag/AgCl}(T_1) \qquad (39a)$$

$$-\frac{2.303RT}{F}pH + E^{\circ,SUP}_{H^+/H_2(aq)} - \frac{RT}{2F}\ln K_{T_0} \qquad (39b)$$

where $E^{\circ,SUP}_{H^+/H_2(aq)}$ is the standard potential for the formation of aqueous hydrogen, and K_{T_0} is

Henry's constant for hydrogen, taken only at the standard state temperature of 298.15 K. Again considering that all of the right hand side of Equation (39a) may be combined in the E^{EPBRE}, Equation (39) is very similar in form to that of Macdonald et al. except for the last two terms in Equation (39b). These are a by-product of the choice of standard state in the SUPCRT92 code:

for aqueous hydrogen, "unit activity of the species in a hypothetical 1 molal solution referenced to infinite dilution at any temperature and pressure."

Finally, though not explicitly illustrated in the work by Lvov and Macdonald,[29] subtraction of Equation (39) from Equation (30) yields

$$E^{YSZ} - E^{Pt} = E^{\circ,SUP}_{Hg/HgO}(T_2) - \frac{RT}{2F}\left(\ln a_{H_2O}\right) - E^{\circ,SUP}_{H^+/H_2(aq)} + \frac{RT}{2F}\ln K^{\circ} \qquad (40)$$

The potential one would expect between the pH sensor and the Pt wire redox electrode as calculated by Equation (40) and (15) are shown in Table 7-3. One can see that the method described in this work compares closely with that of Macdonald very well up to 350°C. Afterwards, the predictions by this study fall considerably more precipitously.

It may not be entirely evident how all the potential relationships above would translate into actual pH measurements in the SCWO environment. Ideally, one would calibrate the EPBRE to the SHE scale by measuring its potential relative to the Pt-hydrogen electrode at various temperatures, in a solution of known pH, saturated with hydrogen. The EPBRE could then be removed from this solution and utilized in the actual SCWO system as a reference point for the YSZ pH sensor.

The relationships above can now be considered in light of this scenario. If one assumes that the pH is known while measuring the Pt wire against the EPBRE, one may rewrite Equation (39) as

$$pH^{calc} = \frac{F\left(-\left(E^{Pt} - E^{EPBRE}\right) - \frac{1}{F}\int_{T_2}^{T_1}\bar{\bar{S}}_{e^-,Ag}\,dT + E_{TLJ} + E_D(T_2)\right)}{2.303RT} \qquad (41a)$$

7-28

$$+ \frac{F\left(E^{\circ,SUP}_{Ag/AgCl}(T_1) + E^{\circ,SUP}_{H^+/H_2(aq)}\right)}{2.303RT} - \frac{\ln K_{T_o}}{2 \times 2.303RT} \tag{41b}$$

where the superscript "calc" indicates the calculated values of pH from the previous section. Similarly, the potential between the calibrated EPBRE and the YSZ pH sensor in an unknown solution then becomes

$$pH^{meas} = \frac{F\left(-\left(E^{YSZ} - E^{EPBRE}\right) - \frac{1}{F}\int_{T_2}^{T_1} \bar{S}_{e^-,Ag} \, dT + E_{TLJ} + E_D(T_2)\right)}{2.303RT} \tag{42a}$$

$$+ \frac{F\left(E^{\circ,SUP}_{Ag/AgCl}(T_1) + E^{\circ,SUP}_{Hg/HgO}(T_2)\right)}{2.303RT} - \frac{\ln a_{H_2O}}{2 \times 2.303RT} \tag{42b}$$

Subtraction of the two relationships allows one to solve for the apparent measured pH as

$$pH^{meas} = pH^{calc} + \frac{F\left(\left(E^{Pt} - E^{YSZ}\right) + E^{\circ,SUP}_{Hg/HgO}(T_2) - E^{\circ,SUP}_{H^+/H_2(aq)}\right)}{2.303RT}$$
$$+ \frac{\ln K_{T_o}}{2 \times 2.303RT} - \frac{\ln a_{H_2O}}{2 \times 2.303RT} \tag{43}$$

7.1.4 Results and Discussion

7.1.4.1 EPBRE Calibration: E^{Pt} vs E^{EPBRE}

The results of the first set of tests utilizing autoclave design "A" (designated A1-A4) for 0.001m NaOH solution are shown in Figure 7-1. A potential hysteresis of nearly 100mV in any one test is not uncommon, and in fact, the direction of this shift is not consistent. That is, the cooling curve may fall above or below the heating curve.

Also, note the sudden decrease in potential exhibited beyond approximately 400°C in all but A2 (where technical difficulties precluded going to such a high temperature). Its origin is one or a mixture of several of the terms in Equation (39). An increase in pH could account for the observed shift. Salt precipitation, while favored in the relatively low pressure supercritical fluids of this research, would produce the opposite effect. Perhaps local temperature and pressure fluctuations in the fluid caused a phase separation: one dense and concentrated, the other more dilute. If the Pt wire is in contact with the more concentrated fluid by virtue of its location in the autoclave, one may expect the increased pH. A decrease in the hydrogen fugacity could account for this as well, with one order of magnitude decrease accounting for the observed 50mV shift at 450°C. The isothermal junction potential is too small to account for this shift, though it is in the correct direction. Finally, it is very difficult to predict what could cause such an abrupt shift in the thermal liquid junction of the EPBRE.

The results for an increase in solution concentration to 0.01m NaOH shown in test A5-A7 are shown in Figure 7-2. The problems with the autoclave caused a limit of 350°C on the first run. Before this, however, an apparently anomalous positive shift of nearly a full volt occurred upon heating the autoclave. Once the cell was allowed to rest at 300°C for a while, a reasonably steady potential was attained. Continuous cooling from 350°C then showed a smooth transition toward the room temperature value of -800 mV. This abrupt shift is most likely an artifact of the rapid heating. While this test initially appeared completely unsuccessful, comparison to the next test in Figure 7-2, shows the same shift in potential at roughly the same temperature of 100°C. Again, the autoclave was heated rather quickly through 100°C, so the shift may be indicative of the same artifact in Figure 7-2.
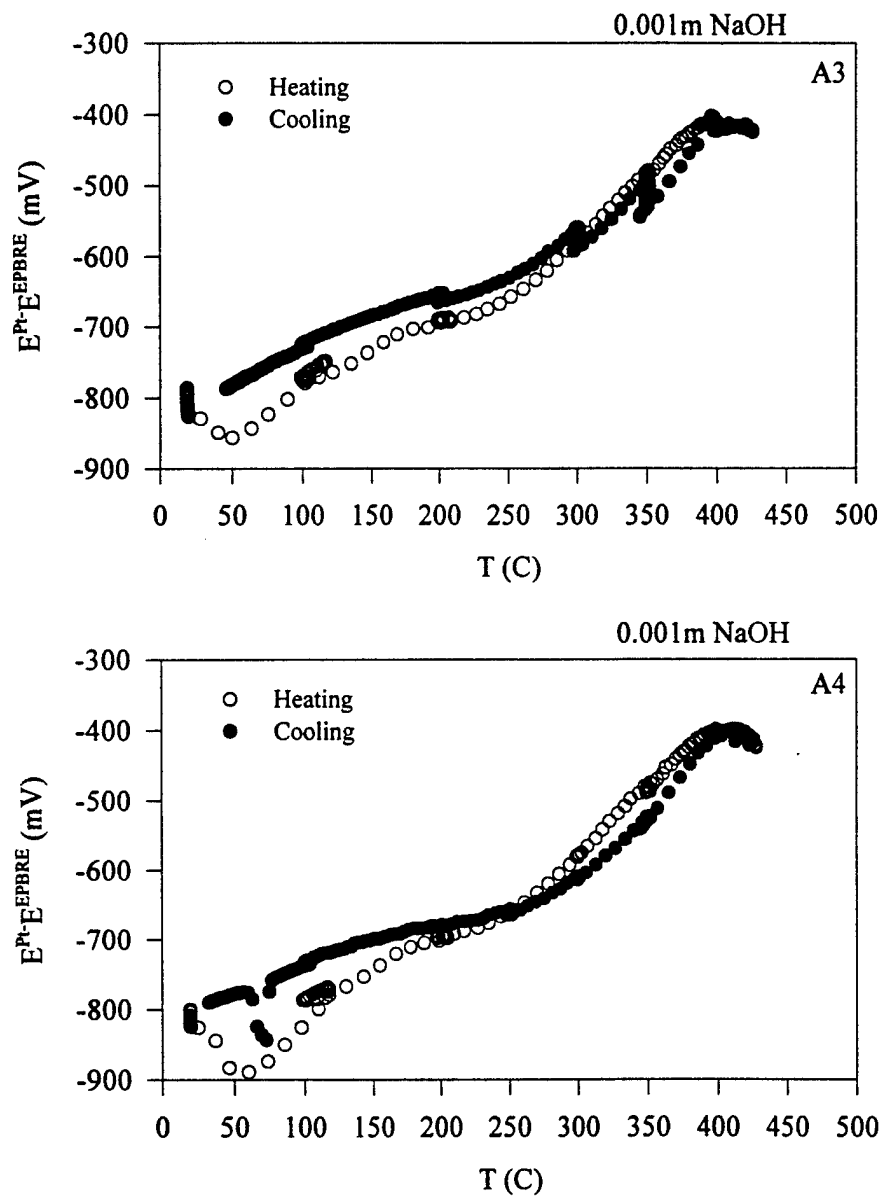
Figure 7-1. Results of the first set of tests utilizing autoclave design "A" (designated A1-A4) for 0.001m NaOH solution.
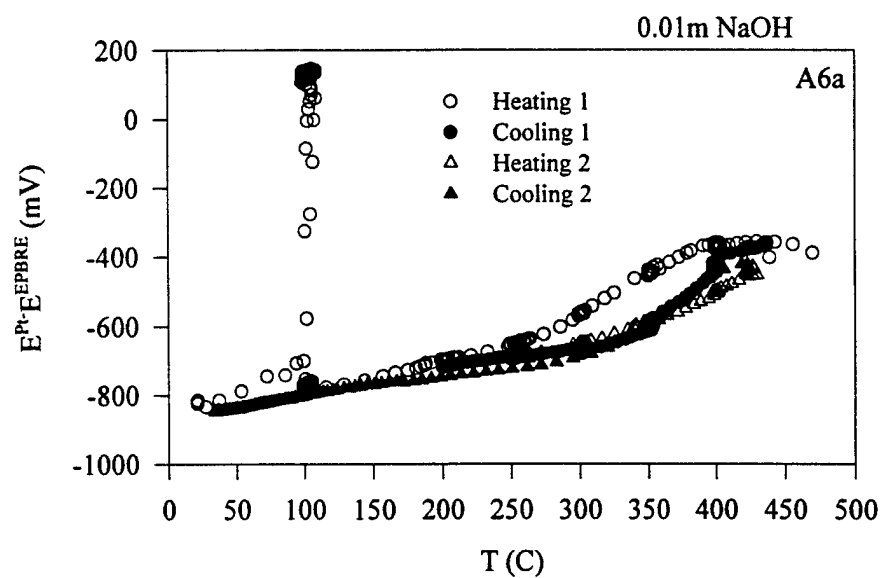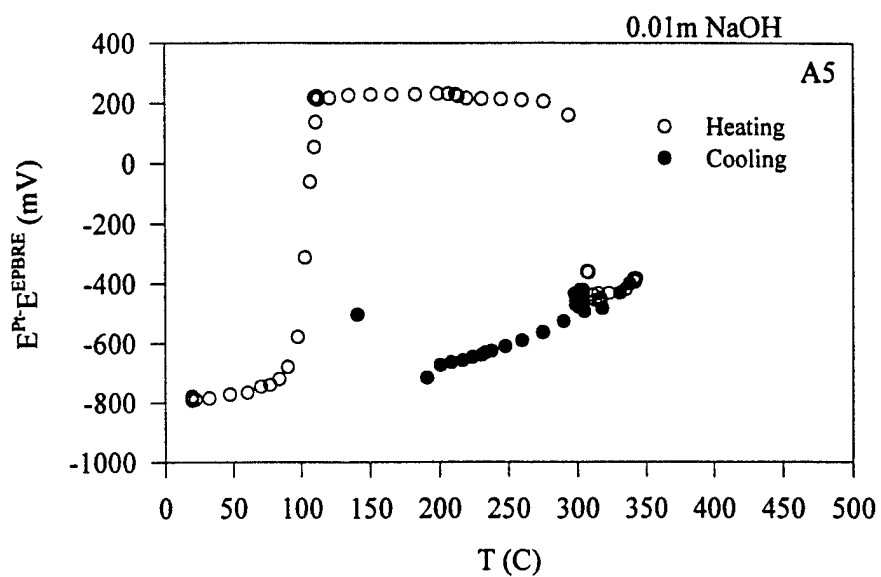
Figure 7-2. Calibration results for 0.01m NaOH solutions, tests A5-A7.

Finally, the results for the most concentrated solution of 0.1m NaOH are shown in Figure 7-3. Unfortunately, problems again with the autoclave prevented reaching a temperature much above the critical point, nor could data be collected on the second cooling run. However, it is already apparent from the data available that the hysteresis in this case is less than that of the more dilute solutions, approximately 30 mV.

Comparison then of all the data for this initial set of experiments is given in Figure 7-4, wherein the final cooling run of the 0.001m and 0.01m NaOH solutions (A4 and A6) are plotted with the heating curve of the 0.1m NaOH solution test (A8). One can see that there is a distinct shift of each curve by approximately 50mV at all temperatures. Consulting Equation (39) again, the change in solution concentration should only affect E_{TLJ}, E_{ILJ}, and $2.0303RT/F \times pH$ terms. The isothermal junction potentials as calculated are nearly the same for any given solution at constant temperature, and could not produce this shift. The negative shift in potentials with increasing NaOH concentration is consistent with the pH dependent term. The magnitude of the shift is on the correct order at room temperature (60 mV per pH unit). This deviation should increase as the autoclave is heated provided the pH difference between solutions remains at roughly one unit. The fact that the curves approach the same point beyond the critical temperature could be indicative of significant ion pairing in this low pressure, low dielectric constant supercritical fluid.

Overall, it would appear that the EPBRE calibration measurements do eventually relax to a somewhat reproducible state. The window of error is still on the order of 50mV, at best. At 300°C, this translates to an error in pH measurement of 0.44 units. The hysteresis observed is
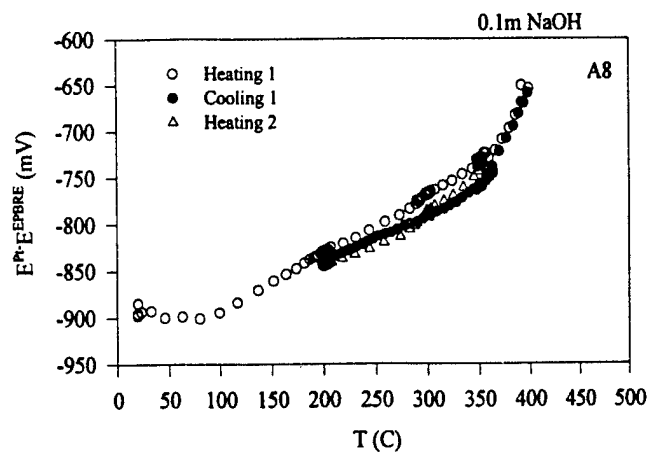
Figure 7-3. Calibration results for 0.1m NaOH solutions, test A8.
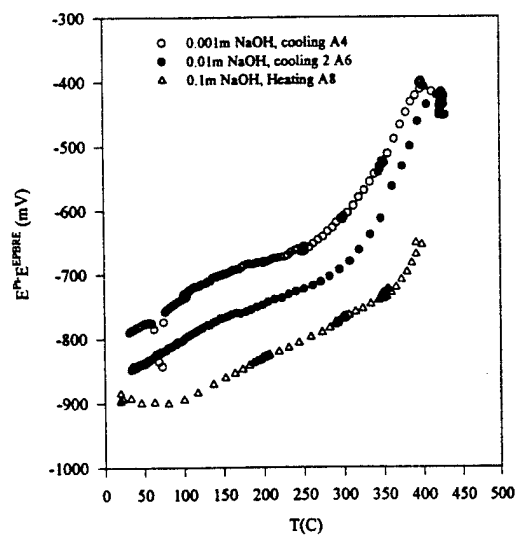
Figure 7-4. Combined calibration results for NaOH solutions.

undoubtedly evidence of shifting concentration gradients in the EPBRE as the Soret steady state is approached. No other term in Equation (39) is likely to produce this effect.

7.1.4.2 E^{YSZ}-E^{EPBRE}, E^{Pt}-E^{EPBRE}, and Resulting pH

The simultaneous responses of the electrodes during the first heating and cooling cycle (B1) are shown in Figure 7-5 for a 0.001m NaOH solution. In both the E^{Pt}-E^{EPBRE} and E^{YSZ}-E^{EPBRE} measurements (Slides B1a and B1b, respectively), one can see a significant shift in potential of nearly +500mV at 350°C. Interestingly, the shift is the same in each measurement, indicating an anomalous behavior of the EPBRE. Subsequent subtraction of the two graphs leads to E^{YSZ}-E^{Pt}, shown in slide B1c. Here the readings are very reproducible only for temperatures greater than 200°C, consistent with the expected limitations of the YSZ sensor.[14] Translation of potential to apparent pH via Equation (43) results in slide B1d, a somewhat more graphic representation of the YSZ limitations. For brevity, all remaining results for E^{YSZ}-E^{Pt} and calculated pH vs T will be restricted to temperatures greater than 200°C as shown in slides B1e and B1f. The change in scale shows more clearly how the apparent measured pH values are very near the expected values. Raw data for E^{Pt}-E^{EPBRE} and E^{Pt}-E^{EPBRE} will still be shown for the entire temperature range for the results that follow.

The second and third runs with the 0.001m NaOH (Figures 7-6 and 7-7, respectively) showed even greater inconsistencies in the E^{Pt}-E^{EPBRE} and E^{YSZ}-E^{EPBRE} than in the first test. Again, however, the steady state values of E^{YSZ}-E^{Pt} and the translation to expected pH values in slides B2c, B2d, B3c, and B4d are still reasonably steady and do not induce much more than a 0.5 pH unit error in the final expected pH. Since the results of E^{YSZ}-E^{Pt} in slide B3c are
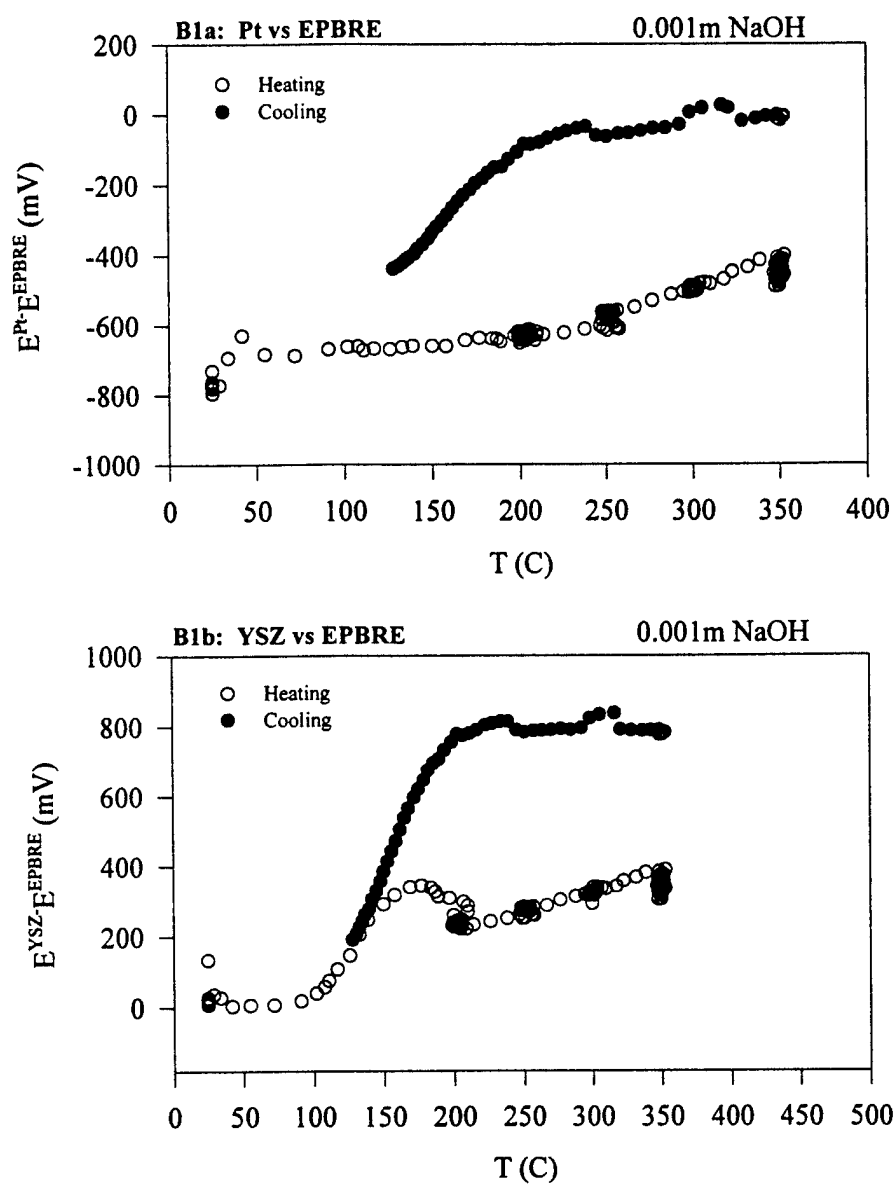
Figure 7-5. Electrode responses for 0.001m NaOH solution, test B1.
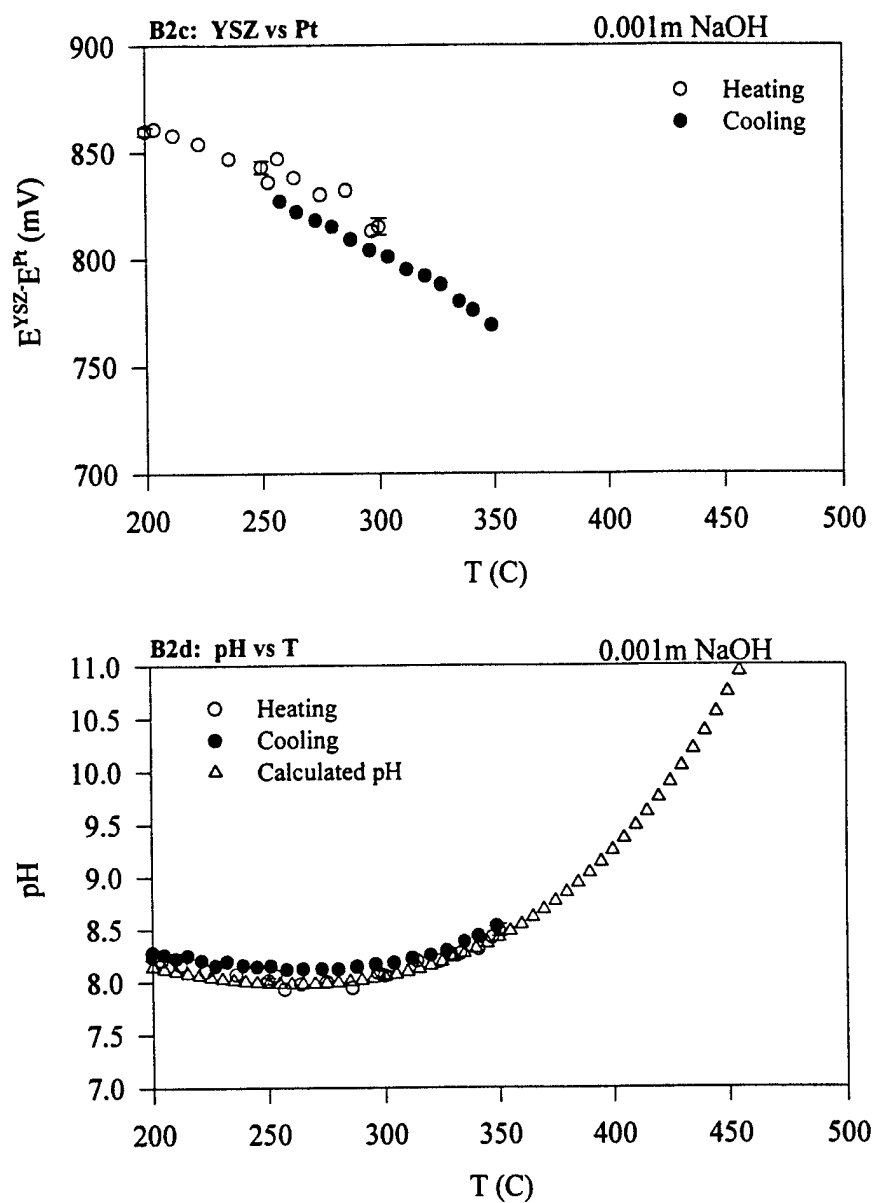
Figure 7-6. Second test run showing the electrode responses for 0.001m NaOH solution.
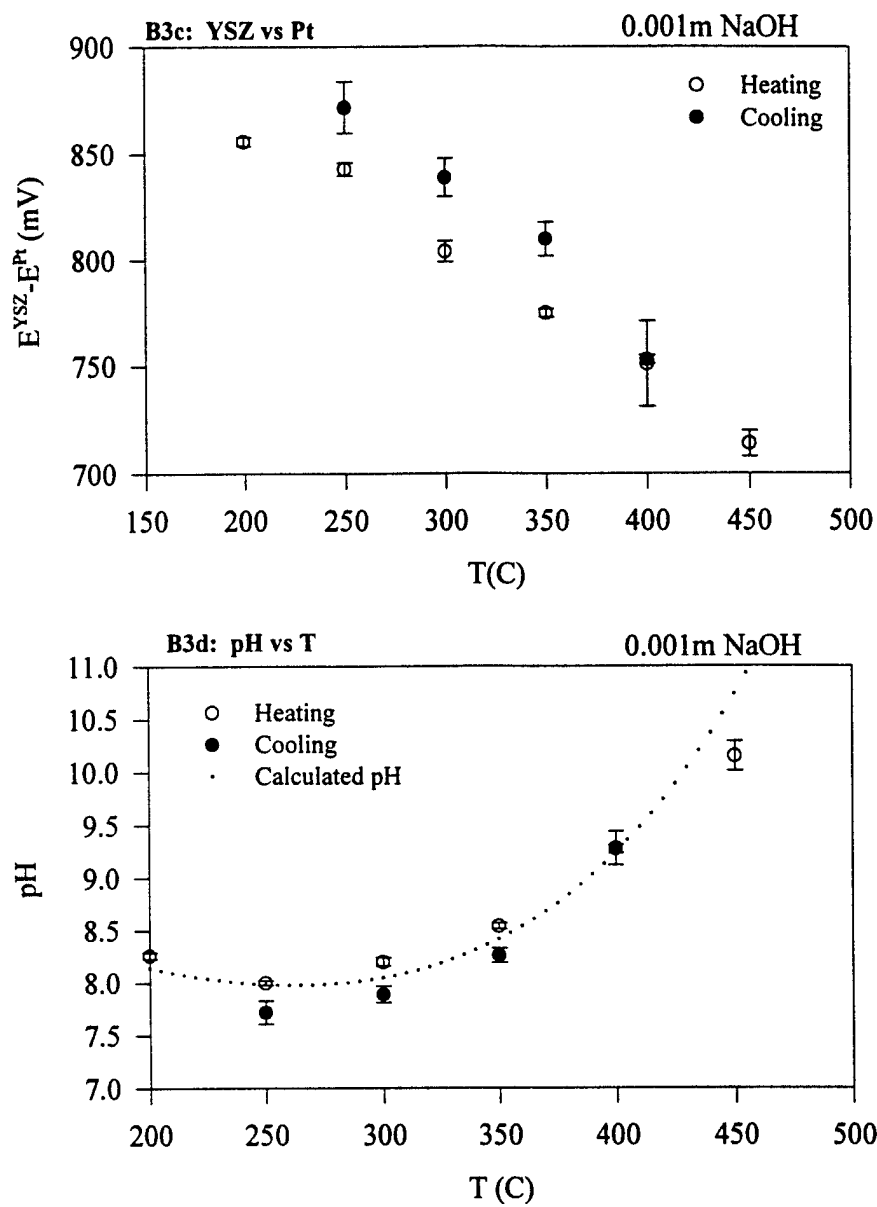
Figure 7-7. Third test run showing the electrode responses for 0.001m NaOH solution.

completely independent of the EPBRE, the hysteresis observed must arise from deviations in the redox or pH sensors. Since this is the first time the Hg/HgO paste had been used to the supercritical region, it is possible that some mercury transition to gas may have occurred. From Equation (40) this could account for the positive shift upon cooling the system. There is the possibility of loss of hydrogen to the autoclave walls, which from Equation (43) could cause the same shift in slide B3c.

The experiments with 0.01m NaOH (Figures 7-8 and 7-9) show somewhat more well behaved responses between the Pt redox electrode, EPBRE, and YSZ pH sensor. In fact, some of the data for $E^{Pt}-E^{EPBRE}$ (slides B4a and B5a) are reminiscent of those measured in the same solution with autoclave "A". The potential between the YSZ and Pt again shows an apparent positive shift on cooling. The standard deviations are relatively small (typically 5 mV) and the overall error translates to only approximately 0.4 pH units. In fact, the response for the $E^{YSZ}-E^{Pt}$ shows extremely reproducible results with small standard deviations. While consistent, the pH expected from these readings would be 0.4 pH units lower than the expected value.

Finally, the 0.1m NaOH solution was utilized in two tests, the results shown in Figure 7-10. Note the "hump" in the data for $E^{Pt}-E^{EPBRE}$ at temperatures around 400°C. This is the response which was expected in the tests in autoclave "A" for the same solution, but which could not be collected at the time. As in the previous tests with 0.01m NaOH tests, the $E^{Pt}-E^{EPBRE}$ values are similar to those collected in autoclave "A". A hysteresis in $E^{YSZ}-E^{Pt}$ of sometimes 60mV are again evident. The standard deviation in the data as the system rests at a given temperature is actually still very low: only 5 to 10 mV. The translation of potential to pH in these tests with 0.01m NaOH are always far lower than one would expect, sometimes as large as 0.7
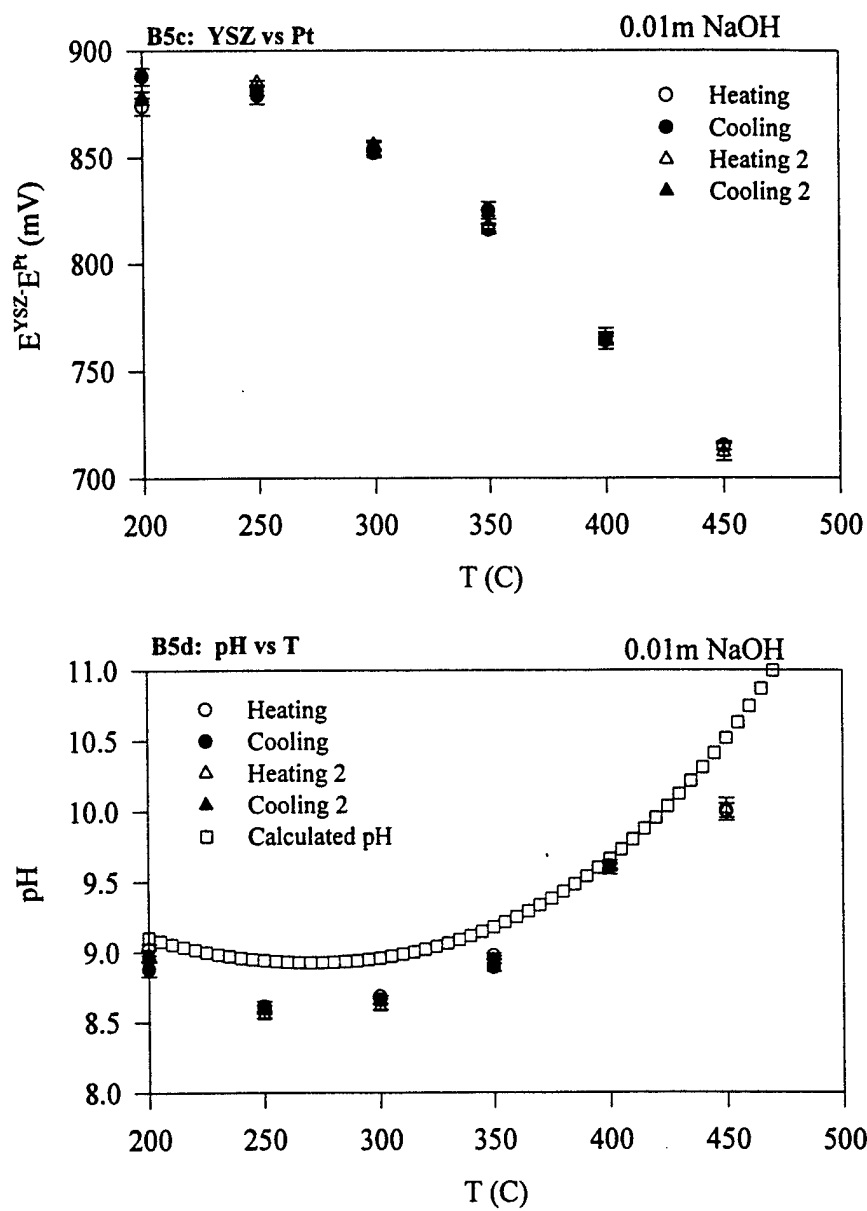
Figure 7-8. Electrode responses for 0.01m NaOH solution, tests B5c and B5d.
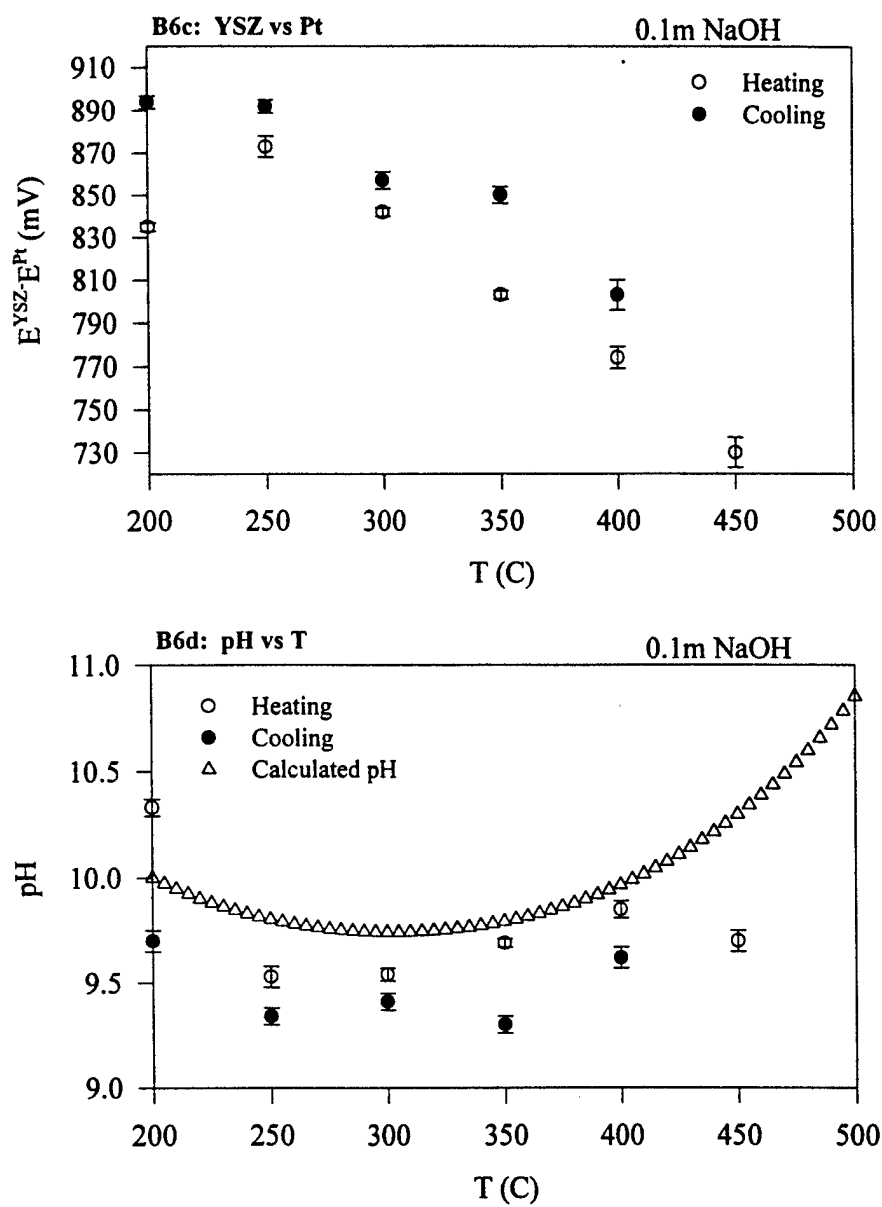
Figure 7-9. Electrode responses for 0.1m NaOH solution, tests B6c and B6d.
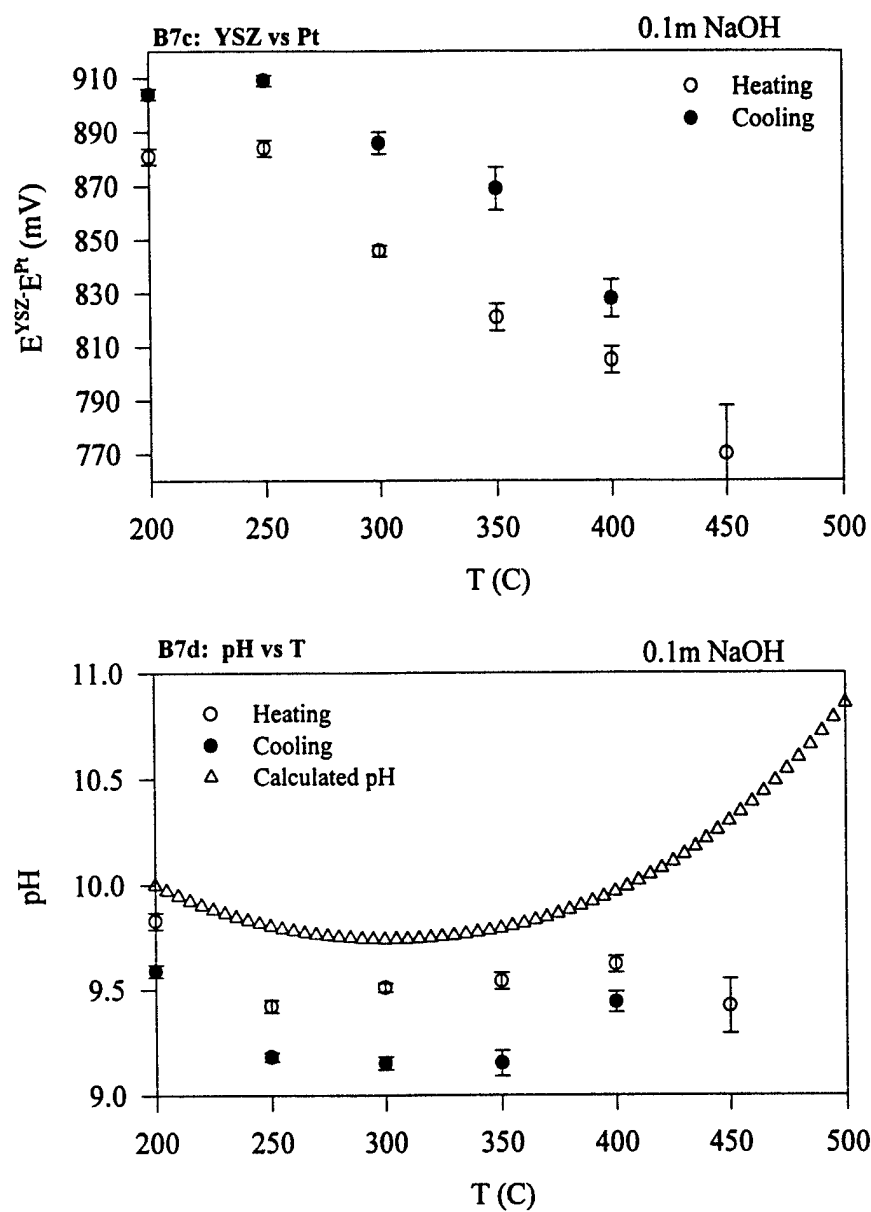
Figure 7-10. Electrode responses for 0.1m NaOH solution, tests B7c and B7d.

pH units. Given that the room temperature pH of the 0.1m NaOH solution is nearly 0.5 units below the theoretically calculated values to begin with, the results may in fact be more indicative of the actual pH.

7.1.4.3 Verification of Nernstian Behavior

As mentioned in the previous chapter, if the electrodes are responding to pH changes and temperature according to the thermodynamic treatment, then from Equation (40), a plot of $E^{Pt\text{-}EPBRE}$ against $E^{YSZ\text{-}EPBRE}$ for all solutions at constant temperature should yield a straight line of unity slope, having a y-intercept corresponding to the negative of the terms on the right hand side of the equation. These plots are completely independent of the pH of the solution or anomalies in the EPBRE. Such plots for 400°, and 450°C are given in Figure 7-11. Only the steady state values are shown with their corresponding standard deviations. In calculating the slope and intercept of the line and the error in each, the points were weighted against the reciprocal of the square of the standard deviation.

First, note that the slopes are always near unity. While the standard deviations in the slopes are relatively small, measured slopes still fall within three standard deviations of unity (equivalent to a 99% confidence interval).

Considering Equation (40), the sources of this potential shift are either in the standard potential of the Hg/HgO paste, in the fugacity of hydrogen, or a combination of both. The standard potential of the Hg/HgO paste is well established thermodynamically. Even if the mercury were to transform to gaseous phase, this should not affect the readings below 350°C. In fact, at 450°C, mercury gas formation could still not account entirely for the difference of -155
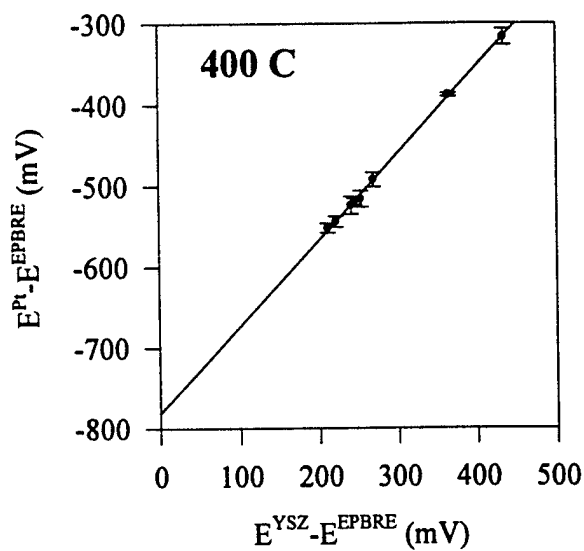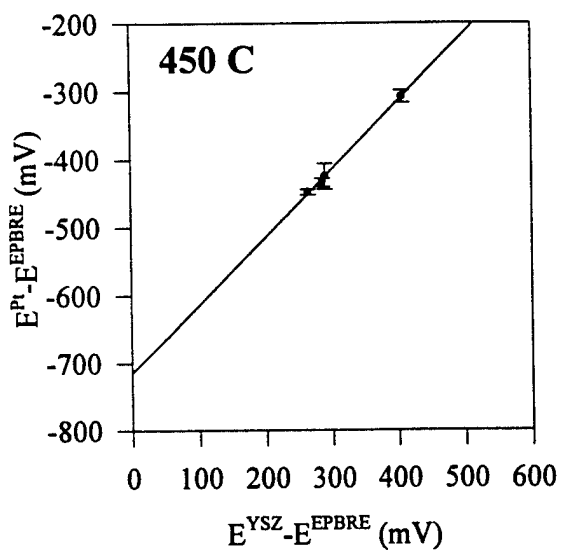
Figure 7-11. Plots of $E^{Pt\text{-}EPBRE}$ against $E^{YSZ\text{-}EPBRE}$ for 400°C and 450°C, with only the steady state values shown with their corresponding standard deviations.

mV observed. A two order magnitude loss of hydrogen is a far more plausible explanation [reflected clearly in (Equation 15)]. This could be a result of hydrogen absorption into the walls of the autoclave, as discussed by Macdonald et al.[13] Also, it is possible that the Pt-hydrogen electrode is responding to a mixed potential between the coiled tip and those portions of the wire sheathed in the alumina tubing which are at a slightly lower temperature. This could give a response indicative of an apparent hydrogen loss in the solution, as discussed in the previous Section.

7.1.4.4 Conclusions

Simultaneous electrochemical experiments between a YSZ pH sensor, EPBRE, and Pt-hydrogen electrode were conducted in aqueous solutions of 0.1m, 0.01m, and 0.001m NaOH to a temperature of 450°C at a pressure of 275 bar to assess the feasibility of pH measurement in supercritical water oxidation systems.

1. The Yttria-Stabilized Zirconia membrane pH sensor behaves in a Nernstian fashion to temperatures as high as 450°C and is therefore a candidate electrode for use in SCWO systems.

2. The EPBRE designed for these experiments was extremely durable and long-lived, and showed some signs of stable calibration against the Normal Hydrogen Electrode. Large hysteresis of its potential response against the Pt-hydrogen electrode were indicative of electrolyte diffusion in the salt bridge.

3. A novel approach employing the commercially available SUPCRT92 program code and an as yet unpublished minimization code allowed the calculation of pH in dilute aqueous solutions to 350°C without the use of empirical formulations.

4. The Thomson effect, which is typically considered to be a negligible factor in the overall potential of non-isothermal electrochemical cells, may in fact be significant for SCWO applications due to the large thermal gradients expected along contact wires of electrodes.

5. An alternative to Hg/HgO for use as the reference paste in the YSZ pH sensor is needed to avoid the hazard of mercury gas formation above 357°C.

7.1.5 References

1. D. Midgley, *Talanta*, **37**(8), 767 (1990).
2. T. E. Edmonds, N. J. Flatters, C. F. Jones, J. N. Miller, *Talanta*, **35**(2), 103 (1988).
3. W. R. Seitz, *Anal. Chem.*, **56**(1), 16A (1984).
4. N. Hara, K. Sugimoto, *J. Electrochem. Soc.*, **137**(8), 2517 (1990).
5. J. V. Dobson, G. Brims, *Electrochim. Acta*, **32**(1), 149 (1987).
6. L. B. Kriksunov, D. D. Macdonald, P. J. Millett, *J. Electrochem. Soc.*, **141**(11), 3002 (1995).
7. L. B. Kriksunov and D. D. Macdonald, Proc. 12th International Conference on the Properties of Water and Steam, Orlando FL, Sept. 1994, Begell House (1995).
8. D. D. Macdonald, S. Hettiarachchi, S. J. Lenhart, *J. Soln. Chem.*, **17**(8), 719 (1988).
9. L. W. Niedrach, *J. Electrochem. Soc.*, **127**(10), 2122, (1980).
10. S. Hettiarachchi, K. Makela, H. Song, D. D. Macdonald, *J. Electrochem. Soc.*, **139**(1), L3 (1992).
11. M. J. Danielson, O. H. Koski, J. Myers, *J. Electrochem. Soc.*, **132**(2), 296 (1985).
12. S. Hettiarachchi, P. Kedzierzawski, D. D. Macdonald, *J. Electrochem. Soc.*, **132**(8), 1866 (1985).
13. D. D. Macdonald, S. Hettiarachchi, H. Song, K. Makela, R. Emerson, M. Ben Haim, *J. Soln. Chem.*, **21**(8), 849 (1992).
14. T. Tsuruta, D. D. Macdonald, *J. Electrochem. Soc.*, **129**(6), 1221 (1982).
15. L. W. Niedrach, *Agnewandte Chemie*, **26**(3), 161 (1987).
16. A. J. Bard, R. L. Faulkner, <u>Electrochemical Methods</u>, John Wiley and Sons, 71 (1980).
17. W. F. Bogaerts, C. Bettendorf, <u>High Temperature Electrochemistry and Corrosion</u>, EPRI Report NP-5863, Section 2 (1998).
18. J. S. Newman, <u>Electrochemical Systems, Second Edition</u>, Prentice Hall, 120 (1991).
19. H. J. V. Tyrrell, G. L. Hollis, *Trans. Far. Soc.*, **48**, 893 (1953).
20. D. D. Macdonald, A. C. Scott, P. Wentrcek, *J. Electrochem. Soc.*, **126**(9) 1618 (1979).
21. J. A. Bierlein, *J. Chem. Phys.*, **23**(1), 10 (1955).
22. S. Lvov, Mimimization code in preparation.
23. G. M. Anderson and D. A. Crerar, <u>Thermodynamics in Geochemistry</u>, Oxford University Press, 440 (1993).
24. E. H. Oelkers, H. C. Helgeson, *Geochimica et Cosmochimica Acta*, **55**, 1235 (1991).
25. L. Haar, J. S. Gallagher, G. S. Kell, <u>NBS/NRC Steam Tables</u>, Hemisphere Pub. (1984).
26. J. Koryta and J. Dvorák, <u>Principles of Electrochemistry</u>, John Wiley and Sons, 38 (1993).
27. J. W. Johnson, E. H. Oelkers, H. C. Helgeson, *Comp. & Geosci.*, **18**(7), 899 (1992).
28. D. D. Macdonald, S. Hettiarachchi, S. J. Lenhart, *J. Soln. Chem.*, **17**(8), 719 (1988).
29. S. N. Lvov, D. D. Macdonald, *J. Electroanal. Chem.*, **405**, 25 (1995).
30. L. W. Niedrach in <u>Advances in Ceramics</u>, **12**, ASC, Ohio, 672 (1983).
31. G. M. Anderson and D. A. Crerar, <u>Thermodynamics in Geochemistry</u>, Oxford University Press, 472-474 (1993).
32. A. S. Quist, W. L. Marshall, *J. Chem. Phys.*, **69**(9), 2984 (1933).
33. J. Pang, program code written for the Center for Advanced Materials staff.
34. J. R. Davis, <u>ASTM Handbook, 9th Edition</u>, **13**, ASM International, 170-171 (1987).

7.2. DEVELOPMENT OF IMMOBILIZED ELECTROLYTE REFERENCE ELECTRODES

7.2.1 Introduction

High temperature aqueous chemistry is a rapidly expanding field. Various electrodes, including pH electrodes, have been developed to monitor the chemistry at subcritical and supercritical conditions. For these electrodes to be truly accurate they must be used in conjunction with a stable reference electrode. The many problems associated with using a standard internal reference electrode at high temperatures have been well documented by Macdonald.[1] External reference electrodes also have problems. They develop thermal gradients due to electrolyte migration toward the Ag/AgCl couple that lead to the formation of a thermal liquid junction potential. The EPBRE (external pressure-balanced reference electrode) developed by Macdonald was an attempt at rectifying this problem by the application of pressure pulses to deter electrolyte migration and to maintain the Soret initial state.[2] Another potential solution could be an electrode in which the electrolyte is dissolved in a solid medium, thus preventing migration. The goal of this research is to design an immobilized electrolyte reference electrode that does not exhibit changes in E_{TLJ} at high temperatures.

There are several approaches to designing an immobilized electrolyte reference electrode (the following all based on a Ag/AgCl couple): 1) Cl⁻ doped glass, 2) polymer gel and 3) silver phosphate or silver borate glass. The first method involves immersing a chloridized silver wire into a saturated sodium salt solution that contains KCl. The salt solution is then heated until it polymerizes and hardens thus trapping the KCl electrolyte within the resulting glass. The second method would utilize a polymer gel matrix to immobilize the salt. This has been tried in the past

7-48

with a commercial epoxy yielding relative success at temperatures up to 250°C.[3] In addition to attempting improvements on the epoxy electrode, we will also investigate other polymers including polyimides which can also form thermosetting resins with very high thermal stability. The third approach would use phosphate or borate glasses containing silver ions as a solid electrolyte.

7.2.2 Experimental Results

The first method has been attempted with several salts. Based on initial results obtained from using $Na_2SiO_3 \bullet 5H_2O$, water glasses were tried using phosphate and borate salts.[4] Electrodes were made by using test tubes containing saturated solutions of the sodium salt with potassium chloride. The test tube was heated over a hot plate until the solution became very viscous (resembling a thick grease) at which point a silver wire coated on one end with silver chloride was inserted into the solution. Heating was continued until the solution began to harden and then the test tube was removed from the heat source and allowed to cool. This crude electrode depicted in Figure 7-12, was then cracked on the bottom (to yield a liquid junction) and immersed into a room temperature saturated solution of KCl. Its potential was measured against a commercial Ag/AgCl reference electrode to test for stability. The original silicate electrode's potential stabilized after 20 minutes with only a ±2 mV fluctuation over a three hour period. Unfortunately, the silicate system did not withstand exposure to basic solution.

Water glasses were attempted using both sodium phosphate tribasic and sodium metaphosphate. Formation of a stable, water insoluble phosphate glass using either

A	Ag wire
B	Glass test tube
C	Water glass/KCl
D	Ag/AgCl
E	Small crack
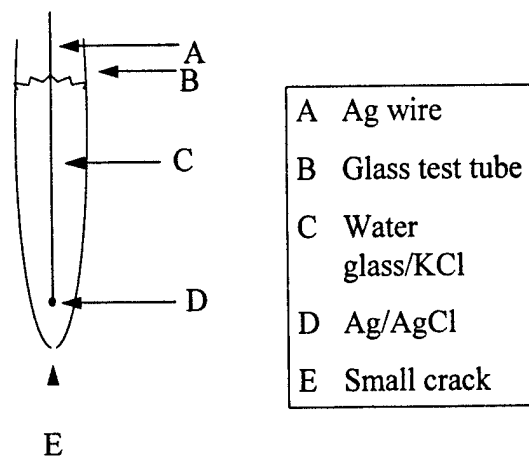
Figure 7-12. Schematic of crude electrode design.

$Na_3PO_4 \cdot 12H_2O$ or $(NaPO_3)_x \cdot Na_2O$ ($x \approx 13$) was not realized. A possible explanation for this will be discussed later in the report.

The borate salts proved slightly more lucrative. Initially borax, $Na_2B_4O_7 \cdot 10H_2O$ was tried but the resulting glass was water soluble. A more stable solid was formed using sodium metaborate, $NaBO_2 \cdot 4H_2O$. The potential of the resulting electrode was measured against a commercial Ag/AgCl reference electrode and these results are shown in Figure 7-14. During Trial 1 the potential decreased dramatically after twenty minutes but then appeared to stabilize for the next two hours. Trial 2 was performed with a different electrode than Trial 1. This electrode was heated longer and was of a more solid nature (instead of a viscous 'grease'). Here the potential seemed to stabilize after twenty minutes with a gradual decrease of less than 4 mV over the next four hours.

7-50
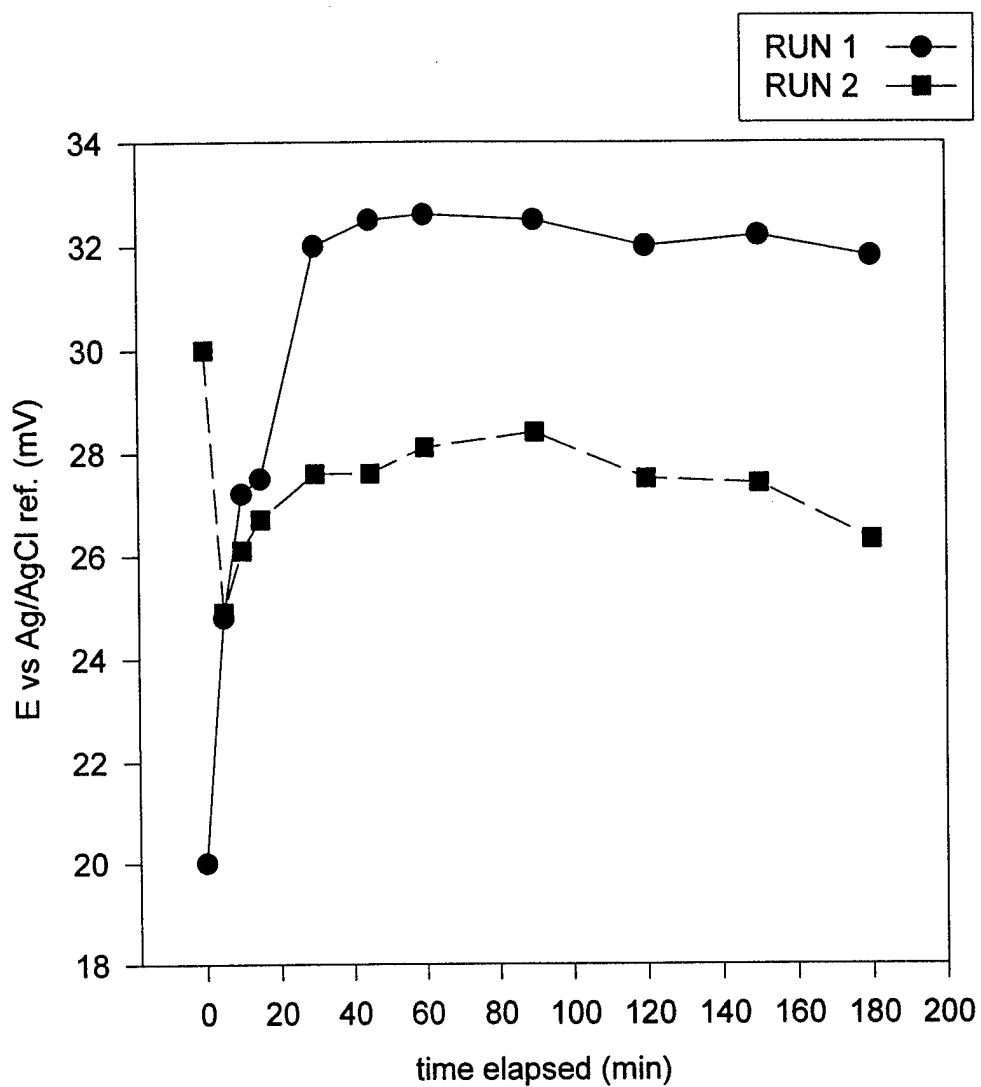
Figure 7-13.   Potential (mV) vs. commercial Ag/AgCl reference for silicate electrode in room
temperature saturated KCl.
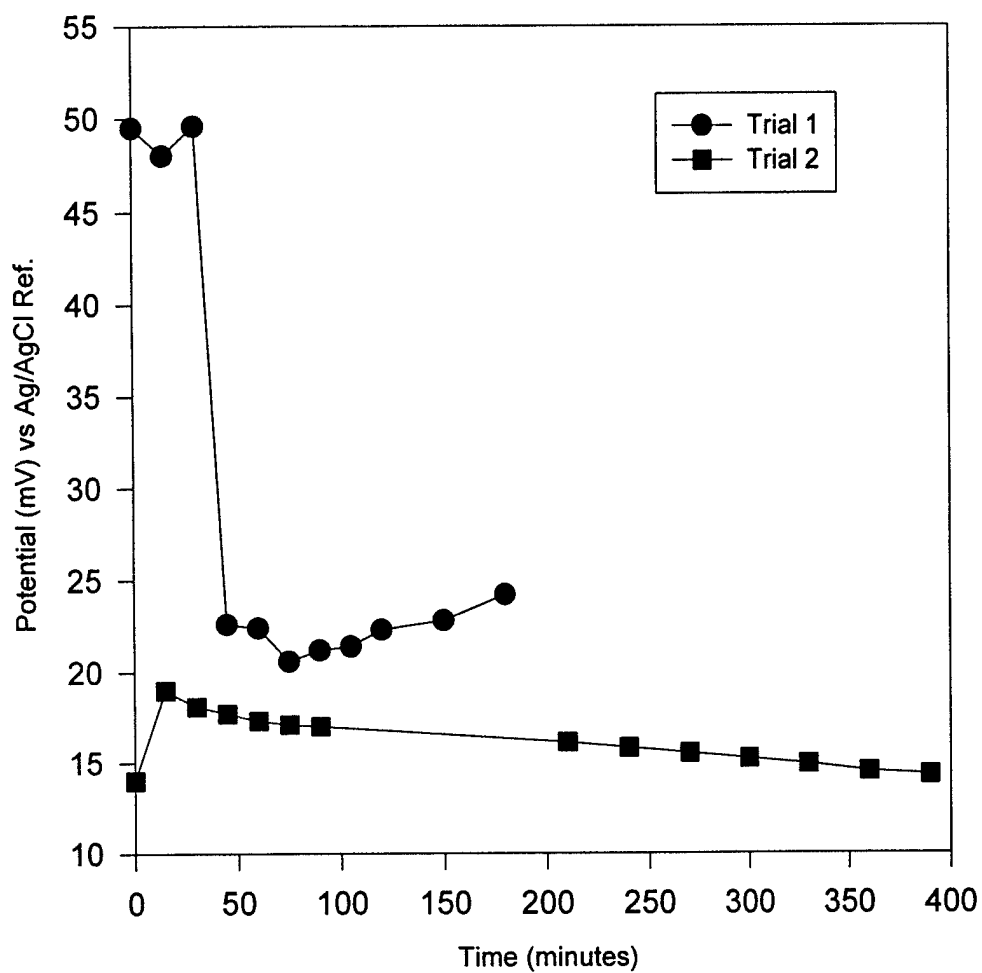
Figure 7-14.   Potential (mV) vs. commercial Ag/AgCl reference for borate/water glass electrode in room temperature saturated KCl.

The failure of the phosphate and borate salts in relation to sodium metasilicate, led the authors to look at the bonding nature of the three systems. Silicates are known to form three dimensional networks while phosphates usually prefer formation of only one dimensional linear chains. The 1-D bonding in phosphates leaves the structure open to attack by water. In contrast, the 3-D network found in silicates successfully blocks infiltration of water molecules, and thus prevents dissolution in aqueous environments (except basic ones). Network formation in borates is slightly more complicated as borate can form either two or three dimensional structures. This could explain why borax exhibited a significantly higher solubility in water than sodium metaborate. Perhaps borax formed only a 2-D network when heated, leaving it susceptible to attack by water, though not as open as the phosphate salt. Some 3-D network formation may have occurred with the metaborate salt, leading to its decreased solubility in aqueous environments.

Based upon this, glass formation was attempted with several mixtures of both the sodium metasilicate and sodium metaborate salts - 70/30, 50/50, 30/70 (mole % sodium metasilicate to sodium metaborate). These solids were prepared using the amounts shown in Table 7-3. It was

Table 7-3. Composition of Various Silicate/Borate Water Glasses.

Mole% SiO$_3$/BO$_2$	NaSiO$_3$•5H$_2$O(g)	NaBO$_2$•H$_2$O(g)	0.1M KCl (mL)
70/30	39.8	8.3	10
50/50	28.5	13.8	10
30/70	8.5	9.6	10

thought that the silicate salt might provide stability by incorporating some three dimensional character to the network. All three mixtures easily formed insoluble solids with the 70 mole percent sodium metasilicate taking slightly longer to reach the glassy stage than the higher borate content electrolytes. The potential of these three electrodes was measured in like manner and the results are displayed in Figure 7-15. The 30/70 SiO_3 to BO_2 appears to be the most stable with the potential changing by less than 5 mV after the first thirty minutes. The 50/50 SiO_3 to BO_2 electrode had a much higher potential than the others, the reason for this is uncertain but again may be due to the consistency of the glass. This mixture formed an opaque solid whereas the other two mixtures formed transparent glasses. The potential did appear to stabilize after 45 minutes and remained stable for the next hour before beginning a gradual increase over the next three and a half hours. The 70/30 SiO_3 to BO_2 underwent a sharp increase in potential after one hour but then stabilized for the next two hours.

7.2.3 Powder X-ray Diffraction

Both the Borate and Silicate samples were subjected to powder x-ray diffraction analysis. The borate sample was shown to be crystalline. Most of the peaks were ascribed to one of three molecular forms of sodium borate hydrate and a few peaks appear to match the pattern for potassium chloride. The silicate sample proved to be crystalline. The sample was found to be mainly composed of Na_2SiO_3 with a small amount of several partially hydrated metasilicate salts. One set of peaks at low theta values appear to match a pattern for $NaSi_7O_{13}(OH)_3 \bullet 4H_2O$. A few peaks also appear to show presence of potassium chloride. The x-ray diffraction patterns are
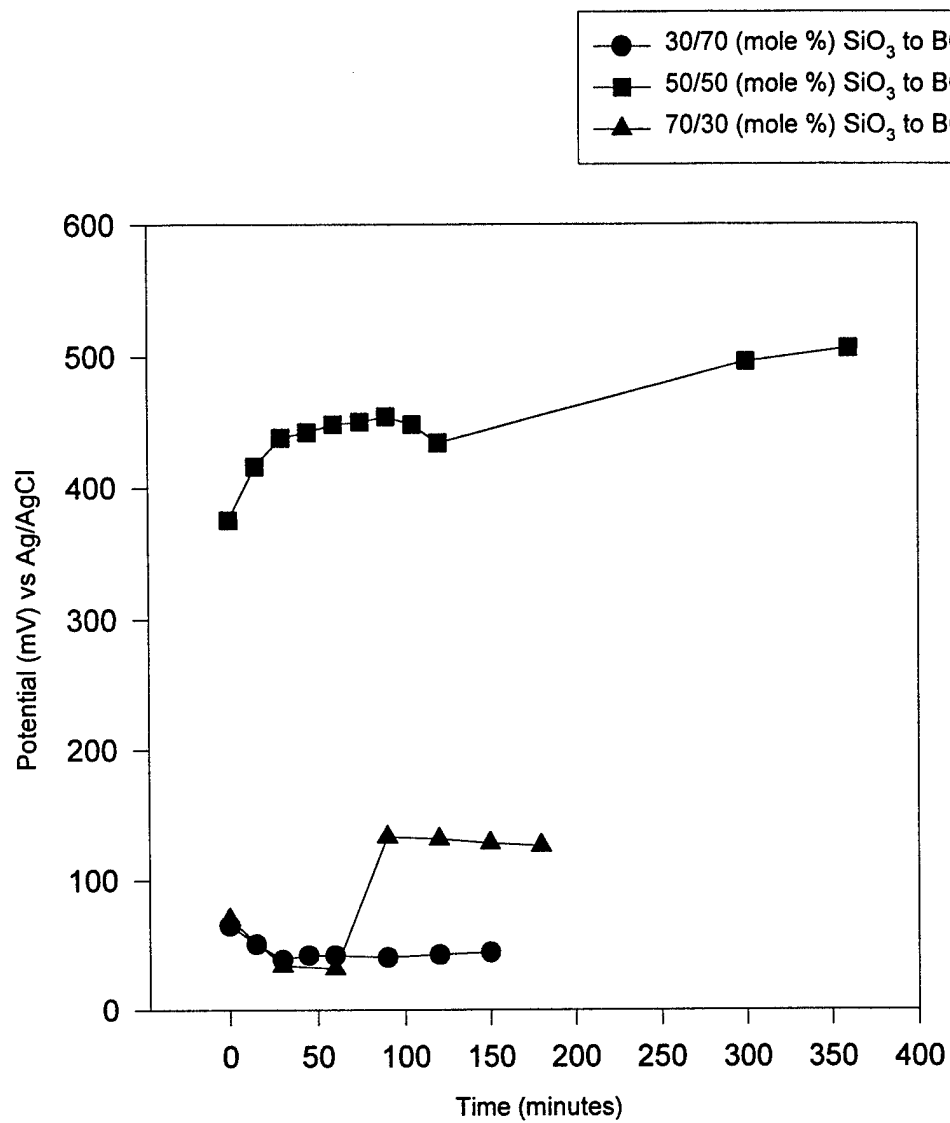
Figure 7-15. Potential (mV) vs. commercial Ag/AgCl reference for borate-silicate/water glass electrodes in room temperature saturated KCl.

shown in Figures 7-16 and 7-17.

7.2.4 Conclusion

Even though the substances prepared were not "glasses" but rather, crystalline masses, they still appear to act as immobilized electrolytes. The electrolytes were insoluble at room temperature and had relatively stable potentials.

This project is still in its initial stages and much work remains. The next stage, currently in progress, involves preparing a silver ion based glass. The glass is based on a combination of B_2O_3 as the glass former, Ag_2O as the network modifier, and a mixture of AgCl and AgI as the electrolyte. A rough schematic of what this electrode will look like is shown in Figure 7-18. These electrodes will be tested at high temperatures using an apparatus like the one shown in Figure 7-19. The apparatus contains a recirculating loop and test cell consisting of an autoclave into which various electrodes can be placed. In order to act as a true reference, the electrode must exhibit a stable potential even upon application of pH changes. This stability will be tested using several buffer solutions. The electrode will also undergo impedance analysis.

7.2.5 References

1. D. D. Macdonald, *Corrosion*, **35**, 75 (1978).
2. D. D. Macdonald, A. C. Scott, and P. R. Wentrcek, *J. Electrochem. Soc.*, **126**, 908 (1979).
3. D. D. Macdonald and S. Hettiarachchi, *J. Electrochem. Soc.*, **134**, 1307 (1987).
4. D. D. Macdonald and H. K. Arthur, project report to DuPont Educational Aid Program.
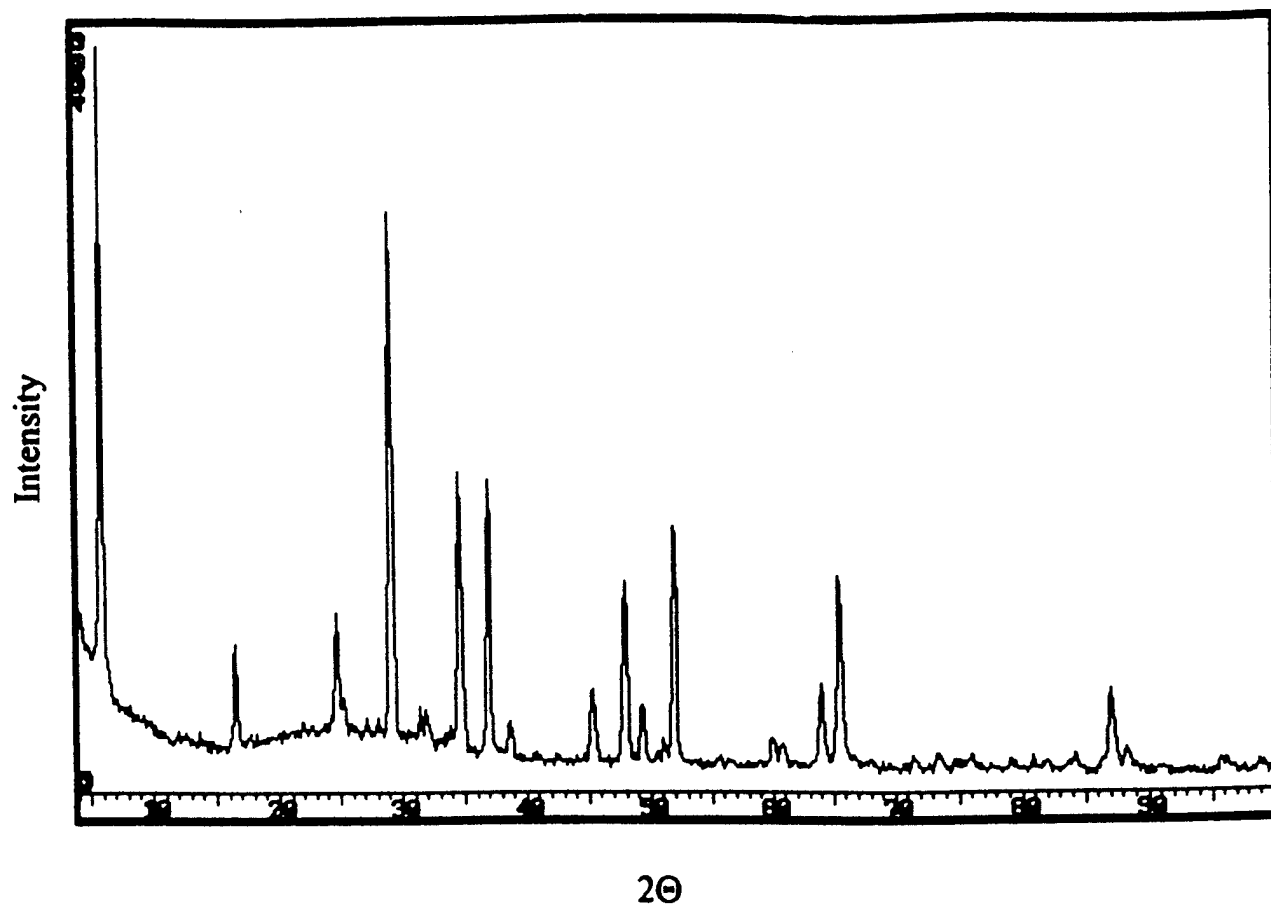
Figure 7-16. Powder x-ray diffraction pattern for sodium silicate sample.
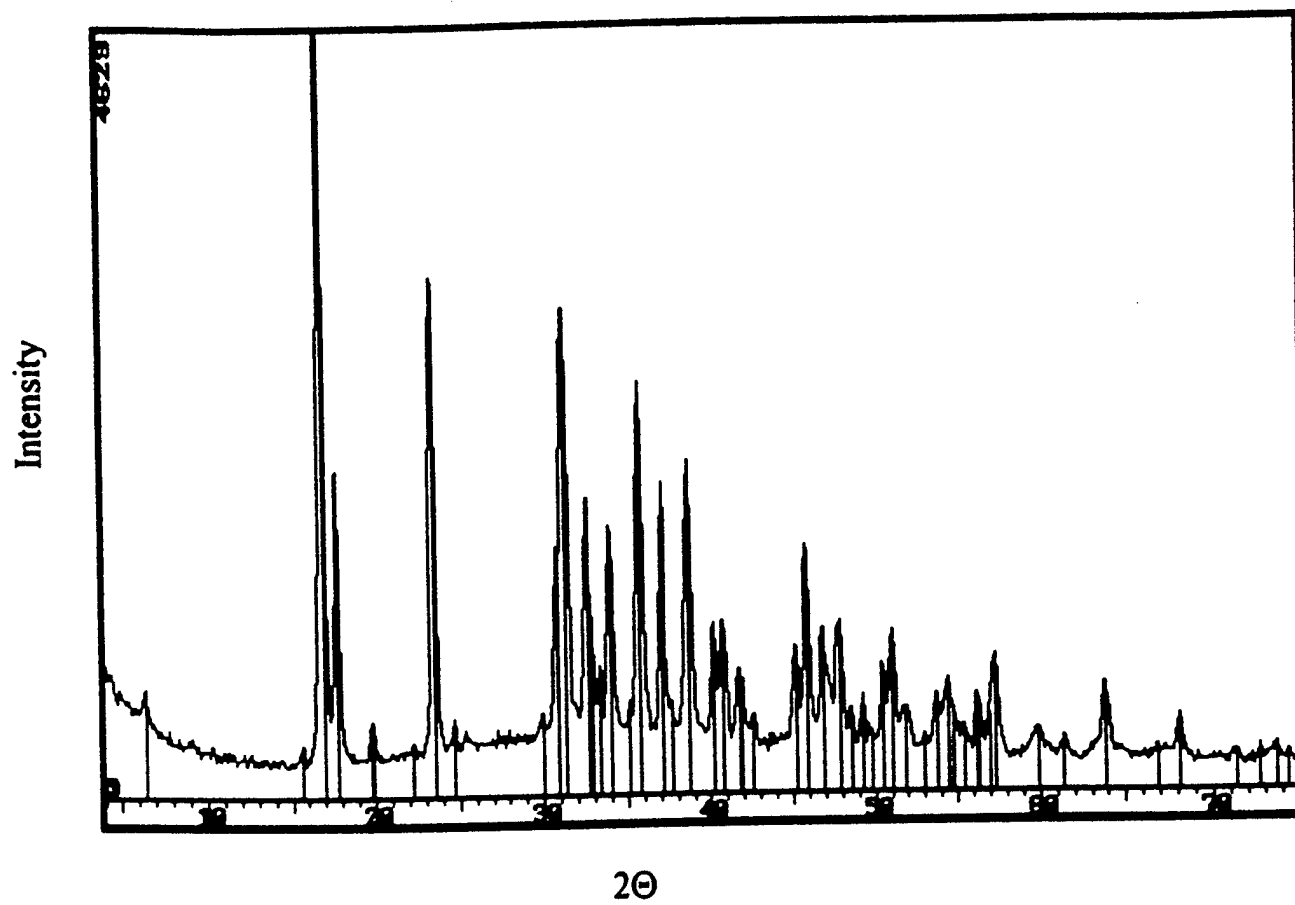
Figure 7-17. Powder x-ray diffraction analysis of sodium borate.
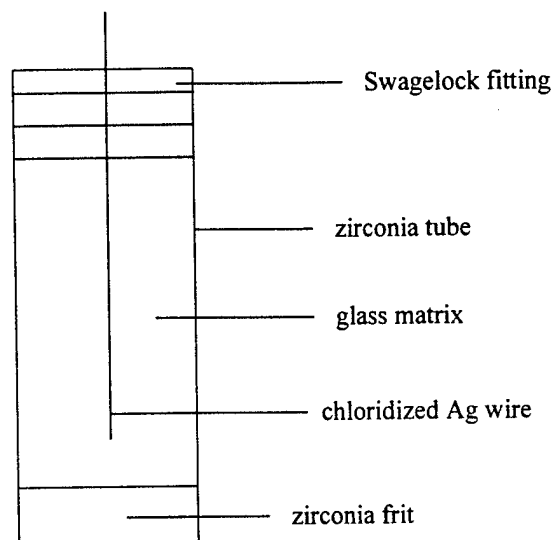
Figure 7-18. Rough schematic of electrode design for Ag ion glasses.
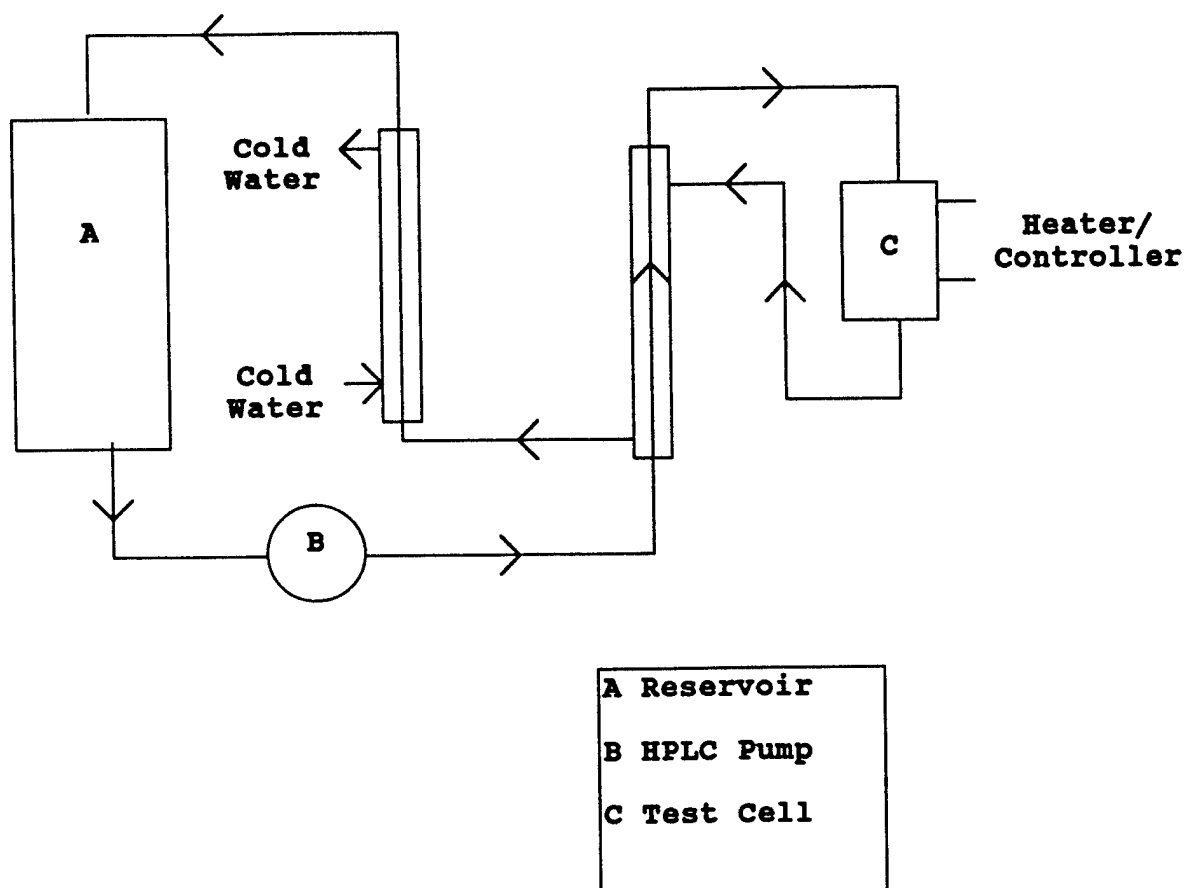
Figure 7-19. Schematic of test circuit to be used for high temperature experiments.

7.3. MEASUREMENT AND STANDARDIZATION OF pH IN SCWO

7.3.1 Standardization of pH in SCW

Knowledge of the pH of the solution is of particular importance for the SCWO process, because the corrosion of common structural materials can be attributed to acid attack. In this project we significantly extended the temperature and pressure ranges of utilization of YSZ (Yttria-Stabilized Zirconia) ceramic membrane based pH sensors and External Pressure-balanced Reference Electrodes (EPBRE) to include supercritical aqueous systems. This pH sensor is suggested for pH measurements in pilot-plant scale SCWO reactors and as the basis for formulating a practical pH scale for supercritical aqueous systems proposed below.

The pH scale for supercritical aqueous systems has not been defined at the present time. Standardization of the pH scale for supercritical systems, analogous to subcritical solutions, must be based upon somewhat arbitrary model assumptions and standard solutions. The pH of standard solutions at relatively low temperatures is usually assigned by assuming values for the dissociation constants of the electrolytes, by employing model calculations of activity coefficients, and in some cases, by estimating liquid junction potentials (E_{LJ}). The pH of any other solution is then determined by measuring the potential (E) of the cell comprised of a pH-sensitive electrode, which has been calibrated in the standard solution, and a pH-independent reference electrode. Because of the paucity of data on potential standard ("buffer") solutions at temperatures above about 300°C, the options that are available for calibrating pH electrodes in high subcritical/supercritical solution are severely restricted compared with the ambient temperature case.

It is also important to note that pH at ambient temperature is defined thermodynamically as the negative logarithm of the activity of hydrogen ion (a_{H+}). The activity at ambient temperatures is usually based on the mol/liter concentration scale. This scale is highly inconvenient for supercritical systems, where the volume is highly dependent upon pressure. Accordingly, we suggest the use of the molal scale in pH standardization at high subcritical and supercritical temperatures.

The unambiguous choice of standard solutions for supercritical aqueous systems is more complicated in comparison with subcritical solutions, because of the poor dissociation of even strong electrolytes and because of relatively low activity coefficients. Experimental data for determining those parameters are scarce, and data for estimating E_{LJ} are practically absent. Additional problems arise from the fact that many fundamental properties of high subcritical and supercritical aqueous solutions are strongly pressure-dependent. In this regard, aqueous solutions at the same temperature, but at significantly different pressures, should be considered as different systems, thereby greatly complicating the specification of pH standards. Large changes in the density, dielectric constant, and the dissociation constant (K_w) of water with pressure, and the pressure-dependence of electrolyte dissociation constants, obviously complicate the specification of pH standards. The problem is even further complicated by the pressure dependence of the potential of the reference electrode, the thermal diffusion liquid junction (TDLJ) potential, and the liquid junction (LJ) potential.

To overcome these difficulties, we propose to define a practical pH scale for supercritical systems somewhat arbitrarily, based on available estimates of dissociation constants (K_d) and activity coefficients (γ) for solutions of some common 1-1 electrolytes, such as HCl and NaOH.

The concentration should be chosen to be reasonably low to allow for complete solubility and to yield reliable model estimates for K_d and γ, but at the same time should be much higher than the concentration of potential impurities and corrosion products in high temperature water. We propose to use as a standard, 0.01 m solutions of HCl and NaOH.

In the proposed standardization procedure, we assume that the contribution of the LJ potential to the cell potential is negligible or has been calculated with sufficient accuracy. The concentration of hydrogen ion in the HCl solution (m_{H+}), for example, may be estimated by considering the HCl dissociation reaction

$$HCl = H^+ + Cl^- \tag{44}$$

along with water dissociation

$$H_2O = H^+ + OH^- \tag{45}$$

For Reactions (44) and (45), we establish the following system of four equations, which include the mass action constants, and the mass balance and charge balance constraints:

$$K_d = \frac{m_{H^+} m_{Cl^-} \gamma_\pm^2}{m_{HCl} \gamma_{HCl}} \tag{46}$$

$$K_W = m_{H^+} m_{OH^-} \gamma_\pm^2 \tag{47}$$

$$m^o_{HCl} = m_{Cl^-} + m_{HCl} \tag{48}$$

$$m_{H+} - m_{Cl^-} - m_{OH^-} = 0 \tag{49}$$

Here $\gamma_\pm$ is the mean molal activity coefficient, and m^o_{HCl} is the total (stoichiometric) molal concentration of HCl in solution.

Combining Equations (46)-(49), and assuming $\gamma_{HCl} = 1$, we obtain

$$m_{H^+}^3 + m_{H^+}^2 \frac{K_d}{\gamma_\pm^2} - m_{H^+} \left[\frac{K_W}{\gamma_\pm^2} + \frac{m^o K_d}{\gamma_\pm^2} \right] - \frac{K_d K_W}{\gamma_\pm^4} = 0 \tag{50}$$

For sufficiently diluted solutions, the activity coefficients can be estimated using Debye-Hückel theory in the following form

$$\gamma_\pm = 10^\wedge \left(\frac{-A\sqrt{I}}{1+\sqrt{I}} \right) \tag{51}$$

where I is the ionic strength, $I = \frac{1}{2}\Sigma C_i z_i^2$, and A is the Debye-Hückel limiting slope, provided that the I is not too high (I < 0.1 M). The molal dissociation constant of HCl, K_d, can be obtained from the data of Frantz and Marshall[3] or by using the SUPCRT92 computer program, developed by Helgeson et al.[4] Data for the density of water, and for K_W as a function of temperature and density can be obtained from Reference 4. The limiting slope for the temperature range of interest can be estimated by employing the dielectric constant and density of water data given in Reference 5. Solution of the system of Equations (50) and (51) yields the molal concentration and activity coefficient of hydrogen ion. A similar model may be formulated for the proposed 0.01 m NaOH standard.

With data on the activity of hydrogen ion in the standard solution available from model estimations, we can establish relationships between the pH and cell potential and hence develop a practical pH scale for supercritical systems. The potential of the cell comprised of a pH sensor (yttria stabilized zirconia membrane) and a reference electrode (silver/silver chloride external pressure-balanced electrode) ($E_{meas.}$) can be written in the following form:

$$E_{meas.} = E_{E.S.P.} - \frac{2.303RT}{F} \left[pH - pH_{st.sol.} \right] + \frac{2.303RT}{2F} \log \frac{a_{H2O}^{st.sol}}{a_{H2O}} \tag{52}$$

where $E_{E.S.P.}$ represents the effective standard potential, in other words, the potential of the cell measured in the standard solution

$$E_{E.S.P.} = E_{meas.}^{st.sol.} \tag{53}$$

$pH_{st.sol.}$ is the value of the pH in the standard solution and a_{H2O} is the activity of water. From Equation (52), we obtain the pH of the solution of interest as

$$pH = \frac{F}{2.303RT} \left[E_{E.S.P.} - E_{meas.} \right] + pH_{st.sol.} + \frac{1}{2} \log \frac{a_{H2O}^{st.sol}}{a_{H2O}} \tag{54}$$

Clearly, an accurate derivation of pH requires knowledge of the activity of water in the test solution as well as in the standard solution.

In summary, the proposed pH standard is based on the concept of a standard solution and effective standard potential of the cell. It requires only one reference measurement in the standard solution at the temperature and pressure of interest.

7.3.2 Measurements of pH

We have used YSZ ceramic membrane pH sensors and external pressure-balanced reference electrodes to directly measure the pH of aqueous solutions at temperatures up to 530°C in a high temperature test cell analogous to that described previously.[1,6] In Figures 7-20 through 7-24 we present the data measured at temperatures of 400, 460, 500, and 525-528°C on cycling the input solution between acid and base conditions.
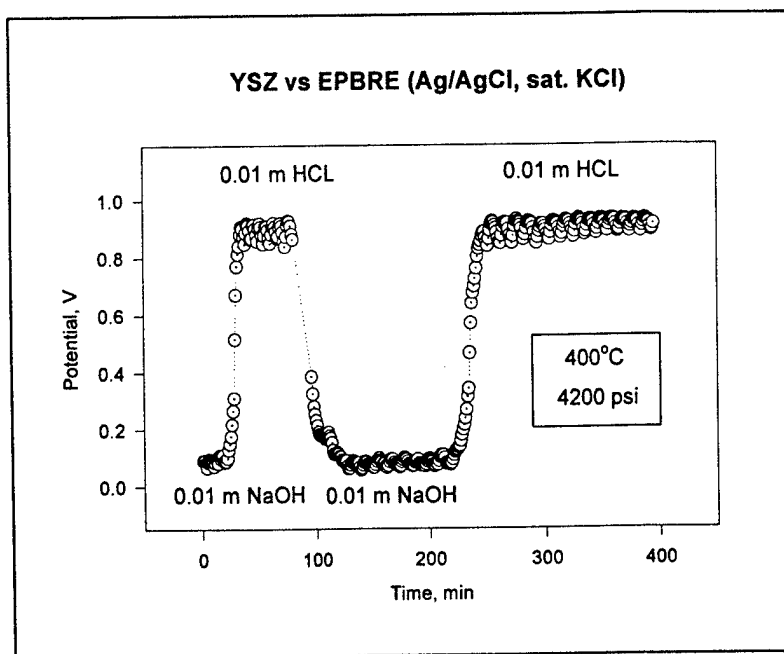
Figure 7-20. Cell potential vs. time at 400°C.
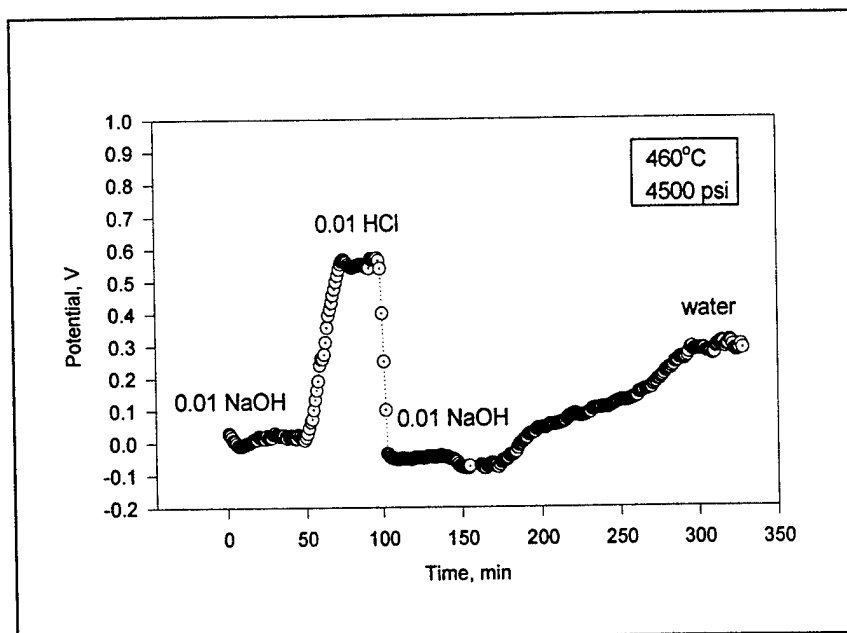
Figure 7-21. Cell potential vs. time at 460°C.
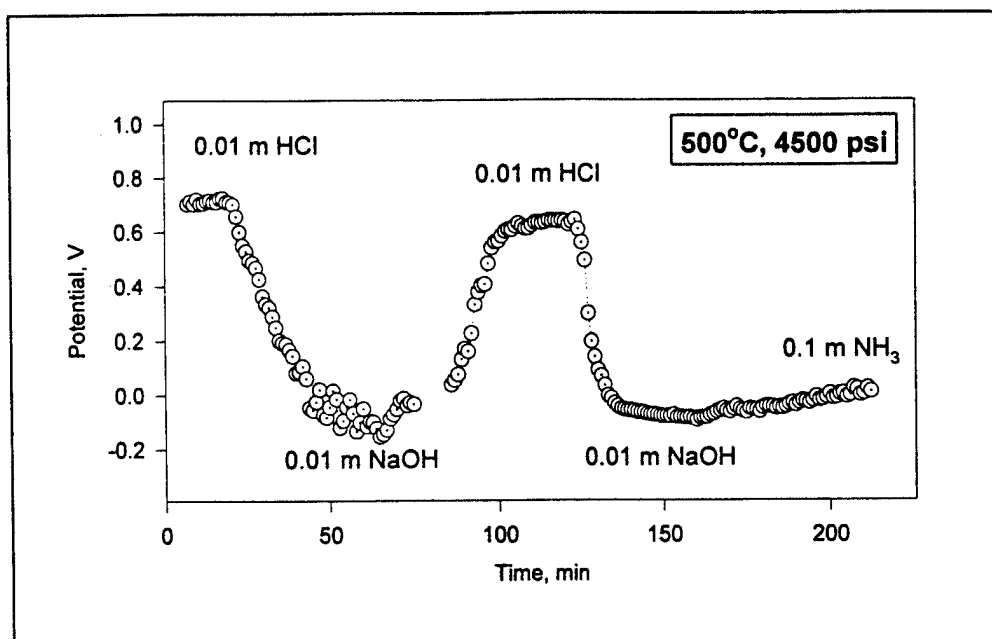
Figure 7-22. Cell potential vs. time at 500°C.
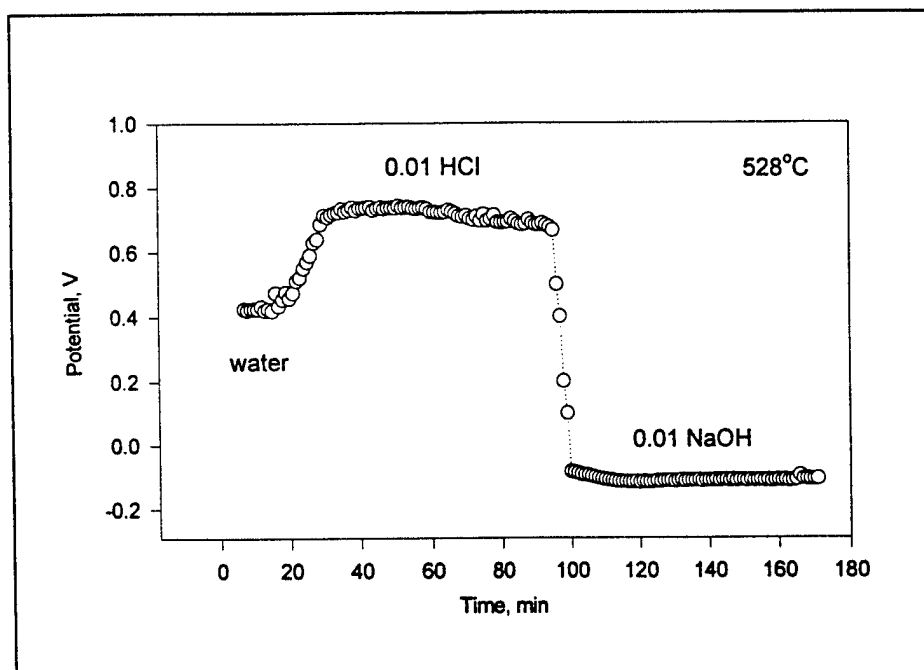
Figure 7-23. Cell potential vs. time at 528°C.
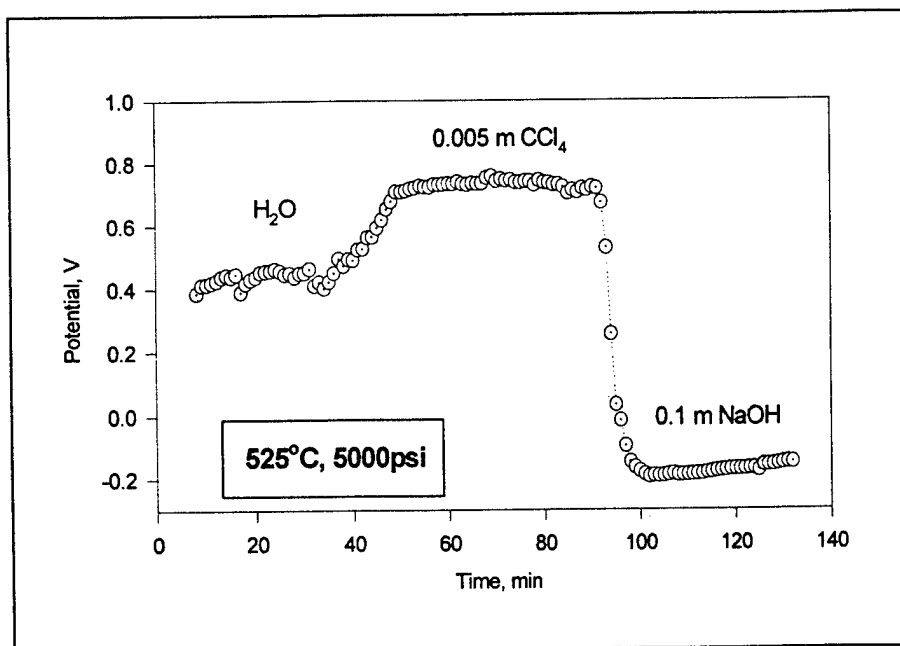
Figure 7-24. Cell potential vs. time at 525°C.
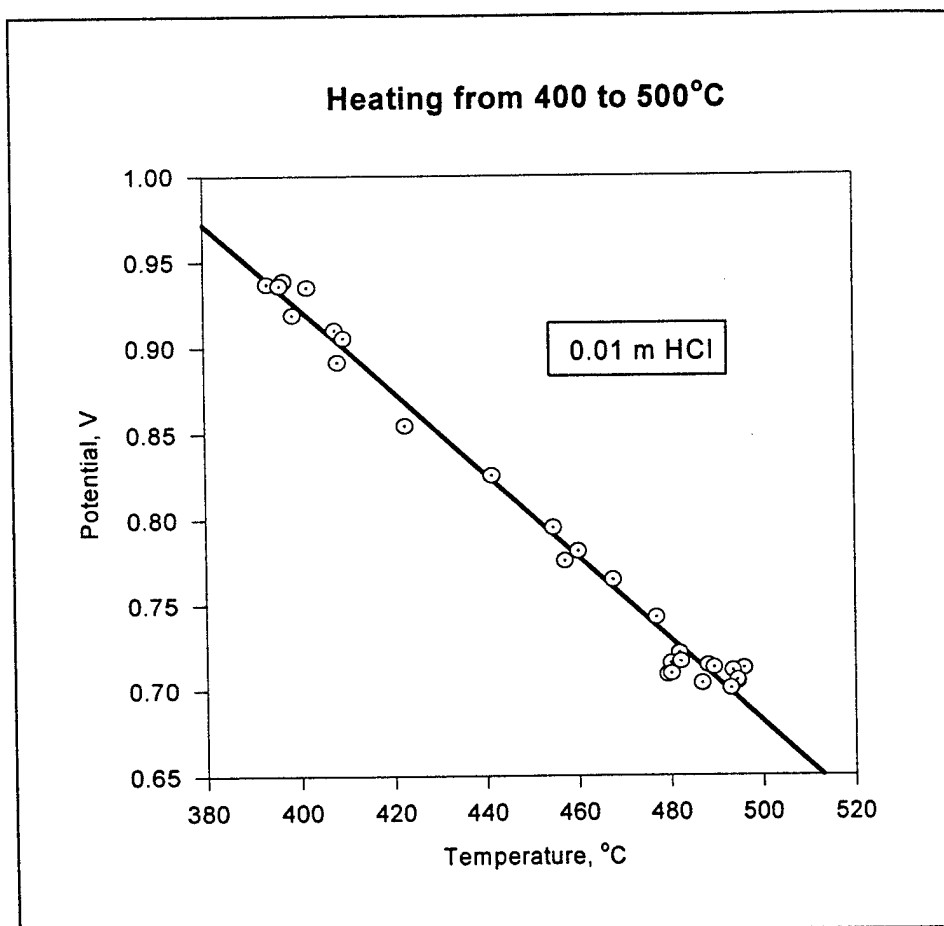
Figure 7-25. Cell potential during heating.

In Figure 7-24, we present results of an experiment in which a model halogenated waste compound was hydrolyzed in SCW in order to demonstrate the viability of the pH measurement techniques for on-line monitoring in SCWO systems. In the initial phase of the experiment, pure water was pumped through the reactor at 5000 psi and at 530°C. We then introduced a solution of approx. 0.005 m CCl_4. The pH of the solution displayed an immediate response, and changed with time to lower values (high cell potentials in Figure 7-24. Compare as well with Figure 7-23). Clearly, carbon tetrachloride undergoes thermal hydrolysis, presumably according to the reaction

$$CCl_4 + 2H_2O = CO_2 + 4HCl$$
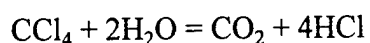
7.3.3 Importance of pH Measurements

Once a pH scale for use at supercritical temperatures has been developed, we can envisage the following applications for pH measurement and on-line pH monitoring:

1) Development of a fundamental understanding of acid-base equilibria, and extraction of dissociation constants (analogous to the use of hydrogen electrodes at subcritical temperatures[7-8]).

2) Specifically, in the case of SCWO of waste, we envisage the following applications for on-line pH monitoring:

   (i) Generation of *in situ* pH data that provide the only accurate picture of corrosion conditions in the reactor. They can be used for fine-tuning the working reactor, in particular for proper dilution or addition of basic reagents. *Ex situ* data are less informative, because of tremendous change in the equilibrium constants of ionic

(including dissociation) and free radical reactions over the temperature range from the working environment to ambient. Another disadvantage of *ex situ* measurements is that they do not yield data on the spatial distribution of corrosion conditions within the reactor.

(ii) Measurements of pH (as well as some other key chemical parameters) could provide vital information on process yields.

7.3.4 References

1. L. B. Kriksunov and D. D. Macdonald, Proc. 12th International Conference on the Properties of Water and Steam, Orlando FL, Sept. 1994, Begell House (1995).
2. L. B. Kriksunov and D. D. Macdonald, Proc. First International Symposium on Supercritical Water Oxidation, Jacksonville, FL (1995).
3. J. D. Frantz and W. L. Marshall, *Amer. J. Sci.*, **284**, 651 (1984).
4. J. W. Johnson, E. H. Oelkers, and H. C. Helgeson, *Computers & Geosciences*, **18**, 899 (1992).
5. ASME Steam Tables. Thermodynamic and Transport Properties of Steam. Sixth Edition, ASME, N.Y. (1993).
6. L. B. Kriksunov, D. D .Macdonald, and P. J. Millett, "Tungsten/Tungsten Oxide pH Sensing Electrode for High Temperature Aqueous Environments", *J. Electrochem. Soc.*, **141**, 3002 (1994).
7. R. E. Mesmer, W. L. Marshall, D. A. Palmer, J. M. Simonson, H. F. Holmes, *J. Solut. Chem.*, **17**, 699 (1988).
8. R. E. Mesmer, D. A. Palmer, J. M. Simonson, in Activity Coefficients in Electrolyte Solutions, Edited by K.S.Pitzer, CRC Press, Boca Raton (1991).

SECTION 8

ESTIMATION OF DISSOCIATION

CONSTANTS

8.1. ESTIMATING DISSOCIATION PARAMETERS AT HIGH TEMPERATURES FROM SPECIFIC CONDUCTANCE DATA

8.1.1 Introduction

Several techniques have been proposed and used for estimating dissociation parameters for electrolytes in aqueous solutions at elevated temperatures from high temperature, high pressure conductivity data. The determination of the degree of dissociation, α, usually includes two steps, as reviewed by Marshall and Frantz[1]: (i) prediction of the equivalent conductance (λ) under the assumption that $\alpha = 1$, and (ii) calculation of α using an equation that involves both predicted and measured data for λ. Most of these techniques involve calculating of the limiting equivalent conductance (λ_o), which is obtained by extrapolating $\lambda(c)$ to infinite dilution, and employ as well extrapolations from high solvent densities (where complete dissociation can be assumed) to low densities. The empirically-justified temperature invariance of the slope of the λ_o vs. ρ dependence above 300°C[1,2] is used for this extrapolation. Another approach employs the semi-empirical Shedlovsky equation, the use of which is somewhat limited[1]. A number of more complicated methods have been developed[3-6], but they usually require higher levels of precision than can be achieved in high temperature/high pressure conductivity experiments.

All of the techniques discussed above involve the limiting equivalent conductance and analyze data obtained at each temperature separately. In this work, we propose a new and simple technique for determining α by using specific conductance data obtained over the whole range of temperature but at a single electrolyte concentration and at a single pressure. The prediction of

the specific conductance for α=1 employs a semi-empirical equation fitted to low-temperature data, where complete dissociation can be assumed.

8.1.2 Results and Discussion

The specific conductance, σ [Scm^{-1}], is defined as the conductance of a 1cm^3 of electrolyte between two electrodes of 1 cm^2 surface area. The specific conductance of a given electrolyte is a function of the volume concentration of charge carriers or ions (C_{ion}) and their mobility (U_{ion}) :

$$\sigma = F(C_{ion}, U_{ion}) \tag{1}$$

The mobility of an ion is a function of temperature, pressure, and viscosity:

$$U_{ion} = F(T, P, \eta) \tag{2}$$

and the volume concentration is a function of the total molal electrolyte concentration (m^o), of the degree of dissociation (α), and of the density of the solution (ρ):

$$C_{ion} = \frac{2\,m^o \rho \alpha}{1 + 0.001 m^o \alpha M} \tag{3}$$

where M is the formula mass of the electrolyte. For a not very concentrated solution, we can take $1 + 0.001 m^o \alpha M \approx 1$, so that:

$$C_{ion} = 2 m^o \rho \alpha \tag{3a}$$

We will use the density of the solvent instead of the density of the solution, because the latter is not readily available at high temperatures and pressures. For simplicity, we consider here only the case of a 1-1 electrolyte. Finally, from Equations (1) - (3), the specific conductance can be represented as follows:

$$\sigma = F(T, P, \eta, m^o, \rho, \alpha) \qquad (4)$$

We express the direct effect of temperature on σ, apart from the temperature influence upon the solution viscosity, by using an Arrhenius-type expression (as was previously applied to conductance data, e.g. in[7,8]), without specifying the exact mechanism of this effect:

$$\sigma = k_1 \exp(-\frac{E}{RT}) \qquad (5)$$

On the other hand, the effect of viscosity on the conductance can be represented by the well-known Stokes equation

$$\sigma = k_2 \frac{1}{\eta} \qquad (6)$$

where k_1 and k_2 are constants. Combining Equations 1-6 we obtain for a constant pressure:

$$\sigma = 2K \exp(\frac{E}{RT}) \frac{\rho m^o \alpha}{\eta} \qquad (7)$$

Here E and K are coefficients characteristic of the given type of electrolyte (more precisely, of the ions of the given electrolyte).

In order to estimate E and K, we can use conductivity data at low and moderately high temperatures, where complete dissociation can be assumed, with reasonable precision (i.e., $\alpha \approx 1$)

$$\sigma = 2K \exp(\frac{E}{RT}) \frac{\rho m^o}{\eta} \qquad (8)$$

The assumption of $\alpha \approx 1$ can be used for the majority of strong electrolytes at temperatures up to 200-250°C. An example of the fitting of this equation to the experimental data of Quist and Marshall[9] for 0.01 m NaCl at 1000 bars is shown in the Figure 8-1 (points marked "predicted" at temperatures over the range 0-200°C). Data for the density and viscosity of water used in

Equation (8) were taken from the ASME steam tables[10]. The parameters E and K were estimated from the fitting procedure of the data[9] over the range 0-200°C. Figure 8-1 indicates that the equation fits the experimental data very well.

Figure 8-1. Predicted (for α=1) and measured[9] specific conductance of 0.01 m NaCl solution at 1000 bars.
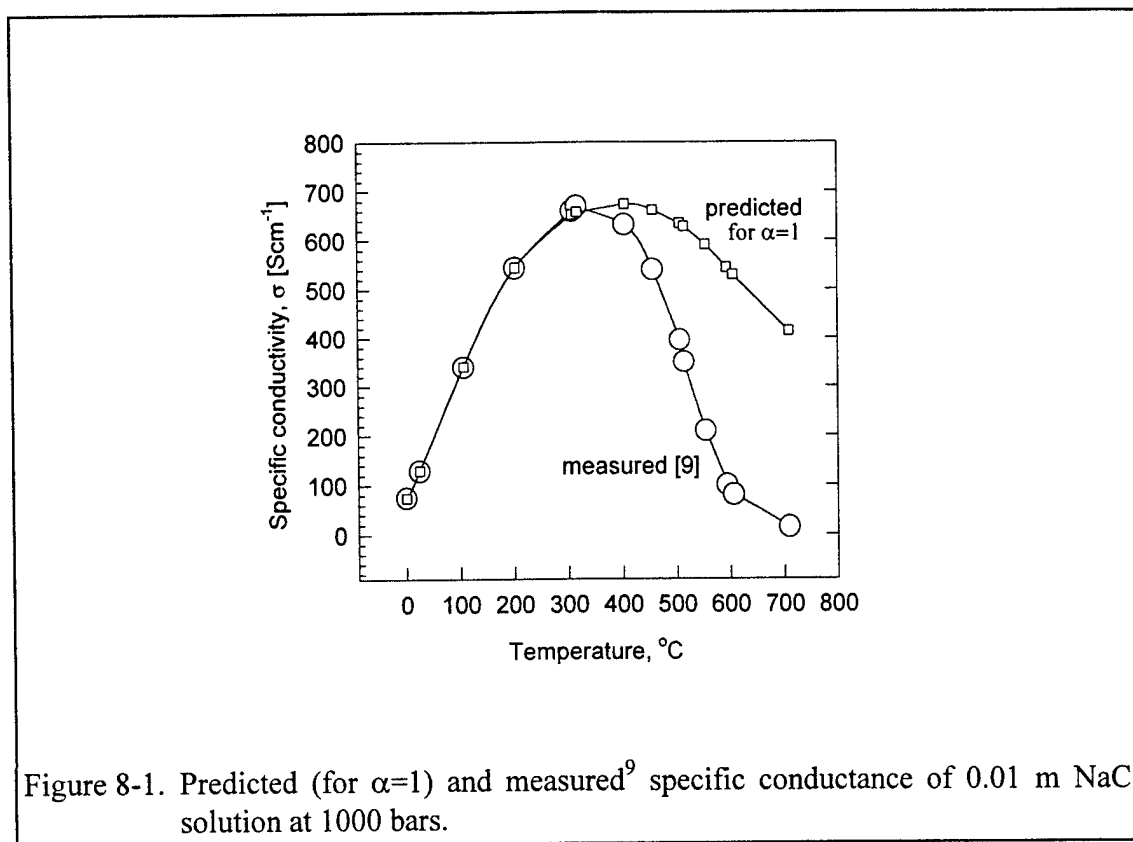
In the second step of this analysis, Equation (8), with the E and K parameters estimated at low temperatures, is used to predict the specific conductance of the electrolyte at higher temperatures, as if there existed no association of the electrolyte (α=1). The predicted σ(T) dependence is shown in comparison with the experimental data in Figure 8-1 (points marked "predicted"). The degree of dissociation can now be estimated from the ratio of the

experimentally-measured and the predicted specific conductances. Indeed, by dividing Equation

(7) by Equation (8) we obtain:

$$\alpha = \frac{\sigma_{exp}}{\sigma_{predict}} \qquad (9)$$

or

$$\alpha = \frac{\sigma_{exp}}{2K\dfrac{\rho m^o}{\eta}exp(\dfrac{E}{RT})} \qquad (10)$$

Equation (9) is somewhat analogous to the technique extensively employed by Marshall et al.[1]

(and relates back to Ostwald's work in the late 1800's) for determining α, in which the ratio of

measured and predicted equivalent conductances is used:

$$\alpha = \frac{\lambda_{exp}}{\lambda_{predict}} \qquad (11)$$

There exist, however, several principal differences between the two methods (besides the

different types of conductances considered). The approach proposed by Marshall et al.[1] employs

the extrapolation of high temperature conductivity data from high densities to lower densities,

and assumes complete dissociation of the electrolyte at high densities. It requires, as well, the

determination of the conductance over a wide range of density (and hence pressure) and employs

the empirical observation by the same authors[2] of a linear dependence of the limiting equivalent

conductance on density of water having an invariant slope at temperatures above 300°C. The

second important difference between the two techniques arises from the use by Marshall et al.[1] of

the Onsager equation for calculating equivalent conductance in the absence of association. It is

necessary, as well, to perform measurements at several (preferentially low) concentrations, in

order to obtain the limiting equivalent conductance by extrapolation to infinite dilution. The approach based on specific conductance, on the contrary, employs data at low temperatures and a single pressure for calculating the predicted values, does not involve the Onsager equation and the limiting conductances, and makes use of data obtained at only one electrolyte concentration. In Figure 8-2 we present the degree of dissociation, calculated using the Equation (8), compared with those estimated from the molal association constant for $NaCl$ (K_a) taken from the literature. The following equation was used for the calculation of the α based on K_a:

$$K_a = \frac{a_{NaCl}}{a_{Na}a_{Cl}} = \frac{m_{NaCl}\gamma_o}{m_{Na}m_{Cl}\gamma_{\pm}^2} = \frac{m^o - m_{Na}}{m_{Na}^2\gamma_{\pm}^2} \qquad (12)$$

In the Equation (12), we assume that the activity coefficient of undissociated NaCl is equal to 1. The mean molal activity coefficient of the ionic species $(\gamma_{\pm})$ was estimated from the Debye-Huckel equation in the form:

$$\log_{10}\gamma_{\pm} = -A\sqrt{I} / (1 + \sqrt{I}) \qquad (13)$$

where I is the ionic strength($I = 0.5\Sigma C_i z_i^2$) and A is the Debye-Huckel limiting slope. The value of A was estimated for temperatures over the range of interest by employing data on the dielectric permittivity taken from Ref. [10]. The ionic strength for the case of a 1-1 electrolyte is equal to the ionic concentration, and can be obtained from the molal concentration (see Equations (3) and (3a)): $I = 1/2(C_{Na} + C_{Cl}) = C_{Na} = m_{Na}\rho$. Substituting Equation (13) into Equation (12) we obtain:

$$K_a = \frac{(m^o - m_{Na})}{m_{Na}^2} 10^{\left[\frac{2A\sqrt{m_{Na}\rho}}{1 + \sqrt{m_{Na}\rho}}\right]} \qquad (14)$$

Values of K_a for NaCl were generated using the computer program Supcrt92, developed by

Helgeson et al.[11]. Those values are based, in part, on data of Quist and Marshall[9]. Equation (14)

was solved numerically for m_{Na}, and the degree of dissociation was then calculated using the

expression

$$\alpha = \frac{m_{Na}}{m^o} \qquad (15)$$

The results of this calculation are compared with estimates of α based on Equation (9) in Figure

8-2. Excellent agreement is observed between the calculations based on literature data for K_a and

the data calculated from the specific conductances, using the technique proposed in the present

paper.
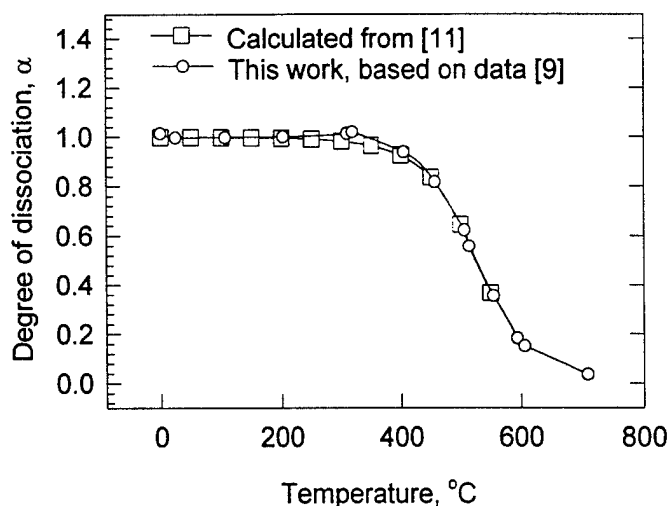
Figure 8-2. Comparison of α calculated by Equation (15) with the calculated based on K_a available in literature.

8.1.3 CONCLUSIONS

In summary, we have developed a new technique for estimating equilibrium the dissociation parameters from conductivity data. This technique is based on the comparison of the "predicted" and measured values of specific conductance, and employs data at lower temperatures in order to calculate the "predicted" values assuming complete dissociation. The ratio of the specific conductance to the predicted value then yields the degree of dissociation. The most important differences between the proposed method and existing techniques are:

1. It is not necessary to know the specific conductance at a number of concentrations and densities (pressures).

2. Low temperature data, which are usually readily available, are employed for the calculation of the "predicted" data.

3. The method can be used at relatively high concentrations of the electrolyte, because it does not involve the Debye-Huckel or Onsager equations for estimating α.

We note, that the approach presented in this paper yields values of α that are in good agreement with the data obtained using other, more classical, techniques. We have shown, that in absence of a large amount of experimental data, especially measured at several, (including low) concentrations and at several pressures, this approach can be successfully used to estimate of α and hence K_a (or K_d).

8.1.4 REFERENCES

1.   W. L. Marshall and J. D. Frantz, in Hydrothermal Experimental Techniques, Edited by G. C. Ulmer and H. L. Barnes, Wiley-Interscience Publ., NY, p. 261 (1987).

2.   W. L. Marshall, J. Chem. Phys., 3639 (1987).

3.   R. M. Fuoss and T. Shedlovsky, J. Amer. Chem. Soc., **71**, 1496 (1947).

4.   G. Zimmerman, M. S. Gruszkiewicz, and R. H. Wood, J. Phys. Chem., in press.

5.   R. M. Fuoss and K. L. Hsia, Proc. Nat. Acad. Sci., **57**, 1550 (1967).

6.   R. Fernandez-Prini, Trans. Faraday Soc., **65**, 3311 (1969).

7.   A. S. Quist and W. L. Marshall, J. Phys. Chem., **72**, 684 (1968).

8.   A. S. Quist and W. L. Marshall, J. Phys. Chem., **69**, 2984 (1965).

9.   A. S. Quist and W. L. Marshall, J. Phys. Chem., **73**, 978 (1969).

10. ASME Steam Tables, Sixth edition, ASME, NY (1993).

11. J. W. Johnson, E. H. Oelkers, and H. C. Helgeson, Computers & Geosciences, **18**, 899 (1992).

SECTION 9

CORROSION STUDIES

9.1. CORROSION MEASUREMENTS AND MODELING

9.1.1 Introduction

Pronounced corrosion damage occurs in regions of the SCWO process stream that are at temperatures around the critical temperature of water, and few materials (mostly, noble metals) are immune to attack[1-7]. The corrosion process is believed to involve acid attack under highly oxidizing conditions, in which the corrosion rate depends on both the concentration of oxygen and on the concentration of H^+. We will outline here a phenomenological model for the development of corrosion damage in SCWO systems, with emphasis on explaining the spatial distribution of damage in relationship to the distribution in temperature (the most pronounced damage is often observed in parts of the reactor that are at temperatures around the critical point, with lesser damage being observed at higher and lower temperatures). We also discuss the effect of pressure (hence solvent density) upon the concentration of aggressive species in supercritical water and upon the corrosion mechanism.

The aggressive species arise from the oxidation of the organic waste that is being destroyed in the reactor, for example

$$C_a H_b X_c + (a + (b - c)/2)O_2 \longrightarrow aCO_2 + ((b-c)/2)H_2O + cH^+ + cX \qquad (1)$$
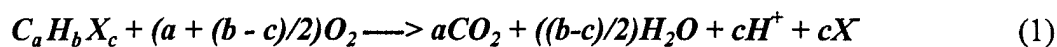
where X represents a heteroatom (typically, a halogen such as Cl). Thus, from a chemical kinetic viewpoint, the rate of corrosion of any metal in contact with the process environment may be written as

$$R = k_c C_{O_2}^d C_{H^+}^n \qquad (2)$$

where k_c is the heterogeneous rate constant and d and n are the kinetic orders of the corrosion reaction with respect to O_2 and H^+, respectively. The oxygen content is determined by the relative rates of addition (by oxygen injection) and consumption (by oxidation of the organic feed stock and corrosion). Provided that the system operates in a steady-state, and that the steady-state concentration of oxygen, which is maintained in great excess, is controlled as a process parameter, it is reasonable to assume that the molal concentration of oxygen (m_{O_2}) is constant throughout the entire system. (This is particularly true because of the highly turbulent conditions that exist in SCWO systems). Accordingly, the three parameters that would seem to govern the spatial distribution of corrosion damage in a SCWO reactor are the temperature (which affects k_c), m_{H+} (the molal concentration of H^+, which is determined by the temperature-dependent dissociation of HX), and density, which affects the molar concentrations of all species in the system. For simplicity, we do not consider X^- as being an aggressive ion, because in high temperature solutions of low pH the prevailing form of corrosion is acid attack and not X-- induced corrosion (e.g., pitting).

9.1.2 Phenomenological Model

Without delving into the detailed mechanisms of corrosion, we can express the corrosion rate in terms of the volume-based (molar) concentrations of aggressive species and the temperature dependence of the heterogeneous rate constant, $k_c=k_c{}^o exp(-E/RT)$, in a form that is obtained from Equation (2)

$$R = k_c^o C_{O_2}^d C_{H^+}^n \ exp(-E/RT)$$

(3)

9-3

where E is the energy of activation of the corrosion process, which may be determined by diffusion or by charge transfer, superscript "o" designates the reference temperature, and C_i is the volume-based (molar) concentration of the i-th aggressive species. We do not take into account here any potential dependence of the corrosion rate. By taking d=n=1, we obtain the relative (or reduced) corrosion rate as:

$$R/R^o = \left[C_{H^+}/C_{H^+}^o \right] * \left[C_{O_2}/C_{O_2}^o \right] exp(-E/RT + E/RT^o)$$

(4)

Equation (4) may be expressed in logarithmic form as follows:

$$log(R/R^o) = log\left[C_{H^+}/C_{H^+}^o \right] + log\left[C_{O_2}/C_{O_2}^o \right] + (-E/RT + E/RT^o) / 2.303$$

(5)

The concentrations C_{H+} and C_{O2} are density(ρ)-dependent and can be obtained from the molal concentrations by

$$C = \frac{m\rho}{1 + 0.001m * \overline{M}}$$

(6)

where $\overline{M}$ is the molecular weight of the dissolved species. For HCl- and O_2-containing solutions, we can approximate $1 + 0.001m * \overline{M} \cong 1$ with reasonable precision for concentrations of up to 1-2 m. Hence, Equation (6) is simplified and can be written for O_2 and H^+ as follows:

$$C_{H+} = \rho m_{H+}$$

(7)

$$C_{O2} = \rho m_{O2}$$

(8)

Because of the unavailability of the data on the density of HCl solutions over the large ranges of the temperature and pressure of interest in this work , we will use the density of water in the following calculations. Substituting Equations (7) and (8) into Equation (5), and assuming that m_{O2} is constant (independent of temperature), we obtain:

$$log(R/R^o) = log\left[m_{H^+}/m_{H^+}^o\right] + 2\,log\left[\rho/\rho^o\right] + \left(-E/RT + E/RT^o\right)/2.303 \tag{9}$$

Equation (9) represents an important relationship showing the various contributions to the relative corrosion rate. The first term shows the effect of changes in the concentration of H^+ (aggressive species), due to the changes in dissociation constant of HCl. The second term represents the effects of the density of water on the concentrations of the two aggressive species in the system; oxygen and H^+. Finally, the third term represents the exponential effect of temperature on the rate constant (Arrhenius dependence).

The value of m_{H+} may be estimated by considering the HCl dissociation reaction

$$HCl = H^+ + Cl^- \tag{10}$$

along with water dissociation

$$H_2O = H^+ + OH^- \tag{11}$$

For Reactions (10) and (11), we establish the following system of four equations, which include the mass action constants, and the mass balance and charge balance constraints:

$$K_d = \frac{m_{H^+}\,m_{Cl^-}\,\gamma_{\pm}^2}{m_{HCl}\,\gamma_{HCl}} \tag{12}$$

$$K_W = m_{H^+}\,m_{OH^-}\,\gamma_{\pm}^2 \tag{13}$$

$$m_{HCl}^o = m_{Cl^-} + m_{HCl} \tag{14}$$

$$m_{H+} - m_{Cl^-} - m_{OH^-} = 0 \tag{15}$$

Here $\gamma_{\pm}$ is the mean molal activity coefficient, and m_{HCl}^o is total (stoichiometric) molal concentration of HCl in solution. Combining Equations (12)-(15), and assuming $\gamma_{HCl} = 1$, we obtain:

$$m_{H^+}^3 + m_{H^+}^2 \frac{K_d}{\gamma_\pm^2} - m_{H^+}\left[\frac{K_W}{\gamma_\pm^2} + \frac{m^o K_d}{\gamma_\pm^2}\right] - \frac{K_d K_W}{\gamma_\pm^4} = 0 \tag{16}$$

The activity coefficients can be estimated using Debye-Hückel theory in the following form:

$$\gamma_\pm = 10^{\wedge}\left(\frac{-A\sqrt{I}}{1+\sqrt{I}}\right) \tag{17}$$

where I is the ionic strength, $I = \frac{1}{2}\Sigma C_i z_i^2$, and A is the Debye- Hückel limiting slope, provided that the I is not too high (I < 0.1 mol/L). The limiting slope was estimated for the temperature range of interest (0 to 550°C) by employing the dielectric permittivity and density of water data given in Reference [8]. The ionic strength of the system is written as:

$$I = 1/2\,C_{total} = 1/2(C_{H^+} + C_{OH^-} + C_{Cl^-}) \tag{18}$$

Because of the electroneutrality of the solution,

$$C_{total} = 2C_{H^+} \tag{19}$$

and we obtain:

$$I = m_{H^+}\rho \tag{20}$$

Substituting Equations (20) and (17) into (16), we finally obtain:

$$m_{H^+}^3 + m_{H^+}^2 K_d 10^{\wedge}\left(\frac{2A\sqrt{m_{H^+}\rho}}{1+\sqrt{m_{H^+}\rho}}\right) - m_{H^+}\left[K_W + m^o K_d\right]10^{\wedge}\left(\frac{2A\sqrt{m_{H^+}\rho}}{1+\sqrt{m_{H^+}\rho}}\right) - K_d K_W 10^{\wedge}\left(\frac{4A\sqrt{m_{H^+}\rho}}{1+\sqrt{m_{H^+}\rho}}\right) = 0 \tag{21}$$

The molal dissociation constant of HCl, K_d, can be obtained from the data of Frantz and Marshall[9] as :

$$\log K_d = -5.405 + 3874.9\,/\,T(K) + 13.93\log\rho \tag{22}$$

We note here that the reliability of the Equation (22) at low temperatures as well as at low

densities is conditional, because it is based on high temperature, high density experimental data.

Data for the density of water, and for K_W as a function of temperature and density were obtained

from Reference [4], and Equation (21) was solved numerically for m_{H+}. The molar

concentrations of the hydrogen ion, C_{H+}, were estimated by employing Equation (7). The C_{H+} vs.

temperature profiles for two molal HCl concentrations are presented in Figure 9-1.
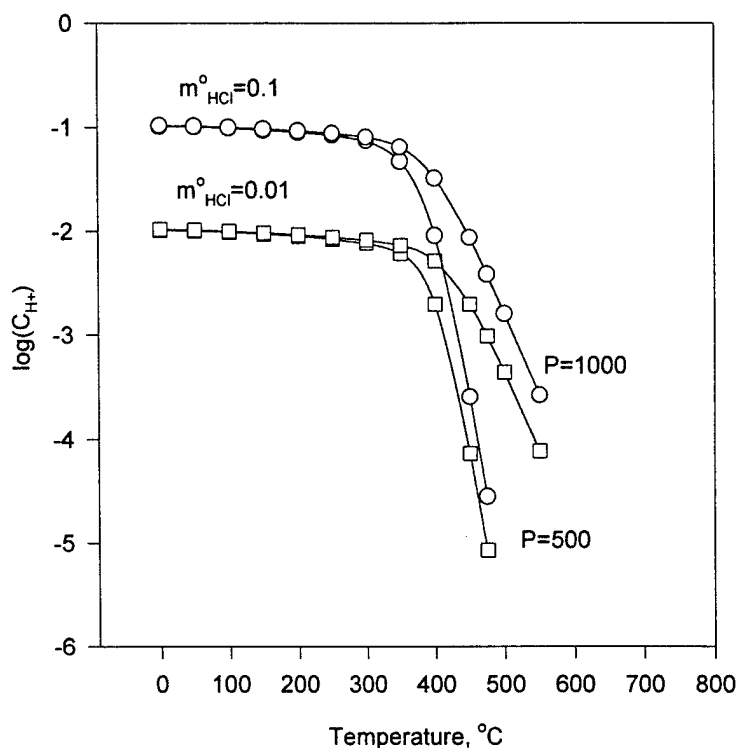
Figure 9-1. Molar concentration of hydrogen ions (C_{H+}) vs. temperature for two total
concentrations of HCl m^o_{HCl} =0.1 and m^o_{HCl} =0.01 at pressures (P) of 500 and 1000
bars.

According to Figure 9-1, the concentration of hydrogen ion is predicted to decrease very rapidly with increasing temperature above 300°C and especially so above the critical point. Furthermore, a one order of magnitude change in the total HCl concentration is predicted to have a relatively small effect upon C_{H+} at supercritical temperatures. In this sense, supercritical water has a buffering effect upon the hydrogen ion concentration. If other electrolytes, with a common anion, are present in the system, C_{H+} will be even lower than that shown in Figure 9-1.

Values for $\log(R/R°)$ derived from Equation (9) are plotted in Figures 9-2 and 9-3 as a function of temperature. The energy of activation, E, was taken to be 25, 50, and 100 kJ/mol. The lowest and highest values were selected to simulate diffusion control and activation control, respectively. The value E=50 kJ/mol was chosen to simulate a mixed control. We find that the
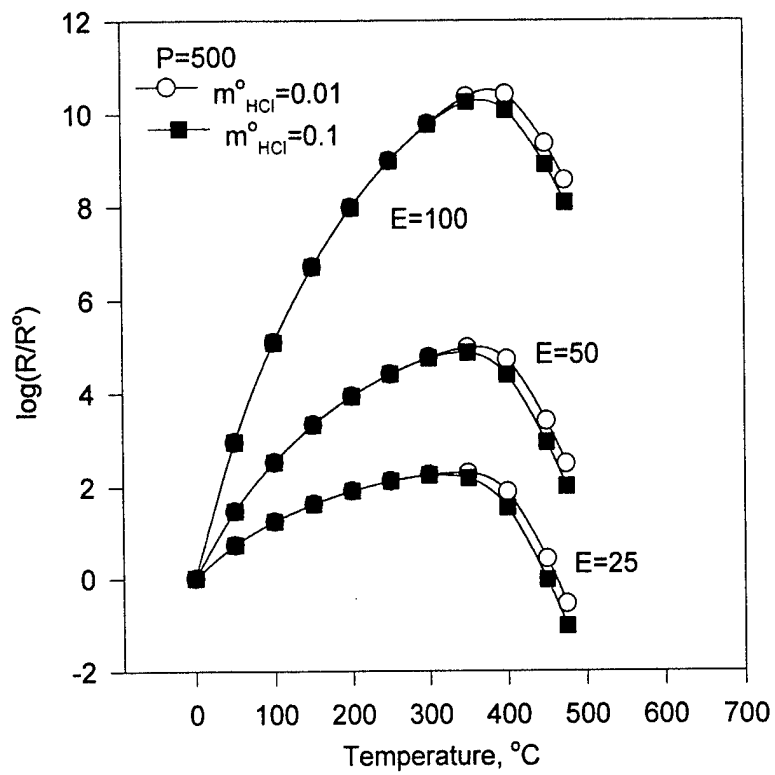
Figure 9-2. Relative corrosion rate vs. temperature at $m^o_{HCl} = 0.1$ and $m^o_{HCl} = 0.01$, pressure (P) of 500 bars and for activation energies (E) of corrosion process of 25, 50, and 100 kJ/mol.
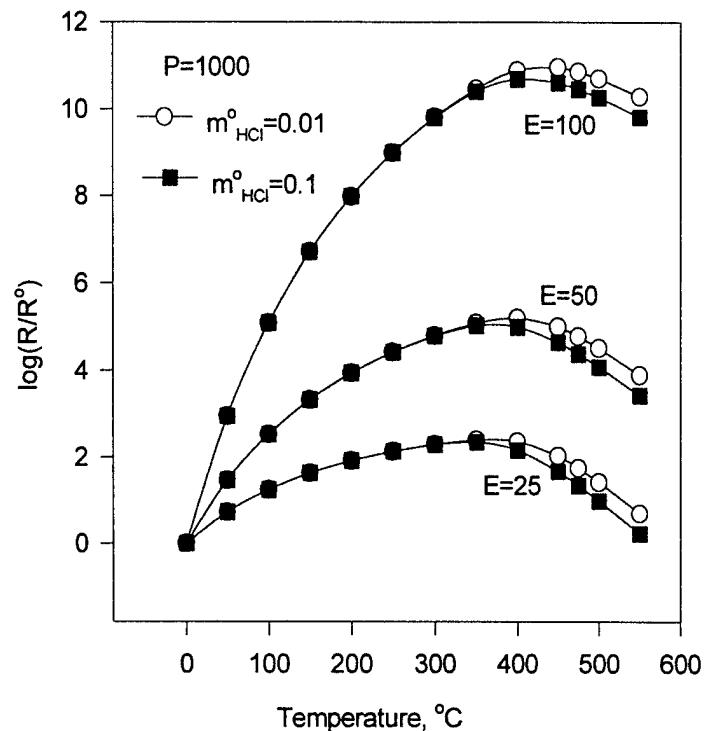
Figure 9-3. Relative corrosion rate vs. temperature at m^o_{HCl} =0.1 and m^o_{HCl} =0.01, pressure (P) of 1000 bars and for activation energies (E) of corrosion process of 25, 50, and 100 kJ/mol.

relative corrosion rate vs. temperature passes through a pronounced maximum in the vicinity of the critical temperature, regardless of the value of the activation energy within the range selected. The initial increase in the relative corrosion rate observed in Figures 9-2 and 9-3 is due to the exponential (Arrhenius) dependence of the rate constant on temperature. The rapid decrease of the concentration of aggressive species in solution at higher temperatures (see Figure 9-1), caused by the decrease of the dissociation constant of the electrolyte and the decrease in the solution density, results in the pronounced maximum of the corrosion damage function in the

vicinity of critical point (Figures 9-2 and 9-3). The decrease in the corrosion rate is not as pronounced at higher pressures, where the water is relatively more dense. Under these conditions, K_d, K_w, and ρ are less dependent upon temperature than they are at lower pressures, so that the drop-off in R/R° at temperatures above the critical temperature, in particular, is less pronounced.

The behavior predicted by Equation (9) is indeed observed in SCWO systems[4-6]. For example, this behavior is well demonstrated by our studies of corrosion activity using reaction zone is changed through the critical temperature (Figure 9-4). Because the increase in pH reflects the extent of metal corrosion due to the reactions

$$Me + 2H^+ = Me^{2+} + H_2 \qquad (23)$$

or

$$Me + 2\,HCl = MeCl_2 + H_2 \qquad (24)$$

in the case of a bi-valent metal, the change in the pH directly corresponds to the corrosion rate (i.e., to the amount of the dissolved metal):

$$C_{Me2+} = \frac{1}{2}\,(C^o_{H+} - C_{H+}) = \frac{1}{2}\,(10^{-pH^\circ} - 10^{-pH}) \qquad (25)$$

We should note that this equation is valid only if the test solution is much more acidic than the solution of the corrosion products (metal salts).

The data presented in Figure 9-4 represent pH of the effluent solution measured during corrosion of the Type 316 Stainless Steel tubing in 0.1 m HCl at 3800-4000 psi (262-276 bars) and at temperatures over the range of 25-700°C. The pH of the effluent solution was found to increase with increasing temperature at temperatures up to the critical temperature of water, indicating a corresponding increase in the corrosion rate. At higher temperatures, we observed a
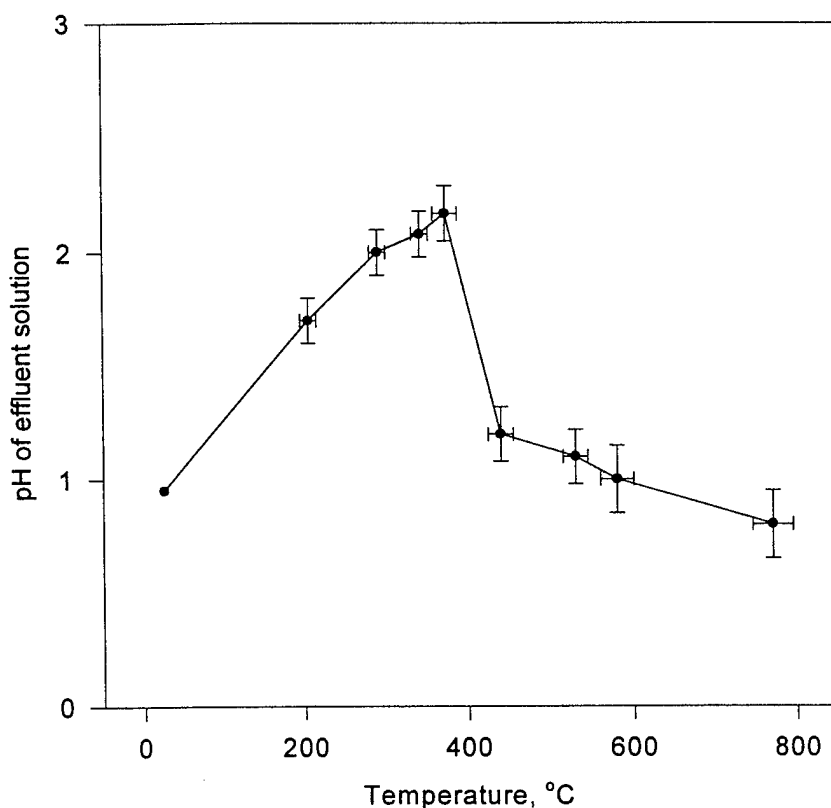
Figure 9-4. Experimental data on the pH of the effluent solution as a function of metal temperature for Type 316 SS in 0.1 m HCl solution.

sharp decrease in the pH with increasing temperature, and eventually the pH of the effluent solution approaches that of the in-going solution. The pronounced maximum in the vicinity of the critical temperature is a manifestation of the phenomenon under consideration in this paper. The decrease in the effluent pH at supercritical temperatures is, however, somewhat faster than the decrease in the corrosion rate, as predicted by the model. This can be explained by the lower value of the pressure, used in the present work, compared with the model calculations (about 270

b in the experiments and 500-2000 b in the calculations). At lower pressures (and hence densities), the effects of the incomplete dissociation of HCl are expected to be much more pronounced [see Equation (22)]. Unfortunately, we cannot perform the calculations at pressures significantly lower than 500 bars, because many of the required thermodynamic data are unavailable for high subcritical and supercritical temperatures at such low pressures.

Another way of viewing the predictions of the model is to note that, at near-critical temperatures and at relatively low densities of the reaction medium, the principal corrosive species changes from hydrogen ion to undissociated HCl, which is somewhat less aggressive. The lower aggressiveness of undissociated HCl is well known[12]. In dry HCl, many metals and alloys are stable and can be successfully used, even at elevated temperatures. However, the presence of moisture, and, hence, dissociation of HCl, significantly increases the corrosion rate, making it similar to the corrosion rate in the aqueous HCl.

From the point of view of the phenomenological model presented above, corrosion mitigation in SCWO systems might be achieved by decreasing the concentration of free hydrogen ion in the supercritical fluid. This can be done by neutralizing the HCl with a basic agent (e.g., NaOH), or by decreasing the dissociation constant of HCl. Dissociation of HCl is drastically decreased at supercritical temperatures by increasing the temperature and/or by decreasing the pressure [Equation (22)]. Consequently, performing oxidation of organic waste at lower pressures and higher temperatures (at a given pressure) could be advantageous for decreasing corrosion rates in SCWO reactors.

9.1.3 Corrosion Mechanism and the Density of Solvent

Electrochemical corrosion usually involves two or more coupled redox reactions (one being the dissolution of the metal), which occur at different sites on the corroding metal surface. In some cases, however, the corrosion process may occur in one act and on one site, without involving coupled reactions. This mechanism of corrosion, which we will refer to as "non-coupled corrosion", is a special case of electrochemical corrosion, but has several distinctive characteristics. Because the process, in the case of the non-coupled corrosion, occurs through direct reaction of aggressive species with the metal in one act (or in several elementary steps, but on one site), no electrons are transferred through the corroding metal from an anodic site to a coupled cathodic reaction site. Accordingly, no ionic current flows through the solution between the anodic and cathodic sites. The limiting case of non - coupled corrosion, presented here only for the purpose of illustration, is the corrosion of a metal in a gaseous atmosphere at elevated temperatures, e.g.,

$$Me + X_2 = MeX_2 \tag{26}$$

$$Me + 2HY = MeY_2 + H_2 \tag{27}$$

$$MeO + 2HY = MeY_2 + H_2O \tag{28}$$

where X_2 represents O_2, Cl_2, etc., and HY represents HCl, H_2S, etc.

In aqueous solutions, the contribution of the non-coupled corrosion mechanism to the development of corrosion damage should increase in systems where (i) highly aggressive non-ionic species are present, and/or (ii) the conductivity of the solution is very small (the limiting case is gas phase corrosion). It is apparent, as well, that these conditions favor the inhibition of coupled corrosion. We note here that, although the contribution of non-coupled corrosion may

increase, the total corrosion damage can increase or decrease, depending upon relative rates of the coupled and non-coupled mechanisms.

The conditions that exist in SCWO systems at sufficiently high temperatures and relatively low densities are favorable for the non-coupled mechanism of corrosion. First of all, the low conductivities of the supercritical aqueous fluids[9, 13] inhibit ionic current flow between coupled reaction sites. The conductivity of an electrolyte solution decreases drastically with increasing temperature at supercritical temperatures and at low water densities as a consequence of: (i) the decrease in the dissociation constants, K_d and K_w, and (ii) the decrease in the molar concentration of the electrolyte, C, due to the decrease in the density of water. All three parameters (K_d, K_w, and C) are directly related to the concentrations of current-transporting species and thus affect the specific conductivity of the electrolyte.

Secondly, the dissociation of HCl, as shown in Figure 9-1 [see as well Equation (22)], decreases precipitously above the critical point, especially at low fluid densities. This as well favors the non-coupled mechanism of corrosion. Undissociated HCl can attack metals directly (e.g., by following reaction):

$$Me + 2HCl = MeCl_2 + H_2 \tag{29}$$

or through multi-step, non-coupled processes, for example:

$$2 Me + HCl = Me\text{-}H + Me\text{-}Cl \tag{30}$$

$$2 Me\text{-}H = 2 Me + H_2 \tag{31}$$

$$2 Me\text{-}Cl = MeCl_2 + Me \tag{32}$$
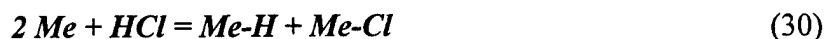
This kind of non-coupled corrosion [Reactions (29) and (30)-(32)] may be described in terms of a transition from the corrosion mechanisms characteristic of liquid phases to those of a gas-phase,

or from an ionic mechanism to a molecular mechanism. In view of this, several important consequences are immediately apparent. First of all, characterization of the aggressiveness of supercritical solutions, especially at medium and low densities, and at temperatures considerably higher than critical temperature, only in terms of pH of the solution may not be viable. The corrosion damage under SCW conditions is determined by the activity (concentration) of undissociated HX and not only by the activity of H^+. Thus, traditional techniques of assessing the corrosion susceptibility, such as by using potential-pH (Pourbaix) diagrams and potential measurements at supercritical temperatures[14], should be supplemented, at least at low solvent densities, by developing diagrams of the corrosion susceptibility vs. concentration (activity) of HX.

Finally, it is of interest to determine whether the maximum in the corrosion rate that is observed at temperatures close to the critical temperature can be accounted for by the "non-coupled" mechanism. We have explored this issue by writing the reduced corrosion rate in a form that is analogous to Equation (9), except that m_{H+} is replaced by m_{HCl}, and we have plotted $\log(R/R^\circ)$ against temperature for three activation energies and a stoichiometric HCl concentration of 0.1 m at two pressures (500 and 1000 bar) (Figure 9-5). Although this analysis is preliminary in nature, the non-coupled mechanism, as developed in this work, does not yield a maximum in the reduced corrosion rate at any temperature within the 0°C to 550°C range employed. Instead, the reduced corrosion rate increases monotonically with increasing temperature, which leads us to conclude that the maximum in the corrosion rate that is observed in the neighborhood of the critical temperature is due to attack involving free (solvated) hydrogen ions in the fluid.
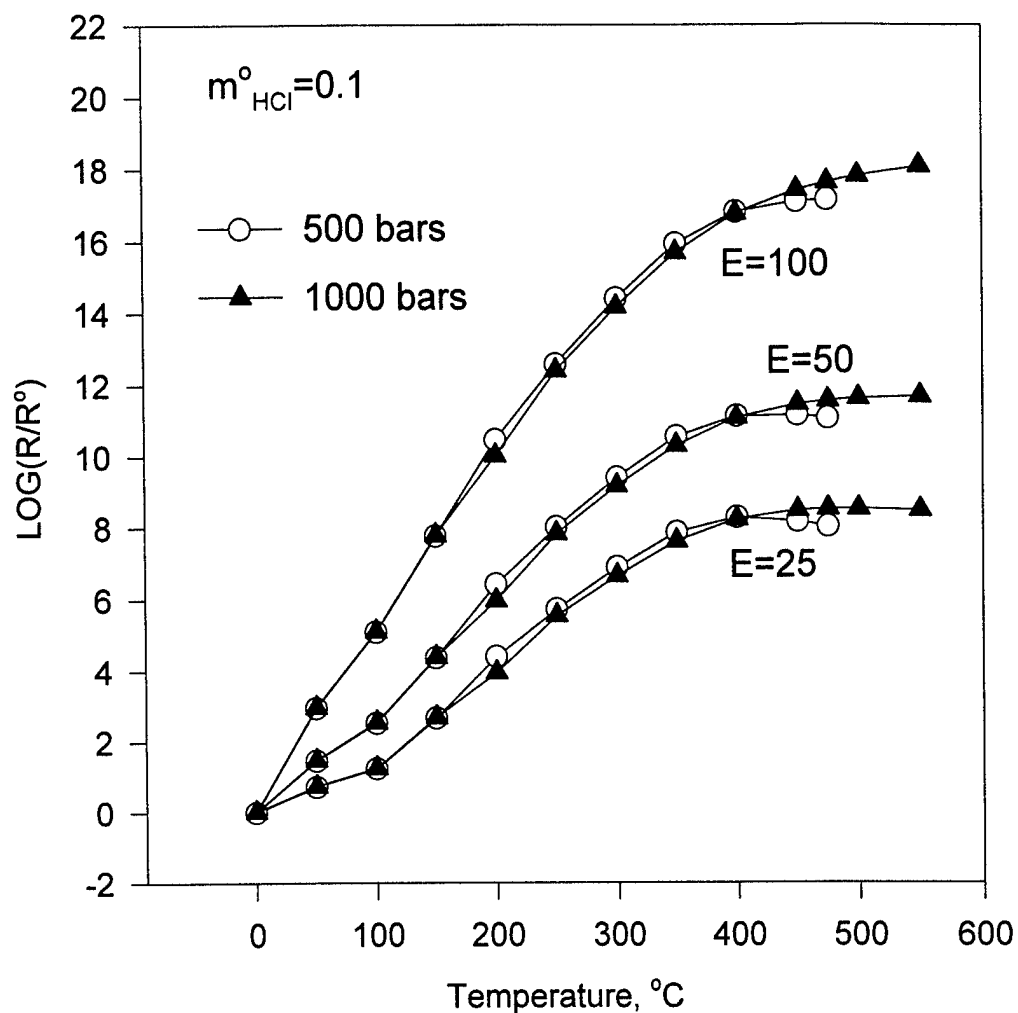
Figure 9-5. Relative corrosion rate vs. temperature for m^o_{HCl} =0.1, for pressures of 500 and 1000 bar, and for activation energies (E) 25, 50, and 100 kJ/mol. Undissociated HCl was considered to be the aggressive species. The concentration of undissociated HCl at temperatures 0-100°C was assumed to be $1*10^{-7}$ m.

Finally, analysis of corrosion phenomena in aqueous systems at high subcritical and supercritical temperatures demonstrates the importance of electrolyte dissociation and the

conductivity of the solution in determining corrosion damage and corrosion mechanisms. A phenomenological model has been developed to simulate corrosion processes at nearcritical and supercritical temperatures in SCWO systems. The following principal conclusions may be drawn from this analysis:

1. The rapid decrease of the concentration of aggressive species in solution at near-critical temperatures, caused by the decreases in the dissociation constant of the electrolyte (e.g., HCl) and solvent density, results in the pronounced maximum of the corrosion damage function in the vicinity of the critical point. The maximum arises from the competing effects of temperature on the reaction rate constant and on the concentrations of H^+ and O_2 through the dissociation of HCl and through the water density. The predictions of the model are in agreement with experimental data.

2. At higher temperatures, where only non-dissociated HCl is present and where the conductivity of solution is very low, the corrosion reaction is predicted to occur via a non-ionic mechanism, without involving coupled partial charge transfer reactions.

9.1.4 Choice of Process Parameters and Materials

From the point of view of the experimental and modeling results presented above, performing oxidation of organic waste at lower pressures and higher temperatures (at a given pressure) could be advantageous for decreasing corrosion rates in SCWO reactors. At the same time, the measurements of polarization curves for metals and alloys, combined with potential-pH diagrams, provides a basis for the choice of the construction materials to be used in different locations and under different conditions (pH, temperature) in SCWO reactors.

Another important issue in the operation of SCWO reactors is the accumulation of inorganic products of oxidation/neutralization reactions (mostly salts) that are sparingly soluble at supercritical temperatures and at low water densities. It is suggested, that after the significant accumulation of salts has occurred, the waste feed to the reactor should be stopped, and temperature decreased to 200-350°C, at which temperature the majority of inorganic salts are significantly soluble in water. During this short cooling down of the system, the salts deposits should rapidly dissolve in the water and be removed from the reactor by the water flow. After several minutes of operation in the lower temperature regime, the temperature would then be increased in order to continue the waste destruction process. This *in situ* approach should allow one to avoid costly mechanical systems for reactor cleaning.

9.1.5 Electrochemical Polarization Studies

The selection of materials for use in many industrial environments, including supercritical power plants and Supercritical Water Oxidation (SCWO) of waste systems requires a broad study of the forms and rates of corrosion of metals and alloys in supercritical (T>374°C) aqueous environments. Nickel is an important component of many alloys and a classic model metal in corrosion studies, extensively investigated at ambient temperatures.

We have developed experimental techniques for performing electrochemical polarization studies at high subcritical and supercritical temperatures. The measurements are performed in a stainless steel high temperature high pressure test cell. Working electrode (Ni) and counter electrode (Pt) are incorporated in an alumina holder with the PTFE support. A silver/silver chloride external pressure balanced electrode was employed as a reference electrode. We have

measured polarization curves at temperatures over the range 20-430°C and at a pressure of 5000 psi in deaerated 0.01 m solution of NaOH.

In Figure 9-6 we present polarization curves obtained in 0.01 m NaOH over the temperature range from 20 to 400°C. The classic behavior of a passive metal is observed at temperatures up to 400-410°C, with the active dissolution "hump" being more pronounced when compared with the ambient temperature behavior. At 430°C and higher temperatures, the conductivity of the solution is very low and polarization measurements have proven to be difficult to perform and interpret. The reproducibility of measurements is illustrated by Figure 9-7, where we present data measured at 400°C with interval of 20 minutes.
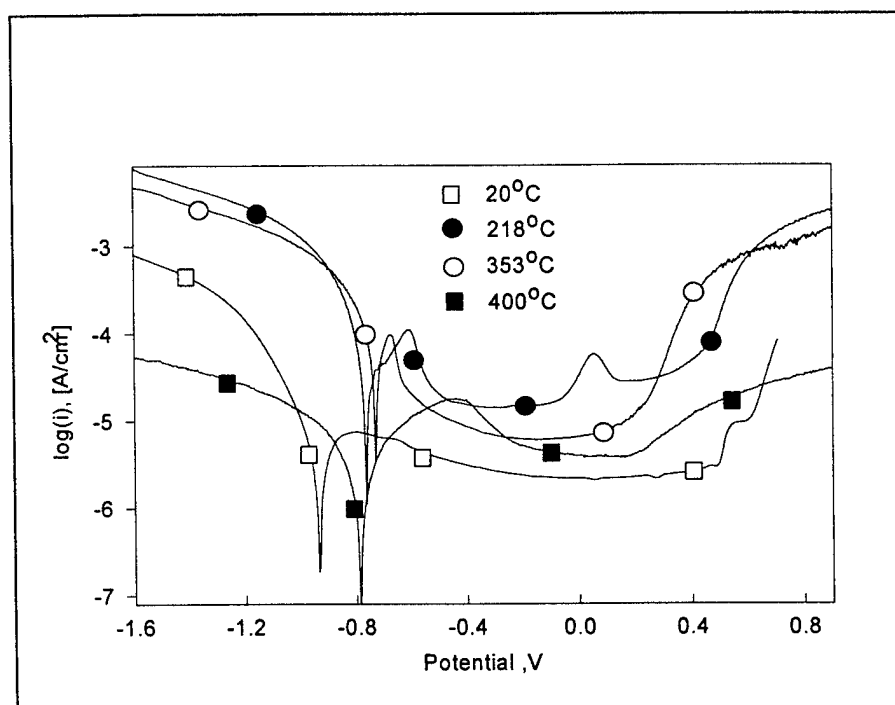
Figure 9-6. Polarization curves of nickel over the range from 20 to 400°C, measured in 0.01 m NaOH at pressure of 5000 psi.
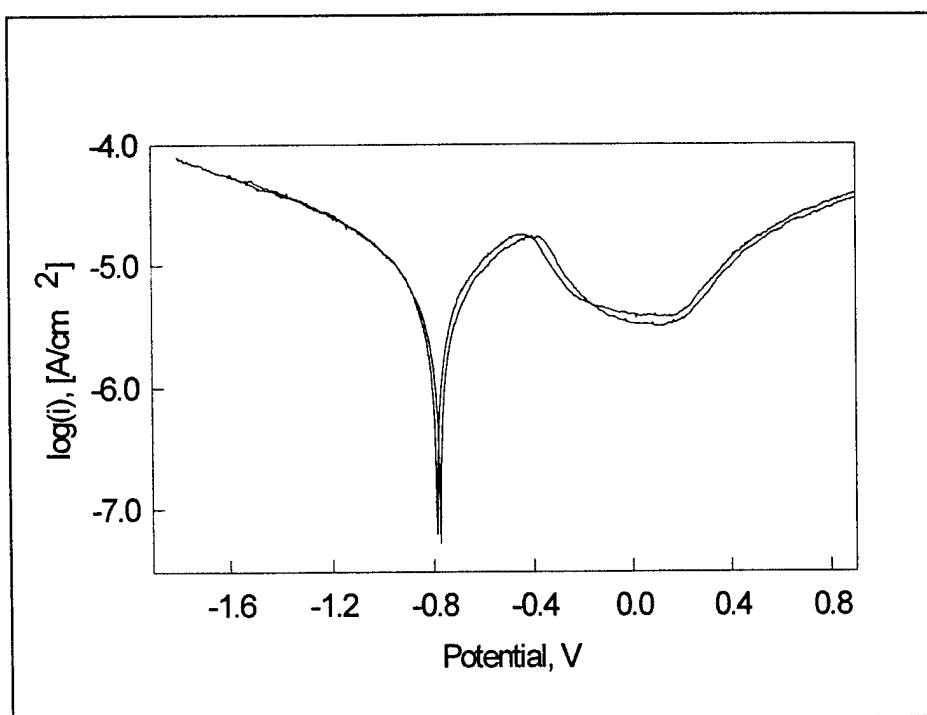
Figure 9-7. Polarization curves of nickel at 400°C, measured with interval of 20 min.

With increasing of the temperature the range of passivity shrinks considerably, as illustrated by Figure 9-8. The strong dependence of the length of the passive region on temperature is observed, because the stability of the metal and metal oxides in solution is temperature dependent. The shrinkage of the passivity region can be caused as well by decrease of the oxygen overvoltage and by the shift of the corrosion (rest) potential towards more positive values. The decrease of the protective properties of nickel oxides can as well result in accelerated passivity breakdown.
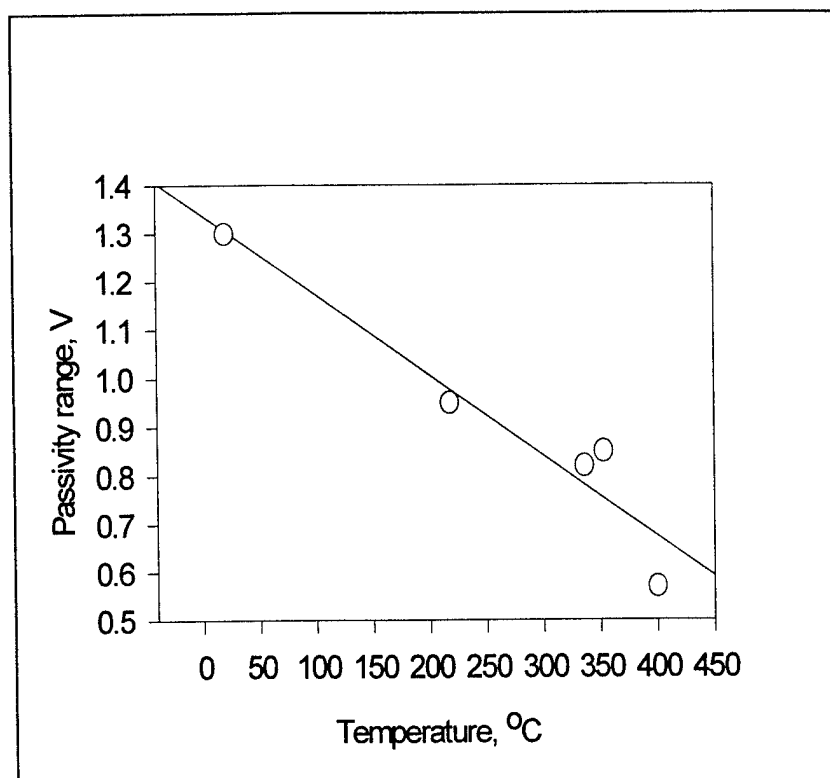
Figure 9-8. The length of passivity range of nickel as a function of temperature.

The value of the current in passive region is very important parameter for the prediction and modeling of the metallic corrosion. In Figure 9-9 we present the current in the passive region as a function of temperature. We note that the passive current goes through a maximum at temperature around 300°C. Passive current is expected to increase with the temperature because it is mainly determined by the transport of ions through the oxide film, that is temperature dependent. From the "solution side" we could predict a dependence of the passive current on temperature due to the "effective" surface area effects (Figure 9-10). Indeed, current on the electrode at a given potential, (in particular, passive current) could be expected to be proportional to density of the solution, because the "contact area" of the electrode (surface area exposed to the solution species) is proportional to the density of the solution. This is illustrated

by Figures 9-10a-9-10d, where in a very simplified form we present an electrode, exposed to solutions of different densities. For simplicity, only molecules of solvent (dipoles of water) are schematically shown. Figure 9-10a corresponds to the water density at reference temperature (20°C), Figure 9-10b illustrates approx. 2.5 times decrease in density with temperature (corresponds to ≈ 400°C at 5000 psi), and Figure 9-10d demonstrates approx. 9 times decrease in water density (corresponds to ≈500°C at 5000 psi).
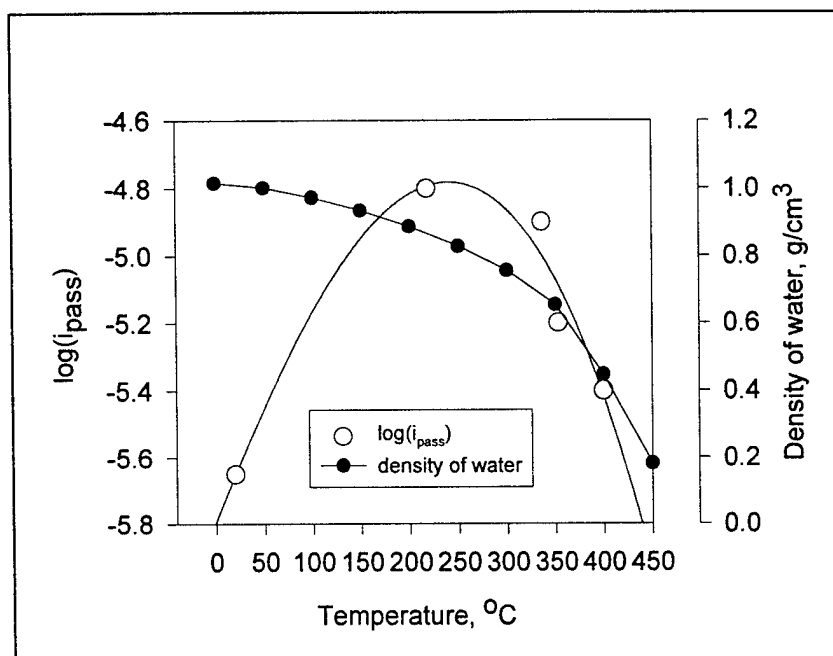
Figure 9-9. Passive current density and water density as a function of temperature at pressure of 5000 psi.

We can as well envisage the situation corresponding to Figure 9-10c, when on the electrode surface exist an adsorbed mono-layer or several layers of undercritical or more dense water. This structure is especially probable if electrolyte phases (or corrosion products) are precipitating on the surface, because solutions of salts usually have higher critical point than pure water. However, the situation corresponding to Figure 9-10c is viable only at temperatures

not much higher than the critical temperature (Tcrit). At temperatures *significantly* higher than Tcrit the energy of solvent and electrolyte molecules will exceed the adsorption energy and we would expect the situation to correspond to Figure 9-10b or 9-10d (we should not anticipate strong ionic specific adsorption because of negligible ionic dissociation at T>>Tcrit).
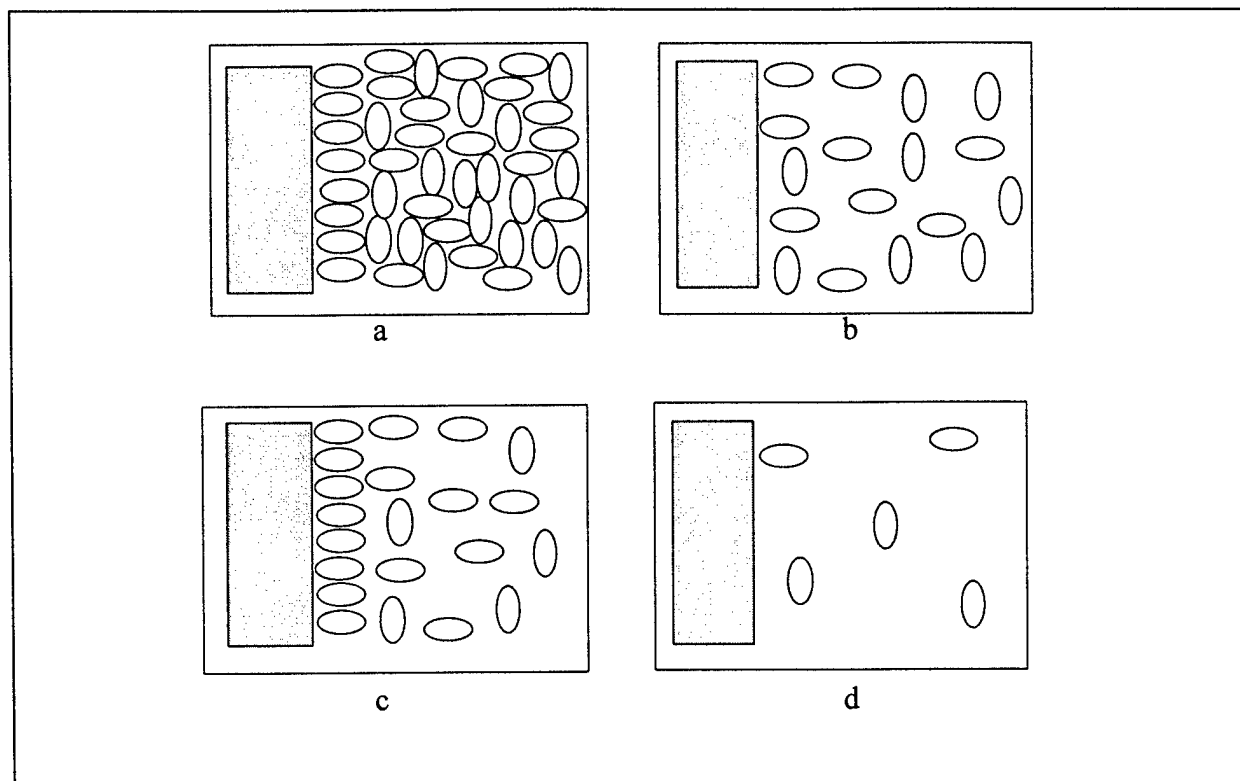
Figure 9-10. Schematic representation of electrode in contact with solution of different densities.

The density of water is presented in Figure 9-9 as well. We note that the current above 300°C is decreasing about 1 order of magnitude, whereas the water density is decreasing about half order of magnitude over same temperature range. Some other effects could contribute to the current decrease, in particular the effects associated with the chemistry of solution: decrease of the concentration of aggressive species (due to density decrease), decrease of dissociation of electrolyte and water and corresponding changes in the pH, etc. Low soluble in near- and

supercritical water corrosion products may as well inhibit the further dissolution of metal. The structure of metal/solution interface (i.e., electric double layer) may significantly change when the density is decreased.

Finally, the maximum on the $\log(i_{pass})$ vs. T°C dependence is probably due to the competition of two effects: increase of the passive current with temperature according to Arrhenius-type dependence and decrease due to effects of density of water (Figure 9-10) and related effects of solution chemistry. Strong effects of density on the electrochemical kinetics from "solution side", namely effects on dissociation of electrolytes and concentration of electroactive species were discussed earlier.

9.1.6 Coupon Tests

We performed coupon tests in HCl solutions at near-critical temperatures. The results are presented in Table 9-1. We note that specimens of Alloy C-22 corroded considerably, and the stainless steel specimen practically dissolved. Interestingly, practically no weight loss was observed for specimens of Nb, Ti, Ta, and Zr. Although these metals have relatively low mechanical strength when compared with Alloy C-22, they can probably be used for the construction of corrosion-resistant internal shells for SCWO reactors.

XPS and SEM analysis has been carried out on selected coupon test samples. We have chosen to analyze the coupon samples of Zircadyne 702 (UNS No. R60702), and Zircadyne 705 (UNS No. R60705) that were exposed to 5 wt. % HCl at 450°C. Chemical compositions of the zirconium alloys are presented in Table 9-2. SEM analysis shows that the thickness of the oxide scale is highly non-homogeneous, indicating non-uniform penetration of HCl solution in the

substrate. XRS analysis indicates that the oxide scale is composed of ZrO_2 (Figure 9-11). With the Zircadyne 705 sample, the alloying elements, Fe, Cr and Nb, were also found in the scale in their oxide states (Figure 9-12). SEM micrographs indicate that the scale formed on Zircadyne 705 shows no difference from that formed on Zircadyne 702. In summary, our coupon tests indicate that, even though zirconium alloys (i.e., Zircadyne 702 and 705) exhibit far better corrosion resistances compared to Alloy C22, these materials still suffer severe general corrosion in the expected supercritical water oxidation environment.

Table 9-1. Results of coupon test at 345°C, 1 m HCl.

Exposure time was 1 hour 10 minutes

number	specimen	weight before g	weight after g	weight loss g	surface area cm^3	corrosion rate g/cm^2/hour
1	C-22	1.005	0.895	0.110	1.384	0.0681
2	C-22	0.457	0.383	0.074	1.005	0.0631
3	SS 316	0.440	dissolved			
4	Ti	0.330	0.328	0.002	2.171	<0.001
5	Nb	0.339	0.339	0.000	1.465	<0.001
6	Zr	0.112	0.111	0.001	0.947	<0.001
7	Ta	0.292	0.291	0.001	1.071	<0.001

Table 9-2.   Chemical composition of zirconium alloys

Chemical Compositions of Zircadyne® Zirconium Alloys				
Grade (UNS No.)	Zircadyne 702 (R60702)	Zircadyne 704 (R60704)	Zircadyne 705 (R60705)	Zircadyne 706 (R60706)
Chemical Compositions. Weight. Percent				
Zr + Hf, min	99.2	97.5	95.5	95.5
Hafnium, max	4.5	4.5	4.5	4.5
Fe + Cr	0.2 max.	0.2-0.4	0.2 max.	0.2 max
Tin	--	1.0-2.0	--	--
Hydrogen, max.	0.005	0.005	0.005	0.005
Nitrogen, max.	0.025	0.025	0.025	0.025
Carbon, max.	0.05	0.05	0.05	0.05
Niobium (Columbium)	--	--	2.0-3.0	2.0-3.0
Oxygen, max.	0.16	0.18	0.18	0.16
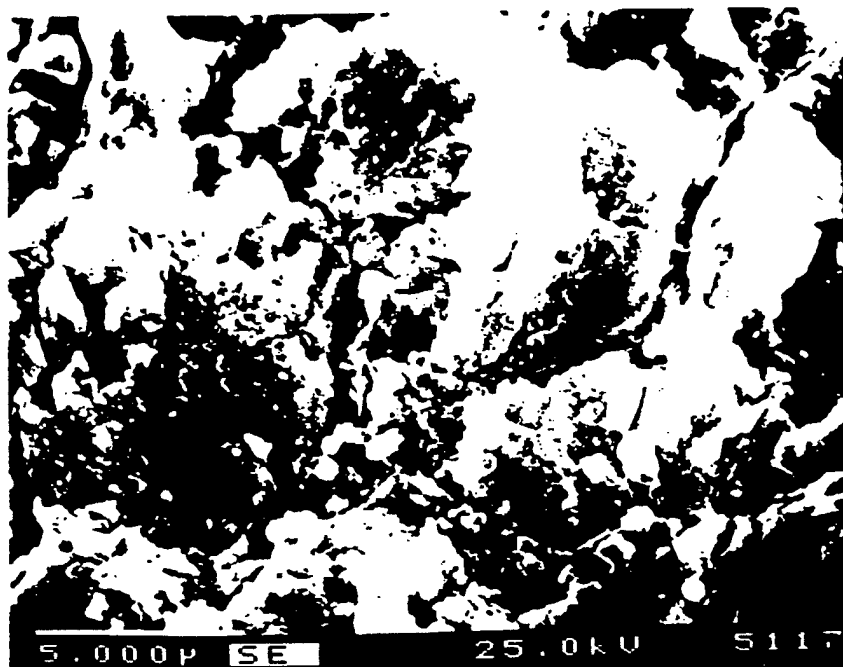
Figure 9-11. SEM morphology of Zircadyne 702, showing structure of ZrO_2 scale after oxidation in 5 wt.% Hcl solution at 450°C, 30 min.
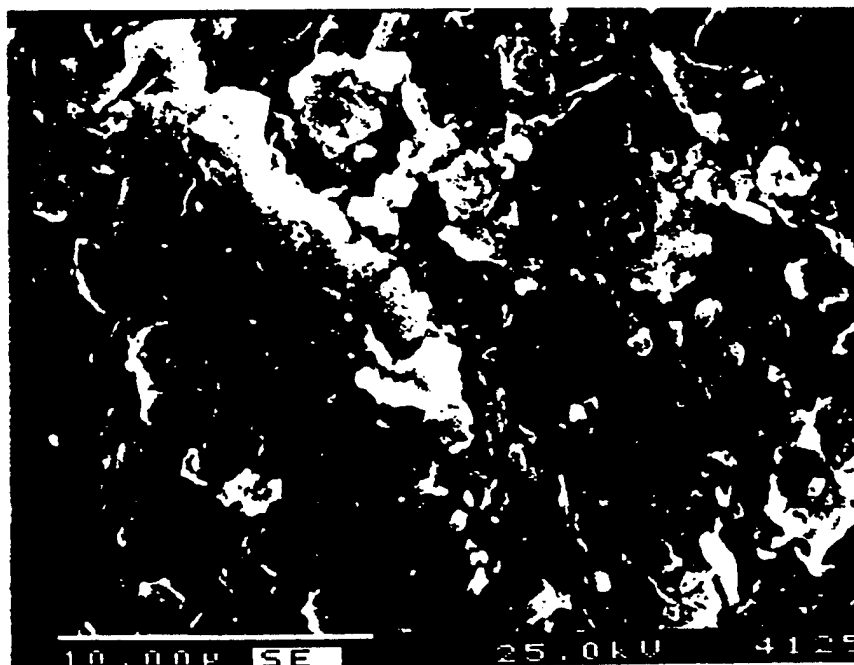
Figure 9-12. SEM morphology of Zircadyne 705, showing structure of ZrO_2 scale after oxidation in 5 wt.% Hcl solution at 450°C, 30 min.

9.1.7 REFERENCES

1. J. W. Tester, H. R. Holgate, F. J. Armellini, P. A. Webley, W. R. Killilea, G. T. Hong, and H. E. Barner, in Emerging Technologies in Hazardous Waste Management III, D.W. Teddear and F.G.Pohland, Editors, ACS Symposium Series 518, ACS, Washington, DC (1993).

2. T. B. Thomason and M. Modell, Haz. Waste 1, 453 (1984).

3. Innovative Hazardous Waste Treatment Technology Series, 1, H. M. Freeman, Editor, Technomic Publ., Lancaster, PA (1990).

4. R. M. Latanision and R. W. Shaw, Corrosion in Supercritical Water Oxidation Systems, Workshop Summary, The Energy Laboratory, MIT (1993).

5. D. A. Hazlebeck, K. W. Downey, D. D. Jensen, and M. H. Spritzer, in Proc. 12 Int. Conf. on the Properties of Water and Steam, Orlando, FL, Sept. 11-16, 1994, Begell House, NY (1995).

6. D. B. Mitton, J. C. Orzalli, and R. M. Latanision, ibid.

7. R. M. Latanision, Corrosion 51, 270 (1995).

8. ASME Steam Tables. Thermodynamic and Transport Properties of Steam. Sixth Edition, ASME, N.Y. (1993).

9. J. D. Frantz and W. L. Marshall, Amer. J. Sci. 284, 651 (1984).

10. L. B. Kriksunov and D. D. Macdonald, in Proc. 12 Int. Conf. on the Properties of Water and Steam, Orlando, FL, Sept. 11-16, 1994, Begell House, NY (1995).

11.   Proceedings of First International Workshop on Supercritical Water Oxidation, February 6-9, 1995, Jacksonville, FL (1995).

12.   M. G. Fontana, Corrosion Engineering, McGraw-Hill, NY, p.352 (1986).

13.   E. U. Frank, Zeitschr. Phys. Chemie, **8**, 192 (1956).

14.   L. B. Kriksunov and D. D. Macdonald, Corrosion, in press (1995).

9.2. ELECTROCHEMICAL NOISE ANALYSIS FOR MONITORING CORROSION ACTIVITY IN SCWO SYSTEMS

9.2.1 Introduction

Most supercritical water oxidation systems are characterized by high corrosion activity.[1-9] All corrosion processes, including general corrosion, pitting attack, crevice corrosion, and stress corrosion cracking, are characterized by fluctuations in the free corrosion potential and in the anodic and cathodic partial currents. These fluctuations are observed as electrochemical noise that is thought to contain significant information about both the activity and mechanism of attack. Electrochemical noise measurements (ENMs) have been used extensively during the past twenty years for monitoring corrosion activity in a variety of systems,[9-24] although the sources of the electrochemical noise is still not clearly defined.[10] In the case of localized corrosion, such as pitting attack, crevice corrosion,[13-17] and stress corrosion cracking,[18-20] the noise frequently arises from discrete events that can be related to the development of damage. In some instance, it has been suggested that ENM can distinguish between different corrosion mechanisms.[22] However, in most cases, viable theories for the origin of the noise have yet to be developed.[11] The main advantage in using electrochemical noise analysis as a corrosion monitoring technique is that it provides real-time information on the activity and mechanism of corrosion processes occurring in the system, which cannot be readily obtained with other methods. To date, most studies reported in the literature have been carried out at ambient temperature and pressure. Although a few studies at high subcritical temperatures have been reported, we can find no previous studies

(other than those carried out in this laboratory) that have been performed above the critical point of water.

In this Chapter, we describe the development of an Electrochemical Noise Analyzer (ENA) for monitoring corrosion activity at temperatures above the critical point of water. The ENA monitors fluctuations in the galvanic coupling current between identical electrodes fabricated from the materials of interest, which, in this case, were carbon steel (SAE-AISI 1013, UNS G10130) and stainless steel (Type 304 SS, UNS S30400).

9.2.2 Experimental Apparatus

The ENA that has been developed in this study is shown schematically in Figure 9-13. The circuit consists of a zero resistance ammeter (ZRA), the output of which passes through a band-pass filter with independently adjustable upper and lower roll-off frequencies. The lower roll-off frequency can be set at 1Hz, 10Hz, 100Hz and 1KHz, while the upper roll-off frequency can be set at 10Hz, 100Hz, 1KHz and 10KHz. Because there is virtually no electrochemical noise at very high frequencies, we have selected 10KHz as the high limit of the upper-roll-off frequency. Therefore, the band-width of the signals that pass this filter can be selected between 10Hz and 10KHz, depending on the selection of upper and lower roll-off frequencies. Amplification of the signals can be regulated through a gain control from 0.1 to 2000. In addition, the sensitivity of the analyzer can be regulated by adjusting the response time over the range from 250ms to 10s. All of these regulation functions are accessible from the front panel of the analyzer. After amplification by the ZRA (AMP-05), and filtering by the band pass filter, the signal is processed by a root-mean square module (RMS, AD636), and is then presented on a

digital display and on a strip-chart recorder. The electronic circuits are carefully shielded in order

to exclude electronic noise from the environment and from sources other than the probes. The

probes consisted of two identical rods fabricated from carbon and stainless steels (f=1.3 mm),

with 12 mm being exposed to the environment through a high pressure fitting in the autoclave.

The probe assembly was located in a pressure vessel that was part of a once-through/

recirculating, high-temperature/high-pressure loop capable of operating at temperatures to 550°C

and at pressures to 310 bar (~4500 psi, or 31.0 MPa).
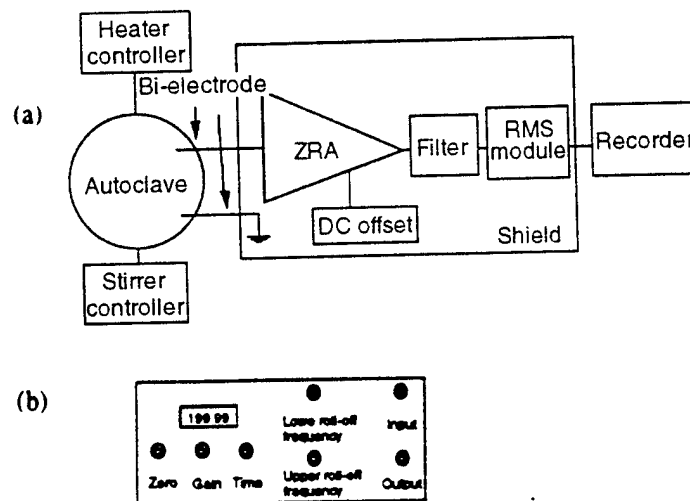
Figure 9-13.   Schematic of the Electrochemical Noise Analyzer (a) Electronic connection, (b)
Front panel layout. (ZRA=Zero Resistance Ammeter, RMS=Root Mean Square).

A schematic of the loop is presented in Figure 9-14. The operating parameters of the loop are such that the density of water in the supercritical region at 500°C could be varied from zero to less than 0.1g/cm^3.[25-26]

9.2.3 Results and Discussion

Electrochemical noise measurements on corroding carbon and stainless steels were carried out at high subcritical (T<374.12°C) and supercritical (T>374.12°C) aqueous environments (in high purity oxygenated water and in 0.1m HCl solution for carbon steel and stainless steel, respectively). Our studies demonstrate that ENMs are a powerful tool for monitoring corrosion activity, as will become evident from the material presented below.
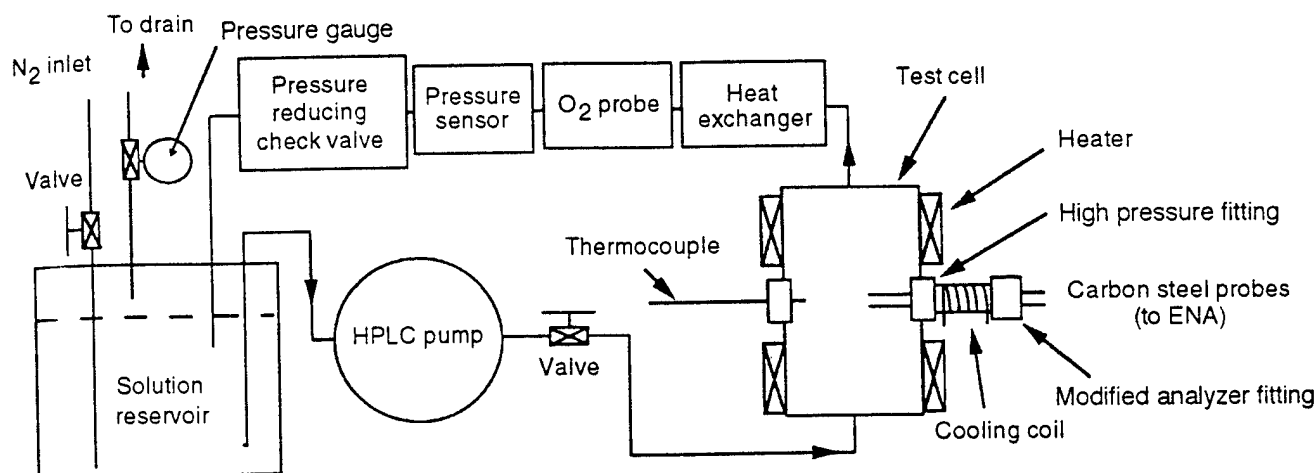
Figure 9-14. Experimental loop (HPLC=High Pressure Liquid Chromatography, HiP=High Pressure Equipment Co.).

In the present design of the monitoring system, we have used a RMS module for signal conditioning. The purpose of this module was to convert any sinusoidal component in the electrochemical noise into a DC output that could be easily displayed on a digital meter. However, the output itself was found to be "noisy", thereby indicating that the electrochemical noise generated is stochastic in nature and is not a simple sinusoidal (Figure 9-15). Other possible sources that may be responsible for the measured noise have been discussed, and it was demonstrated that the measured noise is exclusively generated from the corroding probes in high temperature aqueous environment.[25,26] As shown below, the electrochemical noise consists principally of low frequency components (1-10 Hz), as determined by the band-pass filter.
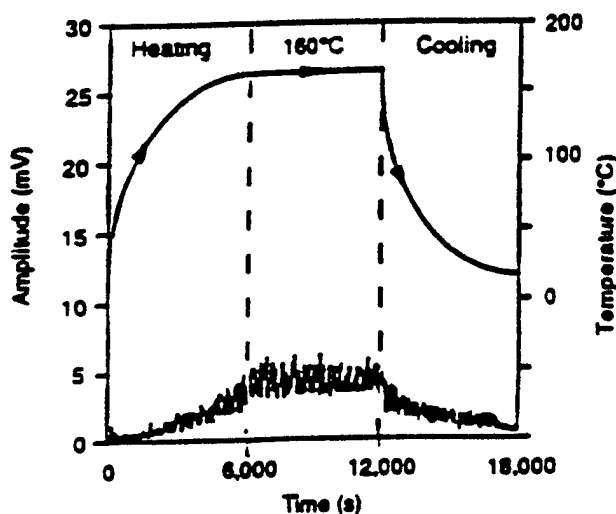
Figure 9-15.   Evolution of electrochemical current noise induced by corrosion of AISI 1013 carbon steel during an experimental heating-cooling cycle (oxygen pressure=40psi (0.28MPa), in-vessel pressure=1200 psi (8.28 MPa), gain=1000, lower roll-off frequency=1Hz, upper roll-off frequency=10Hz).

An important finding of this study is that electrochemical noise is generated on carbon and stainless steels corroding in low density ($r < 0.1 g/cm^3$) supercritical water, and that the noise can be used to monitor corrosion activity. Importantly, the corrosion activity, as measured in

terms of the electrochemical noise amplitude, is found to be most pronounced in the vicinity of subcritical to supercritical transition temperature, as shown with the Type 304 SS sample exposed to oxygen-saturated water and 0.1m HCl solution (see later). To our knowledge, the present work represents the first attempt to perform ENM in supercritical aqueous systems, and, hence, to demonstrate the potential application of this technique in supercritical water oxidation technologies.

9.2.4 The Effect of Temperature

The general response of the electrochemical noise as a function of temperature in subcritical water (liquid phase) is shown in Figure 9-15. The amplitude of the electrochemical noise is observed to increase with increasing temperature. This is an expected response, because elevation of the temperature increases the activity of the corrosion process. The observed electrochemical noise is found to be reversible with respect to temperature, in that lowering the temperature decreases the amplitude of the noise in a predictable, and reversible manner.

In the supercritical region, however, the amplitude of the electrochemical noise versus temperature is found to be rather complicated (Figure 9-16). It is observed that the amplitude of the electrochemical noise initially increases with increasing temperature to a temperature of ~434°C, but then decreases as the temperature increases to 550°C. The origin of the maximum in the electrochemical noise is most likely due to the competing effects of temperature and water density on the corrosion processes. Thus, we speculate that, for T<434°C, the change in the noise amplitude is due principally to the effect of increasing temperature on the kinetics of the (general) corrosion process, but at higher temperatures, decreasing water density exerts a

Figure 9-16. Dependence of electrochemical current noise amplitude for AISI 1013 carbon steel in supercritical water as a function of temperature (data compiled from 3 heating-cooling cycles), and water density (water density data from Reference [27]).

dominant effect. Note that in this figure and subsequent figures the error bars represent the range of fluctuation in the noise signal as observed over a one minute period for the indicated gain and for the stated roll-off frequencies.

9.2.5 The Effect of Pressure

Pressure is found to have strong impact upon the amplitude of the electrochemical noise from corroding carbon steel measured in supercritical water (Figure 9-17). Our experiments have

shown that the amplitude of the electrochemical noise increases sharply on increasing the pressure of the supercritical fluid to 241bar (3500 psi, or 24.1MPa), corresponding to a density increase from $0.062 g/cm^3$ to $0.091 g/cm^3$. The increase in the noise amplitude with increasing density is presumably due to either an increase in conductivity of the fluid between the carbon steel probes or to an increase in the effective concentration of oxygen at the metal surface, or both (Figure 9-17).
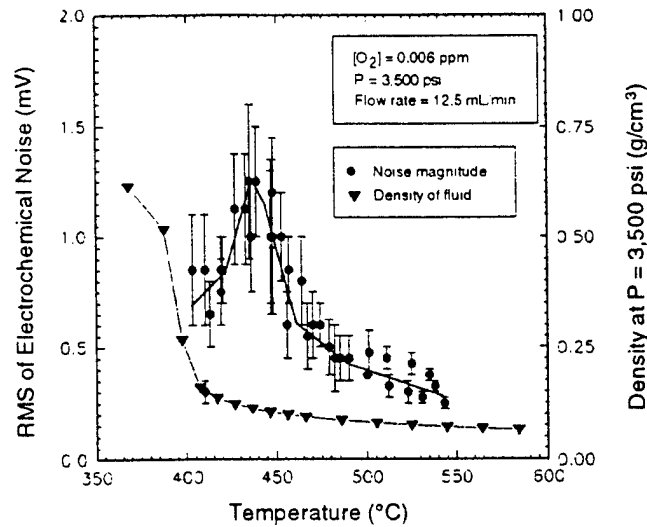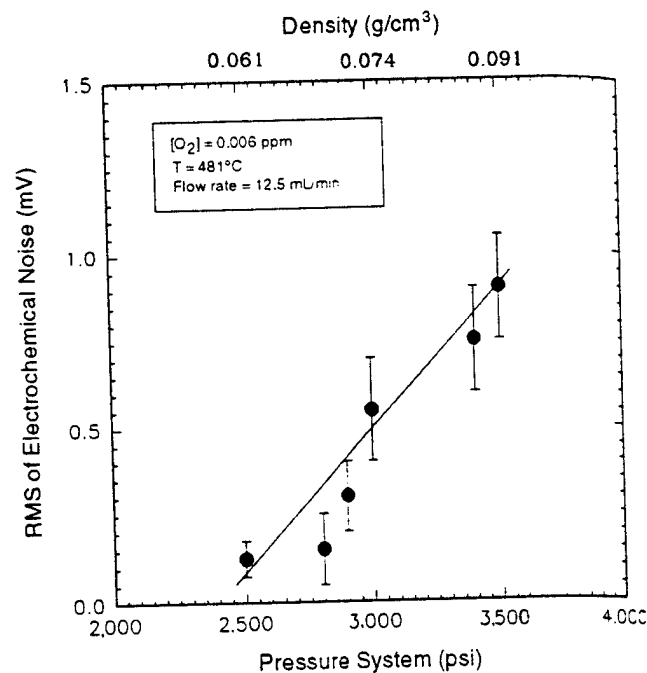

Figure 9-17.   Electrochemical current noise amplitude for AISI 1013 carbon steel in supercritical water as a function of pressure (water density data from Reference [27]).

The effect of bulk flow velocity on the noise generated at a corroding carbon steel/supercritical ater interface has been studied over the range of 0-20ml/min, and the amplitude of the noise was found to increase modestly as the flow rate was increased over the accessible range (Figure 9-19). Part of the observed increase in the noise amplitude may be attributed to a modification of the hydrodynamics of the system, but it is also likely that the high flow rates counteract the consumption of oxygen by corrosion of the loop walls (especially in the hot zone), so that a greater effective oxygen concentration is present in the vicinity of the probes at higher flow rates. The data shown in Figures 9-18 and 9-19 clearly demonstrate the importance of hydrodynamic/mass transport effects in determining the amplitude of the electrochemical current noise induced by the corrosion of carbon steel in subcritical and supercritical water.
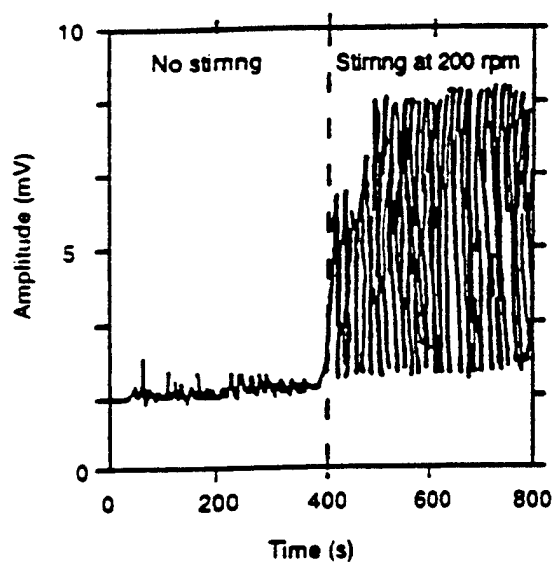
Figure 9-18.   Effect of stirring on the electrochemical current noise induced by corrosion of AISI 1013 carbon steel in water at 244°C (oxygen pressure=40 psi (0.28MPa), in-vessel pressure=1200 psi (8.28MPa), gain=1000, lower roll-off frequency=1Hz, upper roll-off frequency=10Hz).
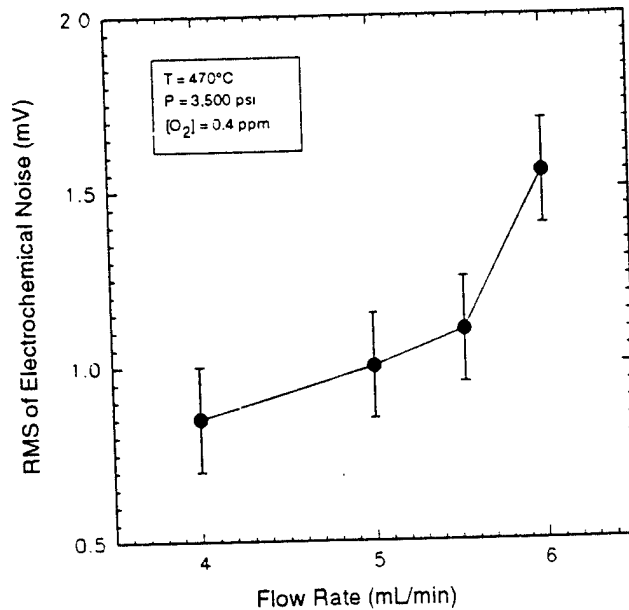
Figure 9-19.   Electrochemical current noise from AISI 1013 carbon steel in supercritical water as a function of flow rate (lower roll-off frequency=1Hz, upper roll-off frequency=10Hz).

9.2.6. The Effect of Oxygen Concentration

The effect of oxygen concentration was studied under both subcritical and supercritical conditions. The solution was prepared to be saturated with pure oxygen (with an oxygen concentration in the solution of $[O_2]= \sim 32$ ppm). The reservoir was then sparged with nitrogen to deaerate the water (Figure 9-14). The pressure in the solution reservoir was maintained slightly higher than one atmosphere to prevent air from entering into the low pressure section of the system. By varying the nitrogen bubbling rate, the oxygen content in the solution could be decreased at a desired rate. The oxygen concentration was measured at ambient temperature

9-41

using a commercial oxygen probe (Ingold Model 170) at the outlet of an autoclave after cooling the process stream. Because a slow deaeration rate was chosen, and because of the small inner channel diameter and volume of the test cell (f=3.18 mm, effective heated length L=101.6mm), the time for the solution to flow from the autoclave to the oxygen probe was an order of magnitude smaller than the time required for a noticeable change in the oxygen concentration. Thus, we conclude that the oxygen concentration measured by the oxygen probe represents the oxygen content in the solution within the test cell, to a reasonable approximation.

In subcritical systems, the magnitude of the electrochemical noise is found to decrease monotonically with decreasing oxygen concentration in the solution (Figure 9-20). Although the data are of only moderate precision, particularly at high oxygen concentrations, the noise amplitude is found to be represented by

$$RMS = 0.01[O_2]^{0.5} \qquad (1)$$

where RMS is the root-mean-square of the noise amplitude, in units of millivolts and $[O_2]$ is the oxygen concentration in ppm. The square root dependence of RMS on $[O_2]$ would appear to indicate that the amplitude of the noise is not controlled by the diffusion of oxygen to the surface, because, in that case a linear dependence might be expected. However, the stirring and flow-rate experiments discussed above clearly demonstrate a mass transport-controlled component in the observed electrochemical noise. At the present time, and until the mechanism of noise generation is better understood, the observed relationship between the electrochemical noise amplitude and the oxygen concentration should be considered purely empirical in nature.
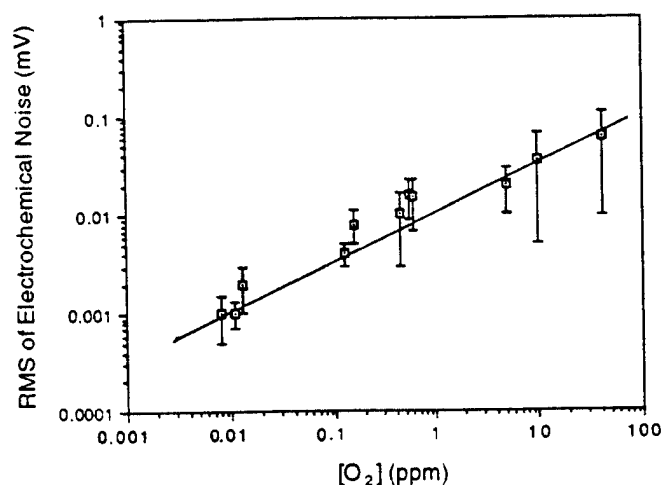
Figure 9-20.   Evolution of electrochemical current noise induced by corrosion of AISI 1013 carbon steel as a function of oxygen concentration in the solution (T=250°C, in-vessel pressure=1400psi (9.66MPa), gain=1, lower roll-off frequency=1Hz, upper roll-off frequency=10Hz).

In supercritical systems (Figure 9-21), the amplitude of the noise was again found to decrease monotonically with decreasing oxygen concentration for $[O_2] > 0.1$ppm, with approximately the same exponent (0.5) as observed at lower temperatures. However, for $[O_2] < 0.1$ppm, the amplitude was found to be independent of $[O_2]$, although the magnitude of the fluctuations in the noise (as expressed by the error bars) renders this observation only semi-quantitative in nature. We note that in this experiment the density of the water is less than 0.1g/cm^3, compared with ~ 0.75g/cm^3 for the subcritical system shown in Figure 9-20. Thus, the data shown in Figure 9-21 may well indicate that the amplitude of the noise at low oxygen level is controlled by the density of the fluid (and, presumably, by the electrical resistance of the fluid

between the probes), and that the effect of oxygen become apparent only for $[O_2] > 0.1$ ppm. This interpretation is consistent with a model which supposes that an electrical analog for the probes employed in this study consists of a series of resistance (R_s), representing the resistance between the probes that is inversely related to the density of the fluid, and two (identical) interfacial independences that describe the corrosion processes that occur at the surface of the two probes. For $[O_2] < 0.1$ ppm, the impedance of the cell is dominated by R_s.
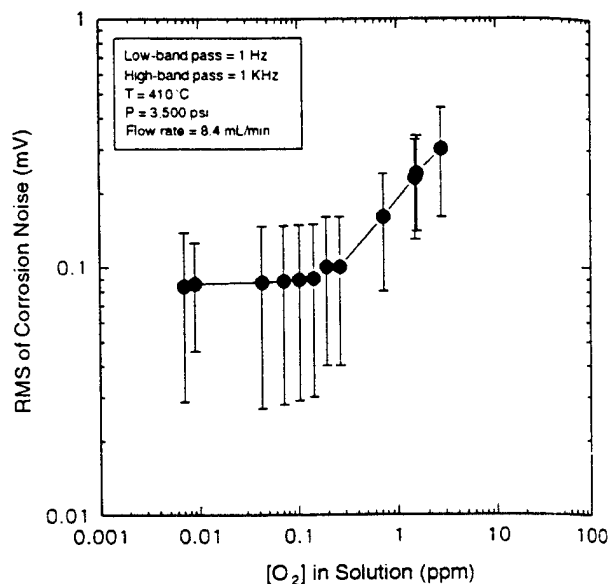
Figure 9-21.   Electrochemical current noise amplitude for AISI 1013 carbon steel in supercritical water as a function of oxygen concentration.

9.2.7 The Frequency Composition

It has been demonstrated in previous studies[28-29] that at high oxygen concentrations and at subcritical temperatures, the electrochemical noise generated by the corrosion of carbon steel is

composed mainly of low frequency components (1-10Hz). A similar distribution in frequency of the components of the electrochemical noise from corroding carbon steel is observed at supercritical temperatures, as shown in Figure 9-22. The spectra show that the noise is composed principally of low frequency components (1-10Hz). Although no literature data are available for the corrosion of carbon steel in supercritical water, data from the literature for systems at ambient temperature show that the electrochemical noise consists principally of low frequency components.[10,22,24]
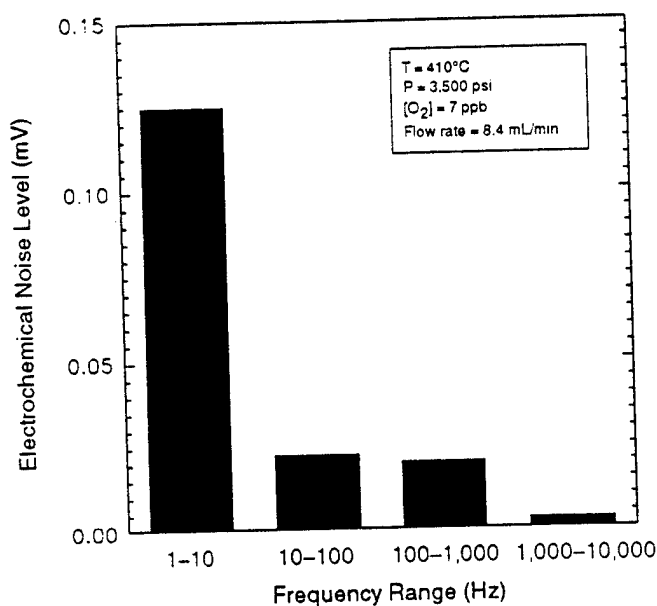
Figure 9-22. The distribution in frequency of the electrochemical noise from AISI 1013 carbon steel in supercritical water (lower roll-off frequency=1Hz, upper roll-off frequency=10KHz, gain=1).

9.2.8 Observation of Pitting Corrosion

During the experiments carried out in this program, certain patterns in the electrochemical noise could be associated with specific experimental conditions. Figure 9-23 shows two different patterns in the magnitude of the electrochemical noise that were observed under two different set of conditions. Shown on the right hand side of Figure 9-23, is a continuous, steady level of the electrochemical noise, while on the left hand side, the noise pattern consists of a series of spikes. The only difference between the two cases is the pressure in the test cell. In searching for a relationship between the noise pattern and the mechanism of corrosion, the surface morphology of the steel specimens before and after exposure to the high temperature water were examined. The occurrence of pitting corrosion during these experiments was clearly demonstrated by the surface morphology.[25-26] While the electrochemical noise pattern shown on the left hand side in Figure 9-23 cannot be directly linked to the occurrence of pitting corrosion, because SEM examination was performed at ambient temperature after disassembling the system, the experiments clearly associate the occurrence of discrete events in the noise pattern with localized corrosion, as has been found for ambient temperature systems.[16]
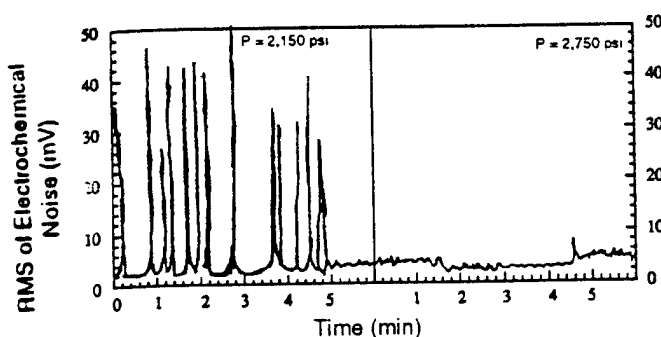
Figure 9-23. The electrochemical current noise from AISI 1013 carbon steel as a function of time in supercritical water (T=405°C, [O₂]=6ppb, flow rate=4.6ml/min, gain=20, lower roll-off frequency=1Hz, upper roll off frequency=10KHz, Pressure=2150 psi (14.84 MPa) and 2750 psi (18.98MPa), as indicated).

9.2.9 Corrosion of stainless steel

We have measured electrochemical noise with probes fabricated from Type 304 SS exposed to oxygen-saturated water and to 0.1m HCl solution. The amplitude of the electrochemical noise, which was continuously monitored as a function of time during variation of the temperature is shown in Figures 9-24 and 9-25. As expected, it is shown that, at the same temperature, the amplitude of the electrochemical noise is higher in the 0.1m HCl solution than in pure water, indicating that more severe corrosion occurs on Type 304 SS in the acidic solution than in pure water.
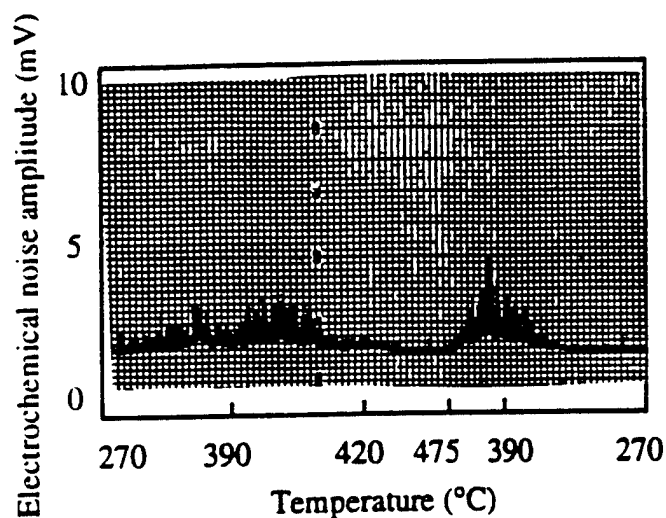
Figure 9-24.   Electrochemical current noise amplitude as a function of time for Type 304 SS in oxygen-saturated water.
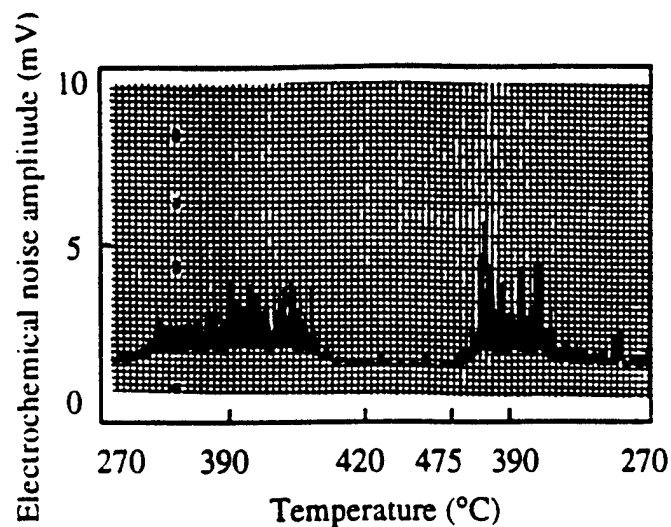
Figure 9-25.   Electrochemical current noise amplitude as a function of time for Type 304 SS in 0.1m HCl solution.

Importantly, the amplitude of the electrochemical noise observed with Type 304 SS, in both cases, is most pronounced in the vicinity of the critical point of water, noting that the critical point of dilute solutions (i.e., 0.1m HCl) is similar to that of pure water. This observation can be explained by a model simulating corrosion processes at near critical and supercritical temperatures that takes into account the rapid decrease in the density and concentrations of aggressive species (e.g., $H+, O_2$) in solution with increasing temperature above the critical point.[30]

9.2.10 Summary and Conclusions

An important finding of this study is that the corrosion activity of metals and alloys exposed to subcritical and supercritical aqueous environments can be monitored through

electrochemical noise analysis. This study shows that the amplitude of electrochemical noise varies with system parameters and fluid properties in a understandable manner, and that the corrosion damage is most pronounced in the vicinity of critical temperature of water.

9.2.11 References

1.   EPA Engineering Bulletin "Supercritical Water Oxidation," EPA 540/S92/006, Office of Research and Development, Risk Reduction Engineering Laboratory, United States Environmental Protection Agency.

2.   R. W. Shaw, T. B. Brill, A. A. Clifford, C. E. Eckert and E. U. Frank, "Supercritical Water, A Medium for Chemstry," C&EN, p. 26 (1991).

3.   H. E. Barner, C. Y. Huang, T. Johnson, G. Jacobs, M. A. Martch and W. R. Killilea, J. Hazardous Materials, 31, 4 (1992).

4.   P. A. Webley, J. W. Tester and H. R. Holgate, Ind. Eng. Chem. Res., 30, 1745 (1991).

5.   T. B. Thomason and M. Modell, Hazard Waste, 1, 453 (1984).

6.   K. C. Chang, L. Li and E. F. Gloyna, J. Hazardous Materials, 33, 51 (1993).

7.   K. D. Johnson, "New Directions in Supercritical Fluid Science and Technology," ACS Symposium Series 406, Eds. K. P. Johnson, J. M. L. Penninger, pub. American Chemical Society, Washington, DC, p. 1 (1989).

8.   P. Köll, B. Brönstrup, J. O. Metzger, "Liquefaction of Biomass with Supercritical Fluids in a High Pressure /High Temperature Flow Reactor," Chem. Eng. at Supercritical Fluid Conditions, Eds. M. E. Paulaitis, J. M. L. Penninger, R. D. Gray Jr. and P. Davidson, pub. Ann Arbor Science, Ann Arbor, MI.

9. D. J. Mills, G. B. Bierwagen, B. Skerry and D. Tallman, "Characterization of Corrosion under Coatings by Electrochemical Noise Methods," Proc. 12th Int. Corros. Congr., Houston, TX, Sept. 1993, Pub. NACE (Houston, TX), **1**, p. 182 (1993).

10. C. Gabrielli, F. Huet and M. Keddam, "Introduction of Metallic Corrosion by Electrochemical Noise Techniques," in Electrochemical and Optical Techniques for the Study and Monitoring of Metallic Corrosion, Eds. M. G. S. Ferreira and C. A. Melendres, Pub. Kluwer Academic Publishers, The Netherlands, p.135 (1991).

11. C. Gabrielli, F. Huet, M. Keddam and M. Macias, "Electrochemical Noise Generated by a Corroding Electrode, Effect of Metallurgy and Inhibitors," In Surface, Inhibition, and Passivation, Eds. E. McCafferty and R. J. Brodd, Proceedings Vol. 86-7, pub. The Electrochemical Society, Inc., (Pennington, NJ), p. 507 (1986).

12. E. Benzaid, F. Huet, C. Gabrielli, M. Jerome, F. Wenger and J. Galland, "Investigation of Electrochemical Noise in the Study of Hydrogen Embrittlement of a 42CD4 Carbon Steel Electrode," in Progress in the Understanding and Prevention of Corrosion (Proc. 10th European Corrosion Congr., July, 1993, Barcelona, Spain), Eds. J. M. Costa and A. D. Mercer, Pub. The Institute of Materials, London, UK, **2**, p. 1304 (1993).

13. K. Hladky and J. L. Dawson, Corros. Sci., **21**, 4, p.317 (1981).

14. J. L. Dawson, D. M. Farell, P. J. Aylott and K. Hladky, "Corrosion Monitoring Using Electrochemical Noise Measurements," NACE Corrosion/89, New Orleans, LA, Paper #31, (NACE, Houston, TX) (1989).

15. M. Kending and D. Anderson, Corrosion, **48**, 3, p. 178 (1992).

16. U. Bertocci, J. L. Mullen and Y. X. Ye, "Electrochemical Noise Measurements for The Study of Localized Corrosion and Passivity Breakdown," in Passivity of Metal and Semiconductors, Ed. M. Froment, Elsevier Science Publishers B. V., New York, p. 229 (1983).

17. J. Flis, J. L. Dawson, J. Gill and G. C. Wood, Corros. Sci., **32**, 8, p. 877 (1991).

18. D. A. Eden, A. N. Rothwell, "Electrochemical Noise Data: Analysis, Interpretation and Presentation," Corrosion 92, The NACE Annual Conference and Corrosion Show, May, Nashville, TN, Paper #292, (NACE, Houston, TX) (1992).

19. D. A. Eden, A. N. Rothwell and J. L. Dawson, "Electrochemical Noise for Detection of Susceptibility to Stress Corrosion Cracking," Corrosion 91, The NACE Annual Conference and Corrosion Show, March, 92, Cincinnati, OH, Paper #444, (NACE, Houston, TX) (1992).

20. J. Stewart, D. B. Wells, P. M. Scott and D. E. Williams, Corros. Sci., **33**, p. 73, (1991).

21. C. Monticelli, G. Brunoro, A. Frignani and G. Trabanelli, J. Electrochem. Soc., **139**, 3, p. 706 (1992).

22. F. Mansfeld, H. Xiao, "Electrochemical Noise Analysis of Iron Exposed to NaCl Solutions of Different Corrosivity," Proc. 12th Int. Corros. Congr., Houston, TX, Pub. NACE (Houston, TX), Vol. 3A, p. 1388 (1993).

23. P. R. Roberge, "Analysis of Spontaneous Electrochemical Noise with Stochastic Pattern Detector Method," in Progress in the Understanding and Prevention of Corrosion (Proc. 10th European Corrosion Congr., July, 1993, Barcelona, Spain), Eds. J. M. Costa and A. D. Mercer, Pub. The Institute of Materials, London, UK, Vol. 2, p. 1345 (1993).

24. N. J. E. Dowling, C. Thual-Duret, G. Auclair, J. P. Audouard and P. Combrade, "Assessment of the Pitting Susceptibility of AISI 303 and 304 Stainless Steels as a Function of Sulphur Content Using Electrochemical Noise," in Progress in the Understanding and Prevention of Corrosion (Proc. 10th European Corrosion Congr., July, 1993, Barcelona, Spain), Eds. J. M. Costa and A. D. Mercer, Pub. The Institute of Materials, London, UK, Vol. 2, p. 1328 (1993).

25. C. Liu, D. D. Macdonald, E. Medina, J. Villa and J. Bueno, Corros., Vol. 50, No. 9, p. 687 (1994).

26. D. D. Macdonald, C. Liu and M. P. Manahan, "Electrochemical Noise Measurements on Carbon and Stainless Steels in High Subcritical and Supercritical Aqueous Environments", Proc. 1st Int. Symp. on Electrochemical Noise Measurement For Corrosion Applications, Montréal, Québec, Canada, (ASTM, Philadelphia, PA) (1994).

27. R. W. Bain, Steam Tables, Pub. Her Majesty's Stationary Office, Edinburgh, UK, (1964).

28. D. D. Macdonald, J. Pang, C. Liu, E. Medina, J. Villa and J. Bueno, "Development of Sensors For In-Situ Monitoring of Corrosion and Water Chemistry Parameters For Electric Power Utility Industry," Proc. 12th Int. Corros. Congr, Houston, TX, Pub. NACE (Houston, TX), Vol. 6, p. 4727 (1993).

29. D. D. Macdonald, J. Pang, C. Liu, L. B. Kriksunov, E. Medina, J. Villa and J. Bueno, "Monitoring Corrosion and Chemistry Phenomena in Supercritical Aqueous Systems," Corrosion 94, The NACE Annual Conference and Corrosion Show, Paper # 627, Baltimore, MD, (NACE International, Houston, TX) (1994).

30. L. B. Kriksunov and D. D. Macdonald, "Phenomenological Analysis of Corrosion in Supercritical Water Oxidation Systems", Proc. 1st Int. Workshop on Supercritical Water Oxidation Technology, Jacksonville, FL (1995).

SECTION 10

CERAMIC-TO-METAL JOINING

10.1. BRAZING OF ZIRCONIA TO METAL FOR DEVELOPMENT OF OXYGEN AND pH SENSORS FOR HIGH-TEMPERATURE, HIGH-PRESSURE AQUEOUS ENVIRONMENTS

10.1.1 Abstract

Zirconia electrodes are routinely used as oxygen sensors at temperatures of 600°C and are now extensively used as pH sensors in high-temperature high-pressure aqueous systems (300°C and 3000 psi). Brazing of zirconia tubes to metal is one approach to making such sensors. A variety of metal supports (304L SS, Ni, Cu), three braze alloys in the Ag-Cu-Ti system and their combinations were investigated in bonding with the zirconia tubes. The important issues were the weakening of the zirconia matrix during brazing, bonding with the metal, and corrosion of the braze under operating conditions of 300°C and 3000 psi in aqueous environments. The results obtained are discussed along with guidelines for further investigations.

10.1.2 Introduction

Zirconia is one of the most widely used oxygen sensor materials because of its unique combination of high strength, chemical stability under a broad range of oxidizing and reducing conditions, and its ability to conduct oxide ions via an oxygen vacancy mechanism through the matrix under proper doping conditions. Zirconia membranes have been successfully used as oxygen sensors in automobiles to provide feedback to control the air/fuel ratio. This same materials is now used extensively as a pH sensor in high-temperature, high-pressure aqueous environments (T>500°C and P>5000 psi). At temperatures above ~200°C, the voltage response

to changes in pH, as measured against a suitable reference electrode, is sufficiently rapid that practical pH monitoring devices are readily fabricated[1-2]. However, the need to pass a brittle ceramic tube through a pressure boundary presents considerable mechanical and reliability problems. These problems would be greatly relieved by joining the ceramic (YSZ) tube to a metal tube, which would serve to penetrate the pressure boundary. Such a configuration has stringent requirements on pressure sealing. An additional constraint in producing a leak-proof braze is that the braze must be able to withstand the corrosive environments to which these pH sensor are frequently exposed. The use of Teflon as a sealing material is satisfactory, as long as the seal can be cooled externally. The cooling requirements limit the placement of these sensors to being mounted in the wall of the pressure vessel. In situations where the sensor has to be placed deep into the pressure vessel and cooling of the seal is not feasible, alternatives to Teflon sealing have to be employed. Brazing is a possible alternative that can provide a leak-proof seal at the temperatures and pressures concerned. The corrosion resistance of the brazed joint has to be carefully considered so as to be compatible with the chemical environment inside the autoclave.

Brazing of zirconia using active metal alloys has been reported extensively in the literature[3-5]. However, the ability of the brazed joint to withstand the corrosive environment has not been thoroughly investigated. Niedrach[6] reported success with active metal brazing of zirconia to titanium support tubes, but in our experience, the system using titanium as the metal support causes extensive reaction with and weakening of zirconia and, hence, was considered unsatisfactory for most applications. In this report, we present the results of our evaluations of braze alloys and support metals to produce a hermetic, corrosion-resistant joint.

10.1.3 Experimental Procedure

The zirconia (yttria-stabilized zirconia, ZDY-4, Coors Ceramics, Golden, CO) used for the evaluation was in the form of a tube, 6.35 mm OD, and 0.8 mm thick wall and 100 mm in length with one end closed. The design of the metal support was chosen such that it would exert compressive pressure on the braze and the zirconia tube during cooling, which would increase the chances of forming a hermetic seal. The metal supports were made from commercially available 304L, Ni, and Cu. The braze alloy, in the form a 50 μm foil, was placed in position before the assembly was heated in a furnace. A schematic of the braze assembly before and after the brazing operation is shown in Figure 10-1.

(a)   (b)

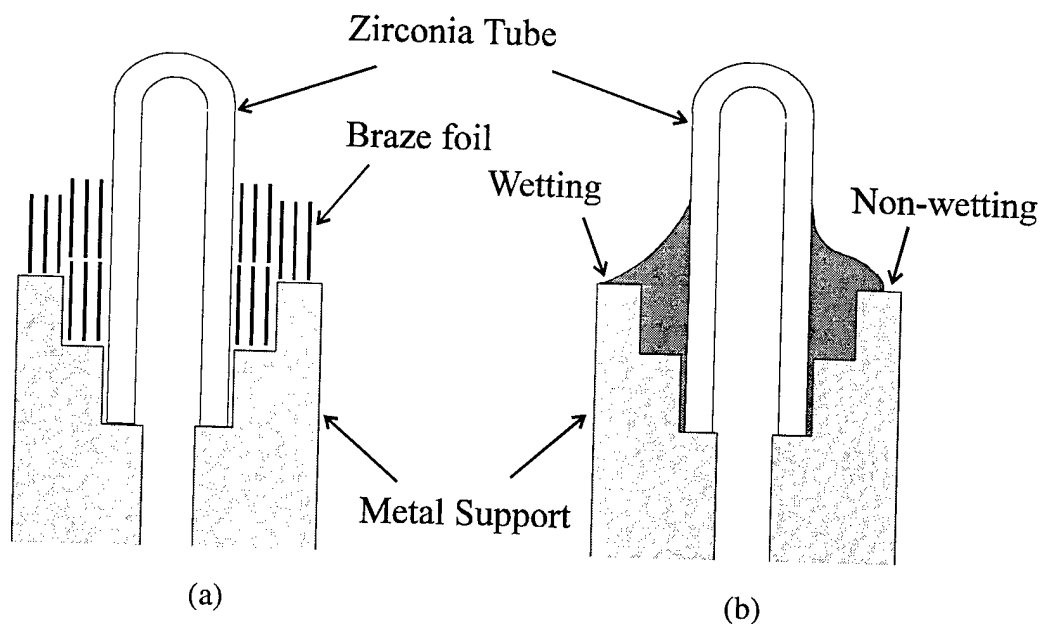Figure 10-1. Schematic of the braze assembly before (a) and after (b) the brazing operation. The braze alloy was placed in the form of three rolls of three windings each; the two inner rolls were used to correct for possible leak paths at the overlap region of each roll, the third roll to consolidate the inner rolls. Schematic (b) shows the nature of the wetting profile for wetting and non-wetting conditions.

The assembly was suspended in a vertical tube; this arrangement allowed the quartz tube to be raised and lowered into the hot zone of the furnace and as a means of accurate temperature control. A measurement thermocouple, in a protective quartz sheath, was placed adjacent to the braze alloy to monitor the temperature of the braze. The furnace was evacuated and back-filled with commercial grade argon before letting the argon flow through the furnace at a slight over-pressure to prevent ingress of oxygen through the joints. Titanium getters were placed upstream in the hot zone to remove any traces of oxygen in the argon. The tube furnace was evacuated with a roughing pump near the end of the brazing cycle while the braze was still molten, to remove any gas bubbles trapped in the braze pool. The temperature profile included time for equalization of temperature (5 minute at 150°C below liquidus), heating to a temperature of 50°C above liquidus in 10 minutes, holding at that temperature for 5 minutes, followed by a gradual cool down to the equalization for another 5 minutes, and then allow the furnace to cool down to room temperature.

The brazed joints were first tested by applying line air pressure to the open end of the metal tube while the joint was immersed in water to check for bubbles, which would indicate a leak. The joints that withstood this test were then fitted into an autoclave and tested in water at 25°C at pressures increasing from atmospheric to 3000 psi. The joints that withstood the maximum pressure were then tested in water at 300°C, while maintaining the pressure at 3000 psi. The end of the metal tube, which was exposed to the ambient, was monitored for any signs of leaking steam.

10.1.4 Results and Discussions

The configurations tested are listed in Table 10-1; the results of each are discussed below in the same order.

Table 10-1. Material combinations used in this study for brazing of zirconia membranes.

Config. Number	Metal Support	Braze alloy compositions (wt%)	Solidus/ Liquidus(°C)	Trade name
1.	304L	68.8Ag/26.7Cu/4.5Ti	830/850	Ticusil*
2.	304L	63Ag/35.25Cu/1.75Ti	780/815	Cusil-ABA*
3.	Ni	63Ag/35.25Cu /1.75Ti	780/815	Cusil-ABA *
4.	Ni	92.75Ag/5Cu/1.25Ti/1.0Al	860/912	Silver-ABA *
5.	Cu	92.75Ag/5Cu/1.25Ti/1.0Al	860/912	Cusil-ABA *

*WESGO Technical Ceramics and Metals, Belmont, CA.

10.1.4.1 304L / Ticusil / Zirconia

Stainless steel was the material of choice, because it has good corrosion resistance in the environments of interest. The active alloy based on the Ag-Cu eutectic and containing 4.5 wt% Ti was chosen for the first configuration; the high Ti alloy was chosen to ensure that enough Ti was available to complete the reaction with the metal and ceramic during brazing. The zirconia underwent extensive discoloration near the braze region and broke in the darkened zone during subsequent handling. The fractures revealed that the zirconia was discolored through the wall thickness, indicating extensive and detrimental reaction with the brazing alloy. This led us to try a brazing alloy with lesser amount of Ti.

10.1.4.2 304L / Cusil ABA / Zirconia

In this configuration, the braze alloy was changed to one containing 1.75 wt% Ti in a Ag-Cu eutectic. The result was a significantly reduced discoloration of the zirconia tube; the strength had also improved and the joint could withstand the rigors of handling. Air pressure tests revealed that the joint hermeticity was not consistent and failure occurred at the metal/braze interface. The lack of flow of the brazing alloy did indicate a non-wetting geometry, as shown in Figure 10-1 (schematic) and in Figure 10-2 (backscattered image). Note that the contact angle is nearly 90° at the braze/steel interface in Figure 10-2. The inability of the Ti in the braze to consistently reduce and wet the stainless steel surface led us to evaluate other possible support tube materials.

10.1.4.3 Ni / Cusil ABA / Zirconia

Nickel was chosen to replace stainless steel since it also has good corrosion resistance in high-temperature water. Once again, the zirconia tube did not show any significant discoloration and that was true for all of the joints made with alloys containing less than 2 wt% Ti. The braze also appeared to have wet the metal with no external signs of porosity or discontinuities. The joint withstood the air-pressure test, the high-pressure/ambient temperature test and the subsequent temperature (300°C) test for three days, after which it leaked. Visual inspection of the joint after the test revealed cave-like formations at the metal-braze interface, indicating that the braze reaction layer/layers had corroded with time; the braze/ceramic interface appeared intact. Cross-sectional analysis of one of the untested specimens is shown in Figure 10-3. The various reaction layers are as marked, with their compositions given in the caption. Which of

these layers initiated the corrosion could not be determined, although we postulated that it was probably the copper-rich phase. To avoid the formation of the copper-containing layer, an alloy with significantly lower amounts of copper was chosen for further evaluation.

10.1.4.4 Ni / Silver ABA / Zirconia

The alloy chosen was Silver ABA. The alloy exhibited poor wetting of the nickel support and the joint leaked in the air pressure test. An assessment of the Ag-Ni phase diagram revealed that even a small addition of Ni to the silver (braze) would cause a significant increase in the melting point of the braze, thus reducing the fluidity of the melt at the brazing temperature. The presence of the copper-containing layer in the previous configuration may have improved the wettability of the braze, even though it had an adverse effect on the corrosion behavior. Based on the chemistry of the braze system, it appeared that either copper or silver, which are the main constituents of this braze system, would be suitable as metal supports.

10.1.4.5 Cu / Cusil ABA / Zirconia

Because using a silver support would have been considerably more expensive, a cooper support was used in the last configuration evaluated. The braze alloy wet the support satisfactorily, and the braze withstood the test at pressure and temperature (300°C and 300 pig) for six days before the test was terminated. The drawback of using copper support is that copper is not very resistant to corrosion in high temperature aqueous systems, particularly in the presence of oxidizing (e.g., O_2) and complexing (Cl^-, NH_3) agents.

Figure 10-2. Backscatter image of a cross-section at a Zirconia/Cusil ABA/304L SS configuration (#2). Zirconia is on the left, SS on the lower right with portions of the braze in between the two and on the shoulder. The poor wetting at the metal/braze interface is evident by the 90 wetting angle (location marked by arrow).
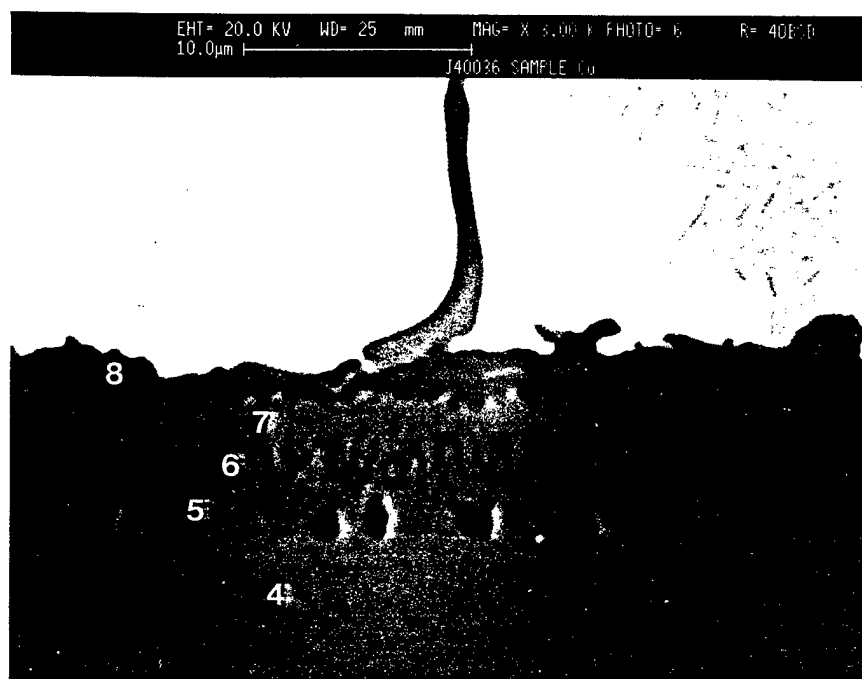
Figure 10-3. Backscatter image of a cross-section at the Zirconia/Cusil ABA/Ni configuration (#3) showing the Ni/braze interface; the location of the corrosion failure. The different reaction layers are evident and are labeled 4 (91Ni/5Ti/2Ag/2Cu), 5 (89Ni/10Ti/1Cu), 6 (75Ni/23Ti/1Cu), 7 (79Ni/17Ti/2Cu), and 8 (50Ni/32.1Ti/0.5Ag/21Cu) with compositions based on EDS spectra and ZAF corrections. The material adjacent to layer #8 is the residual braze alloy and layer #4 is the nickel support with elements from the braze in solution.

10.1.5 Summary

A variety of metal support/braze alloy combinations were evaluated in order to find the best pair for fabricating pH sensors for use in high temperature/high pressure aqueous systems. Only Ti-based active alloys were investigated in this study. The results indicate that high levels of Ti (4.5 wt%) caused extensive reaction with the zirconia ceramic resulting in significant weakening of the zirconia tube. Lower levels of Ti (<2 wt%) were sufficient to form a strong bond at the braze/ceramic interface, but without the weakening. However, the lower levels of active element did not ensure the formation of a hermetic seal at the stainless steel/braze interface. The reaction layers formed at the interface with a nickel support were susceptible to corrosion under the operating conditions. The choice of copper as the support metal proved satisfactory but is susceptible to corrosion in high temperature aqueous environment, particularly in the presence of oxidizing and/or complexing agents.

10.1.6 Conclusions

The results indicate that the choice of the braze system (ceramic/braze/metal) is important not only for strength and hermeticity under the rigors of the operating conditions but also for corrosion resistance. The optimum choice of the metal (support), which is a component of the braze alloy system, is one that ensures satisfactory wetting at the metal/braze interface. Surprisingly, the braze/zirconia interface proved to be rugged enough to withstand the conditions in the autoclave. Given the complex nature of these multicomponent systems, it is still not possible to specify *a priori* the most effective braze alloy composition; this must be determined by experimentation.

10.1.7 ACKNOWLEDGMENTS

10.1.8 REFERENCES

1.   D. D. Macdonald, et. al, J. Soln. Chem., **21**, 849 (1992).

2.   K. Makela, et. al, Proc. 12th Scand. Corros. Congr. & Eurocorr '92, Finland (1992).

3.   E. Park, J. D. Cawley, and D. Hauser, 167-180, Metal-Ceramic Joining, P. Kumar and V. A. Greenhut, eds., TMS Fall Meeting, Detroit, MI, 1990.

4.   B. S. Majumdar and J. Ahmad, 67-99, *ibid.*

5.   C. Peytour, P. Berthet, F. Barbier, A. Revcolevschi, J. Mat. Sci. Lett., 1129-1131, **9**, (1990).

6.   L. W. Niedrach, Advances in Ceramics Science, 672-684 [12].

SECTION 11

PUBLICATIONS

1. L. B. Kriksunov, D. D. Macdonald, "Advances in measuring chemistry parameters in high temperature aqueous systems", in: <u>Physical Chemistry of Aqueous Systems. Meeting the Needs of Industry</u>, Edited by H.J.White et al., Begell House, NY, 1995.

2. L. B. Kriksunov and D. D. Macdonald, "Development of Pourbaix diagrams for Metals in Supercritical Aqueous Media", <u>Proc. First Int'l Workshop on Supercritical Water Oxidation</u>, Jacksonville, FL (1995).

3. L. B. Kriksunov, C. Liu, and D. D. Macdonald, "Oxygen, hydrogen, and redox potential combination sensor for supercritical aqueous systems", <u>Proc. First Int'l Workshop on Supercritical Water Oxidation</u>, Jacksonville, FL (1995).

4. L. B. Kriksunov and D. D. Macdonald, "Phenomenological Analysis of Corrosion Phenomena in Supercritical Aqueous Systems", <u>Proc. First Int'l Workshop on Supercritical Water Oxidation</u>, Jacksonville, FL (1995).

5. C. Liu, L. B. Kriksunov, D. D. Macdonald, "Electrochemical noise analysis in monitoring corrosion activity in SCWO", <u>Proc. First Int'l Workshop on Supercritical Water Oxidation</u>, Jacksonville, FL (1995).

6. L. B. Kriksunov and D. D. Macdonald, "Development of Potential-pH diagrams for supercritical aqueous solutions I. Iron-water system", Corrosion, in press (1996).

7. L. B. Kriksunov and D. D. Macdonald, "Amperometric hydrogen sensor for high temperature water", Sensors and actuators B (Chemical), **B32**, 57 (1996).

8. L. B. Kriksunov and D. D. Macdonald, "Corrosion in supercritical aqueous systems and the density of solvent", <u>Extended Abstracts, 187 Meet. Electrochem. Soc.</u>, Reno, Nevada (1995).

9. L. B. Kriksunov and D. D. Macdonald, "Electrochemical sensors for high temperature aqueous environments", <u>Extended Abstracts, 187 Meet. Electrochem. Soc.</u>, Reno, Nevada (1995).

10. L. B. Kriksunov and D. D. Macdonald, "Corrosion in supercritical water oxidation systems: a phenomenological analysis", Journal of the Electrochemical Society, **142**, 4069 (1995).

11. L. B. Kriksunov and D. D. Macdonald, "Understanding chemical conditions in Supercritical Water Oxidation Systems", Proc. Symposium on Thermal-hydraulics and Combustion of Toxic Waste Destruction Processes, ASME Winter Annual Mtg., San Fransisco, CA (1995).

12. L. B. Kriksunov and D. D. Macdonald, "Corrosion testing and prediction in SCWO environments", Proc. Symposium on Thermal-hydraulics and Combustion of Toxic Waste Destruction Processes, ASME Winter Annual Meeting, San Fransisco, CA (1995).

13. L. B. Kriksunov and D. D. Macdonald, "Understanding corrosion in high subcritical and supercritical aqueous environments," 1995 Summer National Meeting of AIChE, Boston, MA, (1995).

14. L. B. Kriksunov and D. D. Macdonald, "Measurement and standardization of pH in supercritical aqueous systems", Symposium on High Temperature and Pressure Solution Chemistry, Int'l Chem. Congr. of Pac. Basin Soc. (PACIFICHEM), Honolulu, HI (1995).

15. L. B. Kriksunov and D. D. Macdonald, "Estimating dissociation parameters at high temperatures from specific conductance data", Symposium on High Temperature and Pressure Solution Chemistry, Int'l Chem. Congr. of Pac. Basin Soc. (PACIFICHEM), Honolulu, HI (1995).

16. D. D. Macdonald and L. B. Kriksunov, "Critical issues in the supercritical water oxidation of army toxic wastes", ACS, I&EC Division, Symposium on Emerging Technologies in Hazardous Waste Management VII, Atlanta, GA, September 1995.

17. D. D. Macdonald, S. Lvov, and L. B. Kriksunov, "Applications of electrochemistry in high temperature water", Proc. IAPWS Annual Mtg., Paris, France (1995).

18. C. Liu and D. D. Macdonald, "Monitoring dissolved hydrogen in supercritical aqueous environments", Extended Abstracts, 187 Meet. Electrochem. Soc., Reno, Nevada (1995).

19. C. Liu and D. D. Macdonald, "An Advanced Pd/Pt Relative Resistance Sensor for the Continuous Monitoring of Dissolved Hydrogen in Aqueous Systems at High Subcritical and Supercritical Temperatures", J. Supercritical Fluids, 8, 263 (1995).

20. N. Hara and D. D. Macdonald, "Oxygen Response of Yttria-Stabilized Zirconia Sensors with Ag Powder Electrodes in Gaseous and Aqueous Systems", Proc. 4th Int'l Symp. On Supercrit. Fluids, Sendai, Japan, May 11-14, 1997.

21. N. Hara and D. D. Macdonald, "Development of Dissolved Hydrogen Sensors Based on Yttria-Stabilized Zirconia Solid Electrolyte", <u>Proc. 4th Int'l Symp. On Supercrit. Fluids</u>, Sendai, Japan, May 11-14, 1997.

22. D. D. Macdonald, "Chemistry Sensors for the Universal Solvents--Supercritical Aqueous Systems", <u>Proc. 4th Int'l. Symp. Supercrit. Fluids</u>, Sendai, Japan, May 11-14, 1997.

23. G. P. Kelkar, R. Biswas, A. Bertuch, and D. D. Macdonald, "Brazing of Zirconia to Metal for Development of Oxygen and pH Sensors for High-Temperature, High-Pressure Aqueous Environments", <u>Proc. 98th Annual ACERS Mtg. And Expo.</u>, Session-Joint Synthesis III: Chemistry.

24. N. Hara and D. D. Macdonald, "Oxygen Response of Yttria-Stabilized Zirconia Sensors with Ag Powder Electrodes in Gaseous and Aqueous Systems", submitted to the J. Electrochem. Soc. (1997).

25. N. Hara and D. D. Macdonald, "Development of Dissolved Hydrogen Sensors Based on Yttria-Stabilized Zirconia Solid Electrolyte", submitted to the J. Electrochem. Soc. (1997).

SECTION 12

SCIENTIFIC PERSONNEL SUPPORTED BY THIS PROJECT AND DEGREES AWARDED DURING THIS PROJECT

The following scientific personnel were financially supported by this project:

- Dr. Digby D. Macdonald

- Dr. Leonid Kriksunov

- Ms. Heidi Arthur

- Mr. Ritwik Biswas

- Mr. Theodore Inniss

The following scientific personnel were not financially supported by this project, but contributed significantly to the completion of this work:

- Dr. Nobuyoshi Hara

- Dr. Girish Kelkar

- Dr. Chun Liu

- Dr. Serguei Lvov

- Dr. Jan Mankowski

- Mr. Keith Eklund

The following degrees were awarded during this project:

- Mr. Keith Eklund, M.S.